



# Mechanical properties of nanocrystalline materials

M.A. Meyers<sup>\*</sup>, A. Mishra, D.J. Benson

*Department of Mechanical and Aerospace Engineering, Materials Science and Engineering Program,  
Mail Code 0411, University of California, San Diego La Jolla, CA 92093, United States*

Received 1 November 2004; revised 1 May 2005; accepted for publication 1 August 2005

---

## Abstract

The mechanical properties of nanocrystalline materials are reviewed, with emphasis on their constitutive response and on the fundamental physical mechanisms. In a brief introduction, the most important synthesis methods are presented. A number of aspects of mechanical behavior are discussed, including the deviation from the Hall–Petch slope and possible negative slope, the effect of porosity, the difference between tensile and compressive strength, the limited ductility, the tendency for shear localization, the fatigue and creep responses. The strain-rate sensitivity of FCC metals is increased due to the decrease in activation volume in the nanocrystalline regime; for BCC metals this trend is not observed, since the activation volume is already low in the conventional polycrystalline regime. In fatigue, it seems that the  $S$ – $N$  curves show improvement due to the increase in strength, whereas the  $da/dN$  curve shows increased growth velocity (possibly due to the smoother fracture requiring less energy to propagate). The creep results are conflicting: while some results indicate a decreased creep resistance consistent with the small grain size, other experimental results show that the creep resistance is not negatively affected. Several mechanisms that quantitatively predict the strength of nanocrystalline metals in terms of basic defects (dislocations, stacking faults, etc.) are discussed: break-up of dislocation pile-ups, core-and-mantle, grain-boundary sliding, grain-boundary dislocation emission and annihilation, grain coalescence, and gradient approach. Although this classification is broad, it incorporates the major mechanisms proposed to this date. The increased tendency for twinning, a direct consequence of the increased separation between partial dislocations, is discussed. The fracture of nanocrystalline metals consists of a mixture of ductile dimples and shear regions; the dimple size, while much smaller than that of conventional polycrystalline metals, is several times larger than the grain size. The shear regions are a direct consequence of the increased tendency of the nanocrystalline metals to undergo shear localization.

---

<sup>\*</sup> Corresponding author. Tel.: +1 858 534 4719; fax: +1 858 534 5698.  
E-mail address: [mameyers@ucsd.edu](mailto:mameyers@ucsd.edu) (M.A. Meyers).

The major computational approaches to the modeling of the mechanical processes in nanocrystalline metals are reviewed with emphasis on molecular dynamics simulations, which are revealing the emission of partial dislocations at grain boundaries and their annihilation after crossing them.

© 2005 Published by Elsevier Ltd.

---

## Contents

1.	Introduction . . . . .	429
2.	History . . . . .	431
3.	Classification . . . . .	433
4.	Synthesis . . . . .	434
4.1.	Inert gas condensation . . . . .	435
4.2.	Mechanical alloying . . . . .	436
4.3.	Electrodeposition . . . . .	438
4.4.	Crystallization from amorphous solids . . . . .	438
4.5.	Severe plastic deformation . . . . .	440
5.	Mechanical properties of nanocrystalline metals and alloys . . . . .	443
5.1.	Yield strength . . . . .	444
5.2.	Ductility . . . . .	445
5.3.	Inverse Hall Petch effect: fact or fiction . . . . .	448
5.4.	Strain hardening . . . . .	453
5.5.	Strain-rate sensitivity . . . . .	455
5.5.1.	Strain-rate sensitivity of ultrafine grained and nanostructured HCP metals . . . . .	458
5.5.2.	Mechanical behavior of iron as a representative BCC metal . . . . .	458
5.6.	Creep of nanocrystalline materials . . . . .	460
5.7.	Fatigue of nanocrystalline materials . . . . .	464
6.	Nanocrystalline ceramics and composites . . . . .	468
7.	Deformation mechanisms in nanostructured materials . . . . .	479
7.1.	Pile-up breakdown . . . . .	479
7.2.	Grain-boundary sliding . . . . .	482
7.3.	Core and mantle models . . . . .	488
7.4.	Grain-boundary rotation/grain coalescence . . . . .	497
7.5.	Shear-band formation . . . . .	501
7.6.	Gradient models . . . . .	504
7.7.	Twinning . . . . .	505
7.7.1.	Mechanical twins . . . . .	505
7.7.2.	Growth twins . . . . .	508
7.8.	Grain-boundary dislocation creation and annihilation . . . . .	511
8.	Fracture . . . . .	518
9.	Numerical modeling . . . . .	521
9.1.	Finite element simulations . . . . .	525
9.2.	Molecular dynamics simulations . . . . .	533
9.3.	The quasicontinuum method . . . . .	539
9.4.	Shock-wave propagation in nanocrystalline metals . . . . .	540
10.	Summary and conclusions . . . . .	543
	Acknowledgements . . . . .	548
	References . . . . .	549

---

## 1. Introduction

The landmark paper by Gleiter [1] redirected a significant portion of the global research efforts in materials science. The importance of this paper can be gauged by its 1300+ citations and the thousands of papers that appeared on this topic since its publication. Actually, this paper was preceded by an earlier, lesser known Gleiter paper, from 1983 [2]. In this paper, Gleiter points out the outstanding possibilities of what he called then “microcrystalline materials”. The name “nanocrystalline” has since taken over. The mechanical behavior of nanocrystalline materials has been the theme of approximately 500 publications. A significant number of review articles have been published. Table 1 shows the most important review articles as well as their foci.

Nanocrystalline materials have been the subject of widespread research over the past couple of decades with significant advancement in their understanding especially in the last few years [3]. As the name suggests, they are single or multi-phase polycrystals with nano scale ( $1 \times 10^{-9}$ – $250 \times 10^{-9}$  m) grain size. At the upper limit of this regime, the term “ultra-fine grain size” is often used (grain sizes of 250–1000 nm). Nanocrystalline materials are structurally characterized by a large volume fraction of grain boundaries, which may significantly alter their physical, mechanical, and chemical properties in comparison with conventional coarse-grained polycrystalline materials [4–6], which have grain sizes usually in the range 10–300  $\mu\text{m}$ . Fig. 1 shows a schematic depiction of a nanocrystalline material. The grain-boundary atoms are white and are not clearly associated with crystalline symmetry.

As the grain size is decreased, an increasing fraction of atoms can be ascribed to the grain boundaries. This is shown in Fig. 2, where the change of the volume fraction of inter-crystal regions and triple-junctions is plotted as a function of grain size. We can consider

Table 1  
Principal review articles on nanostructured materials [only first author named]

Author	Year	Title
Gleiter [1]	1989	Nanocrystalline materials
Birringier [6]	1989	Nanocrystalline materials
Gleiter [349]	1992	Materials with ultrafine microstructures: retrospectives and perspectives
Suryanarayana [3]	1995	Nanocrystalline materials: a critical review
Lu [39]	1996	Nanocrystalline metals crystallized from amorphous solids: nanocrystallization, structure, and properties
Weertman [361]	1999	Structure and mech. behavior of bulk nanocrystalline materials
Suryanarayana [350]	2000	Nanocrystalline materials—current research and future directions
Valiev [56]	2000	Bulk nanostructured materials from severe plastic deformation
Gleiter [22]	2000	Nanostructured materials: basic concepts and microstructure
Furukawa [66]	2001	Processing of metals by equal-channel angular pressing
Mohamed [351]	2001	Creep and superplasticity in nanocrystalline materials: current understanding and future prospects
Kumar [352]	2003	Mechanical behavior of nanocrystalline metals and alloys
Veprek [353]	2005	Different approaches to superhard coatings and nanocomposites
Wolf [354]	2005	Deformation of nanocrystalline materials by molecular-dynamics simulation: relationship to experiments?
Weertman [363]	2005	Structure and mechanical behavior of bulk nanocrystalline materials
Weertman [374]	2002	Mechanical behavior of nanocrystalline metals

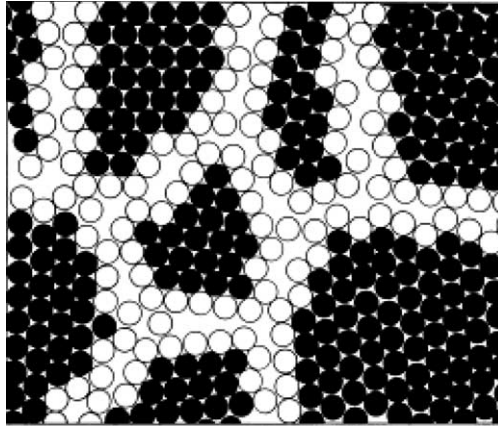


Fig. 1. Two-dimensional model of a nanostructured material. The atoms in the centers of the crystals are indicated in black. The ones in the boundary core regions are represented as open circles [22].

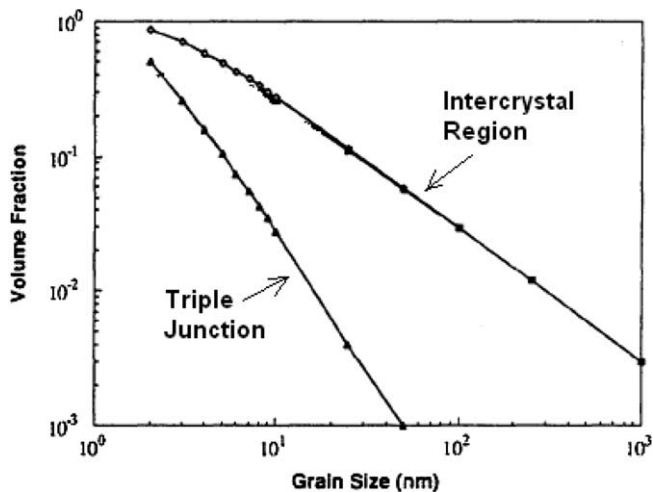


Fig. 2. The effect of grain size on calculated volume fractions of intercrystal regions and triple junctions, assuming a grain-boundary thickness of 1 nm [124].

two types of atoms in the nanocrystalline structure: crystal atoms with neighbor configuration corresponding to the lattice and boundary atoms with a variety of interatomic spacing. As the nanocrystalline material contains a high density of interfaces, a substantial fraction of atoms lie in the interfaces. Assuming the grains have the shape of spheres or cubes, the volume fraction of interfaces in the nanocrystalline material may be estimated as  $3\Delta/d$  (where  $\Delta$  is the average interface thickness and  $d$  is the average grain diameter). Thus, the volume fraction of interfaces can be as much as 50% for 5 nm grains, 30% for 10 nm grains, and about 3% for 100 nm grains.

Nanocrystalline materials may exhibit increased strength/hardness [7–9], improved toughness, reduced elastic modulus and ductility, enhanced diffusivity [10], higher specific

heat, enhanced thermal expansion coefficient (CTE), and superior soft magnetic properties in comparison with conventional polycrystalline materials. This has been the incentive for widespread research in this area, and lately, with the availability of advanced tools for processing and characterization, there has been an escalation of work in this field.

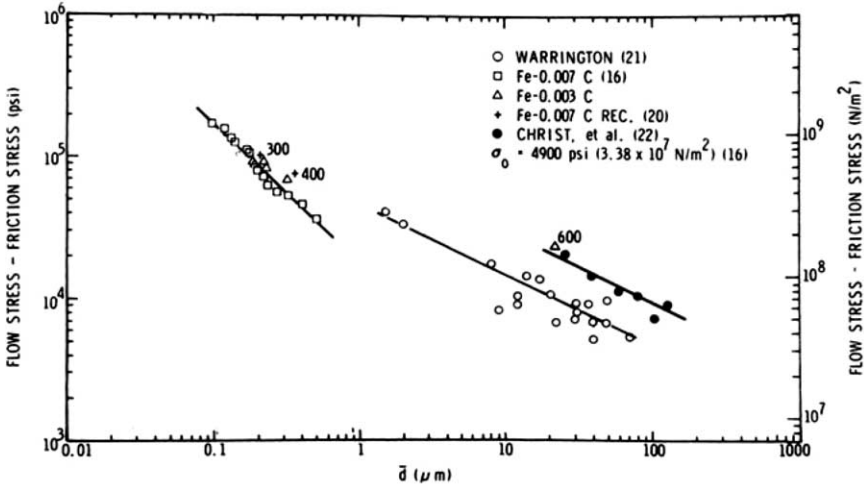
Nanostructured materials provide us not only with an excellent opportunity to study the nature of solid interfaces and to extend our understanding of the structure–property relationship in solid materials down to the nanometer regime, but also present an attractive potential for technological applications with their novel properties [11]. Keeping this incentive in mind, the purpose of this paper is to provide an overview of the basic understanding of the mechanical properties of these materials.

A number of techniques have surfaced over the years for producing nanostructured materials, but most of them are limited to synthesis in small quantities. There has been a constant quest to scale up the process to bulk processing, and lately, a few advances seem to hold technological promise. This has made research in this area exciting to a higher level. The most important methods are presented in Section 4.

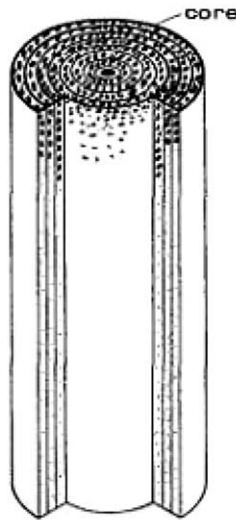
## 2. History

The synthesis and use of nanostructures are not new phenomena. In 1906, Wilm [12] observed age hardening in an Al–Cu–Mg–Mn alloy. Merica et al. [13] proposed in 1919 that the age hardening was caused by the precipitation of submicrometer-sized particles, which were later confirmed by X-ray and transmission electron microscopy (TEM). The precipitates are known as GP zones, GPII zones ( $\theta''$ ) and metastable ( $\theta'$ ) precipitates, and are typically 10 nm in thickness and 100 nm in diameter. In particular, the GP zones (named after Guinier and Preston, who suggested their existence through diffuse X-ray scattering) have thicknesses on the order of 1 nm. The accidental introduction of these precipitates into aluminum in the early 1900s revolutionized the aluminum industry, since it had a dramatic effect on its strength which enabled its widespread use in the burgeoning aircraft industry. Many important defects and phenomena in the mechanical behavior of materials take place at the nanoscale; thus, the realization that nanoscale is of utter importance has been a cornerstone of materials science for the past half century.

The quest for ultrafine grain sizes started in the 1960s by Embury and Fischer [14] and Armstrong et al. [15]. The driving force behind this effort was the possibility of synthesizing materials with strengths approaching the theoretical value ( $G/10$ ) by reducing the grain size, a reasonable assumption from the Hall–Petch relationship. A great deal of effort was also connected with superplasticity, since it is known that the smaller the grain size, the higher the strain rate at which this phenomenon is observed. Langford and Cohen [16] and Rack and Cohen [17] carried out detailed characterization of Fe–C and Fe–Ti wires cold drawn to true strains of up to 7. They observed a dramatic reduction in the scale of the microstructure, with grains/subgrains/cells with sizes as low as 300 nm. This reduction led to significant increases in the flow stress, shown in Fig. 3(a). The flow stress was increased to 1 GPa. The early effort by Schladitz et al. [18] to produce polycrystalline iron whiskers is also noteworthy. These whiskers, a section of which is shown in Fig. 3(b), had grain sizes between 5 and 20 nm. One could say that this is the first nanocrystalline metal. Jesser et al. [19] calculated the strength using the H–P equation ( $\sigma_0 = 70$  MPa;  $k = 17$  MPa m<sup>-1/2</sup>) and arrived at a predicted value of 5.5 GPa for  $d = 10$  nm. Unfortunately, these whiskers, produced by CVD, have diameters not exceeding 20  $\mu$ m.



(a)



(b)

Fig. 3. (a) Strength of wire drawn and recovered Fe-0.003C as a function of transverse linear-intercept cell size [17]; (b) Schladitz whisker, which can be considered the first nanocrystalline metal. The whisker is comprised of “onion-skin layers” with approximately 100 nm; these layers are composed of grains with diameters in the 5–20 nm range (from [19]).

Nanostructured materials as a major field in modern materials science did not start, however, until 1981 when Gleiter synthesized nanostructured metals using inert gas condensation (IGC) and in situ consolidation [20]. This involved generating a new class of materials with up to 50% or more of the atoms situated in the grain boundaries. Since the landmark paper of Gleiter, there has been increasing interest in the synthesis, processing, characterization, properties, and potential applications of nanostructured materials.

Accordingly, a number of techniques have been developed to produce nanoscale particles as well as bulk nanostructured materials. They are briefly described in Section 4, since the synthesis method has a direct and important bearing on the resultant mechanical properties.

### 3. Classification

Siegel [21] classified nanostructured materials into four categories according to their dimensionality: 0D—nanoclusters; 1D—multilayers; 2D—nanograined layers; 3D—equiaxed bulk solids. For the major part of this review, we will focus our attention on 3D equiaxed bulk solids. We will not include nanocrystalline coatings. For information on this,

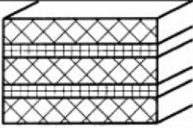
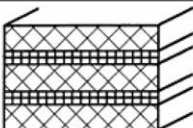
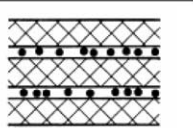
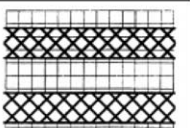
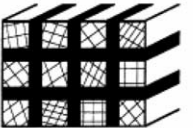

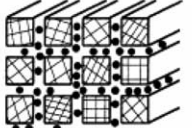
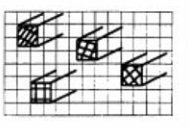
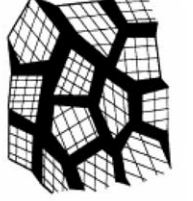
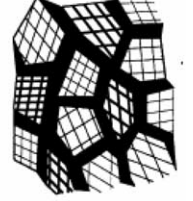
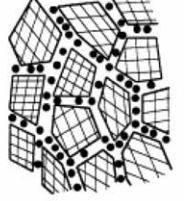
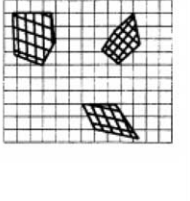
Chem. comp. of crystallites	Same	Different for different crystallites	Composition of boundaries and crystallites different	Crystallites dispersed in matrix of different composition
Shape of crystallites				
Layer-shaped				
Rod-shaped				
Equiaxed crystallized				

Fig. 4. Classification scheme for nanostructured materials according to their chemical composition and their dimensionality (shape) of the crystallites (structural elements) forming the nanostructure. The boundary regions of the first and second family are indicated in black to emphasize the different atomic arrangements in the crystallites and in the boundaries [22].

the reader is referred to Verpek [336]. However, nanowires, that are one-dimensional nanostructures, have important electronic properties.

Classification can also be made based on the grain size: ultrafine grain sized materials, where the grain sizes are above approximately 500 nm (usually in the sub-micrometer range) and nanograined materials, where the grain sizes are below 500 nm and usually in the vicinity of 100–200 nm. Based on the starting material from which nanomaterials are made, they can be further classified as nanomaterials crystallized from amorphous solid or nanomaterials made from other methods where the starting material is usually crystalline.

Gleiter [22] further classified the nanostructured materials according to composition, morphology, and distribution of the nanocrystalline component as shown in Fig. 4. He used three shapes: rods, layers, and equiaxed grains. His classification includes many possible permutations of materials and is quite broad. According to the shape of the crystallites, three categories of nanomaterials may be distinguished: layer-shaped crystallites, rod-shaped crystallites (with layer thickness or rod diameters in the order of a few nanometers), and nanostructures composed of equiaxed nanometer-sized crystallites. Depending on the chemical composition of the crystallites, the three categories of nanomaterials may be grouped into four families. In the simplest case, all crystallites and interfacial regions have the same chemical composition. Examples of this family are semicrystalline polymers or nanomaterials made up of equiaxed nanometer-sized crystals, e.g., of Cu. Nanomaterials belonging to the second family consist of crystallites with different chemical compositions. Quantum well structures are the most well known examples of this type. If the compositional variation occurs primarily between the crystallites and the interfacial regions, the third family of nanomaterial is obtained. In this case, one type of atom segregates preferentially to the interfacial regions so that the structural modulation is coupled to the local chemical modulation. Nanomaterials consisting of nanometer-sized W crystals with Ga atoms segregated to the grain boundaries are an example of this type. An interesting new example of such materials was recently produced by co-milling  $\text{Al}_2\text{O}_3$  and Ga. The fourth family of nanomaterials is formed by nanometer-sized crystallites dispersed in a matrix of different chemical composition.

#### 4. Synthesis

Nanocrystalline materials can be synthesized either by consolidating small clusters or breaking down the polycrystalline bulk material into crystalline units with dimensions of nanometers. These approaches have been classified into *bottom-up* and *top-down*. In the *bottom-up* approach we have to arrange the nanostructure atom-by-atom, layer-by-layer. In the *top-down* approach we start with the bulk material and break down the microstructure into a nanostructure. The principal synthesis methods are:

- Inert gas condensation
- Mechanical alloying
- Electrodeposition
- Crystallization from amorphous material
- Severe plastic deformation
- Cryomilling
- Plasma synthesis



- Chemical vapor deposition
- Pulse electron deposition
- Sputtering
- Physical vapor deposition
- Spark erosion [344]

We describe below the five most common methods.

#### 4.1. Inert gas condensation [1]

The inert gas condensation technique, conceived by Gleiter [1], consists of evaporating a metal (by resistive heating, radio-frequency, heating, sputtering, electron beam heating, laser/plasma heating, or ion sputtering) inside a chamber that is evacuated to a very high vacuum of about  $10^{-7}$  Torr and then backfilled with a low-pressure inert gas like helium (Fig. 5(a)). The evaporated atoms collide with the gas atoms inside the chamber, lose their kinetic energy, and condense in the form of small particles. Convection currents, generated by the heating of the inert gas by the evaporation source and by the cooling of the liquid nitrogen-filled collection device (cold finger) carry the condensed fine powders to the collector device. The deposit is scraped off into a compaction device. Compaction is carried out in two stages: (a) low pressure compacted pellet; (b) high pressure vacuum compaction. The scraping and compaction processes are carried out under ultrahigh vacuum conditions to maintain the cleanliness of the particle surfaces and to minimize the amount of trapped gases. The inert gas condensation method produces equiaxed (3D) crystallites. The crystal size of the powder is typically a few nanometers and the size distribution is narrow. The crystal size is dependent upon the inert gas pressure, the evaporation rate, and the gas composition. Extremely fine particles can be produced by decreasing either the gas pressure in the chamber or the evaporation rate and by using light rather than heavy inert gases (such as Xe).

A great deal of the early work on mechanical properties of nanocrystalline materials used the inert gas condensation technique. One shortcoming is the possibility of contamination of powders and porosity due to insufficient consolidation. There is also the possibility of imperfect bonding between particles, since most of the early work used cold consolidation. Nevertheless, the results obtained using specimens prepared by this method led the foundation of our understanding. The important contributions of Weertman, Siegel, and coworkers [23–27] have used materials produced by this method. They were the first systematic studies on the mechanical properties of nanocrystalline metals (Cu and Pd) and were initiated in 1989. Fig. 5(b) shows the bright field image TEM micrograph of TiO<sub>2</sub> nanoparticles prepared by this technique.

Nanocrystalline alloys can also be synthesized by evaporating the different metals from more than one evaporation source. Rotation of the cold finger helps in achieving a better mixing of the vapor. Oxides, nitrides, carbides, etc. of the metals can be synthesized by filling the chamber with oxygen or nitrogen gases or by maintaining a carbonaceous atmosphere. Additionally, at small enough particle sizes, metastable phases are also produced. Thus, this method allows the synthesis of a variety of nanocrystalline materials. The peak densities of the as-compacted metal samples have been measured with values of about 98.5% of bulk density. However, it has been established that porosity has a profound effect on the mechanical strength, especially in tension.

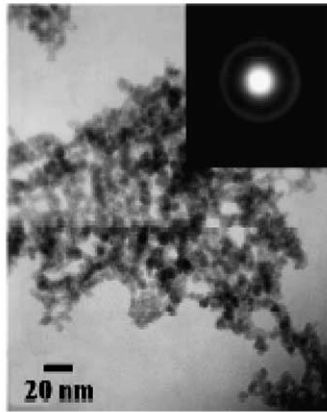
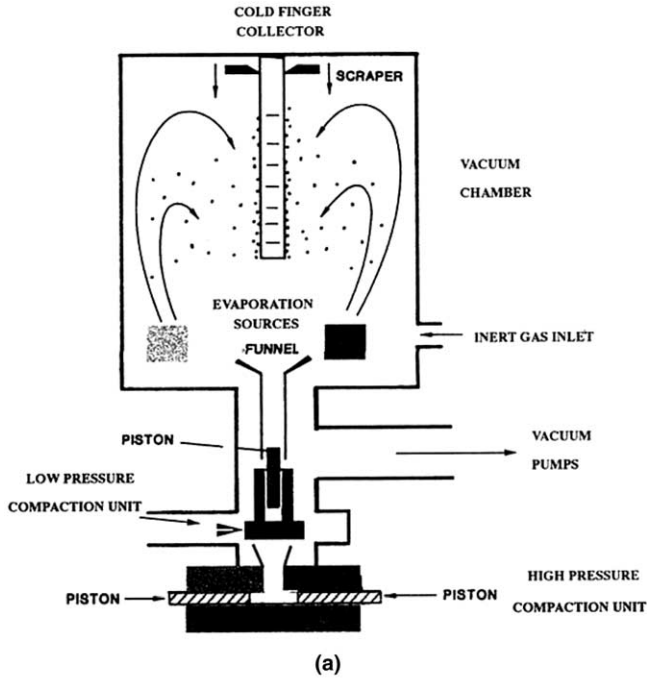


Fig. 5. (a) Schematic drawing of the inert gas condensation technique for production of nanoscale powder [365]; (b) bright field TEM micrograph of  $\text{TiO}_2$  nanoparticles prepared by inert gas condensation [366].

#### 4.2. Mechanical alloying

Mechanical alloying [28–31] produces nanostructured materials by the structural disintegration of coarse-grained structure as a result of severe plastic deformation. Mechanical alloying consists of repeated deformation (welding, fracturing and rewelding) of powder particles in a dry high-energy ball mill until the desired composition is achieved. In this process, mixtures of elemental or pre-alloyed powders are subjected to grinding under a

protective atmosphere in equipment capable of high-energy compressive impact forces such as attrition mills, shaker mills and ball mills. Fig. 6(a) shows the set-up for ball milling process. It has been shown that nanometer-sized grains can be obtained in almost any material after sufficient milling time. The grain size decreases with milling time down to a minimum value that appears to scale inversely with melting temperature. It was suggested by Fecht et al. [29] that localized plastic deformation creates shear bands that show evidence of rotational dynamic recrystallization similar to the ones obtained in high-strain rate deformation (that are discussed in Section 7.5). Fig. 6(b) shows a dark-field TEM

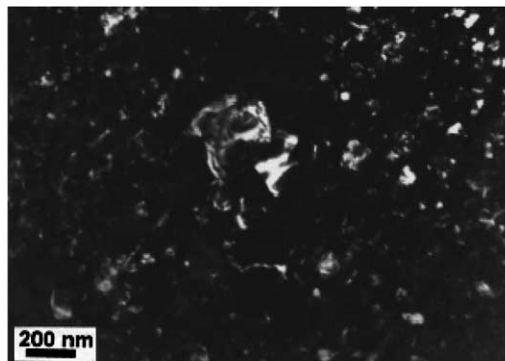
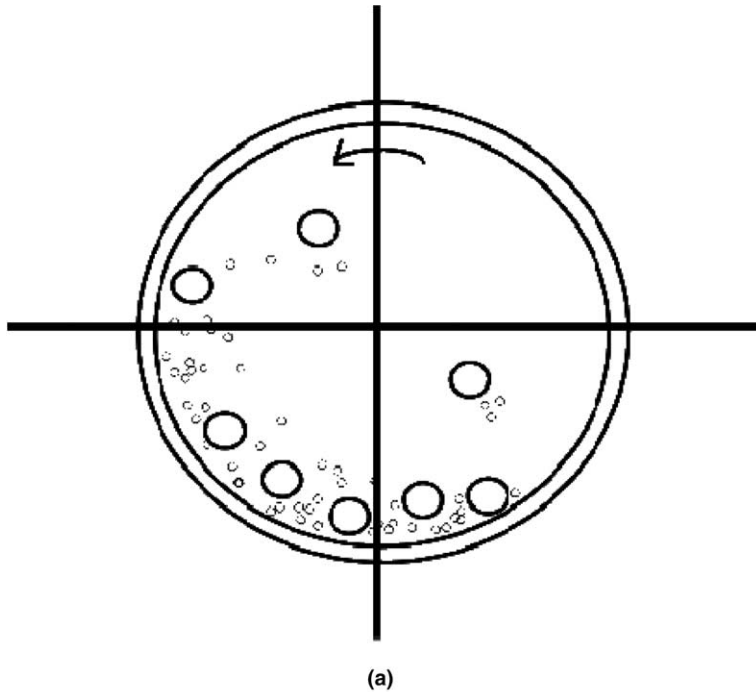


Fig. 6. (a) Mechanical milling as a means of synthesis of nanostructured material. (b) Dark field image of nanocrystalline Al-Mg alloy synthesized by cryogenic ball milling and annealed at 150 °C for 1 h [367].

of an Al–Mg alloy processed by ball milling at 77 K and annealing at 150 °C. The grain size distribution varying from 20 to 200 nm is clearly shown. Cryomilling is a variation of ball-milling that has been extensively used by Lavernia and coworkers [32–35].

### 4.3. Electrodeposition

The electrodeposition technique has significant advantages over other methods for synthesizing nanocrystalline materials: (1) potential of synthesizing large variety of nanograin materials—pure metals, alloys and composite systems with grain sizes as small as 20 nm, (2) low investment, (3) high production rates, (4) few size and shape limitations, and (5) high probability of transferring this technology to existing electroplating and electroforming industries.

Fig. 7(a) shows schematically the pulse electrodeposition sequence. As the current spikes, the metal cations are deposited in crystalline and amorphous patches. Fig. 7(b) shows the TEM micrograph of pulse electrodeposited Ni sample. Commercially synthesized (Integran) 5 mm thick plates are available in a range of compositions.

Over the past few years, Erb et al. [36] have studied the synthesis, structure and properties of nanocrystalline nickel synthesized by pulse electrodeposition. They demonstrated that grain refinement of electroplated nickel into the nanometer range results in unique and, in many cases, improved properties as compared to conventional polycrystalline nickel. Electrodeposition of multilayered (1D) metals can be achieved using either two separate electrolytes or much more conveniently using one electrolyte by appropriate control of agitation and the electrical conditions. Also, 3D nanostructure crystallites can be prepared using this method by utilizing the interface of one ion with the deposition of the other. It has been shown that electrodeposition yields grain sizes in the nanometer range when the electrodeposition variables are chosen such that nucleation of new grains is favored rather than growth of existing grains. This was achieved by using high deposition rates, formation of appropriate complexes in bath, addition of suitable surface-active elements to reduce surface diffusion of ad-atoms, etc. This technique can yield porosity-free finished products that do not require subsequent consolidation processing. Furthermore, this process requires low capital investment and provides high production rates with few shape and size limitations. Recent results by Shen et al. [37] and Lu et al. [38] indicated that a highly twinned structure can be produced under the right electrodeposition condition. This high annealing twin density is responsible for the enhancement of ductility which will be discussed later.

### 4.4. Crystallization from amorphous solids

The basic principle for the crystallization method from the amorphous state [39] is to control the crystallization kinetics by optimizing the heat treatment conditions so that the amorphous phase crystallizes completely into a polycrystalline material with ultrafine crystallites. The metallic glasses can be prepared by means of the existing routes, such as melt-spinning, splat-quenching, mechanical alloying, vapor deposition, or electrodeposition [40]. Crystallization of amorphous solids has been successfully applied in producing nanometer-sized polycrystalline materials in various alloy systems, e.g., in Fe-, Ni-, and Co-based alloys [41–44], as well as some elements. The complete crystallization of amorphous solids is a promising method for the synthesis of nanocrystalline materials because it possesses some unique advantages, the most important being porosity-free product and

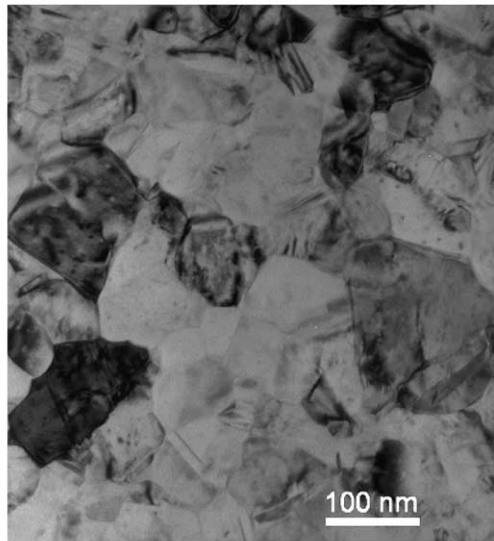
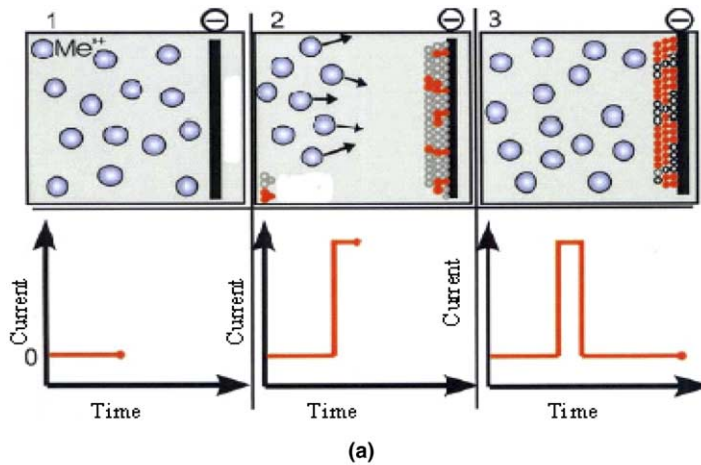


Fig. 7. (a) Pulsed electrodeposition set-up for synthesizing nanocrystalline materials. (b) Pulsed electrodeposited Ni. (Courtesy of M. Goeken, Univ of Erlangen, Germany.)

the ease of synthesizing nanocrystalline, intermetallics, supersaturated metallic solid solutions, and composites.

The amorphous solids are in thermodynamic metastable states and they transfer into more stable states under appropriate circumstances. The driving force for the crystallization is the difference in the Gibbs free energy between the amorphous and crystalline states. Usually, amorphous solids may crystallize into polycrystalline phases when they are subjected to heat treatment [45], irradiation [46], or even mechanical attrition. Of these techniques, conventional thermal annealing is most commonly utilized in investigations of amorphous solids.

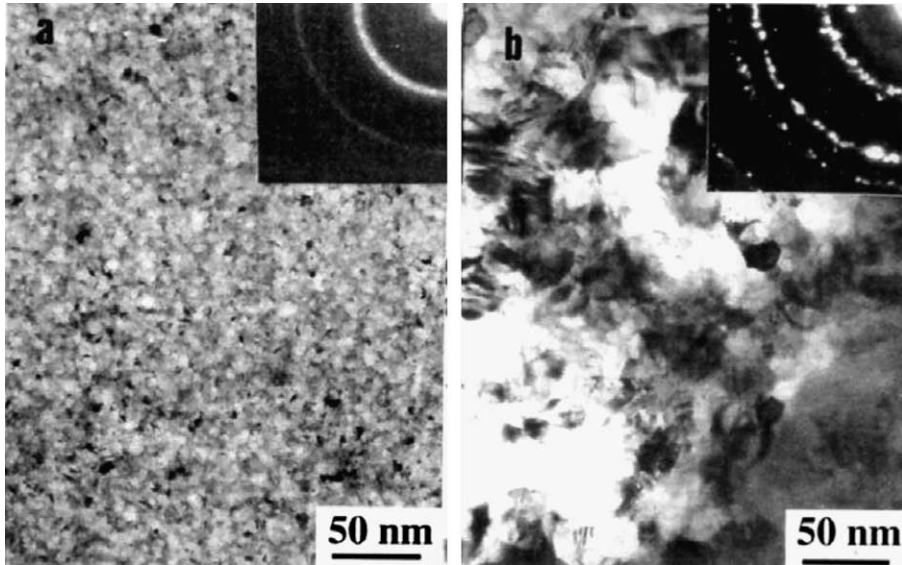


Fig. 8. TEM images and selected area diffraction patterns in the Ni-25.0at%W alloy annealed from amorphous state at (a) 723 K and for (b) 873 K for 24 h in vacuum. In (a), grain sizes between 5 and 8 nm is observed. (b) shows the random orientation of the grains [368].

TEM images and the selected area diffraction patterns of Ni-25at%W alloys annealed at 723 K and 873 K for 24 h in vacuum show that extremely small sized grains can be crystallized from amorphous materials as shown in Fig. 8. However, nanocrystalline structures are unstable at high temperatures because of the large excess free energy and significant grain growth has been observed. On the other hand, stabilization of the nanocrystalline grain structure was observed in many materials after continuous annealing.

Grain growth is described by the equation:

$$d^n - d_0^n = K_0 t \exp\left(\frac{-Q}{RT}\right) \quad (1)$$

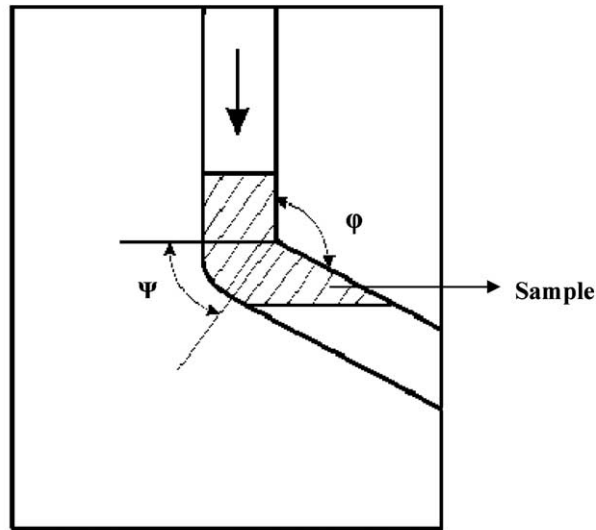
where  $d_0$  and  $d$  are the initial and current grain sizes,  $t$  is the annealing time,  $T$  the absolute temperature,  $R$  the gas constant,  $Q$  the activation energy for grain growth, and  $n$  and  $K_0$  are material constants. Under ideal conditions,  $n = 2$ . The temperature sensitivity is given by an Arrhenius expression. Assuming  $d_0 = 0$ , it can be seen that the growth rate decreases as the grain size increases.

#### 4.5. Severe plastic deformation

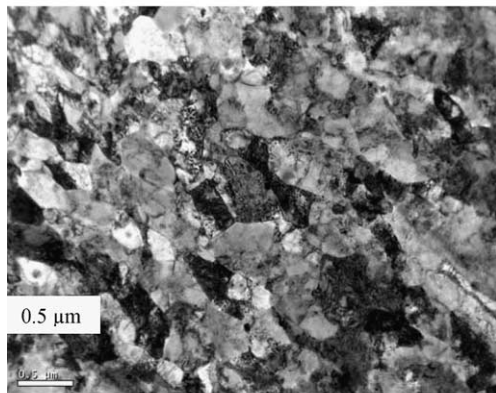
Severe plastic deformation breaks down the microstructure into finer and finer grains. As early as 1960, Langford and Cohen [16] and Rack and Cohen [17] demonstrated that the microstructure in Fe-0.003%C subjected to high strains by wire drawing exhibited sub-grain sizes in the 200–500 nm range. The use of severe plastic deformation (SPD) for the processing of bulk ultrafine-grained materials is now widespread [47–62]. Again, this is not a new technology, since piano wire, known for over a century, owes its strength to an

ultrafine grain size. Although any means of introducing large plastic strains in metals may lead to the reduction of the grain size, two principal methods for subjecting a material to severe plastic deformation have gained acceptance: these are known as equal-channel angular pressing (ECAP) [47,63–69] and high-pressure torsion (HPT).

ECAP was first proposed in the Soviet Union in the 80s. As illustrated in Fig. 9(a), ECAP uses a die containing two channels, equal in cross-section, intersecting at an angle  $\Phi$  that is generally close to  $90^\circ$ . The test sample is machined to fit within these channels. It is pushed down from the upper die by a piston (as shown by arrow) and is forced around a sharp corner. The strain imposed on the sample in ECAP is dependent upon both the channel angle between the two channels, and the angle defining the outer arc of curvature



(a)



(b)

Fig. 9. (a) A section through an ECAP die showing the two internal angles  $\phi$  and  $\Psi$ . Notice the front end shape of sheared part of the sample. (b) Bright field image of Cu processed by 8 ECAP passes using route  $B_C$  in a  $90^\circ$  die (transverse section sample).

where the two channels intersect. It can be shown that an equivalent strain close to  $\sim 1$  is introduced when the channel angle is  $90^\circ$  for all values of the angle defining the arc of curvature. Since the cross-sectional dimensions of the sample remains unchanged on passage through the die, repetitive pressings may be used to attain very high strains. Fig. 9(b) shows a copper specimen subjected to eight repetitive passes in ECAP by rotating the specimen by  $90^\circ$  at each stage (route  $B_C$ ). The TEM reveals a structure containing grains of approximately 200 nm. Although grains as small as 50 nm can be reached in Al alloys, the more common size is  $\sim 200$  nm. In a strict sense, one calls this “ultrafine” grain size.

An alternative procedure to introduce high plastic strains, illustrated in Fig. 10(a), is called high pressure torsion (HPT) [70,71]. A small sample, in the form of a disk, is held

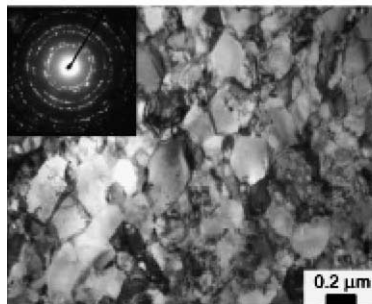
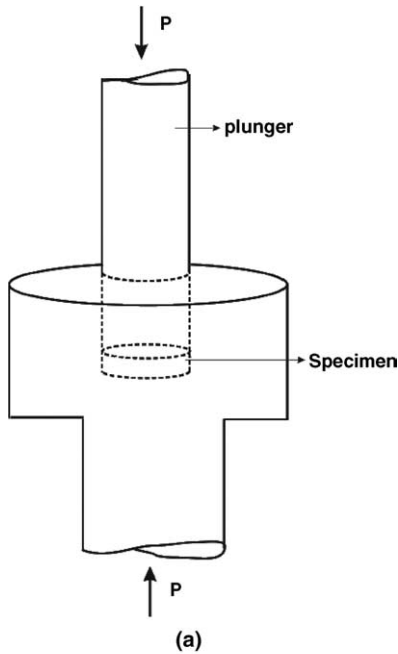


Fig. 10. (a) Schematic of high pressure torsion set-up. (b) TEM microstructure of pure nickel at the center of the disk produced by high pressure torsion together with the associated SAED for  $N = 5$  at applied pressure of 9 GPa [70].



under a high pressure and then subjected to torsional straining. Processing by HPT has the advantage of producing exceptionally small grain sizes, often in the nanometer range (<100 nm), and the ability to process brittle materials such as intermetallics and semiconductors. Nevertheless, HPT has the disadvantage that the specimen dimensions are generally fairly small, with maximum disk diameters of  $\sim 20$  mm and thickness of  $\sim 1$  mm. Fig. 10(b) shows as an illustration, the TEM image of a Ni specimen subjected to HPT. The grain size shows a bimodal distribution with the smaller grains less than 100 nm and the larger grains with approximately 500 nm size.

## 5. Mechanical properties of nanocrystalline metals and alloys

In this section, we review the principal mechanical properties of nanocrystalline metals: yield stress, ductility, strain hardening, strain-rate sensitivity and dynamic response, creep and fatigue. At the outset, it should be emphasized that porosity is of utmost importance and can mask and/or distort properties. The early “bottom-up” synthesis methods often resulted in porosity and incomplete bonding among the grains.

Processing flaws like porosity are known to be detrimental to the properties of nanocrystalline materials. Fig. 11 shows the Young’s modulus as a function of porosity for nanocrystalline Pd and Cu as shown by Weertman et al. [72]. This decrease in Young’s modulus with porosity is well known and is indeed expressed in many mechanics simulations. One of the equations is Wachtman and MacKenzie [73,74]:

$$E = E_0(1 - f_1p + f_2p^2) \quad (2)$$

where  $p$  is the porosity and  $f_1$  and  $f_2$  are equal to 1.9 and 0.9, respectively. For relatively low porosity,  $p^2$  can be neglected and we have, approximately  $\frac{E}{E_0} = 1 - 1.9p$ . The yield stress and tensile ductility are simultaneously affected. Fig. 12 shows as an illustration,

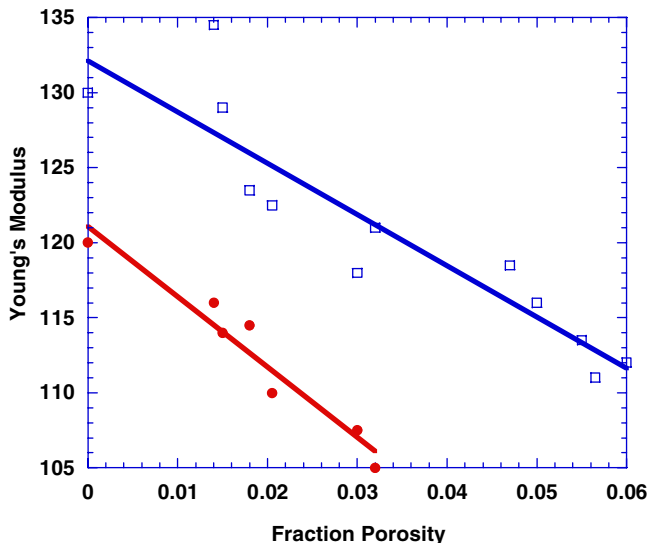


Fig. 11. Young’s modulus as a function of porosity for nanocrystalline Pd and Cu [72].

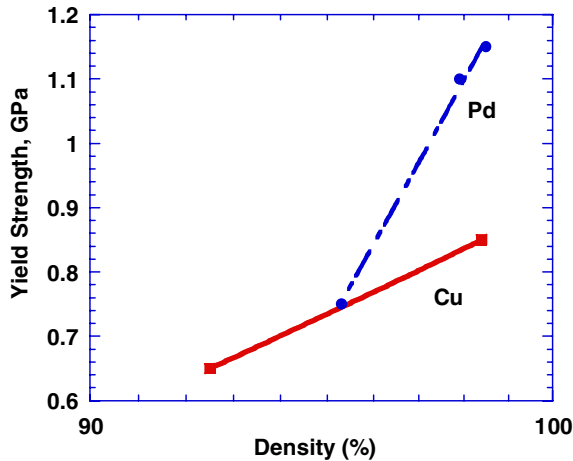


Fig. 12. Compressive yield strength of Cu and Pd as a function of consolidation density. (Data plotted from Youngdahl et al. [27].)

a plot of the yield stress as a function of density for Cu and Pd. The decrease in strength is obvious. The existing pores provide initiation sites for failure.

### 5.1. Yield strength

Grain size is known to have a significant effect on the mechanical behavior of materials, in particular, on the yield stress. The dependence of yield stress on grain size in metals is well established in the conventional polycrystalline range (micrometer and larger sized grains). Yield stress,  $\sigma_y$ , for materials with grain size  $d$ , is found to follow the Hall–Petch relation:

$$\sigma_y = \sigma_0 + kd^{-1/2} \quad (3)$$

where  $\sigma_0$  is the friction stress and  $k$  is a constant. This is indeed an approximation, and a more general formulation is to use a power expression with exponent  $-n$ , where  $0.3 \leq n \leq 0.7$ .

The mechanical properties of FCC metals with nano-range grain sizes have been estimated from uniaxial tension/compression tests and micro- or nano-indentation. Often micro-size tensile samples are used to avoid the influence of imperfections [72], e.g., voids that might adversely influence the mechanical response of the material.

The compressive yield stresses of nanocrystalline Cu and Pd samples synthesized by IGC are summarized in Table 2 [27], and the plot is given in Fig. 12. Weertman and coworkers [72] observed that nanocrystalline Cu and Pd samples were remarkably stronger than their coarse-grained counterpart and this was a strong function of density. Their strain to failure was also higher. Suryanarayana et al. [75] reported compressive yield strength of  $\sim 500$  MPa from their strongest nano Cu sample. Table 2 gives the values of the Vickers hardness,  $H_v$  divided by 3, which approximates to the yield strength if the work-hardening is not large. Unlike the case of tensile yield strength, the compressive values of  $\sigma_y$  scale well with  $H_v/3$ . Weertman et al. [76], observed a large increase in hardness

Table 2

Compressive yield strength of nanocrystalline Cu and Pd synthesized by inert gas condensation method (from [27])

Sample #	Compaction temperature (°C)	Density (% theor.)	Grain size (nm)	$\sigma_y$ (GPa)	Hardness/3 (GPa)
Pd1	335	98.5	54	1.15	1.0
Pd2	183	97.9	38	1.10–1.13	1.1
Pd3	RT	95.3	24	0.75	0.75
Cu1	106	92.5	19	0.65	0.77
Cu2	106	98.4	20	0.85	0.87

for the nanocrystalline Cu and Pd samples made by IGC as compared to the annealed coarse-grained samples. It was difficult to separate the magnitude of the strengthening effect of the small grain size from the weakening effect due to the bulk sample defects which are inherent to the IGC synthesis method (mainly pores).

## 5.2. Ductility

In the conventional grain size regime, usually a reduction in grain size leads to an increase in ductility. Thus one should expect a ductility increase as the grain size is reduced to nanoscale. However, the ductility is small for most grain sizes <25 nm for metals that in the conventional grain size have tensile ductilities of 40–60% elongation [77]. Koch [78] identified three major sources of limited ductility in nanocrystalline materials, namely: (1) artifacts from processing (e.g., pores); (2) tensile instability; (3) crack nucleation or shear instability. It is difficult to process nanostructured materials free from the artifacts that mask the inherent mechanical properties. As a result, molecular dynamics simulation has been considered to be a valuable tool in aiding our understanding of their deformation mechanism [79–84]. This is treated in greater detail in Section 9. The results of the atomistic simulations have allowed several investigators to suggest different plastic deformation mechanisms as a function of grain size [85,86]. There seems to be agreement in the existence of three regimes: (a) grain size  $d > 1 \mu\text{m}$  regime in which unit dislocations and work hardening control plasticity; (b) smallest grain size  $d < 10 \text{ nm}$  regime, where limited intragranular dislocation activity occurs and grain-boundary shear is believed to be the mechanism of deformation. The intermediate grain size regime (10 nm–1  $\mu\text{m}$ ) is less well understood. This will be discussed in detail in Section 7. These mechanisms are thought to affect ductility significantly.

Fig. 13(a) shows data on normalized yield strength (strength/strength of conventional polycrystalline) versus percentage elongation in tension for metals with grain sizes in the nanocrystalline range. There is a clear decrease in ductility as strength is increased. By comparison, ultrafine grained materials (100–500 nm), Fig. 13(b), exhibit increased yield strength along with good ductility in comparison to nanograined materials.

Zhang et al. [87–89] varied the microstructure of nanostructured/ultrafine grain size of Zn by changing the milling times. A very dramatic modulated cyclic variation of hardness was observed as a function of milling time at liquid nitrogen temperature. The sample cryomilled for 4 h exhibited an optimum combination of strength and ductility. The grain size distribution in this sample contained 30% volume fraction of grains larger than 50 nm along with the smaller nano-scale grains. This optimum microstructure, which exhibits

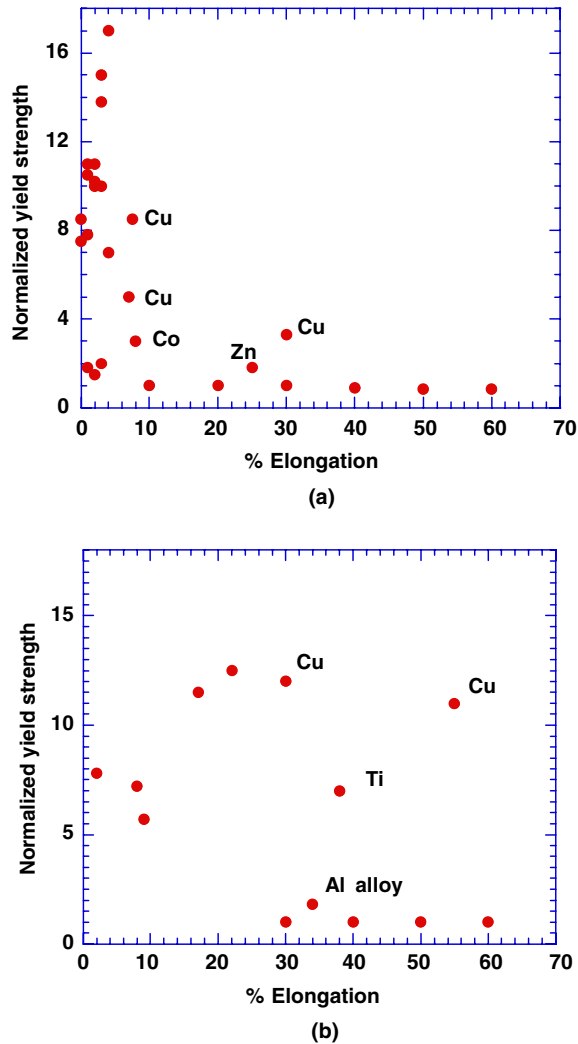


Fig. 13. (a) Compilation of yield stress versus % elongation showing the reduced ductility of nanocrystalline metals [96]. (b) Compilation of yield strength versus % elongation of various ultrafine grained metals [96].

more strain hardening than samples milled for either shorter or longer time, combined the strengthening from the reduced grain size along with the strain hardening provided by dislocation activity in the larger grains. This strain hardening, in turn, provided ductility. Thus, a bimodal grain size distribution is a possible means to increase ductility.

Nonequilibrium grain boundaries [90] have also been proposed as a mechanism to enhance ductility. It has been argued that such boundaries provide a large number of excess dislocations for slip [91] and can even enable grains to slide or rotate at room temperature, leading to a significant increase in the strain hardening exponent. These boundaries will be discussed further in Section 7.2. Another way of increasing ductility is to decrease the strain rate in order for the specimen to sustain more plastic strain prior to necking [92].

Fig. 14(a) [93] shows the expected ductility of metals as a function of a normalized strength (strength in the conventional grain size domain). As expected, as the strength increases, the ductility decreases. This defines the grey region. However, there are five data points above this boundary. They all apply to copper. Three factors contribute to and in fact determine ductility: the work hardening, the strain rate sensitivity and thermal softening. The increased ductility that is exhibited in some cases comes, basically, from the inhibition of shear localization. The strain rate sensitivity,  $m$ , can be expressed as [94]:

$$m = \frac{3^{1/2}kT}{V\sigma_y} \quad (4)$$

where  $V$  is the activation volume for plastic deformation (which is directly related to the physical mechanism of deformation),  $T$  is the temperature, and  $\sigma_y$  is the yield/flow stress. The higher strain-rate sensitivity ( $m = \partial \ln \sigma / \partial \ln \dot{\epsilon}$  or  $\frac{1}{\sigma_y} \frac{\partial \sigma}{\partial \ln \dot{\epsilon}}$ ) is indicative of a smaller activation volume, as pointed out by Lu et al. [94]. This, in turn, is connected to a change in

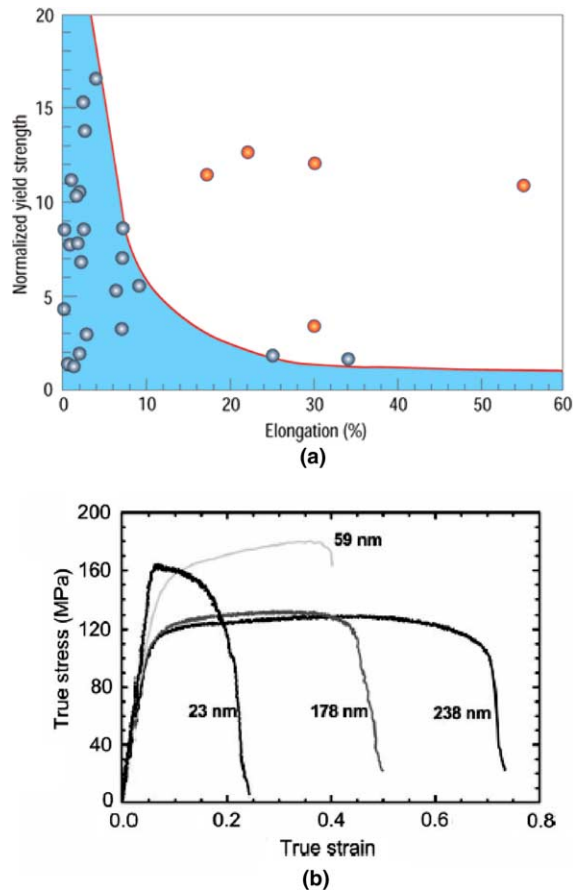


Fig. 14. (a) Increased ductility in the nanocrystalline regime as indicated by experimental points in right-hand side of diagram [93]; (b) reduction of ductility as grain size is reduced for ball milled Zn tested at a constant strain rate of  $10^{-4}$ – $10^{-3} \text{ s}^{-1}$  at room temperature [87].

the nanostructure (presence of twins). Thus, ductility, strain rate sensitivity, and deformation mechanisms are connected and it is possible, through the manipulation of the nanostructure to increase ductility. Zhu and Liao [93] were able to increase ductility of their nanocrystalline metals by increasing significantly the density of growth (annealing) twins. This will be discussed in Section 7.7.2.

Fig. 14(b) shows the mechanical response of nanocrystalline zinc samples with different grain sizes. There is a significant drop in ductility as the grain size goes down from 238 nm to 23 nm. Zhang et al. [120] suggested that the reduction of elongation with the reduction of grain size could be an inherent property of nanocrystalline materials given that there is no porosity and bonding was complete during synthesis. Earlier results have shown that the mechanical properties of nanocrystalline materials can be misinterpreted because of the lack of attention to the details of the internal structure [62]. As mentioned earlier, contaminants and porosity are found to be extremely detrimental to ductility.

### 5.3. Inverse Hall Petch effect: fact or fiction

Table 3 gives a partial list of publications on the phenomenon of inverse Hall–Petch. For ease of reading, the H–P plots in this section are expressed in (nanometers)<sup>−1/2</sup> and for rapid conversion into linear dimensions, we provide the conversion chart of Table 4. It should be noted that the entire conventional (microcrystalline) range ( $d > 1 \mu\text{m}$ ) corresponds to  $d^{-1/2} < 0.031 \text{ nm}^{-1/2}$ .

Table 3  
Partial list of papers on inverse Hall–Petch relationship [only first author named]

Author	Year	Title
Chokshi [97]	1989	On the validity of the Hall–Petch relationship in nanocrystalline materials
Fougere [355]	1992	Grain-size dependent hardening and softening of nanocrystalline Cu and Pd
Lu [356]	1993	An explanation to the abnormal Hall–Petch relation in nanocrystalline materials
Malygin	1995	Breakdown of the Hall–Petch law in micro- and nanocrystalline materials
Konstantinidis [252]	1998	On the “anomalous” hardness of nanocrystalline materials
Song [357]	1999	A coherent polycrystal model for the inverse Hall–Petch relation in nanocrystalline materials
Schiotz	1999	Softening of nanocrystalline metals at very small grain sizes
Chattopadhyay [358]	2000	On the inverse Hall–Petch relationship in nanocrystalline materials
Conrad [250]	2000	On the grain size softening in nanocrystalline materials
Takeuchi [359]	2001	The mechanism of the inverse Hall–Petch relation of nanocrystals
Wolf	2003	Deformation mechanism and inverse Hall–Petch behavior in nanocrystalline materials

Table 4  
Conversion chart as an aid for reading H–P plots

$d^{-1/2}$ (nm <sup>−1/2</sup> )	$d$ (nm)
0.025	1600
0.031	1000 (microcrystalline limit)
0.05	400
0.1	100
0.2	25
0.32	10

The Hall–Petch relationship predicts that the yield stress increases with the inverse of the square root of the grain size (Eq. (3)). However, experimental results on materials reveal that the Hall–Petch relationship recorded at large grain sizes cannot be extrapolated to grain sizes of less than  $\sim 1 \mu\text{m}$ . Fig. 15 shows the Hall–Petch plot for Cu taken from different sources. As can be clearly seen, there is ambiguity in the trend of the plot as the grain size falls down to a value below  $\sim 25 \text{ nm}$  ( $d^{-1/2} = 0.2$ ). While some results predict a plateau, others show a decrease. The Hall–Petch trend for different nanocrystalline samples crystallized from amorphous solids is plotted in Fig. 16(a). Again, the two trends are seen: the formation of a plateau and a decrease in  $\sigma_y$  as  $d$  is decreased below 25 nm. One simple rationalization for this behavior is provided by Fig. 16(b) for pure Ni and Ni–P alloy [95]. The curve was extended all the way to the amorphous limit, which corresponds to a hardness of  $\sim 6 \text{ GPa}$ . It is evident that this is the correct approach: the amorphous state is the lower limit of the nanocrystalline state. The plot shows a slight decrease. The breakdown in the Hall–Petch trend has been attributed to different deformation mechanisms that become dominant once the grain size is reduced down below a critical value [96].

Chokshi et al. [97] were the first to report the negative Hall–Petch effect by performing measurements on nanocrystalline Cu and Pd samples made by IGC. Both metals exhibited a negative slope, shown in Fig. 17(a). This landmark paper has received close to 300 citations. They attributed this negative trend to diffusional creep in nanocrystalline samples at room temperature analogous to grain-boundary sliding in conventionally-grained samples at high temperature. There have been reports of a similar trend in the Hall–Petch relationship from other sources [98–101,104]. Fig. 17(b) shows, in contrast, results obtained by

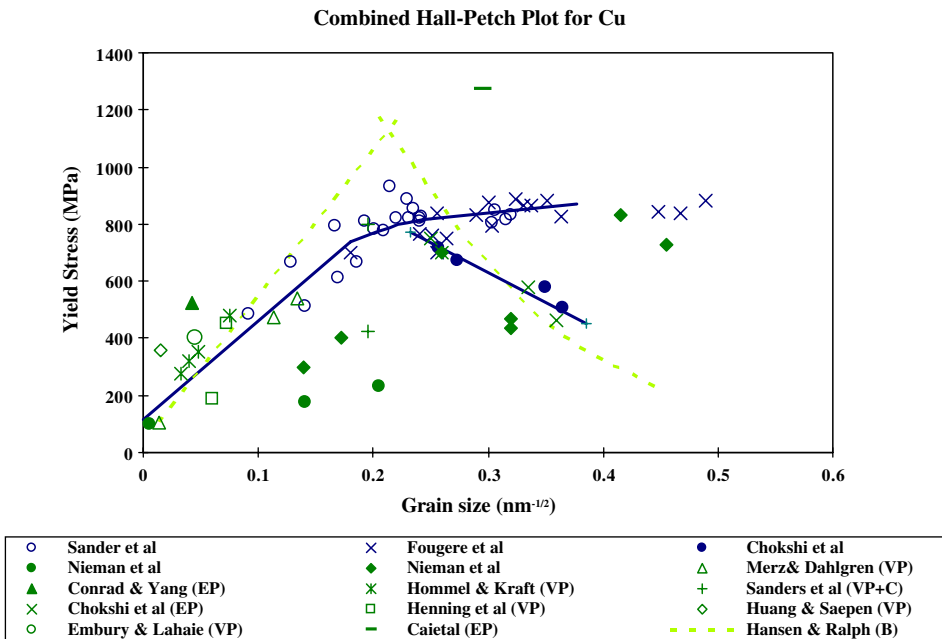


Fig. 15. Compiled yield stress versus grain size plot for Cu from various sources ranging from coarse to nanograin size. The plots show different trend as the grain size falls below a critical size.

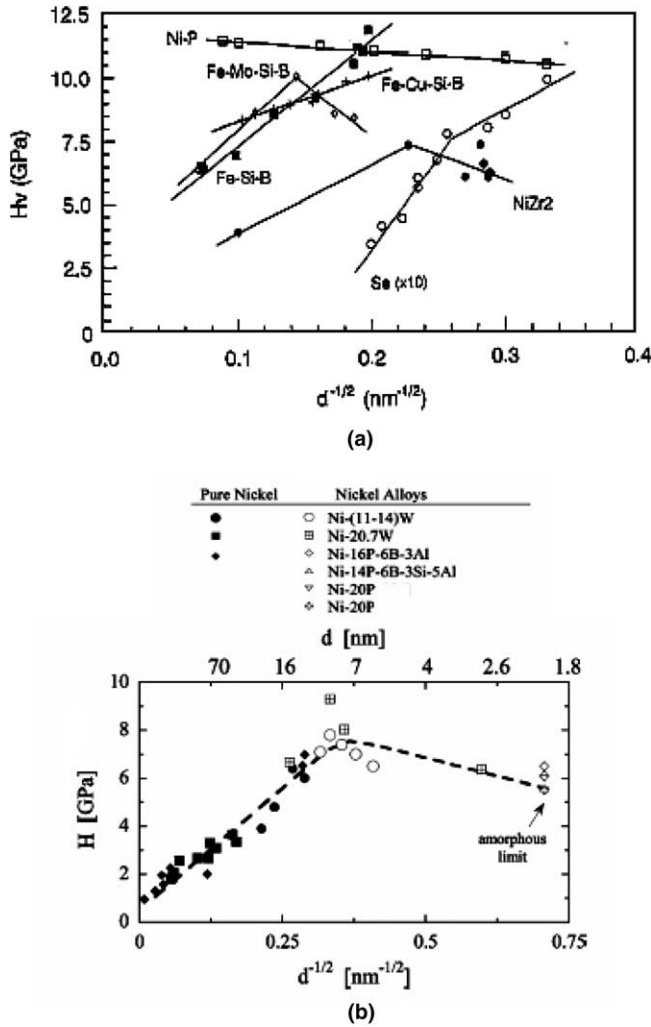


Fig. 16. (a) Hall–Petch plots for different nanocrystalline samples crystallized from amorphous solids [39]; (b) Hardness as a function of grain size for pure Ni and Ni–P alloy going all the way to amorphous limit [95].

Weertman [102] which do not show this trend through hardness measurements, although they show it in tensile results. The decrease in  $\sigma_y$  at smaller grain sizes was attributed by Weertman [102] to the presence of flaws. In their synthesis technique, inert gas condensation method was used, followed by ambient temperature densification through uniaxial pressing. The data points are also later shown in Fig. 46(b), where they are discussed in connection to the core-and-mantle mechanism. Weertman [102] suggested that the negative slope obtained by Chokshi et al. [97] was due to the use of a single sample subjected to repeat anneals to change the grain size. Thus, it was a heat treatment artifact.

Chokshi et al. [97] argued that the negative slope for nanocrystalline copper arose from the occurrence of rapid diffusion creep at room temperature. Coble creep was considered as the deformation mechanism,



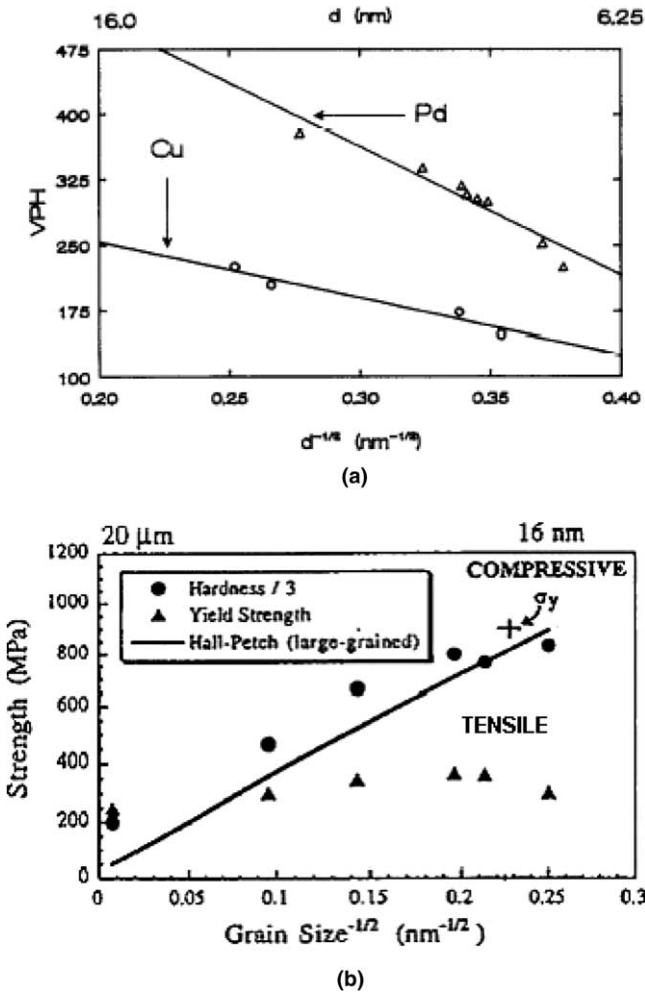


Fig. 17. (a) Inverse Hall Petch trend for Cu and Pd as shown by Chokshi et al. [97]. (b) Positive Hall–Petch slope with higher values for compressive (from hardness measurements) than for tensile strengths [27].

$$\dot{\epsilon} = \frac{150\Omega\delta D_{gb}\sigma}{\pi kT d^3} \tag{5}$$

where  $\dot{\epsilon}$  is the strain rate,  $\Omega$  is the atomic volume,  $\delta$  is the grain-boundary width,  $D_{gb}$  is the grain-boundary diffusion,  $\sigma$  is the stress,  $k$  is Boltzmann’s constant and  $T$  is the absolute temperature. Chokshi et al. [97] assumed:

$$\Omega = 1.3 \times 10^{-29} \text{ m}^3, \quad \delta = 1 \text{ nm}, \quad D_{gb} = 3 \times 10^{-9} \exp(-62000/RT) \text{ m}^2 \text{ s}^{-1} \tag{6}$$

and for stresses of 100 MPa and 1000 MPa at 300 K, the plots of strain rate as a function of grain size are shown in Fig. 18. It can be seen from the plot that the strain rate at which these grain-boundary diffusional processes become important ( $\sim 10^{-3} \text{ s}^{-1}$ ) corresponds to

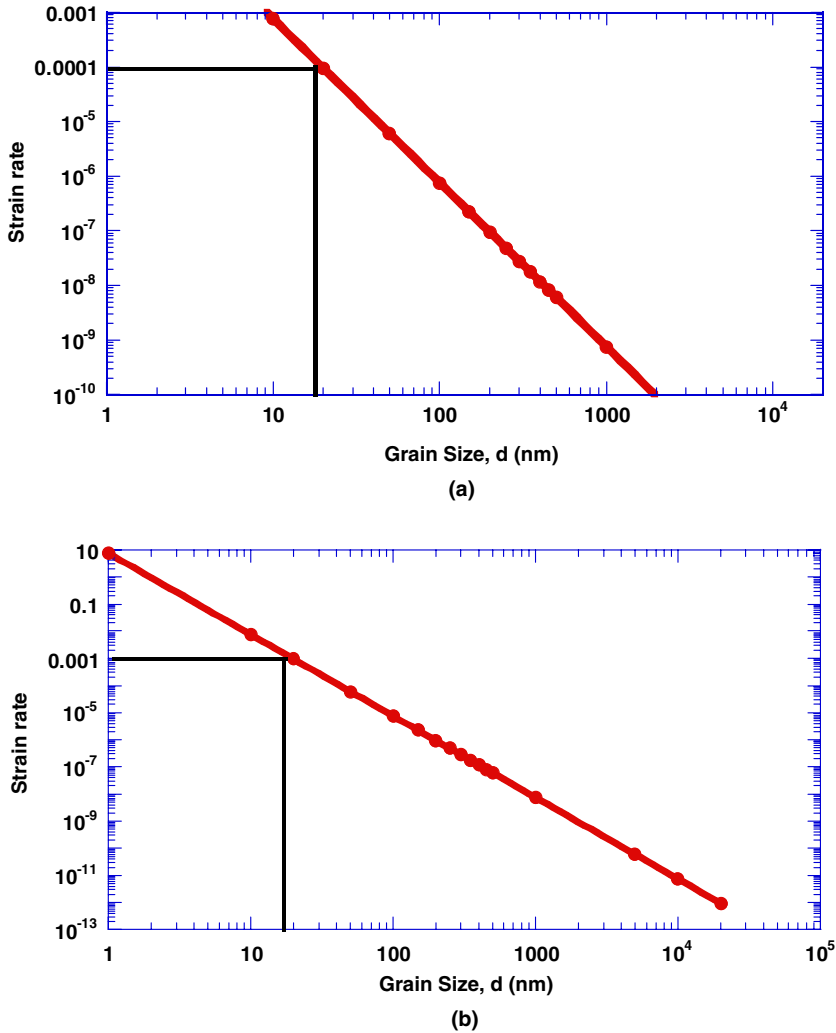


Fig. 18. Log-log plot of strain rate versus grain size for stresses of (a) 100 MPa and (b) 1000 MPa for Coble creep as used by Chokshi et al. [97].

grain sizes around 20 nm. These points are marked in plots. It has to be noted that the role of plastic deformation is ignored in the Chokshi et al. [97] analysis. However, plastic deformation is required for the grains to slide past each other. This plastic accommodation has been treated by Fu et al. [103] and this will be discussed later (Section 7.2).

The Hall–Petch trends for a range of grain sizes from the micro to the nanocrystalline are plotted in Fig. 19 for four different metals: Cu, Fe, Ni and Ti. Data points have been collected from different sources for grain sizes ranging from micrometer to nanometer range. Note that the data points in the conventional polycrystalline range for most of these plots overlap while they are more spread out in the nanocrystalline range. The Hall–Petch curve for the nanocrystalline range clearly shows a deviation from the regular trend in the

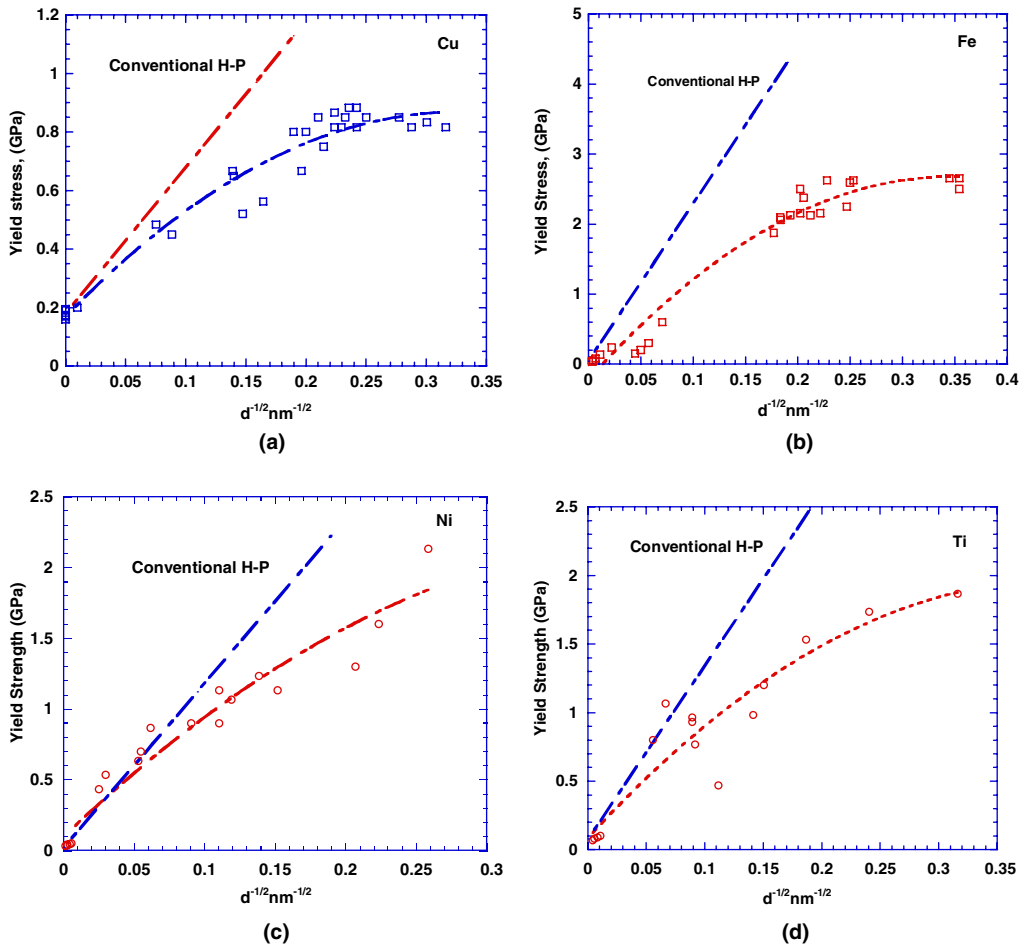


Fig. 19. Plots showing the trend of yield stress with grain size for different metals as compared to the conventional Hall–Petch response: (a) copper, (b) iron, (c) nickel and (d) titanium.

microcrystalline range; there is a significant decrease in the slope for small grain sizes. However, there is no clear evidence on the nature of the curves at grain sizes below  $\sim 10\text{--}15$  nm. Though researchers have debated the existence of the negative Hall Petch effect, there is insufficient information to validate the existence of this effect. The most probable behavior is that the yield strength plateaus below a critical grain size. The real trend is still to be determined along with the knowledge of whether it varies for different materials.

#### 5.4. Strain hardening

Nanocrystalline and ultrafine grained materials cannot generally sustain uniform tensile elongation. Several reports show virtually no strain hardening after an initial stage of rapid strain hardening over a small plastic strain regime ( $\sim 1\text{--}3\%$ ) which is different from the response of coarse grained polycrystalline metals [77–79,105,106].

The density of dislocations in a nanocrystalline sample saturates due to dynamic recovery or due to the annihilation of dislocations into the grain boundaries. This is discussed in Section 7 and leads to a low strain hardening rate. It is only during large additional strain that work hardening is observed. Dynamic recovery is known to occur during severe plastic deformation [56,107,108]. Due to the rise in the temperature, recovery converts the deformed microstructure into ultrafine grains having both low-angle and high-angle grain boundaries. Low strain hardening behavior has been observed for samples processed by both equal angular channel pressing and powder consolidation [107]. Fig. 20 shows the stress–strain curves in compression and tension for UFG copper produced by ECAP (8 passes). The work hardening (in compression) is virtually absent. This leads to necking at the yield stress (in tension), and the net result is a low tensile ductility. Such a trend has also been observed for ECAP Cu [108].

The stress–strain response of a nanocrystalline metal, e.g., copper, under tension shows a rapid peak and subsequent softening due largely to necking. The absence of strain hardening ( $d\sigma/d\varepsilon = 0$ ) causes localized deformation leading to low ductility. Flat compression curves have also been observed for other nanocrystalline metals including Fe (BCC) [109] and Ti (HCP) [107]. Necking is observed in most cases with the severe case of instability, and shear bands form in the consolidated Fe [109,110].

Room temperature dynamic recovery is common in nanocrystalline samples. Competition between the generation of dislocations during plastic deformation and the annihilation during recovery determines the steady state dislocation density. Though still debatable, the dislocations during deformation are thought to be generated at the grain boundaries which also act like sinks. It is, however, possible that dislocations are still the carriers of plastic deformation. As can be expected, the role of dislocations in the deformation process is difficult to determine since they arise and disappear in the large volume fraction of grain boundaries available. Other deformation mechanisms are not

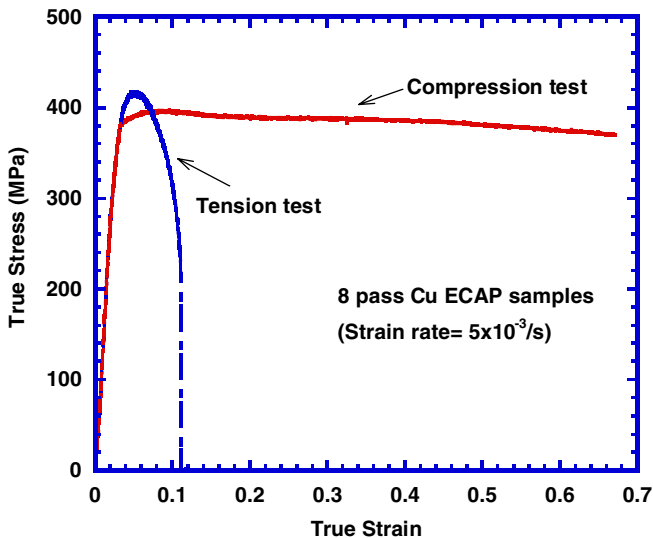


Fig. 20. Compressive and tensile stress–strain curves (tensile:engineering) for copper subjected to ECAP.

expected to be dominant until the grain size is in the range of 10–15 nm [80,111]. These mechanisms are discussed in detail in Section 7.

### 5.5. Strain-rate sensitivity

There have been reports of both increased and decreased strain rate sensitivity with decreasing grain size in metals. Iron, which is normally rate sensitive, with a strain rate exponent  $m$  (defined as  $m = \frac{\partial \ln \sigma}{\partial \ln \dot{\epsilon}}$  or  $\frac{1}{\sigma_y} \frac{\partial \sigma_y}{\partial \ln \dot{\epsilon}}$ ) hardening exponent on the order of 0.04, goes down in the value to 0.004 when the grain size is 80 nm. Malow et al. [112] prepared nano-crystalline Fe using ball milling and consolidation, and found a low  $m \sim 0.006$  at  $d \sim 20$  nm.

An opposite effect was found by Gray et al. [113] on ultrafine grained FCC metals produced by ECAP: Cu, Ni and Al–4Cu–0.5Zr. Their mechanical response was found to depend on the applied strain rate, which ranged from 0.001 to  $\sim 4000$  s<sup>-1</sup> as shown in Fig. 21. The strain rate sensitivity,  $m$ , based on the above strain rate range, was measured to be 0.015 for Cu, 0.006 for Ni and 0.005 for Al–4Cu–0.5 Zr. Gray et al. [113] attributed the

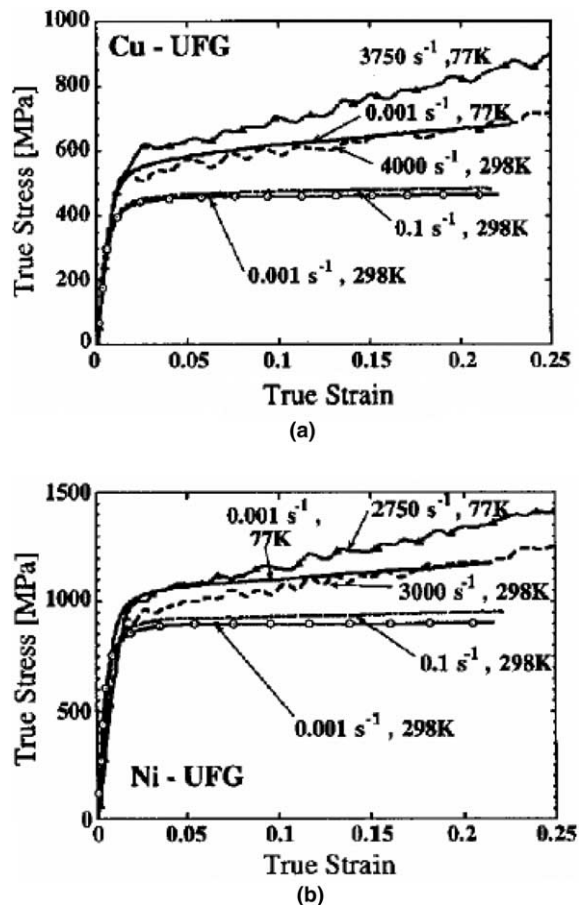


Fig. 21. Stress–strain response of ultrafine grained: (a) Cu, (b) Ni [113].

relatively high rate sensitivity, coupled with the nearly zero post-yield work-hardening rates in the ultrafine grained Cu and Ni, to a high pre-existing dislocation density.

Higher values of  $m$  have also been reported for nanocrystalline Ni [114], nanocrystalline Au [115], and electrodeposited Cu [116]. However, these observations were only made in creep tests where grain-boundary deformation is dominant [114]. In normal quasistatic tensile tests, none of these nanocrystalline metals exhibited a high  $m$ . These small values of  $m$  are insufficient to keep material deformation from shear localizing, which is similar to the response of amorphous alloys [106]. A Newtonian viscous metal, which does not localize, has  $m \sim 1$ .

Results by Wei et al. [369] show in a clear fashion that the strain rate sensitivity is increased at grain sizes below a critical value. These results are shown in Fig. 22. This enhanced strain rate sensitivity has also been measured through nanoindentation hardness tests. Results by Göken and coworkers [118] are shown in Fig. 23. The strain-rate sensitivity observed in pulse electrodeposited Ni remains about the same down to  $d = 60$  nm (Fig. 23(b)). However, the slope for the  $d = 20$  nm specimens is higher. A similar effect is observed for aluminum produced by ECAP. The ultrafine grain sized Al has a slope  $m = 0.027$ , whereas the strain-rate sensitivity for conventional polycrystalline Al is less than one third of this ( $m = 0.007$ ) [117], Fig. 23(a). The increased strain rate sensitivity is directly related, to a change in the rate controlling mechanism for plastic deformation. It can be seen through Eq. (4) that  $m \propto V^{-1}$ , i.e.,  $m$  is inversely proportional to the activation energy. Conventional FCC metals have a large activation volume,  $V$ :

$$V \sim 10^2 - 10^3 b^3$$

This is associated with dislocations cutting through forest dislocations. On the other hand, the activation volume for grain-boundary diffusion processes is much lower, on the order of the atomic volume:

$$V \sim (1 - 10)b^3$$

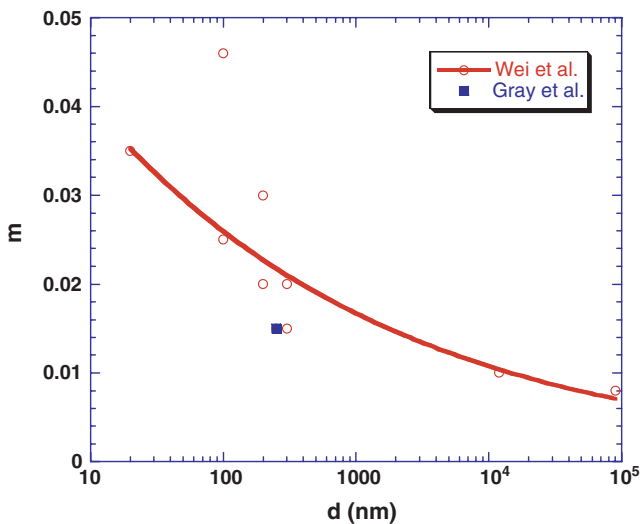


Fig. 22. Strain rate sensitivity plot for Cu as a function of grain size [113,369].

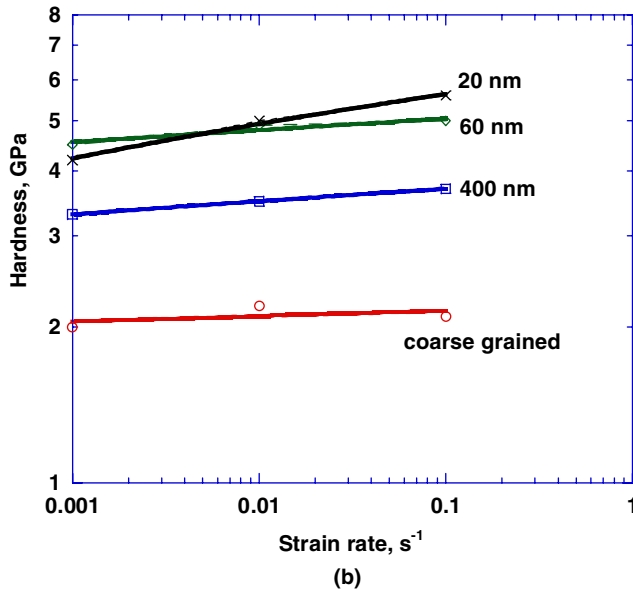
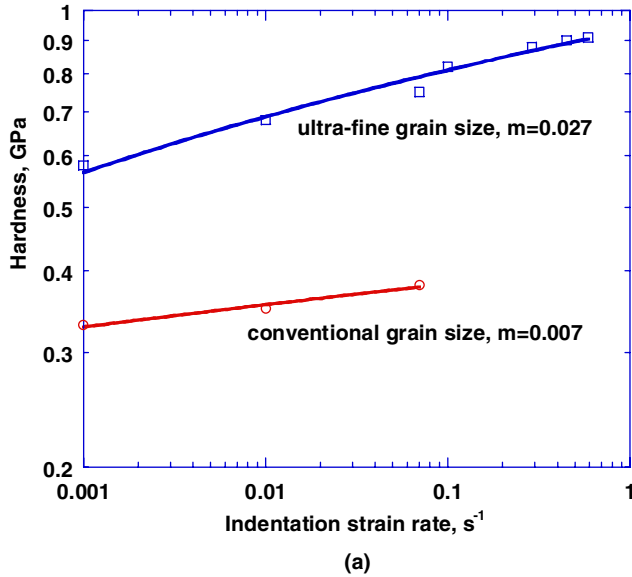


Fig. 23. (a) Comparison of strain rate sensitivity (from hardness measurements) for conventional and ultrafine grain sized aluminum. (Courtesy M Göken, Univ Erlangen-Nürnberg, Germany.) (b) Strain rate sensitivity plot (from hardness measurement) for pulse electrodeposited Ni. (Courtesy M Göken, Univ Erlangen-Nürnberg, Germany.)

This represents the lower bound for  $V$ . Thus, the increasing influence of atomic-size exchanges manifests itself by a decrease in  $V$ . Hoppel et al. [119] observed in ECAP copper that  $m$  had the following values:

2 passes ( $\gamma \sim 2$ ):  $m = 0.06$

16 passes ( $\gamma \sim 16$ ):  $m = 0.14$

This significant increase in strain-rate sensitivity with the number of passes was not attributed by them to a change in mechanism to grain-boundary sliding, but rather to the switch to thermally-activated dislocation annihilation at grain boundaries. This conclusion is sound, since cutting of forest dislocations is a mechanism that cannot operate at ultrafine grain sizes because of the scale effect.

### 5.5.1. Strain-rate sensitivity of ultrafine grained and nanostructured HCP metals

The effects of temperature, strain rate and grain size on the flow behavior of Zn (representative HCP metal) have been studied to reveal the deformation mechanisms in UFG and nanocrystalline HCP structured metals [120]. Tensile test results for 3 h ball-milled Zn samples tested at different temperatures, but the same strain rate ( $10^{-4} \text{ s}^{-1}$ ), are shown in Fig. 24. The grain size after 3 h ball milling was 238 nm. The yield stress ( $\sigma_y$ ), as well as the strain ( $\epsilon$ ) to failure decreased with an increase of test temperature. The strain hardening under quasistatic conditions in samples tested at different temperatures was low [120]; at 200 °C, it ceased to exist. By increasing the ball milling time, the grain size was progressively decreased. This, on its turn, leads to an increase in yield stress and a decrease in work hardening, as seen earlier in Fig. 14(b). Jump tests (strain rate changes by factor of 2) also were performed at 20, 40, and 60 °C on the ball milled Zn samples. The results are shown in Fig. 25. The calculated  $m$  values were 0.15 for tests at 20 and 40 °C and about 0.17 for test at 60 °C. As can be noticed, these values are significantly higher compared to the value of  $m$  for ultrafine Cu and Ni discussed earlier. However, one should bear in mind that Zn is HCP, while Cu, Ni and Al are FCC.

### 5.5.2. Mechanical behavior of iron as a representative BCC metal

Nanocrystalline iron has been the focus of widespread research primarily to understand the mechanism of shear band formation [110,121]. Fig. 26 shows the true stress–strain curves of the consolidated iron with various average grain sizes, obtained from quasistatic

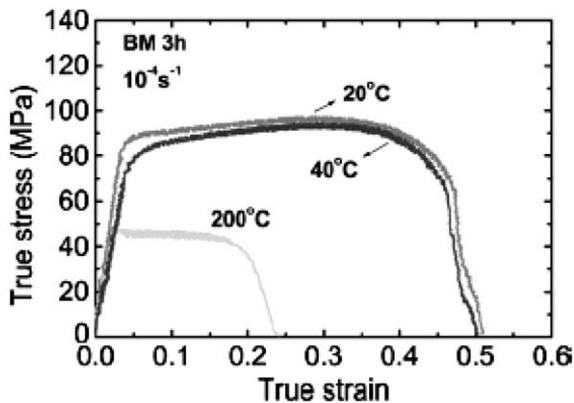


Fig. 24. Tensile stress–strain curve for ball milled (3 h) Zn tested at 20, 40 and 200 °C at a constant strain rate of  $10^{-4} \text{ s}^{-1}$  [87].



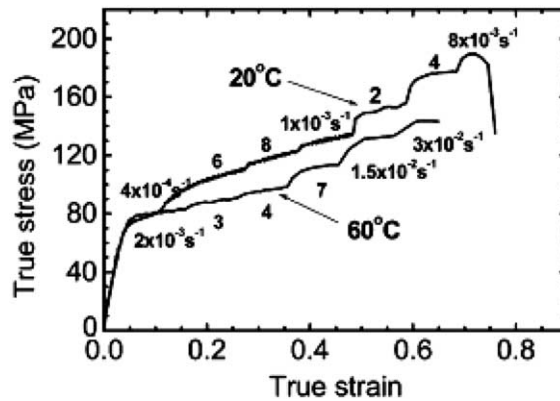


Fig. 25. Strain-rate jump tests (compression) performed on ball milled (3 h) Zn at 20 and 60 °C [87].

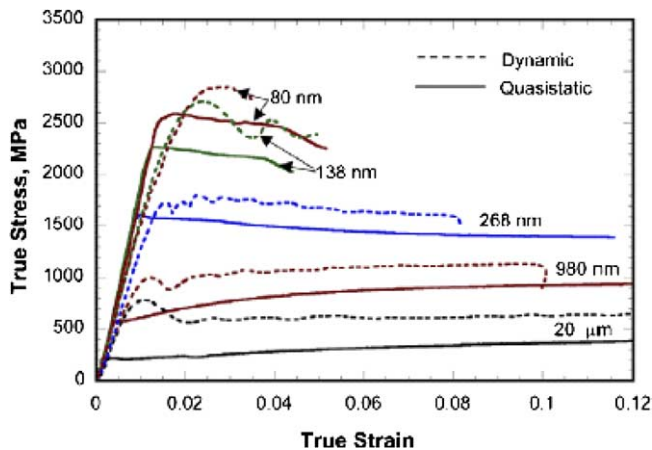


Fig. 26. Typical stress–strain curves obtained for consolidated iron under quasistatic and high-strain rate uniaxial compression for different grain sizes [121].

and dynamic compression (split Hopkinson bar) tests [121]. The plot suggests that strain hardening decreases with decreasing grain size which is surprising in the polycrystalline regime but expected in the nanocrystalline regime. As seen earlier, this is probably due to a change in the deformation mechanism at smaller grain sizes. On the other hand, the reported influence of strain rate on strain hardening is insignificant, which is also typical of BCC metals. The calculated strain rate sensitivity values  $m$  are: 0.009 for grain size of 80 nm, 0.012 for grain size of 138 nm, 0.023 for grain size of 268 nm, 0.045 for grain size of 980 nm and 0.08 for grain size of 20  $\mu\text{m}$ . In BCC metals, the activation volume for plastic deformation is much lower than FCC metals and therefore the change in rate controlling mechanism is not expected to occur.

Jia et al. [121] used a physically-based constitutive model that describes the rate-dependent behavior of BCC iron over the entire range of strain rates from  $10^{-4}$  to  $10^4 \text{ s}^{-1}$ :

$$\tau = \tau_{a0} + \beta d^{-1/2} + g(\gamma) + \bar{\tau}_0 \left[ 1 - \left( \frac{kT}{\Delta G_{k0}} \ln \left( \frac{\dot{\gamma}_{0k}}{\dot{\gamma}} \right) \right)^{2/3} \right]^2 \quad (7)$$

The model represents the application of the MTS constitutive equation by Kocks et al. [122]. The first three terms in Eq. (7) are the athermal components of the stress:

$$\tau_{\text{athermal}} = \tau_{a0} + \beta d^{-1/2} + g(\gamma) \quad (8)$$

The last term is the thermal component.

The strain hardening function  $g(\gamma)$  is included in the athermal part because experimental evidence indicates that the strain hardening is not affected by strain rate or temperature. However, this is not typical of BCC metals, as shown by Zerilli and Armstrong [123].

### 5.6. Creep of nanocrystalline materials

Creep in coarse grained materials has been widely studied for approximately one century and accurate models exist that capture deformation features and explain mechanisms involved therein. Creep in nanocrystalline materials has been studied only in recent years owing to several complications involved. First of all is the limitation of synthesizing bulk nanomaterial free of defects (porosity and impurities) with uniform grain size distribution that could provide reliable data to explain the deformation process. Second is the significant increase in the volume fraction of grain boundaries and intercrystalline defects such as triple lines and quadruple junctions that renders the creep mechanism complicated and leads to associated challenges in developing a model that could explain the deformation process. Third, grain growth occurs at much lower temperature as compared to coarse-grained materials limiting the testing temperatures to a low fraction of the melting point.

Since the volume fraction of grain boundaries is high, diffusion creep is considered to be significant. The high temperature deformation of crystalline materials is given by the following (Bird–Dorn–Mukherjee) equation:

$$\dot{\epsilon} = \frac{ADGb}{kT} \left( \frac{b}{d} \right)^p \left( \frac{\sigma}{G} \right)^n \quad (9)$$

where  $\dot{\epsilon}$  is the strain rate,  $A$  is a dimensionless constant,  $G$  is the shear modulus,  $b$  is the magnitude of the Burgers vector,  $k$  is Boltzmann's constant,  $T$  is the absolute temperature,  $p$  is the inverse grain size exponent, and  $n$  is the stress exponent. Among the established diffusional creep mechanisms in coarse grained materials are the Nabarro–Herring creep that involves vacancy flow through the lattice and Coble creep that involves vacancy flow along the grain boundaries. The associated equations are:

$$\dot{\epsilon}_{\text{NH}} = \frac{A_{\text{NH}} D_{\text{L}} G b}{kT} \left( \frac{b}{d} \right)^2 \left( \frac{\sigma}{G} \right) \quad (10)$$

where  $D_{\text{L}}$  is the lattice diffusion coefficient, the exponents  $p = 2$ ,  $n = 1$ , and the dimensionless constant  $A_{\text{NH}} = 28$ . On the other hand, Coble creep involves vacancy flow along grain boundaries, and the related equation is

$$\dot{\epsilon}_{\text{CO}} = \frac{A_{\text{CO}} D_{\text{gb}} G b}{kT} \left( \frac{b}{d} \right)^3 \left( \frac{\sigma}{G} \right) \quad (11)$$

where  $D_{gb}$  is the grain-boundary diffusion coefficient, the exponents  $p = 3$ ,  $n = 1$ , and the dimensionless constant  $A_{CO} = 33$ .

Palumbo et al. [124] considered a regular 14-sided tetrakaidecahedron as the grain shape to estimate total intercrystalline component and showed that it increases from a value of  $\sim 0.3\%$  at a grain size of  $1 \mu\text{m}$ , to a maximum value of  $87.5\%$  at a  $2 \text{ nm}$  grain size (see Fig. 2). In accessing the individual elements of the intercrystalline fraction, it was noted that the triple junction volume fraction displays greater grain size dependence than grain boundary. Wang et al. [125] modified the standard diffusion creep equation to accommodate for diffusion along triple lines and this leads to the following expression for triple-line diffusion creep:

$$\dot{\epsilon}_{TL} = \frac{K_{TL} D_{TL} \Omega \delta^2 \sigma}{k T d^4} \quad (12)$$

where  $K_{TL}$  is a constant depending on the geometry and boundary conditions,  $D_{TL}$  is the triple-line diffusion coefficient,  $\Omega$  is the atomic volume and  $\delta$  is the grain-boundary width. Chokshi [126] proposed the following form for the Bird–Mukherjee–Dorn equation (Eq. (9)) for conditions under which transition takes from one diffusion creep mechanism to the other and also from diffusion controlled mechanism to intergranular dislocation power-law creep:

$$\dot{\epsilon}_{PL} = \frac{A D_L G b}{k T} \left( \frac{\sigma}{G} \right)^n \quad (13)$$

where  $n \geq 3$ ,  $p = 0$  and  $D = D_L$  in the Bird–Mukherjee–Dorn equation.

Among the first reports on creep of nanocrystalline materials are the ones by Wang et al. [127] on  $28 \text{ nm}$  grain size Ni–P alloy (Fig. 27(a)), Deng et al. [128] on the same alloy, and Nieman et al. [129] on nanocrystalline Pd. In Fig. 27(a), one can see that the slope of the plot,  $n = 1$ , supports either Coble or Nabarro–Herring creep (Eqs. (10) and (11)). Wang et al. [127] attributed the creep response to grain-boundary diffusion and in their following work [128] concluded that while grain-boundary diffusion is the operating mechanism in nanocrystalline creep; a combined mechanism involving dislocation creep and grain-boundary diffusion governs deformation in coarse grained materials.

Hahn et al. [130] performed tests on compressive creep response of  $\text{TiO}_2$ . The value of  $n$  obtained from their results is shown from the slope in Fig. 27(b):  $n = 2$ . Nieman et al. [129] reported no significant room temperature creep for nanocrystalline Pd under loads much larger than the yield stress of a coarse-grained Pd sample. They concluded that grain-boundary diffusional creep is not an appreciable factor in directly determining room temperature mechanical behavior in nanocrystalline Pd. Sanders et al. [131] carried out creep tests over a range of temperatures ( $0.24\text{--}0.64 T_m$ ) and stresses on samples of nanocrystalline Cu, Pd, and Al–Zr made by inert gas condensation and compaction. The experimentally observed creep rates were two to four orders of magnitude smaller than the values predicted by the equation for Coble creep. The predicted creep rates as a function of temperature for different grain sizes are shown in Fig. 28. The figure shows calculated creep curves assuming grain-boundary diffusion for different grain sizes (notice increase in strain rate by six orders of magnitude when grain size is decreased from  $1 \mu\text{m}$  to  $10 \text{ nm}$ ). Sanders et al. [131] concluded that prevalence of low-energy grain boundaries together with inhibition of dislocation activity caused by small grain sizes is responsible for low strain rates and higher than expected creep resistance.

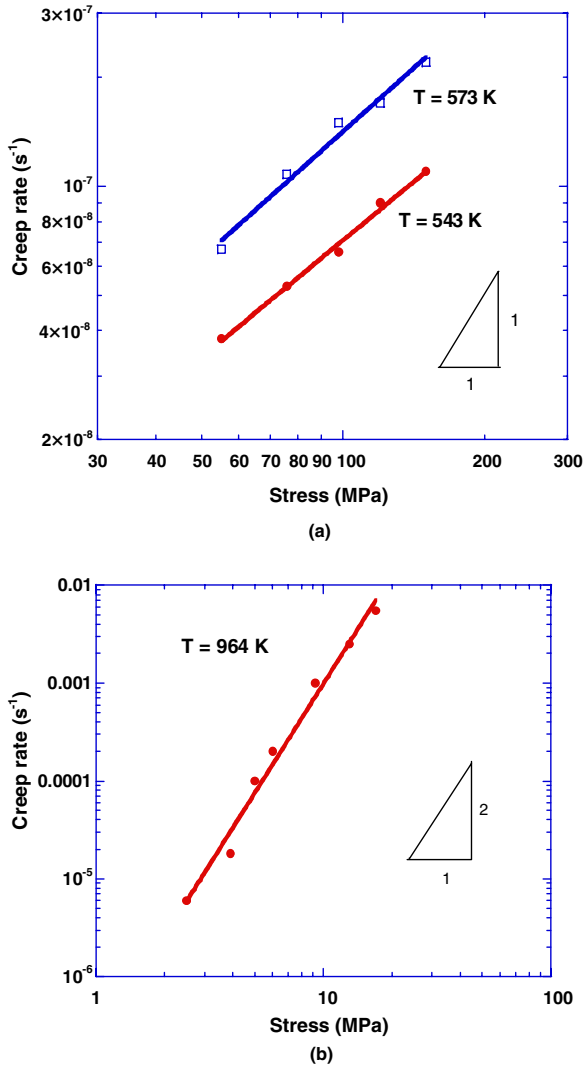


Fig. 27. Stress versus strain rate plots for (a) nanocrystalline ( $d = 28 \text{ nm}$ ) Ni-P [127] and (b) nanocrystalline  $\text{TiO}_2$  [130].

Ogino [132] compared the lower (by several orders of magnitude) strain rates experimentally observed to the theoretically calculated values from the theory of Coble creep. He attributed the effect to an increase in grain-boundary area due to deformation of grains at an initial stage of creep. Wang et al. [133] studied the effect of grain size on the steady state creep rate of nanocrystalline pure nickel that was synthesized by electrodeposition. They argued that at high stress levels, grain-boundary sliding becomes the major deformation mechanism at room temperature. The contribution from diffusion creep mechanisms through intercrystalline regions can be significant for smaller grain sizes. It was suggested that dynamic creep should be taken into account when analyzing the stress–strain curves

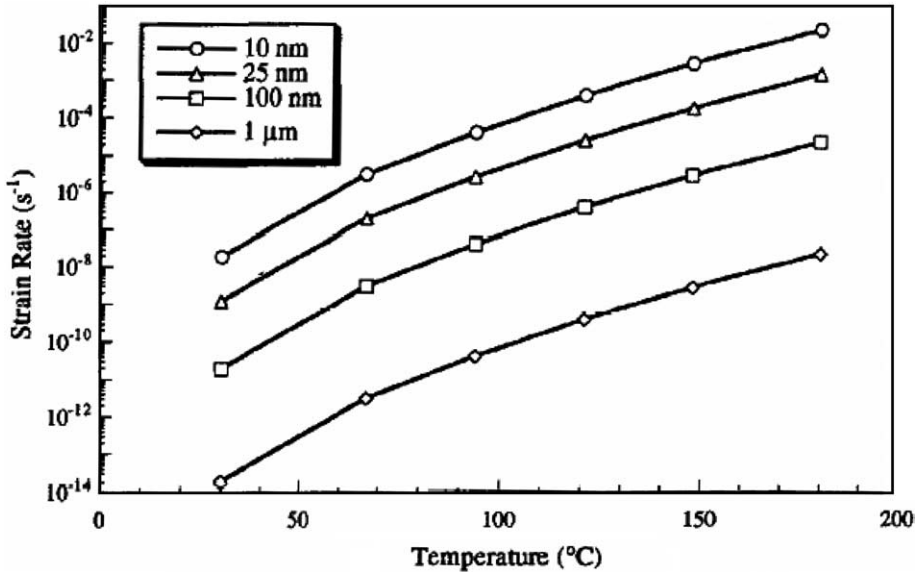


Fig. 28. Calculated creep curves assuming grain-boundary diffusion for different grain sizes; notice increase in strain rate by six orders of magnitude when grain size is decreased from 1  $\mu\text{m}$  to 10 nm [131].

of nanocrystalline materials. Cai et al. [134] conducted tensile creep of nanocrystalline pure Cu with an average grain size of 30 nm prepared by electrodeposition in the temperature range 20–50 °C ( $0.22\text{--}0.24T_m$ ). The steady state creep rate was found to be proportional to an effective stress  $\sigma_e = \sigma - \sigma_0$ , where  $\sigma$  is the applied stress, and  $\sigma_0$  is the threshold stress. Using  $\sigma_e$ , the creep rates were found to be of the same order of magnitude as those calculated from the equation for Coble creep (Eq. (11)). The existence of a threshold stress implied that the grain boundaries do not act as perfect sources and sinks of atoms (or vacancies). The mechanism of creep was identified as ‘interface controlled diffusional creep’. Li et al. [135] refuted the result of Cai et al. [134] by attributing the high value of minimum creep rate (that led to the proposal of Coble creep) to premature fracture. Grabovetskaya et al. [136], using nanostructured copper, nickel, and Cu–Al<sub>2</sub>O<sub>3</sub> composite as examples, studied characteristic features of creep of nanostructured materials produced by severe plastic deformation at temperatures  $T < 0.3T_m$ . They concluded that the steady-state creep rate of nanostructured copper and nickel is well described by a power law where the exponent  $n$  is equal to  $\sim 5.5$  for copper and  $\sim 8$  for nickel. They postulated the development of meso- and macrobands of localized deformation during deformation of fine grained materials. They also estimated the apparent creep activation energies of nanostructured copper and nickel in the temperature interval of  $0.2\text{--}0.3T_m$  to be 2.5 times lower than the coarse-grained counterpart. Using direct experimental methods, they showed that this difference is due to the significant contributions to the overall deformation of grain-boundary sliding controlled by grain-boundary diffusion.

There have also been attempts to study creep in nanostructured materials closer to the real situation. Estrin et al. [137] studied diffusion controlled creep in nanocrystalline materials under conditions of concurrent grain growth. The Nabarro–Herring and Coble mechanisms were modified to account for the effect of attendant vacancy generation on creep.

Several models for creep in nanocrystalline materials have been proposed based on molecular-dynamics simulations. Yamakov et al. [138] simulated fully three-dimensional, nanocrystalline face-centered cubic metal microstructures to study grain-boundary (GB) diffusion creep. The simulations were performed at elevated temperatures where the distinct effect of GB diffusion is clearly identifiable. In order to prevent concurrent grain growth and thus to enable steady-state diffusion creep, the microstructure was tailored to have uniform grain shape (nm size) and to contain only high-energy grain boundaries. Results indicated that under relatively high tensile stresses these microstructures exhibited steady-state diffusion creep that is homogeneous, with a strain rate that agrees with that given by the Coble creep equation. The grain size scaling of the creep was found to decrease from  $d^{-3}$  (typical of Coble creep) to  $d^{-2}$  (typical of Nabarro–Herring creep) when the grain diameter was of the order of the grain-boundary thickness. Direct observation of grain-boundary sliding as an accommodation mechanism for the Coble creep, known as Lifshitz sliding, was also reported. Haslam et al. [139] in their MD simulation accounted for the effect of concurrent grain growth on grain-boundary diffusion creep (like the study by Estrin et al. [137]) and grain-boundary sliding during high-temperature deformation of a nanocrystalline Pd model microstructure. Prior to the onset of significant grain growth, the deformation was shown to proceed via the mechanism of Coble creep accompanied by grain-boundary sliding. While grain growth is generally known to decrease the creep rate due to the increase of the average grain size, the results obtained in this study revealed an enhanced creep rate at the onset of the grain growth, when rapid boundary migration occurs. The enhanced creep rate was shown to arise from topological changes during the initial growth phases, which enhanced both the stress-induced grain-boundary diffusion fluxes and grain-boundary sliding. Dislocations generated as a result of grain-rotation-induced grain coalescence and grain-boundary decomposition in the vicinity of certain triple junctions were also shown to contribute to the deformation.

In recent work, experimentally measured grain size compensated diffusion creep rates were shown to be identical in cubic, tetragonal and monoclinic zirconia by Chokshi [140], suggesting a similarity in the absolute magnitudes of their grain-boundary diffusion coefficients. Grain growth in tetragonal zirconia was shown to be substantially slower due to significant grain-boundary segregation.

The recent creep test results by Yin et al. [141] showed that both minimum creep rate and creep strain significantly decrease with increasing sulfur or by doping nanostructured nickel with boron. The stress exponent,  $n$  in the expression of Coble-type creep increased to around five at 373 K and 473 K from two at room temperature. A model for grain-boundary sliding, in which grain-boundary dislocations and back stress are introduced, was proposed to explain the large stress exponent. The calculated back stress indicated that the interstitials in grain boundaries effectively retard the sliding of grain-boundary dislocations.

### 5.7. Fatigue of nanocrystalline materials

There have not been many reports on the fatigue properties of nanocrystalline materials. Among the earliest study is Whitney et al. [142] on tension–tension cycling of nanocrystalline copper prepared by inert gas condensation, with a maximum stress that ranged from 50% to 80% of the yield stress. The minimum stress was 10 MPa. After several hundred thousand cycles, a moderate increase in grain size was observed (approx-

imately 30%). The samples were shown to elongate slightly in the course of a prolonged fatigue test. The amount of strain is similar to the room temperature creep strain observed previously in nanocrystalline copper under a constant stress comparable to the maximum cyclic stress. The cyclic deformation appeared to be elastic. However, an elastic modulus was measured that is a factor of 2 smaller than the modulus for ordinary copper.

Yan et al. [143] performed tensile fatigue tests of nanosized yttria stabilized zirconia with average grain size of  $100 \pm 20$  nm. Samples of the same chemical composition with submicron grains were simultaneously tested for comparison. It was documented by AFM imaging that localized superplastic deformation of the 100 nm grains at and near the fatigue fracture surfaces was generated while in the submicron grain-sized samples, the grains retained their original equiaxed morphology. The micromechanism responsible for the above mentioned phenomenon was thought to be essentially governed by grain-boundary diffusion. It was also suggested that a minor role might be played by dislocation climb and multiplication.

Vinogradov et al. [144] investigated cyclic behavior of commercial purity ultrafine-grained titanium obtained by severe plastic deformation through equal channel angular pressing (ECAP). It was shown that fine grained Ti processed by ECAP revealed considerable increase in fatigue life and fatigue limit under constant load testing when compared with those in the coarse-grain state. The  $S-N$  (Wöhler) plot for ECAP Ti is shown in Fig. 29. Contrary to typical wavy-slip materials such as copper and Al-alloys, which show significant degradation in strain-controlled cyclic properties as suggested by Pelloux [145], it was shown that Ti did not demonstrate any reduction in its fatigue performance under constant plastic strain cyclic testing as is evidenced by nearly the same Coffin–Manson behavior in the fine-coarse grain size conditions. It was concluded that both grain-refinement and the work hardening due to the increase of the average dislocation density play important role in resultant properties of materials obtained by severe plastic deformation.

Patlan et al. [146,147] studied the fatigue response of 5056 Al–Mg alloy and reported that while a certain enhancement of fatigue performance was observed [148] in the

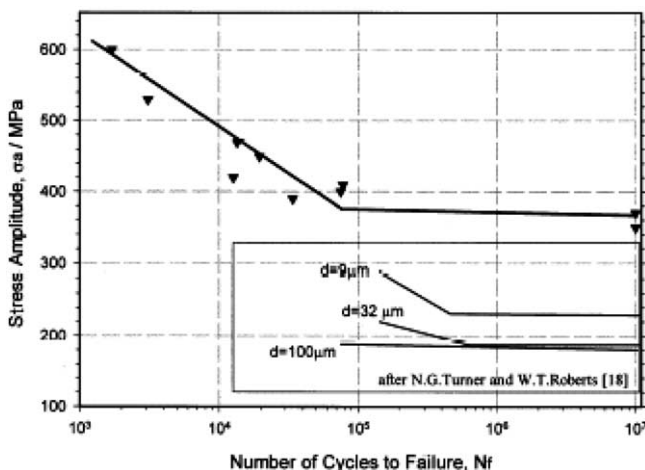


Fig. 29.  $S-N$  diagram of ECAP titanium (inset box shows  $S-N$  diagram for conventional polycrystalline Ti with grain sizes  $d = 9$ , 32, and 100  $\mu\text{m}$  [144]).

high-stress regime if compared with the conventional O-temper material, this advantage disappeared during the plastic strain controlled tests in the low-cyclic regime. They pointed out that the susceptibility of the ECAP materials to strain localization can be a main factor which limits their tensile and fatigue ductility and determined their fatigue weakness in comparison with conventional materials. The suggestion was made that a short annealing at moderate temperatures may dramatically improve the ductility of the ECAP Al alloys mainly due to partial recovery of grain boundaries. They reported that annealing at 150 °C for 15 min resulted in considerable improvement of low-cyclic fatigue life at constant plastic strain amplitude.

Chung et al. [149] studied the mechanical properties and fatigue behavior of solid solution treated 6061 Al alloy processed by ECAP. They reported a remarkable enhancement in fatigue life, by a factor of about 10, compared to a T6 treated commercial 6061 Al alloy. This occurred in both low- and high-cycle regimes after a single ECAP pass. Further deformation by ECAP, however, was reported to virtually eliminate this improvement especially in the high cycle regime. A fine-grained microstructure with low-grain boundary misorientation angles, typical after one ECAP pass, was proposed to yield the best result in the fatigue performance in a 6061 Al alloy. It was pointed out that one needs to pay attention to a single pass material rather than multi-passed material if improvement in fatigue life is a primary concern for engineering applications.

Kim et al. [150] tested ultrafine grained low carbon (0.15 wt.% C) steel processed by ECAP for fatigue properties, including cyclic softening and crack growth rate. ECAP steel was shown to exhibit cyclic softening. After the first cycle, tension and compression peak stresses were shown to decrease gradually with number of cycles. The ECAPed steel was shown to exhibit slightly higher crack growth rates and a lower  $\Delta K_{th}$  with an increase in  $R$  ratio. This was attributed to a less tortuous crack path. Kim et al. [151] studied the effect of grain size (varying in the range of 1–47  $\mu\text{m}$ ) on the fatigue behavior of AISI 304 SS and showed that a beneficial effect on the fatigue behavior of the steel is obtained by decreasing grain size.

Fatigue strength of two ultrafine grained steels (grain sizes 0.8 and 1  $\mu\text{m}$ ) was investigated by Chapetti et al. [153] who showed that important improvement on fatigue strength was observed in ultrafine grained steels when compared with similar steels of coarser grains. The results were shown to obey the Hall–Petch relation observed between smooth fatigue limit and grain size  $d$ .

Chapetti et al. [157] showed for ultrafine grained steel (grain size 1  $\mu\text{m}$ ) that the threshold for fatigue crack propagation is relatively low which is in good agreement with previous evidence. However, it was shown that when compared at medium and high applied stress intensity range level and the same applied mean stress, the ultrafine grained steel showed a lower crack propagation rate than a SM 490 steel or a HT 80 steel. Lukas et al. [158] studied the fatigue notch sensitivity of ultrafine grained copper of purity 99.9% produced by ECAP as cylindrical specimens with circumferential notches of different radii and compared results with the notch sensitivity of conventional copper. It was demonstrated that the fatigue notch sensitivity of ultrafine grained copper produced by ECAP technique is higher than that of standard polycrystalline copper. The ECAP copper of 99.9% purity was shown not to be prone to grain coarsening during cycling. The grain structure within plastic zone around the cracks was shown to differ substantially from the outside the plastic zone: the grains were found markedly elongated, but their size was shown to be preserved.



Mughrabi et al. [154] studied the cyclic deformation and fatigue behavior of ultrafine-grained metals produced by ECAP to determine cyclic softening, microscopic shear banding and fatigue lives. Low cycle (strain amplitude  $\sim 10^{-3}$ – $10^{-2}$ ) and high cycle (strain amplitude  $\sim 10^{-4}$ ) tensile microyielding, unloading and reloading tests were carried out on high-purity UFG copper and on commercial purity UFG aluminum. For copper, in the as-ECAP processed condition, the unloading and reloading stress–strain curves for the ultrafine grained sample were reported to be highly non-linear with an appreciable microplastic back–forward flow during unloading/reloading, whereas the coarse grained material was shown to exhibit an essentially linear elastic unloading/reloading stress–strain behavior. It was concluded that the non-linear unloading/reloading behavior is characteristic of ultrafine grained materials and that, in the ultrafine grained materials, much larger internal back stresses are induced during straining than in coarse grained material. The low cycle fatigue behavior was found to be worse than coarse grained material while the high cycle fatigue behavior was reported to show remarkable improvement over coarse grained sample. After an optimized annealing treatment (which probably leads to a bimodal distribution of grain size) ultrafine grained copper showed a markedly enhanced low cycle fatigue life; in fact, better than coarse grained copper. Fig. 30 shows the fatigue lives of ultrafine grain copper, plotted as an  $S$ – $N$  Woehler plot (stress amplitude  $\Delta\sigma/2$  versus  $\log N_f$ ). Ding et al. [155] viewed the ultrafine grained materials as a composite with soft grain interiors and hard grain boundaries and considered the resistance of this microstructure to fatigue crack propagation. An important aspect of the model is the incorporation of appropriate cyclic stress–strain curve—“saturation” stress versus ( $\Delta\epsilon_{pl}/2$ ). The model provided a good fit to experimental data.

Kim et al. [156] examined the fatigue properties of fine-grained AZ31 magnesium alloy produced by ECAP and reported a reduction of fatigue life by more than a factor of 10 in both low- and high-cycle fatigue region compared to the unECAPed sample. The ECAPed sample was shown to demonstrate 13% reduction in fatigue endurance life at  $N = 10^7$ . The ultimate tensile and yield strengths of the ECAPed samples were demonstrated to be lower than those of the unECAPed samples and comparison of fatigue behavior between the two conditions indicated that the fatigue life has a correlation with the yield strength in AZ 31

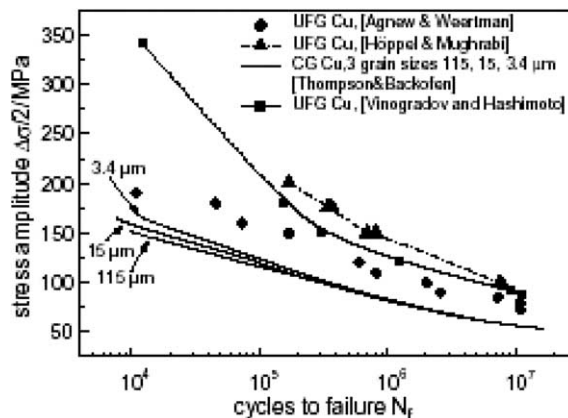


Fig. 30.  $S$ – $N$  (Woehler) plot of fatigue life of ultrafine grain copper, ECAP copper and coarse grained copper [154].

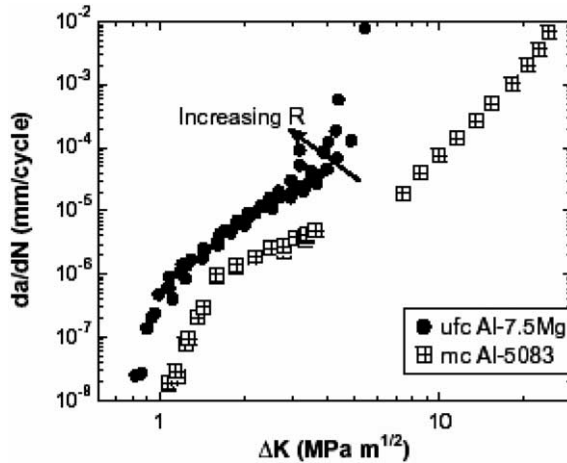


Fig. 31. Variation of fatigue crack growth rate,  $da/dN$ , as a function of stress intensity factor range,  $\Delta K$ , for cryomilled Al-7.5Mg at  $R = 0.1$ – $0.5$  at a fatigue frequency of 10 Hz at room temperature [152].

alloy. Unlike earlier reports on fatigue of nanocrystalline materials, AZ alloy with fine grains was shown to exhibit higher crack threshold and lower crack growth rate. It was suggested that enhanced ductility due to grain refinement in the ECAPed AZ 31 alloy resulted in increasing crack growth resistance because of its better ability to accommodate plastic strains during cycling.

Hanlon et al. [152] investigated the fatigue response of electrodeposited nanocrystalline pure Ni and a cryomilled ultrafine-crystalline Al–Mg alloy. They showed that grain refinement can have a substantial effect on total life under stress-controlled fatigue and on fatigue crack growth. Fig. 31 shows the  $da/dN$  versus  $\Delta K$  curve for the ultrafine grained Al–Mg alloy tested at  $R = 0.1$ – $0.5$  over the entire range of fatigue crack growth rates. This is compared with the crack growth data for commercial 5083 aluminum alloy at  $R = 0.33$ . Fully dense nanocrystalline and ultrafine grained Ni produced by electrodeposition exhibited much higher resistance to stress-controlled fatigue compared to conventional microcrystalline Ni. However, fatigue growth rate results showed that grain refinement in the nanocrystalline range had a deleterious effect on the resistance to subcritical fatigue fracture. These results were corroborated by results on cryomilled Al-7.5Mg alloy.

As a conclusion, it can be stated that there is fair agreement among the different results. The fatigue life, as measured by  $S$ – $N$  (Wöhler) type plots, is enhanced for nanocrystalline metals by virtue of their higher yield stress. On the other hand,  $\Delta K_{th}$  decreased and  $da/dN$  is increased for nanocrystalline metals. This latter effect is attributed to the smoother fracture path in nanocrystals.

## 6. Nanocrystalline ceramics and composites

There is a wealth of information available on nanostructured ceramics and composites primarily focusing on different synthesis techniques for specific composition and structure driven by the fact that the nanostructured ceramics could demonstrate improved properties as compared to their micro/coarse grained counterparts. Table 5 lists publications on

Table 5  
 Partial list of papers on synthesis techniques of common nanocrystalline ceramics

Material	First author	Year	Synthesis technique	Grain size (nm)
ZrO <sub>2</sub>	Thangadurai [169]	2004	Chemical co-precipitation	10–13
	Zhang [166]	2004	Agglomeration	12
	Ramaswamy [174]	2004	Amorphous citrate route	8
	Feng [180]	2004	Reduction of ZrCl <sub>2</sub> by Na	17
	Luscalea [187]	2004	pH controlled nitrate–glycine gel-	5–8
	Frolova [188]	2003	Combustion	–
	Robert [203]	2001	Co-precipitation	10–20
	Juarez [211]	2000	Pechini process	10
	Popp [219]	1998	Nitrate–citrate combustion route	10–100
	Lamas [220]	1998	Evaporation of solid mater with CO <sub>2</sub> laser	12–13
	Lamas [221]	1998	Nitrate–citrate gel route	10–20
	Duran [225]	1996	Pyrolysis-nitrate sol. with citric	9
	Qui [226]	1995	Acid/glycine	200
	Demyanets [227]	1995	Co-precipitation <i>n</i> -Butanol azeotropic distillation Chemical precipitation	15
	TiO <sub>2</sub>	Li [161]	2005	Sol–gel
Duan [159]		2004	High pressure sintering	<100
Dhage [175]		2004	Gel conversion	10
Lee [192]		2003	Spark plasma sintering	>1000
Liao [214]		1999	High <i>P</i> and low <i>T</i> sintering	38
Bykov [228]		1995	Sintering	15
BaTiO <sub>3</sub>	Buscaglia [162]	2004	Spark sintering	40–60
	Luan [183]	2004	Spark plasma technique	13
	Kim [186]	2004	Two-step sintering	1000
	Ragulya [218]	1998	Non-isothermal and rate controlled decomposition of organic precursors	20–25
Mn <sub>3</sub> O <sub>4</sub>	Anilkumar [164]	2005	Gel to crystal conversion	50
	Chang [165]	2004	Chemical bath deposition	–
	Zhang [171]	2004	Solvothermal technique	–
	Finocchio [167]	2004	Co-precipitation	–
SiC	Cheng [193]	2005	CVD and liquid precursor infiltration to prepare	–
	Zhang [224]	1996	Nanosize tubules followed by dissolution of alumina in HF	50
CeO <sub>2</sub>	Zhang [166]	2004	Agglomeration	18
	Markmann [198]	2002	Yttrium doping and colloidal processing	–
MgO	Ehre [168]	2004	Hot-pressing	10
PbTiO <sub>3</sub>	Forrester [172]	2004	Mechanical alloying/sintering	20
	Lemos [177]	2004	Pechini method	100
YAG	Pradhan [185]	2004	Co-precipitation	5–7
	Lu [202]	2002	From aq. sol. of Al, Yt and NyCl <sub>2</sub>	–
Perovskite	Xue [195]	2002	Mechanically activating oxides	–
BaSnO <sub>3</sub>	Lu [163]	2005	Hydrothermal reaction and crystallization	27.6

(continued on next page)

Table 5 (continued)

Material	First author	Year	Synthesis technique	Grain size (nm)
Hydroxyapa	Han [182]	2004	Citric acid sol–gel combustion	–
TiB <sub>2</sub>	Gu [196]	2003	Benzene-thermal reaction of Na with B powder and TiCl <sub>4</sub>	15–40
TiC	Xinkun	2001	Mechanical alloying	7
	Meyers [362]	1995	Spark erosion	5–50

this topic classified according to the composition. The most often researched compositions are ZrO<sub>2</sub>, TiO<sub>2</sub>, BaTiO<sub>3</sub>, and SiC. Superhard coatings made of nanocomposites have also been widely researched. The article by Veprek [337] reviews the subject. In this section we will attempt to capture the advances that have taken place in the field of mechanical properties of nanoceramics and nanocomposites over the last few years built on the understanding developed over years of research in this field.

There has been extensive effort to fabricate nanostructured ceramics. Methods such as hot-pressing, hot isostatic pressing, spark plasma sintering etc. have been employed. Conventional pressureless sintering is the most common low cost approach to sinter ceramics but it is difficult to realize densification without grain growth. This has stimulated researchers to develop new and fancy synthesis methods that can partly/fully deal with the limitations of powder processing synthesis techniques.

Duan et al. [159] demonstrated the preparation of Al<sub>2</sub>O<sub>3</sub>/TiO<sub>2</sub> nanocomposite by high-pressure sintering where addition of nano-MgO powder improved the densification and retarded grain growth. Fig. 32 is an illustration of a ceramic nanocomposite prepared by high-pressure sintering. The SEM micrograph is taken from a fracture surface. The grains are on the order of 100 nm. The nanocomposite contains grains of alumina, titania, and magnesia. Although the pressure (~1 GPa) and temperature (~850 °C/30 min) are high, no significant grain coarsening occurred because of the different compositions.

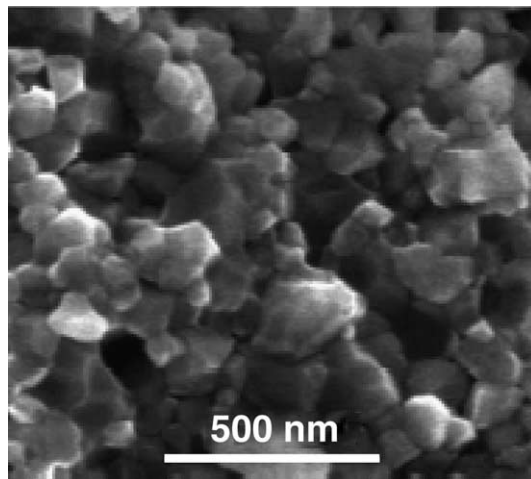


Fig. 32. SEM micrograph of fracture surface in Al<sub>2</sub>O<sub>3</sub>–TiO<sub>2</sub>–MgO nanocomposite consolidated by high pressure ( $P \sim 1$  GPa) at 850 °C for 30 min [159].

Kear et al. [160] developed two production methods, one method called transformation assisted consolidation (TAC) that utilized hot pressing to consolidate a flame-synthesized metastable nanopowder which took advantage of a pressure-induced phase transformation to suppress grain growth during consolidation. The second method utilized plasma spraying of an aggregate powder feed to generate a splat-quenched metastable phase with extended solid solubility.

Li et al. [161] used anatase titania nanopowder with mean particle sizes of 7, 14, 26 and 38 nm synthesized by sol–gel technique to sinter bulk TiO<sub>2</sub> nanoceramics. Buscaglia et al. [162] synthesized dense nanocrystalline barium titanate (BaTiO<sub>3</sub>) ceramic by spark plasma sintering technique (at 800 °C) of nanopowders produced by a wet chemical process. Lu et al. [163] prepared a BaSnO<sub>3</sub> powder with a crystallite size of 27.6 nm through a hydrothermal reaction of a peptised SnO<sub>2</sub> · xH<sub>2</sub>O and Ba(OH)<sub>2</sub> at 250 °C and following crystallization of the hydrothermal product at 330 °C. Anilkumar et al. [164] followed a simple gel to crystal conversion route for the preparation of nanocrystalline tetragonal Mn<sub>3</sub>O<sub>4</sub> powders at 80–100 °C under refluxing conditions. Various other methods for preparing nanocrystalline Mn<sub>3</sub>O<sub>4</sub> powders such as chemical bath deposition [165], solvothermal [166] and coprecipitation [167] have also been reported. Densification of pure nanocrystalline MgO powder with 10 nm particle size by hot-pressing was investigated by Ehre et al. [168] in the temperature range 700–800 °C, applied pressure range 100–200 MPa, and for duration of up to 240 min. The final grain size was shown to decrease with increasing applied pressure.

Thangadurai et al. [169] prepared La<sub>2</sub>O<sub>3</sub> doped nanocrystalline zirconia (ZrO<sub>2</sub>) by chemical co-precipitation method for 3, 5, 8, 10, 15, 20 and 30 mol% concentrations of La<sub>2</sub>O<sub>3</sub>. Gaikwad et al. [170] applied a simple coprecipitation technique for the preparation of pure ultrafine single-phase CaBi<sub>2</sub>Ta<sub>2</sub>O<sub>9</sub> (CBT). Ammonium hydroxide and ammonium oxalate were used to precipitate Ca<sup>2+</sup>, Bi<sup>3+</sup> and Ta<sup>5+</sup> cations simultaneously. Zhang et al. [171] weakly agglomerated nanocrystalline ceramic oxides (ZrO<sub>2</sub>, CeO<sub>2</sub>, and Y<sub>2</sub>O<sub>3</sub>) powders in the presence of anionic starburst dendrimers poly (amidoamine), PAMAM with surface carboxylate groups. The PAMAM dendrimer was shown to be an inhibitor for crystal formation and affected the crystal morphology and particle size during the preparation. The pressure-less sintering behavior of PbTiO<sub>3</sub> powders synthesized by mechanical alloying TiO<sub>2</sub> and PbO was investigated by Forrester et al. [172] using dilatometry and X-ray diffraction. As-synthesized, the powders were shown to be nanocrystalline with a mean particle size of 20 nm. Pressureless sintering in the range 500–1050 °C gave single phase ceramics with densities of 85–90% and crystallite sizes in the range 80–400 nm. Silva et al. [173] synthesized nanocrystalline CoFe<sub>2</sub>O<sub>4</sub> powders using metallic nitrates dispersed in aqueous media precipitated by stoichiometric amount of NH<sub>4</sub>OH. The obtained amorphous powder was washed, dried at 80 °C and heat-treated at various temperatures for 2 h for crystallization of the material. Ramaswamy et al. [174] synthesized nanocrystalline zirconia powder with a fairly narrow particle size distribution by the amorphous citrate route. The powder obtained was shown to have a high surface area of 89 m<sup>2</sup> g<sup>-1</sup>. Rietveld refinement of the powder XRD profile of the zirconia sample suggested stabilization of zirconia in the tetragonal phase with around 8% monoclinic impurity. Smaller crystallite size was shown to play a role in the stabilization of zirconia into the tetragonal phase. Dhage et al. [175] followed a simple gel to crystal conversion route for the preparation of TiO<sub>2</sub> at 80–100 °C under refluxing conditions. Freshly prepared titanium hydroxide gel was allowed to crystallize under refluxing and stirring conditions for 6–12 h. Formation of

nanocrystals of anatase was confirmed by X-ray diffraction (XRD) study. Chen et al. [176] prepared nanocrystalline titanium diboride ( $\text{TiB}_2$ ) by the reaction of  $\text{TiCl}_4$  with  $\text{NaBH}_4$  in the temperature range of 500–700 °C in an autoclave. TEM images showed particle morphology, with average grain size of 15 nm for the powder obtained at 600 °C. Lemos et al. [177] synthesized ytterbium modified lead titanate ceramics by the Pechini method. The materials were calcinated under flowing oxygen at different temperatures, from 300 °C to 700 °C. Nanostructured PYbT was obtained by high-energy milling and investigated using different techniques that revealed that the obtained materials were formed by nanometric particles. Rajesh et al. [178] prepared nanocrystalline lanthanum phosphate having average crystallite size 10–12 nm by a controlled precipitation reaction from lanthanum nitrate and orthophosphoric acid. The precipitate obtained was calcined in the range 300–800 °C and further sintered as compacted discs at a temperature of 1250 °C. An average grain size of 1–2  $\mu\text{m}$  was obtained on sintering at 1250 °C. Li et al. [179] synthesized nanosized  $\text{Sr}_{0.5}\text{Ba}_{0.5}\text{Nb}_2\text{O}_6$  (SBN50) ceramic powder by an aqueous organic gel route. Homogeneous Sr–Ba–Nb precursor gels on calcinations at 800 °C for 2 h produced a pure tungsten bronze SBN phase and the corresponding average particle size was reported to be in the range of 30–50 nm. Feng et al. [180] synthesized cubic  $\text{ZrO}_2$  nanocrystals through a novel reduction–oxidation route, in which metal zirconium was reduced from zirconium tetrachloride ( $\text{ZrCl}_4$ ) by sodium, and then oxidized in atmosphere. Using X-ray powder diffraction and TEM analysis, it was shown that cubic nanocrystalline  $\text{ZrO}_2$  with high crystallinity was obtained, which consisted dominantly of spherical particles with an average size of 17 nm or so. Zhang et al. [181] prepared nanocrystalline  $\text{Ce}_{0.8}\text{Gd}_{0.2}\text{O}_{2-\delta}$  powder from a homogeneous precipitation system using hexamethylenetetramine as a precipitate. The powder calcined at 700–800 °C was shown to exhibit optimal sinterability, and could be sintered to nearly full density at a temperature as low as 1250 °C. Han et al. [182] used the citric acid sol–gel combustion method for the synthesis of nanocrystalline hydroxyapatite (HAP) powder from calcium nitrate, diammonium hydrogen phosphate and citric acid. The HAP powder was sintered into microporous ceramic in air at 1200 °C with 3 h soaking time. Luan et al. [183] obtained fine-grained  $\text{BaTiO}_3$  ceramic at a low sintering temperature of 900 °C within a short sintering period by means of a new sintering technique called spark plasma sintering (SPS). The ceramic was shown to be highly densified to more than 99% of the theoretical X-ray density with homogeneous microstructures, signifying that the SPS process is effective for densification. Piticescu et al. [184] demonstrated that polar ceramics with high homogeneity, high sinterability and nanocrystalline structure can be obtained by hydrothermal procedures. They studied the influence of the hydrothermal reaction conditions on the properties of a PZT powder synthesized from soluble salts of Pb(II), Ti(IV) and Zr(IV). Chemical quantitative analysis and microstructural investigations were performed and based on these results a mechanism of hydrothermal synthesis of PZT was proposed. Technique for processing of transparent nanoceramics was presented by Pradhan et al. [185] who synthesized Nd:YAG nanoparticles by coprecipitation. The powders prepared by the coprecipitation technique were shown to display significantly less agglomeration of crystallites, indicating higher sinterability. Crystallite size dependence on calcination temperature was shown to suggest optimum temperature of 1100 °C, at which phase purity of YAG nanopowder with highest sinterability could be obtained. It was demonstrated that the optimum temperature for vacuum-sintering is about 1785 °C for uniaxially pressed samples. This resulted in transparent ceramic with uniform particle size of about 5–7  $\mu\text{m}$ , and above this temperature, large grain growth

occurred and facilitated large pores formation in the intergrain region that made the ceramic fragile at the grain boundary. Kim et al. [186] employed two-step sintering method to consolidate nanosize  $\text{BaTiO}_3$  powders. This comprised initial heating at relatively higher temperature and following low-temperature sintering for a long period of heating. Pressed green bodies of  $\text{BaTiO}_3$  were first heated to  $1300\text{ }^\circ\text{C}$  to achieve an intermediate density, then cooled down and held at  $1100\text{ }^\circ\text{C}$  for 0–20 h until they became fairly dense. Slight grain growth was shown to occur during the second step (with the final grain size of  $1\text{ }\mu\text{m}$ ), whereas the density was shown to decrease significantly. Luscalea et al. [187] investigated the synthesis of nanocrystalline  $\text{ZrO}_2$ –15mol% $\text{CeO}_2$  powders by a pH-controlled nitrate–glycine gel-combustion process. It was claimed that the metastable tetragonal phase could be fully retained due to the small crystallite size of the powders (5–8 nm). Frolova [188] used coprecipitation method to produce stable sols of the binary oxides ( $\text{ZrO}_2$ – $\text{GeO}_2$ ). Binary oxides exhibited high dispersity and homogeneity. A heat-treatment of  $\text{ZrO}_2$ – $\text{GeO}_2$  xerogels (dried in air sols) was shown to result in transformation of amorphous materials into homogeneous nanocrystalline glass–ceramic composition. Dhage et al. [189] applied a simple co-precipitation technique for the precipitation of pure ultra-fine single phase  $\text{SrBi}_2\text{Ta}_2\text{O}_9$ . Ammonium hydroxide was used to precipitate  $\text{Sr}^+$ ,  $\text{Bi}^{3+}$  and  $\text{Ta}^{5+}$  cations simultaneously. No pyrochlore phase was found while heating powder at  $800\text{ }^\circ\text{C}$  and pure  $\text{SrBi}_2\text{Ta}_2\text{O}_9$  phase confirmed by X-ray diffraction. Synthesis of nanocrystalline titanium carbonitride materials at different pyrolysis temperatures via polymer-to-ceramic transformation of synthesized poly(titanylcarbodiimides) and their structural and nanochemical characterization using high-resolution and analytical electron microscopy, in combination with quantum mechanical calculations was reported by Lichtenberger et al. [190]. Pyrolysis at  $800\text{ }^\circ\text{C}$  was shown to form a mixture of amorphous carbon and titanium nitride as crystalline particles of about 4 nm in size while pyrolysis at  $1100\text{ }^\circ\text{C}$  yielded titanium carbonitride as crystalline particles of 20–30 nm in size. Nersisyan et al. [191] investigated the combustion process of  $\text{TiO}_2$ –Mg and  $\text{TiO}_2$ –Mg–C systems with NaCl as an inert diluent. The values of combustion parameters and temperature distribution on a high-temperature wave according to the amount of sodium chloride were obtained by thermocoupling technique. The leading stages of combustion processes were reported and the sizes of reactionary zones were estimated. It was shown that the introduction of NaCl in an initial mixture promotes the formation of a nanocrystalline structure of the final product.

Lee et al. [192] investigated the effect of spark plasma sintering (SPS) on the densification of  $\text{TiO}_2$  ceramics. A fully-dense  $\text{TiO}_2$  specimen with an average grain size of  $\sim 200\text{ nm}$  was reported by spark plasma sintering at  $700\text{ }^\circ\text{C}$  for 1 h. In contrast, it was reported, that a theoretical density specimen could only be obtained using conventional sintering above  $900\text{ }^\circ\text{C}$  for 1 h with an average grain size of 1–2  $\mu\text{m}$ . Cheng et al. [193] used polymeric and oligomeric carbosilanes having Si atoms linked by methylene ( $-\text{CH}_2$ ) groups to prepare nanosized tubules and bamboo-like SiC structures by both CVD and liquid precursor infiltration and pyrolysis inside of nanoporous alumina filter disks, followed by dissolution of the alumina template in  $\text{HF}_{(\text{aq})}$ . In the case of the CVD-derived SiC nanotubes, annealing these structures up to  $1600\text{ }^\circ\text{C}$  in an Ar atmosphere was shown to yield a nanocrystalline  $\beta$ -SiC or  $\beta$ -SiC/C composite in the shape of the original nanotubes, while in the case of the liquid precursor-derived nanostructures, conversion to a collection of single crystal SiC nanofibres and other small particles was reported. Panda et al. [194] reported synthesis of nanocrystalline powders of stoichiometric and non-stoichiometric strontium bismuth

tantalite starting from an aqueous precursor solution. Complete dehydration of the precursor solution was shown to generate a precursor which on direct calcinations at 700–750 °C for 2 h resulted in phase-pure  $\text{Sr}_{1-x}\text{Bi}_{2+y}\text{Ta}_2\text{O}_9$  powders, with particle size in the range of 23–33 nm.

Xue et al. [195] synthesized a large number of ceramic perovskites by mechanically activating constituent oxides at room temperature. The activation-synthesized ferroelectrics and piezoelectrics were shown to exhibit a nanocrystalline structure that is not shown by the materials prepared by any other processing route.

Synthesis of titanium diboride ( $\text{TiB}_2$ ) via a benzene-thermal reaction of metallic sodium with amorphous boron powder and titanium tetrachloride at 400 °C in an autoclave was reported by Gu et al. [196]. The processing temperature was reported to be much lower than that of traditional methods. Nordahl et al. [197] demonstrated that seeding nanocrystalline transition alumina powders is a viable option for producing high quality, alumina based ceramic where by using  $\alpha\text{-Al}_2\text{O}_3$  seed particles, the sintering temperature was reduced from 1600 °C for unseeded  $\gamma\text{-Al}_2\text{O}_3$  to 1300–1400 °C in dry pressed powders. Markmann et al. [198] exhibited that the combination of yttrium doping and colloidal processing allowed for the synthesis of dense nanocrystalline cerium oxide by pressureless sintering. Cerium oxide was synthesized by the direct homogeneous precipitation method using hexamethylenetetramine (HMT). Kim et al. [199] prepared nanocrystalline indium tin oxide powder with different particle size using a coprecipitation process. They examined the sintering characteristics of the powder at different heating rates. Decrease of particle size in nanosized powder regime promoted the densification in normal rate sintering as temperature increased, while this was shown to retard severely the densification at high temperature in rapid rate sintering. Bab et al. [200] synthesized nanocrystalline HfN powders by mechanically assisted gas–solid reaction. The results showed the formation of an interstitial solid solution  $\alpha\text{-Hf}$ , prior to its transformation to cubic HfN. Zhu et al. [201] investigated the synthesis of TiC powder by mechanical alloying and showed that the nanocrystalline TiC powder is fabricated in a very short time at room temperature and that the mechanism is self-propagating reactive synthesis conducted by mechanical alloying. Lu et al. [202] claimed to develop a new generation of solid-state laser and optical materials on the basis of highly transparent nanocrystalline yttrium aluminum garnet  $\text{Y}_3\text{Al}_5\text{O}_{12}$  (YAG) ceramic that was synthesized using aqueous solutions of aluminum, yttrium and neodymium chlorides.

Laberty-Robert et al. [203] used a Pechini process for preparation of yttria-stabilized zirconia gels and powders. The decomposition of this gel which was shown to be based on a thermally induced anionic redox reaction yielded nanostructured powders at 325 °C that is agglomerated with an average of 10–20 nm primary particles.

Li et al. [204] reported synthesis of nanocrystalline  $\text{CeO}_2$  powders of high sinterability by a mimic alkoxide method, which employed alcohols as solvent, cerium nitrate hexahydrate as cerium source and diethyl-amine (DEA) as precipitant.

An overview of the emerging cost-effective electrostatic spray-assisted vapour deposition (ESAVD) based method for the synthesis of nanocrystalline oxide and non-oxide ceramic films and powders was presented by Choy [205]. ESAVD process involves spraying atomized precursor droplets across an electric field and if the droplets undergo heterogeneous chemical reaction near the vicinity of the heated substrate, a stable solid film with excellent adhesion onto a substrate results. This produces highly pure materials with structural control at low processing temperatures. Different films that were studied are



Y<sub>2</sub>O<sub>3</sub>:Eu film, TiO<sub>2</sub> film, ZnS film, and CdS film. It was shown that the structure and properties of the synthesized materials can be optimized by varying processing parameters. The process, apparently, is superior to chemical vapor deposition (CVD) and physical vapor deposition (PVD) methods since the depository efficiency is higher. Also, ESAVD based methods can be performed in an open atmosphere without the use of sophisticated reactor and vacuum system.

Zawadzki et al. [206] prepared nanocrystalline and nanoporous ceramics composed of a network of alumina and zinc aluminate doped with Tb ions. It was claimed that the textural properties make these structures interesting as a host lattice for active systems such as rare earth ions. Kear et al. [160] developed two methods for the production of nanostructured bulk ceramics. The first method involved hot pressing to consolidate a flame-synthesized metastable powder that took advantage of a pressure-induced phase transformation to suppress grain growth during consolidation. This process called transformation assisted consolidation (TAC) was used to prepare test samples of single phase nanocrystalline ceramic. The second method employed plasma spraying of an aggregated powder feed to generate a splat-quenched metastable phase with extended solid solubility.

Jose et al. [207] developed a single step process for the synthesis of nanoparticles of YBa<sub>2</sub>ZrO<sub>5.5</sub>, a complex perovskite ceramic oxide which did not involve a calcination step. The powder obtained by self-sustained combustion of a precursor complex of the respective metal ions, was reported to be in the range of 5–50 nm.

Das [208] reported an innovative sucrose process for synthesizing a variety of nanocrystalline ceramic powders using metal ion–sucrose solution. The process involved the dehydration of metal ion–sucrose solution to a highly viscous liquid, which on decomposition produced the precursor material. Calcination of the precursors at low temperatures was reported to produce nanocrystalline ceramic powders. The examples discussed included PbZr<sub>0.6</sub>Ti<sub>0.4</sub>O<sub>3</sub> (PZT) and spinel ferrites MFe<sub>2</sub>O<sub>4</sub> (M = Co, Ni, Zn). Lu et al. [209] claimed to have developed an innovative colloid-gel process using inorganic salts as starting material for preparing ferroelectric strontium bismuth tantalate (SrBi<sub>2</sub>Ta<sub>2</sub>O<sub>9</sub>) powder. The technique involved preparation of a mixture of Ta(OH)<sub>5</sub> colloid with the aqueous solutions of strontium and bismuth cations, followed by the addition of ethylene glycol and citric acid as gel-forming reagents. During the calcination process, the fluorite phase was formed as an intermediate that was subsequently converted into the SrBi<sub>2</sub>Ta<sub>2</sub>O<sub>9</sub> phase. After calcination at 750 °C, pure ultrafine SrBi<sub>2</sub>Ta<sub>2</sub>O<sub>9</sub> polycrystalline powder with a narrow particle size distribution was obtained (40 nm). Li et al. [210] reported synthesis of nanocrystalline  $\alpha$ -alumina powders with a primary mean particle diameter of 10 nm from alumina nitrate and ammonia solution using a precipitation method. The combined presence of 5 wt.%  $\alpha$ -alumina seed crystals, 100 nm in diameter, and 44% ammonium nitrate was reported to reduce the  $\theta$ -Al<sub>2</sub>O<sub>3</sub>  $\rightarrow$   $\alpha$ -Al<sub>2</sub>O<sub>3</sub> transformation temperature from 1200 °C to 900 °C.

Juárez et al. [211] presented a nitrate–citrate combustion route to synthesize nanocrystalline yttria-doped zirconia powders for tetragonal zirconia polycrystal (TZP) ceramic. The route was based on the gelling of nitrate solutions by the addition of citric acid and ammonium hydroxide, followed by an intense combustion process due to an exothermic redox reaction between nitrate and citrate ions. Yue et al. [212] reported preparation of a nitrate–citrate gel from metal nitrates and citric acid by sol–gel process, in order to synthesize Ni<sub>0.25</sub>Cu<sub>0.25</sub>Zn<sub>0.50</sub>Fe<sub>2</sub>O<sub>4</sub> ferrite. The nitrate–citrate gel exhibited self-propagating combustion behavior and after combustion, the gel directly transformed into

single-phase, nanosized NiCuZn ferrite particles with spinel crystal structure. The synthesized powder was densified at temperature lower than 900 °C and the sintered body possessed fine-grained microstructure, good frequency stability and high-quality factor compared to the sample prepared by conventional ceramic route. Das et al. [213] synthesized nanocrystalline (30 nm) lead zirconate–titanate (PZT) ceramics, with Zr/Ti ratio 60:40 by a chemical method starting from a mixed metal ion–tartarate ( $Zr^{4+}$ ,  $Ti^{4+}$ )–EDTA ( $Pb^{2+}$ ) complex solution. After complete evaporation of the mixed complex solution, a fluffy dried mass, known as precursor material was obtained. Heat-treatments of the precursor material at 400 °C for 2 h resulted in single phase PZT. The process was shown to provide a technically simple route for the preparation of nanocrystalline PZT powders at low preparation temperatures. Liao et al. [214] produced bulk nanocrystalline  $TiO_2$  by high pressure/low temperature sintering. Nanophase  $TiO_2$  powder with metastable anatase structure and particle size  $\sim 38$  nm was used as the starting material. During sintering, the anatase phase transformed to either rutile or srilankite phase, depending on the pressure/temperature combination. Grain growth was limited by the low sintering temperature and multiple nucleation events in the parent phase. The transformed rutile phase was reported to decrease with sintering pressure, due to increasing nucleation rate and decreasing growth rate with high pressure. It was demonstrated that in contrast to previous researchers who found exaggerated grain growth during sintering of nanocrystalline ceramics, it is possible to produce a dense sintered compact with grain size even smaller than that of the starting powder by proper selection of sintering parameters. Shantha et al. [215] investigated the influence of mechanical activation on the formation of  $Bi_2VO_{5.5}$ , bismuth vanadate (BiV) phase, by ball milling a stoichiometric mixture of bismuth oxide and vanadium pentoxide. Jiang et al. [216] synthesized nanocrystalline zinc ferrite powders with a partially inverted spinel structure by high-energy ball milling from a mixture of  $\alpha$ - $Fe_2O_3$  and ZnO crystalline powders in equimolar ratio. The resulting  $ZnFe_2O_4$  particles were reported to be in the superparamagnetic state at ambient temperature.

Haber et al. [217] showed that solution-phase processing affords nanoparticles and nanocomposites of a wide range of materials, including metals, alloys, intermetallics, and ceramics, with substantial control of particle size, particle morphology, microstructure, and composite microstructure. It was claimed that the particle size of nanocrystalline Cu produced by the reduction of CuCl could be varied between 10 and 30 nm by changes in reducing agent and solvent, while that of nano-Al could be varied between 45 and 180 nm. The morphology of nano-AlN produced by nitridation of nano-Al could be varied from almost entirely equiaxed to almost entirely whisker-like. Nanocrystalline nickel aluminides were synthesized by reacting  $NiCl_2$  and  $LiAlH_4$  in organic solvents, followed by solid state heating. Reactions performed in aromatic solvents were shown to produce a porous phase with highly sintered microstructure, while reactions performed in ethereal solvents yielded nanosintered nickel aluminide particles in an amorphous alumina matrix. Nanocrystalline composites of AlN and Al were prepared by suspending the AlN particles in organic solvent, and performing solution-phase chemistry to produce nano-Al. Ragulya [218] reported synthesis of nanocrystalline powders of barium titanate by non-isothermal and rate-controlled decomposition of organic precursors. The nanograined barium titanate powder sintered under rate-controlled conditions produced dense and fine-grained ceramic and it was pointed out that the thermal activated processes should be optimal through the entire temperature–time processing schedule. Popp et al. [219] synthesized

nanocrystalline ceramic powders of  $\text{ZrO}_2$ ,  $\text{Al}_2\text{O}_3$ ,  $\text{Si}_3\text{N}_4$ ,  $\text{AlN}$  by evaporation of solid materials in the focus of a  $\text{CO}_2$  laser followed by recondensation in a carrier gas stream. The production rates were reported to be in the range of  $40\text{--}100\text{ g h}^{-1}$  (oxides) or more than  $200\text{ g h}^{-1}$  (nitrides). The particle size distribution was shown to be influenced by different parameters of the formation process like laser power, area of the laser focus, pulse length in the case of pw mode, streaming velocity and type of the carrier gas. The powder consisted of nearly spherical particles with diameters in the range of  $10\text{--}100\text{ nm}$ . Powders of tetragonal zirconia polycrystals (TZP) ceramic were synthesized by Lamas et al. [220] using a nitrate–citrate gel combustion process. These powders were compacted by uniaxial pressing and fired at  $1400\text{--}1500\text{ }^\circ\text{C}$  for  $3\text{--}5\text{ min}$ , obtaining fine-grained, dense ceramic. Lamas et al. [221] utilized wet chemical methods to obtain yttria or calcia-doped zirconia powders for synthesizing partially stabilized zirconia ceramics. This method was based on pyrolysis of nitrate solutions with the addition of citric acid or glycine as a fuel. Pinckney et al. [222] produced nanocrystalline glass–ceramic with high elastic modulus and moderate strength and toughness from a wide area in the  $\text{SiO}_2\text{--Al}_2\text{O}_3\text{--MgO--ZnO--TiO}_2$  system. Pal et al. [223] grew barium hexaferrite phase of composition  $\text{BaO}\cdot 6\text{Fe}_2\text{O}_3$  of dimensions in the range of  $8.2\text{--}17.6\text{ nm}$  within a glass medium by subjecting the latter to a suitable heat treatment. Large bulk and fully dense SiC based nanoceramics with average grain size of  $50\text{ nm}$  and  $20\text{--}30\text{ wt.}\%$  nanometer sized  $\alpha\text{-Sialon}$ ,  $\text{Al}_x\text{Si}_{3-x}\text{O}_6$  and  $\alpha\text{-SiO}_2$  interfacial phases were prepared by crystallization of interfacial glass, using LMAS glass-coated SiC powder as starting material by Zhang et al. [224]. Durán et al. [225] prepared powders of yttria-doped tetragonal zirconia ( $3\text{ mol}\%$ ) with a narrow pore size distribution and ultrafine particle size ( $\sim 9\text{ nm}$ ) by the mixed organic and inorganic precursors coprecipitation method. The compaction behavior of almost agglomerate-free calcined powders was studied, and their sintering behavior using both isothermal and non-isothermal techniques were evaluated. Reports of fully dense nanoscale ceramics with an average grain size below  $95\text{ nm}$  were presented after sintering at  $1200\text{ }^\circ\text{C}$  for  $20\text{ min}$ . Qui et al. [226] by using heterogeneous *n*-butanol azeotropic distillation in the treatment of an aqueous coprecipitation gel, produced weakly agglomerated and sinterable nano- $\text{ZrO}_2$  powder with high density ( $99.5\%$ ) and fine-grain ( $\sim 200\text{ nm}$ ). Kats-Demyanets et al. [227] reported preparation of amorphous to nanocrystalline  $\text{ZrO}_2\text{--CeO}_2$  alloy powders by chemical precipitation. It was shown that sintering at  $1300\text{ }^\circ\text{C}$  for  $2.5\text{ h}$  was followed by grain growth between  $1000\text{ }^\circ\text{C}$  and  $1600\text{ }^\circ\text{C}$  and for  $2\text{--}20\text{ h}$ . Sintering of nanocrystalline powder material— $\text{Al}_2\text{O}_3\text{--ZrO}_2$  (grain size  $15\text{ nm}$ ) and  $\text{TiO}_2$  was studied by Bykov et al. [228].

Fracture toughness studies on nanocrystalline tetragonal zirconia with low yttria content carried out by Bravo-Leon et al. [229] showed that they could reach toughness between  $16$  and  $17\text{ MPa m}^{1/2}$ . It was shown that maximum toughness occurs just below the critical grain size of  $90$  and  $110\text{ nm}$ , respectively, i.e. just before spontaneous transformation to the monoclinic phase occurs. Moving away from the critical grain size, towards smaller grains, was shown to decrease toughness monotonically up to a factor of  $5$ . The critical parameter for maximizing toughness in nanocrystalline zirconia ceramics was pointed out to be proximity to the phase transformation boundary.

One of the attractive features of densified nanocrystalline ceramics is their ability to be subjected to superplastic forming at strain rates considerably higher than their conventional polycrystalline counterparts. This is a direct consequence of the added interfacial surfaces available for intergranular sliding. Mayo [241] synthesized  $\text{ZrO}_2$  powders by a chemical precipitation and agglomerated them by sinter forging. When they deformed

these consolidated nanocrystalline ceramics under compression ( $d = 80$  nm) they found that the strain rate obtained was 34 times higher than conventional zirconia ( $d = 0.3$   $\mu\text{m}$ ). Fig. 33 shows the stress versus strain rate curves for the two grain sizes. The fact that the two lines are parallel indicates that the same deformation mechanism is operating in them. This increased strain rate is important in superplastic forming. Superplastic forming processes that would require impractically long times can be applied, if the grain size is sufficiently reduced.

Superplasticity in fine-grained partially stabilized zirconia was demonstrated by Wakai et al. [230] at lower temperatures, particularly when the grain size is well below 100 nm. Jimenez-Melendo et al. [231] presented a list of all studies on the creep and superplastic deformation on these ceramics at temperatures above  $0.5T_m$ . Nanocrystalline oxide powder synthesized by Mayo et al. [232] as shown to exhibit superplastic strain rates  $\sim 100$  times faster than in comparable undoped systems, due to the dopant's role in lowering of the activation energy for diffusion along grain boundaries. Enhanced specific grain-boundary conductivity study in nanocrystalline  $\text{Y}_2\text{O}_3$ -stabilized zirconia carried out by Mondal et al. [233] showed that the specific grain-boundary conductivity of the nanocrystalline samples is 1–2 orders of magnitude higher than that of the microcrystalline samples since the conductivities of the bulk and the grain-boundary regions were the same irrespective of grain size. This was also attributed to the low Si-content and its grain size-dependent segregation in the nanocrystalline samples. Ductility study of nanocrystalline zirconia based ceramic at low temperature by Betz et al. [234] showed that a maximum elongation of about 60% can be achieved with a  $\text{ZrO}_2 + 10$  wt.%  $\text{Y}_2\text{O}_3 + 12$  wt.%  $\text{A}_2\text{O}_3$  composite ceramic at 1250 °C. The results were related to a deformation model based on mesoscopic grain-boundary sliding. Betz et al. [235] observed total strains exceeding 0.2 and strain rates as high as  $10^{-5} \text{ s}^{-1}$  without failure in nanocrystalline 5 mol% yttria stabilized zirconia ceramics with relative densities of about 80% and grain sizes between 30 and 60 nm. Porosity was not found to be critical for the ability to deform without cracking while

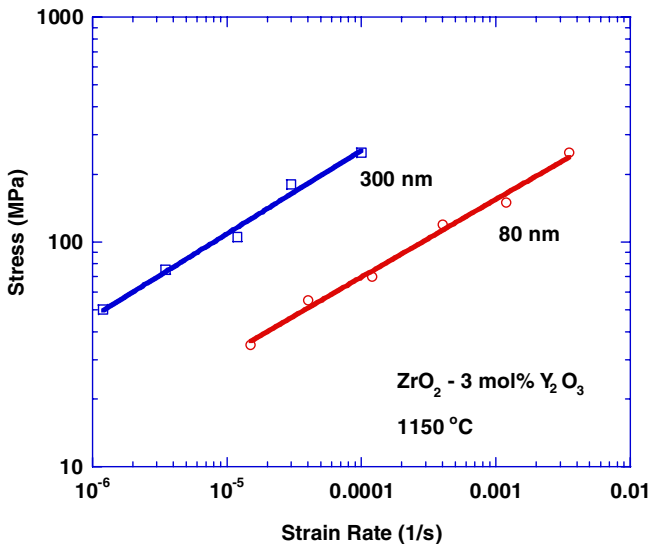


Fig. 33. Superplastic deformation of nanocrystalline and submicron-grained  $\text{ZrO}_2\text{-3mol\%Y}_2\text{O}_3$  [241].

the grain size exponent in the constitutive equation for superplastic flow yielded a value of 1.3. Winnubst et al. [236] showed that the deformation strain rate of nanocrystalline Y-TZP increased by a factor of 4 if the grain size decreased from 200 to 100 nm. It was demonstrated that these materials showed real superplastic deformation (strain rate  $> 10^{-4} \text{ s}^{-1}$ ) at relatively low temperature (1100–1200 °C). Grain boundary analysis indicated partial removal of an ultra-thin (1 nm), yttrium-rich grain-boundary layer after deformation. He et al. [237] reported synthesis of ultrafine grained TZP by a gel precipitation and sinter-forging. The resulting structure was shown to have improved grain-boundary structure with reduced flaws. Sánchez-Bajo et al. [238] carried out microstructural analysis of yttria-partially stabilized zirconia (Y-PSZ) as a high performance ceramic using X-ray materials. Creep study on yttria-partially stabilized zirconia with a grain size of 40 nm in compression at temperatures ranges between 1100 °C and 1200 °C and strain rates between  $5 \times 10^{-7} \text{ s}^{-1}$  and  $10^{-4} \text{ s}^{-1}$  as demonstrated by Gutiérrez-Mora et al. [239] showed that these ceramics probably cannot be deformed superplastically. The creep parameters reported were  $n = 1.4$  and  $Q = 660 \text{ kJ/mol}$ . Mayo [240] argued that the unusual trends in room temperature strain rate sensitivity of nanocrystalline materials may reflect thermally activated dislocation glide past synthesis-generated defects, rather than a true change in deformation mechanism at ultrafine grain sizes.

## 7. Deformation mechanisms in nanostructured materials

The expansion of the understanding of deformation of conventional polycrystalline materials to materials with grain sizes in the range of nanometer is, at present, an evolving process. Though several mechanisms have been proposed, there still exists widespread disagreement in the research community. Most striking of all is the observation of “Inverse Hall–Petch” phenomenon which is still in question ever since Chokshi et al. [97] reported it in 1989.

This section reviews the fundamental physical mechanisms responsible for the specific behaviors. From the previous sections, it can be concluded that nanocrystalline materials exhibit a high strength, albeit not as high as the extrapolated Hall–Petch prediction from the conventional regime of grain sizes (100–300  $\mu\text{m}$ ). Concomitantly, the nanocrystalline materials tend to exhibit much reduced ductility, due in part to a low work hardening rate leading to early strain localization and failure and also due to a reduced ability of the materials to accommodate the progression of cracks by extensive plastic deformation.

### 7.1. Pile-up breakdown

The concept of pile-ups has been at the root of the traditional explanation for the H–P effect. As the grain size is decreased, the number of dislocations piled up against a grain boundary decreases, at a fixed stress level, since this number is a function of the applied stress and of the distance to the source. Conversely, an increased stress level is needed to generate the same number of dislocations at the pile-up. At a critical grain size, we can no longer use the concept of a pile-up to explain the plastic flow. Fig. 34(a) shows pile-ups for a grain size in the micrometer regime. The sources are assumed to be in the center of the grain, leading to positive and negative dislocation pile-ups generated by the activation of a Frank–Read source. As the grain size is reduced to the nanocrystalline regime, the number of dislocations at the pile-up is eventually reduced to one. Thus, the

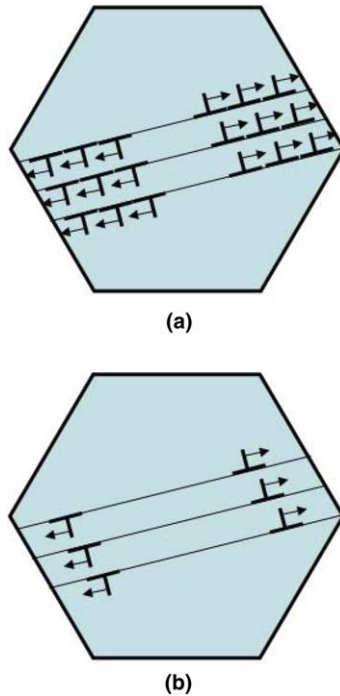


Fig. 34. Breakup of dislocation pile ups: (a) microcrystalline regime and (b) nanocrystalline regime.

multiplying effect on the stress field is lost. This is shown in Fig. 34(b). This mechanism was first proposed by Pande et al. [242] and further developed by Armstrong and coworkers [243–245].

As seen in Section 5, Koch et al. [246] performed microhardness tests on Fe samples produced by ball milling and observed that the hardness increased as the grain size decreased, as typically observed in coarse grained samples. Nieman et al. [101] observed that the hardness for nanocrystalline Pd followed a Hall–Petch dependence with a smaller slope than for coarse-grained Pd. Iyer et al. [105] observed a similar reduction in slope for Cu in the nanocrystalline range. These results are in contrast to the study of Chokshi et al., which show not only a decrease in slope, but a negative one.

Wadsworth and Nieh [247] predicted the grain size in various materials at which the Hall–Petch relationship would break down by assuming that there is a point at which each individual grain in a polycrystalline sample will no longer be able to support more than one dislocation. The critical equilibrium spacing between dislocations,  $l_c$ , from their calculation is

$$l_c = \frac{3Gb}{\pi(1-\nu)H} \quad (14)$$

where  $H$  is the hardness. In principle, when the grain size,  $d$  is smaller than  $l_c$ , there will be no dislocation pile-ups and the Hall–Petch relation will break down. Thus,

$$d = \frac{3Gb}{\pi(1-\nu)H} \quad (15)$$

Another interesting pile-up breakup model proposed by Pande et al. [242] considers the stress at the tip of any number of dislocations in the pile-up and equates it to the barrier stress required to free the dislocations.

The stress at the tip is given as

$$\sigma_{tip} = [(n + m - 1)/m]\sigma \tag{16}$$

where  $n$  is the number of dislocations in pile up,  $mb$  is the Burgers' vector of the locked superdislocation, and  $\sigma$  is the applied stress. Yielding occurs when  $\sigma_{tip}$  equals the barrier stress  $\sigma^*$ . Hence at yield,

$$\sigma^* = [(n + m - 1)/m]\sigma \tag{17}$$

The relationship between  $n$ , the number of dislocations and  $L$ , the pile-up length is given by

$$L^{-1/2} = (A/2\sigma)^{1/2}[2(n + m - 1)^{1/2} - \beta(4(n + m - 1))^{-1/6}] \tag{18}$$

where  $\beta = 1.85575$ ,  $A = Gb/\pi\sigma^*$  for a screw dislocation,  $b$  is the magnitude of the Burgers vector and  $G$  is the shear modulus. By eliminating  $n$  in (17) and (18), the stress is

$$\sigma = (2Am\sigma^*)^{1/2}L^{-1/2}f(L) \tag{19}$$

where  $f(L)$  is a function of  $L$  and  $m$ . The results are shown in Fig. 35, where it can be seen that the linear Hall–Petch relation is valid for  $n > 20$  but for values of  $n < 20$ , the exact and approximate curves exhibit discrete steps and begin to level off. Hence, the H–P relationship breaks down when the number of dislocations in the pileup approaches unity.

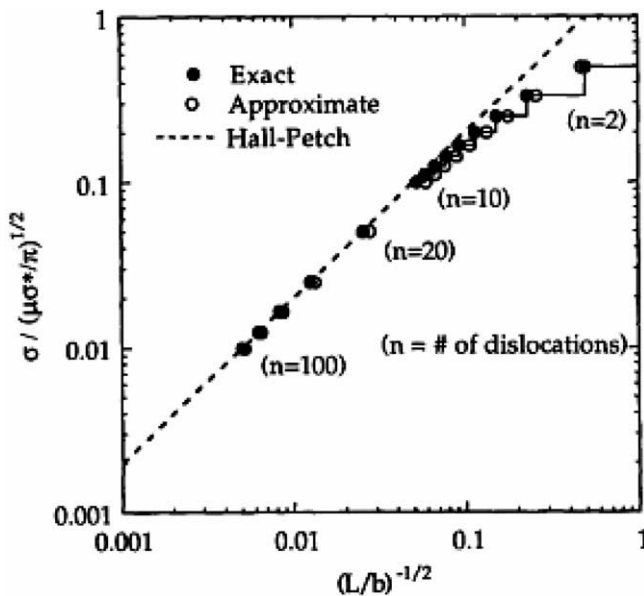


Fig. 35. Exact and approximate comparison of the Pande et al. model with Hall–Petch [242].

### 7.2. Grain-boundary sliding

The phenomenon of superplasticity has led to detailed study of grain-boundary sliding as the dominant deformation mechanism [248]. Fig. 36 shows a schematic in which one layer of grains slides with respect to the other, producing a shear strain in the process. Plastic deformation has taken place by virtue of the top layer of grains translating to the right with respect to the bottom layer of grains. This requires grain-boundary sliding and is the principal mechanism in superplasticity. For nanocrystalline materials, this has been proposed to be the dominant deformation mechanism at grain sizes <50 nm. Hahn et al. [249] proposed two hardness relationships,

$$H_v = H_0 + \frac{k}{\sqrt{d}} \quad \text{in the dislocation dominated regime and} \quad (20)$$

$$H_v = H_{v0} - \frac{m_1}{d} (d - m_2)^{1/2} \quad \text{in the grain boundary sliding regime.} \quad (21)$$

where  $m_1$ ,  $m_2$ , and  $k$  are material parameters and  $d$  is the grain size. Conrad and Narayan [250], employing the concept of thermally-activated shear, proposed that the macroscopic

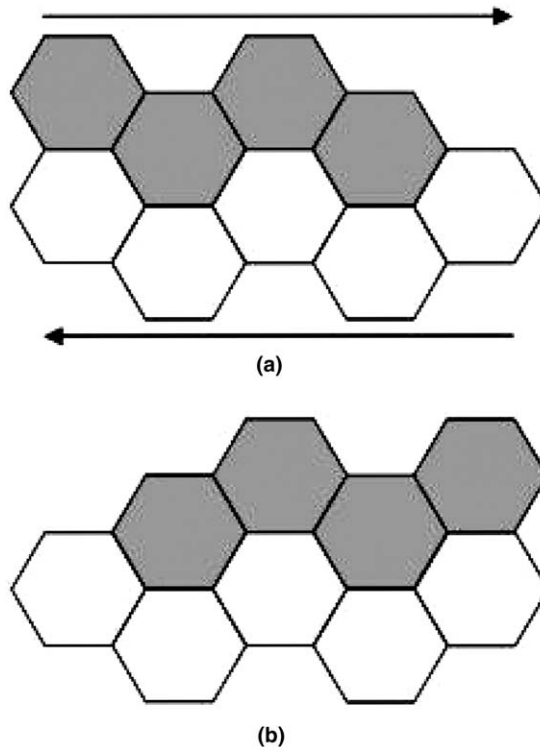


Fig. 36. Grain boundary sliding model: (a) initial position of grains and (b) position after top layer has slid to right.



shear rate, produced by the independent, atomic shear events at the grain boundary, is given by

$$\dot{\gamma} = N_v A b v \exp \left[ \frac{-\Delta G(\tau_e)}{kT} \right] \quad (22)$$

where  $N_v$  is the number of places per unit volume where thermally-activated shear can occur,  $A$  is the area swept out per successful thermal fluctuation,  $v$  is the frequency of vibration and  $\Delta G$  the Gibbs free activation energy, which is a decreasing function of the effective shear stress  $\tau_e = \tau - \tau_0$ , where  $\tau$  is the applied stress and  $\tau_0$  a back stress or threshold stress. Reasonable expressions for the parameters on the right side of Eq. (22) are  $N_v = \frac{\delta}{db^2}$ , where  $\delta \approx 3b$  is the grain-boundary width,  $A = b^2$ ,  $v = v_D (\approx 10^{13} \text{ s}^{-1})$  the Debye frequency. The free energy is expressed as:  $\Delta G = \Delta F - V\tau_e$ , where  $\Delta F$  is the Helmholtz free energy and  $V = b^3$  the activation volume.  $\Delta F$  was approximated by the energy for atom–vacancy interchange in the lattice or grain-boundary diffusion. Inserting activation the above values into Eq. (22) and considering both forward and backward jumps resulted in

$$\dot{\gamma} = \frac{6\delta v_D}{d} \sinh \left( \frac{V\tau_e}{kT} \right) \exp \left( \frac{-\Delta F}{kT} \right) \quad (23)$$

where  $\sinh x \approx x$  for  $x \leq 0.5$  and  $\sinh x \approx 1/2 \exp x$  for  $x \geq 2$ . Eq. (23) thus predicts  $\tau_e$  proportional to  $d$  for small values of  $\frac{V\tau_e}{kT}$  and varying as  $\ln(d)$  for large values.

Conrad [85] analyzed data on the effect of grain size  $d$  in the range of  $\mu\text{m}$  to  $\text{nm}$  on the flow stress of Cu. Three regimes were identified:

*Regime I* ( $d > 10^{-6} \text{ m}$ ): Dislocation pile-up is considered to be the dominant deformation mechanism. The rate controlling mechanism is given by

$$\tau = M\alpha Gb \left[ (\rho_0(T, \dot{\gamma}))^{1/2} + \frac{\beta(T, \dot{\gamma})\gamma}{bd^{1/2}} \right] \quad (24)$$

where  $M$  and  $\alpha (=0.3\text{--}0.5)$  are parameters, and  $\rho_0$  is the dislocation density. The first term contains the thermal component while the second term contains the  $d^{-1/2}$  dependence.

*Regime II* ( $d \approx 10^{-8}\text{--}10^{-6} \text{ m}$ ): Grain boundary shear promoted by the pileup of dislocations is considered to be the deformation mechanism. The governing equation is given by

$$\tau = \alpha Gb\rho^{1/2} + \left[ \left( \Delta F^* - kT \ln \left( \frac{\dot{\gamma}_0}{\dot{\gamma}} \right) \right)^{1/2} \left( \frac{Gb}{\pi V} \right)^{1/2} \right] d^{-1/2} \quad (25)$$

where  $\Delta F^*$  is the Helmholtz free energy,  $V$  is the activation volume,  $\rho$  is the dislocation density.

*Regime III* ( $d < 10^{-8} \text{ m}$ ): Grain boundary shear is considered to dominate deformation in this regime. The corresponding equation is given by

$$\tau - \tau_0 = \left( \frac{kT}{V} \ln \left( \frac{\delta v_D}{\dot{\gamma}} \right) + \frac{\Delta F^*}{V} \right) + \frac{kT}{V} \ln d \quad (26)$$

where  $\tau_0$  is threshold stress for shearing,  $\delta$  is the grain-boundary width,  $v_D$  is the frequency of vibration ( $\sim 10^{13} \text{ s}^{-1}$ ),  $\Delta F^*$  is the Helmholtz free energy. These three regimes are shown in Fig. 37. The continuous lines represent the application of Eqs. (24)–(26) above, while the experimental points shown represent the compilation of several investigations.

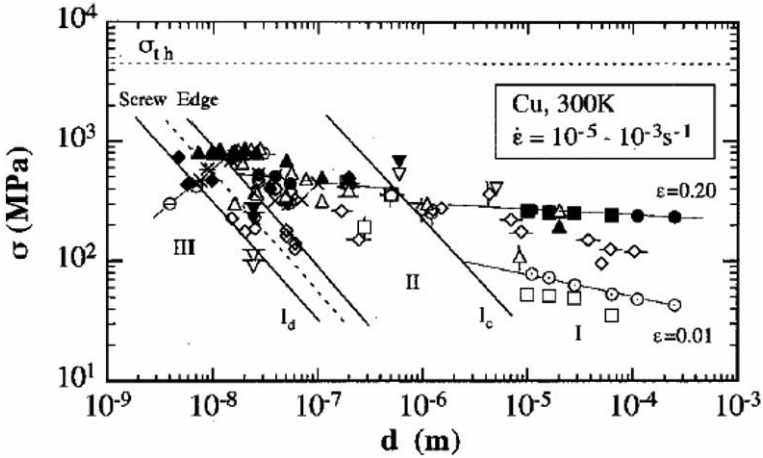


Fig. 37. Variation of flow stress with grain size for copper (300 K) on a log–log plot; notice three regimes I, II, III governed by different plastic deformation mechanisms [370].

For Regime I, the lines are given for two values of strain,  $\gamma$ : 0.01 and 0.2; the slope is smaller than  $-1/2$ . Since the dependence is expressed in a log–log form, the magnitude of the slope in Regime II is higher. However, for Regime III a negative slope is shown. This represents the regime dominated by grain-boundary shear.

The phase mixture model, or rule of mixture [251,252] is one common approach to explaining the deformation mechanism of nanocrystalline materials. Kim et al. [251] considered a nanostructured material as consisting of crystallites, grain-boundary surfaces, triple line junctions, and quadratic nodes. The volume fraction of each was expressed in terms of the grain size and the grain-boundary width. The composite hardness was expressed as

$$H = H_{cr}f_{cr} + H_{gb}f_{gb} + H_{tj}f_{tj} + H_{qn}f_{qn} \quad (27)$$

where the subscripts cr, gb, tj and qn represent crystallites, grain boundary, triple line junction, and quadratic node, respectively. The model was found to agree well with the experimental hardness results for Fe, Ni and Cu specimens. Similar phase mixture models have attempted to explain the mechanical properties of nanocrystalline materials, such as the grain size dependence of hardness and yield strength [251,253], the grain size and porosity dependence of the elastic modulus and the hardness [253,254] and the ductile–brittle transition behavior of nanocomposites [254]. This model is presented in greater detail in Section 7.3 since it has a significant core-and-mantle component. In this mixture model, the grain-boundary sliding is accommodated by the grain-boundary component.

Van Swygenhoven et al. [255,258] carried out molecular dynamics simulations that revealed sliding along boundaries. They show that grain-boundary sliding is the primary deformation mechanism in nanocrystalline materials and that such a sliding mechanism results in a build up of stress across neighboring grains. This stress, in turn, is relieved by grain boundary and triple junction migration. The degree to which this occurs depends on grain size since for small grain sizes, less planar interfaces provides reduced steric hindrance to concurrent grain sliding. Such grain-boundary sliding activity is mainly facilitated by atomic shuffling and stress-assisted free volume migration [254].

Van Swygenhoven et al. [309] performed MD simulations on two model FCC metals, Ni and Cu, having different stacking fault energies to address the question of grain-boundary structure and of the mechanism of plastic deformation as a function of grain size (5–12 nm) [256]. Analysis on the atomic level showed that all the deformation is accommodated in the grain boundaries while at greater grain sizes, intragrain deformation was detected by the presence of stacking faults inside the grains.

A discussion of grain-boundary sliding was introduced by Meyers et al. [257]. An important consideration in grain-boundary sliding not discussed by Kim et al. [251] or Conrad et al. [250] is the compatibility of deformation. These models are based on the Coble creep equation, which expresses the strain rate as proportional to a  $d^{-3}$  term. As  $d$  decreases, the contribution to plastic flow coming from grain-boundary sliding increases. However, the simple Coble equation ignores the necessity of plastic flow to accompany sliding in order to accommodate the grains. It is clear that sliding alone cannot accomplish this deformation in the simple schematic of Fig. 36. Ashby and Verall [261] addressed this problem successfully for superplastic deformation and proposed a neighbor exchange mechanism capable of effecting plastic strain. This gliding/plastic deformation/neighbor exchange is illustrated in Fig. 38.

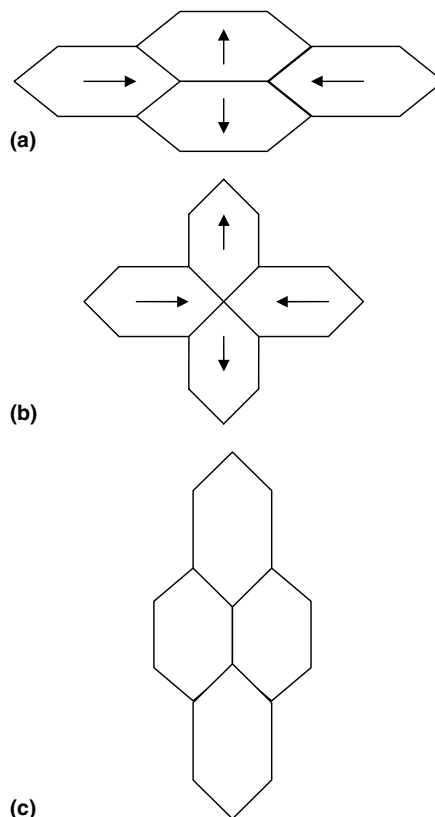


Fig. 38. Ashby–Verall mechanism for accommodating plastic flow through grain-boundary sliding coupled with plastic deformation and neighbor exchange: (a) original position of four neighboring grains; (b) convergence of vertices and (c) exchange of positions—neighbors become next neighbors and vice versa.

Thus, a plastic accommodation term has to be added to grain-boundary sliding. Fu et al. [103] have shown that the incorporation of the plastic accommodation term into the diffusion results in significant changes in the stress–strain curve. Grain-boundary sliding can be represented by a viscous and a plastic accommodation term,

$$\tau_a = (\eta_i + \eta_D)\dot{\gamma} + \tau_p \quad (28)$$

where  $\tau_a$  is the shear stress,  $\eta_i$  is an intrinsic grain-boundary viscosity,  $\eta_D$  is a diffusional component of the accommodation process, and  $\tau_p$  is a plastic deformation term. Fig. 39 shows an idealized polycrystal (similar to the one in Fig. 36) subjected to a shear stress  $\tau_a$ . There is a need for accommodation since sliding in polycrystals is not fully compatible;

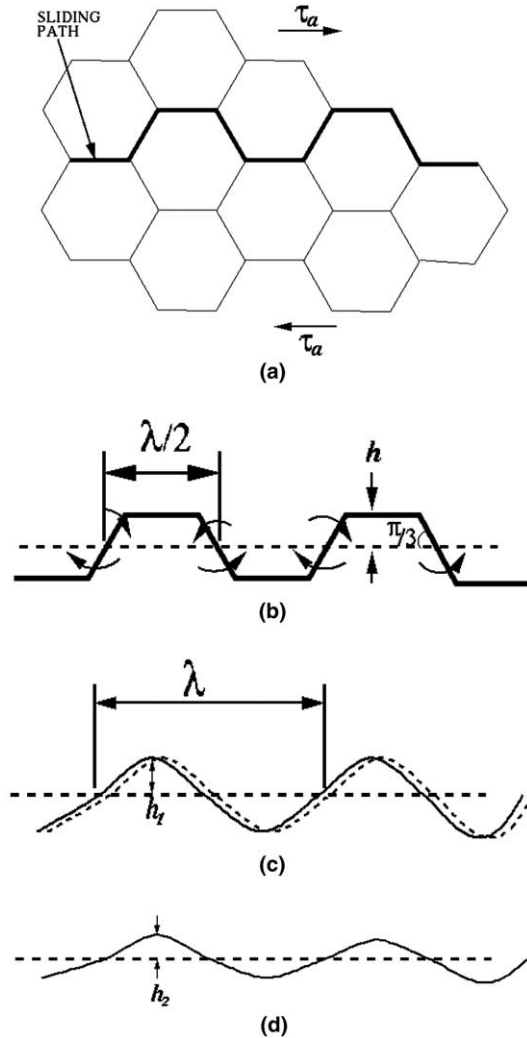


Fig. 39. (a) Schematic representation of grain-boundary sliding in polycrystal; (b) grain-boundary sliding path; (c) idealized sinusoidal path with diffusional migration of boundary according to Raj and Ashby [260]; (d) decrease in wave amplitude  $h$  with increasing plastic strain [103].

this is shown by the jagged grain-boundary sliding path in Fig. 39(a). Raj and Ashby [259] treated grain-boundary sliding, in their classic 1971 paper, by assuming that the plastic accommodation between adjacent grains occurs by diffusion alone. Whereas Fig. 39(b) shows the grain-boundary sliding path, Fig. 39(c) shows the sinusoidal shape assumed in the Raj and Ashby [259] calculations. Taking both grain-boundary and bulk diffusion into consideration, they obtained an expression for the sliding rate,  $\dot{u}$ ,

$$\dot{u} = \frac{du}{dt} = \frac{2}{\pi} \frac{\tau_a \Omega}{kT} \frac{\lambda}{h^2} D_V \left( 1 + \frac{\pi \delta}{\lambda} \frac{D_B}{D_V} \right) \quad (29)$$

The parameters  $\lambda$  and  $h$  are the wavelength and amplitude, respectively, defining the sinusoidal boundary in Fig. 39(c);  $\Omega$  is the atomic volume;  $\delta$  is the thickness of the boundary;  $D_V$  and  $D_B$  are the volume and boundary diffusion coefficients, respectively. At temperatures significantly below  $T_m/2$ ,  $D_B \gg D_V$  and

$$\frac{\pi \delta}{\lambda} \frac{D_B}{D_V} \gg 1 \quad (30)$$

Giving

$$\dot{u} \approx \frac{2\delta\Omega D_B}{kT} \tau_a \left( \frac{1}{h^2} \right) \quad (31)$$

If it is assumed that each grain-boundary layer will generate an identical sliding rate, a strain rate can be defined as

$$\dot{\gamma} = \frac{\dot{u}}{2h} = \frac{\delta\Omega D_B}{kT} \tau_0 \left( \frac{1}{h^3} \right) \quad (32)$$

The amplitude of the sinusoidal wave,  $h$ , is taken as  $d/4$ . And therefore,

$$\dot{\gamma} = \frac{64\delta\Omega D_B}{kT} \left( \frac{1}{d^3} \right) \tau_a \quad (33)$$

For a constant amplitude and grain size, a number of parameters can be grouped and Eq. (33) can be expressed as

$$\dot{\gamma} = \left( \frac{1}{\eta_e} \right) \tau_a \quad (34)$$

where  $\eta_e$  is an effective viscosity. This is the equation for Newtonian viscous flow. The dependence of  $\dot{\gamma}$  on  $h$ , in Eq. (32), is a clear suggestion that deformation will localize as  $h$  decreases. As plastic deformation proceeds, it is easily visualized how the jaggedness of the interface, measured by  $h$ , decreases, as shown in the transition from Fig. 39(c) to (d). In nanocrystalline materials the flow localization, in the form of shear bands, is indeed observed.

Fig. 40 shows a plot of  $\dot{\gamma}$ , calculated from the diffusional Raj and Ashby equation (Eq. (33)) as a function of grain size  $d$ . The stress levels were varied and are obtained from the compressive flow stresses for the various grain sizes calculated from the computational procedure. They vary from 100 to 900 MPa, for grain sizes of 100  $\mu\text{m}$  to 26 nm, respectively. These stresses are converted into shear stresses assuming a von Mises criterion (i.e., dividing them by  $\sqrt{3}$ ). The values of the other parameters are:  $\delta$  ( $\sim 3b$ ) = 0.75 nm [249];  $\Omega = 0.0087 \text{ nm}^3 (= 4/3\pi r^3)$ ,  $r$  being the atomic radius for copper;  $T = 298 \text{ K}$ . The grain-boundary diffusion coefficient room temperature was taken as  $D_B = 10^{-21} \text{ m}^2/\text{s}$  at

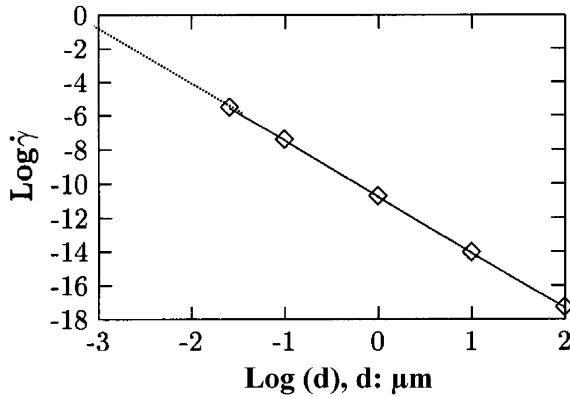


Fig. 40. Calculated strain rates from diffusively-driven grain-boundary sliding as a function of grain size (copper deformed at 300 K); extrapolated results indicated by dashed line [103].

$T/T_m = 0.225$ . This value is lower than the extrapolation from Shewmon [259] ( $10^{-22}$  m<sup>2</sup>/s) and higher than the one used by Kim et al. [251] ( $2.6 \times 10^{-20}$  m<sup>2</sup>/s). The five calculated strain rates are marked on plot and the data are well represented by a straight line. Extrapolation to smaller grain sizes (shown by a dashed line) reveals striking results: for  $D \leq 10$  nm, the strain rate due to diffusional sliding along grain boundaries by a Raj–Ashby [259] mechanism can reach significant values ( $\dot{\gamma} \geq 10^{-4}$  s<sup>-1</sup>). It should be pointed out that plastic flow, not considered by Raj and Ashby, can also assist in the accommodation process at these temperatures. Thus, it is concluded that grain-boundary sliding can contribute to the plastic deformation at grain sizes  $d \leq 10$  nm, corroborating recent calculations [250,251,258].

### 7.3. Core and mantle models

In 1963, Li [259] proposed that grain-boundary ledges (which he had earlier called grain-boundary jogs [260]) acted as sources of dislocations at the onset of plastic deformation and that these dislocations created, by a double slip mechanism, a work hardened layer around the grain boundaries. A significant aspect of the Li [259,260,262] proposal is that he was able to calculate the spacing between the ledges from the HP slopes. The values obtained reveal that the ledge spacing,  $l$ , is of a nanometer scale:

Cu:  $l = 50b$

Al:  $l = 100b$

Mo:  $l = (2.5 \rightarrow 33)b$

Fe, steel:  $l = (0.5 \rightarrow 5)b$

Zn:  $l = (2.5 \rightarrow 10)b$

Zr, Ti:  $l = 5b$

This is insufficient to promote plastic deformation in the nanocrystalline regime. Thus, one can envisage a grain size below which ledges can no longer operate.

This concept was later extended by Ashby [263,264] who proposed that geometrically necessary and statistically stored dislocations were involved in polycrystalline deformation.

Subsequently Hirth [267] analyzed the incompatibility stresses at the grain boundaries. Thompson [268] and Margolin [269] proposed similar models. Although these models have taken several forms, the basic idea, illustrated in Fig. 41, is that the deformation within a grain is composed of two parts: (1) the core, or grain interior, which is subjected to a more homogeneous state of stress; and (2) the mantle, or grain-boundary region, in which several factors contribute to increased resistance to plastic flow and work hardening: grain-boundary sources, change in orientation in the plane of maximum shear, elastic and plastic incompatibility. This leads to enhanced cross-slip, as shown in Fig. 42 which depicts a grain in the conventional polycrystalline regime. In the grain interior (core), slip system  $S_1$  is activated, corresponding to easy glide and a low work hardening rate. In the grain-boundary mantle region, cross-slip into system  $S_2'$  leads to increased work hardening.

Fig. 41 shows how the relative fractions of these two regions vary with grain size. As the grain size is decreased into the nanocrystalline region, the mantle dominates the plastic flow process. Fig. 41(a) represents, in a schematic fashion, a grain with the scale of micrometers, whereas Fig. 41(b) represents a nanosized grain, in which the mantle predominates.

A model is presented here that was proposed by Meyers and Ashworth [266] and extended by Fu et al. [265] to the nanocrystalline regime. The compatibility requirement at the grain boundaries due to the differences in orientation applied to anisotropic crystals creates additional stresses,  $\tau_I$ . Meyers and Ashworth [266] found for nickel that

$$\tau_I = 1.37\sigma_{AP} \quad (35)$$

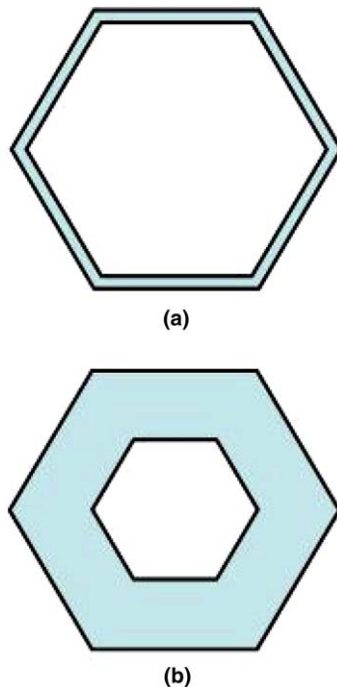


Fig. 41. Core and mantle model, showing relative fractions of grain boundary and grain interior regions in the (a) microcrystalline and (b) nanocrystalline regimes.

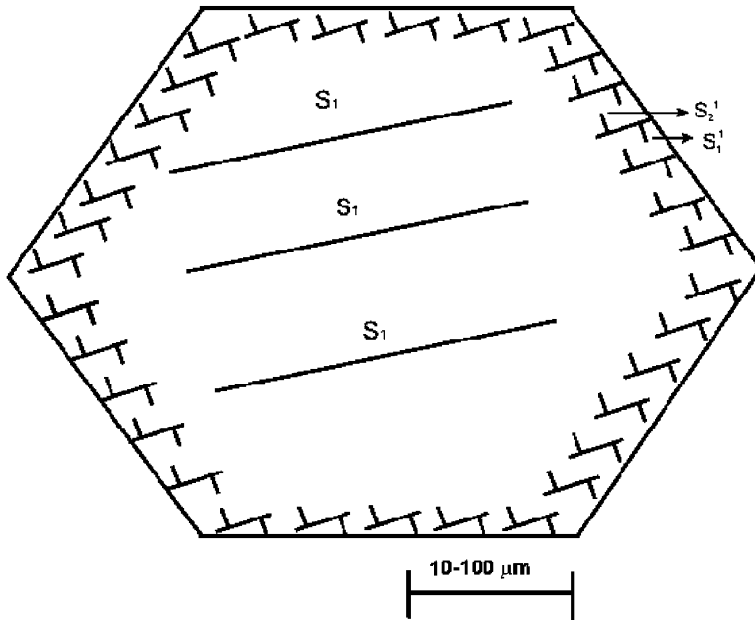


Fig. 42. Schematic depiction of a deformed grain showing the more intense cross slip and work hardening along the grain-boundary regions.

where  $\sigma_{AP}$  is the applied normal stress. In a uniform, homogeneous material, the maximum shear stress is  $\tau = \sigma/2$ . Thus, the shear stress at the interface is between 2 and 3 times the maximum shear stress in a homogeneous material. It is therefore logical to expect the initiation of plastic flow to take place in the grain-boundary regions. Other factors that contribute to this are that grain boundaries are sources of dislocations. As discussed above, this is a well-known phenomenon: grain-boundary ledges and grain-boundary dislocations can initiate plastic deformation. Additionally, grain boundaries segregate impurities and foreign atoms, and their mechanical properties differ from the grain interiors.

As a result, while the grain interiors can be considered to harden by the classic easy glide/linear hardening/parabolic hardening sequence, the grain boundaries show a much faster rise in the dislocation density and the hardening rate. This is exemplified by the result shown by Hirth and Lothe [267] for a bicrystal. Although this is a compatible bicrystal, the activation of a second slip system around the boundary is seen. This conceptual frame is extended to a polycrystal in Fig. 43. The grain-boundary regions are shown with pronounced slip activity on two slip systems; this leads to a much higher hardening rate than the grain interiors. Recent results on copper polycrystals show a much greater tendency for slip on two or three systems in the regions close to the boundaries. Note that grain-boundary corners are regions especially prone to concentrated plastic deformation. Results by Gray [270] confirm the higher hardening in the regions adjacent to the grain boundaries and triple points. This serves a basis for the model developed by Meyers and Ashworth [266]. This predominance of dislocations along grain boundaries at early stages of plastic flow is eloquently illustrated by the transmission



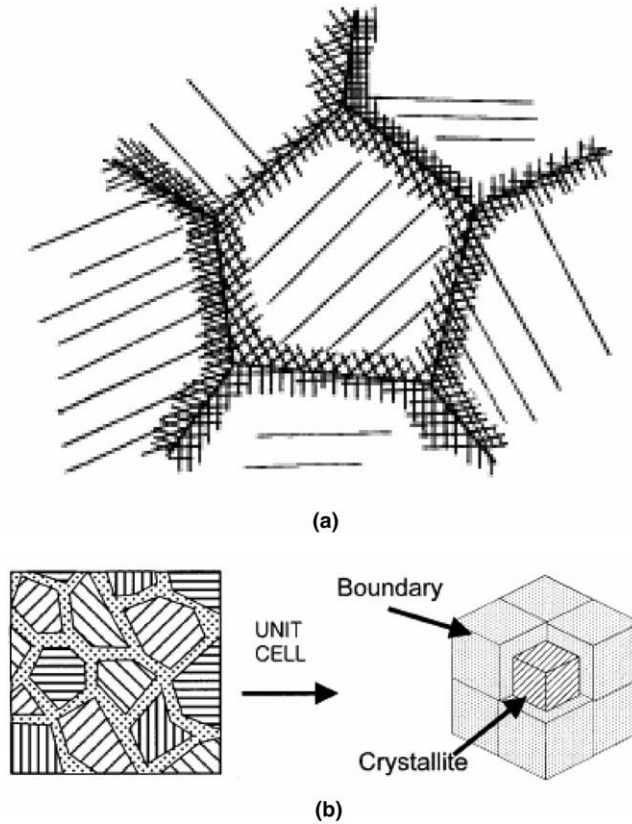


Fig. 43. Core and mantle models for a polycrystalline aggregate: (a) Meyers–Ashworth model [266]; (b) Kim et al. model [251].

electron micrographs of Murr and Hecker [271]. This build up of plastic deformation has also been recently measured by Sun et al. [272]. The use of electron back-scattering diffraction in orientation imaging microscopy of an aluminum bicrystal deformed to a strain of 0.1 revealed a significantly higher dislocation density in the vicinity of the grain boundary.

Fig. 44 shows the stages of deformation as the applied stress,  $\sigma_{AP}$ , is increased. As the applied stress increases, a work hardened layer along the grain boundaries is formed. Once this work hardened grain-boundary layer is formed, the stress within the polycrystalline aggregate homogenizes. Stages a–c in Fig. 44 represents the dominance of the elastic compatibility strains and the formation of a grain boundary work-hardened layer. Stages d–f represent the response of a composite material, consisting of dislocation-free grain interiors, with a flow stress  $\sigma_{fG}$ , and grain-boundary layers, with a flow stress  $\sigma_{fgb}$ . The flow stress of the grain aggregate is obtained in approximate fashion from

$$\sigma_y = A_G \sigma_{fG} + A_{gb} \sigma_{fgb} \quad (36)$$

$A_G$  and  $A_{gb}$  are the areal fraction of grain interior and grain boundary, respectively.

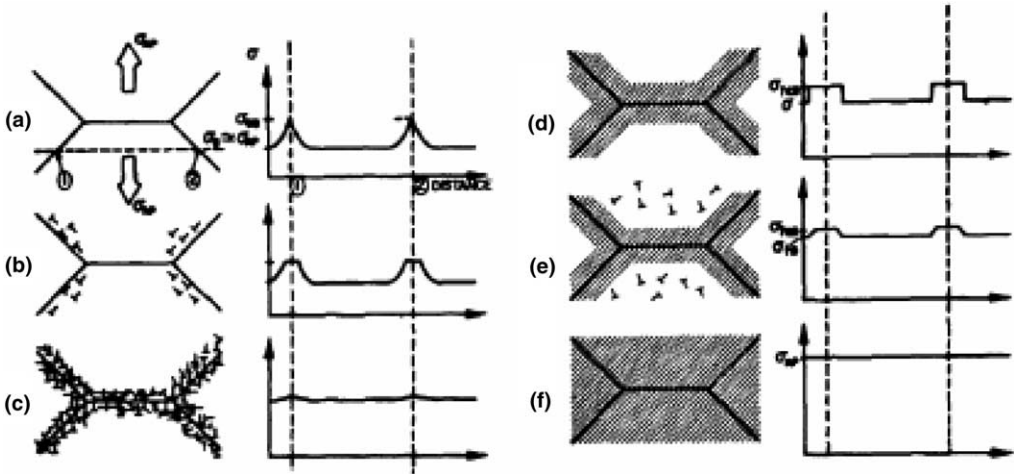


Fig. 44. Sequence of stages in polycrystalline deformation, starting with (a,b) localized plastic flow in the boundary regions (microyielding), forming a grain-boundary work-hardened layer (c,d) that effectively reinforces the macrostructure, and leading to (e,f) macroyielding in which the bulk of the grains undergo plastic deformation [265].

Fig. 45 is an idealized representation of the aggregate. Grains are assumed to be spherical, with a diameter  $d$ ; the grain-boundary layers are assumed to have a thickness  $t$  (in each grain,  $t < d/2$ ). The diametral areal fractions are expressed by

$$A_{gb} = \frac{1/4\pi[d^2 - (d - 2t)^2]}{1/4\pi d^2} = 4 \left[ \frac{t}{d} - \left(\frac{t}{d}\right)^2 \right],$$

$$A_G = \frac{1/4\pi(d - 2t)^2}{1/4\pi d^2} = 1 - A_{gb} \tag{37}$$

Substituting Eqs. (37) into Eq. (36):

$$\sigma_y = \sigma_{fG} + 4(\sigma_{fgb} - \sigma_{fG})td^{-1} - 4(\sigma_{fgb} - \sigma_G)t^2d^{-2} \tag{38}$$

Different sections, marked  $S_1, S_2, S_3, S_4$  and  $S_5$  in Fig. 45(b), produce different areal fractions  $A_G$  and  $A_{gb}$ . Hence, it is more correct to use the mean values of  $t$  and  $d$ ,  $\bar{t}$  and  $\bar{d}$ , respectively, so that:

$$\sigma_y = \sigma_{fG} + 4(\sigma_{fgb} - \sigma_{fG})\bar{t}\bar{d}^{-1} - 4(\sigma_{fgb} - \sigma_G)\bar{t}^2\bar{d}^{-2} \tag{39}$$

Meyers and Ahsworth estimated these mean values. As

$$\bar{d}^- = \frac{\pi}{4}d, \quad \bar{t} = 1.57t \tag{40}$$

The term  $\bar{t}\bar{d}^{-1}$  is approximately equal to  $2td^{-1}$ , giving

$$\sigma_y = \sigma_{fG} + 8(\sigma_{fgb} - \sigma_{fG})td^{-1} - 16(\sigma_{fgb} - \sigma_G)t^2d^{-2} \tag{41}$$

The variation of the thickness of the work hardened grain-boundary layer has to be considered. First, as the grain size is decreases, the stress field fluctuations vary with  $d$ , leading to a dependency  $t = k_1d$ ; secondly, as the dislocation spacing is unchanged, and

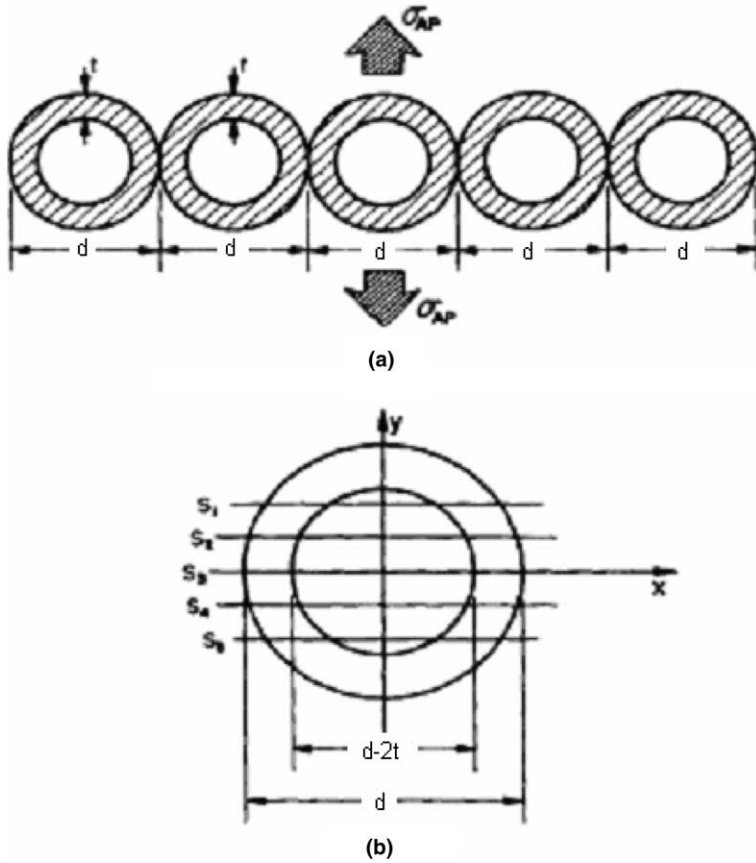


Fig. 45. (a) Polycrystalline aggregate viewed as composite material composed of bulk and grain-boundary material, with flow stresses  $\sigma_{gb}$  and  $\sigma_{fgb}$ , respectively. (b) Idealized spherical grain of diameter  $D$  with grain-boundary layer of thickness  $t$ ; sections  $S_1$ ,  $S_2$ ,  $S_3$ ,  $S_4$ , and  $S_5$  reveal different proportions between the areas of the bulk and the grain-boundary material [265].

the dislocation interactions will dictate a constancy in  $t$ , thus, a relationship  $t = k_2 d^0$ . The geometric mean would be  $(k_1 k_2 d)^{1/2}$ . This produces the expected Hall–Petch dependence, as shown below. Hence

$$t = (k_1 k_2 d)^{1/2} = k_{MA} d^{1/2} \tag{42}$$

Substituting Eq. (42) in Eq. (41), we get,

$$\sigma_y = \sigma_{fG} + 8k_{MA}(\sigma_{fgb} - \sigma_{fG})d^{-1/2} - 16k_{MA}^2(\sigma_{fgb} - \sigma_{fG})d^{-1} \tag{43}$$

For large grain sizes (the micrometer range) the  $d^{-1/2}$  term dominates and a Hall–Petch relationship is obtained. The Hall–Petch slope  $k_{HP}$  is equal to

$$k_{HP} = 8k_{MA}(\sigma_{fgb} - \sigma_{fG}) \tag{44}$$

As the grain size is decreased, the  $d^{-1}$  term becomes progressively dominant, and the  $\sigma_y$  versus  $d^{-1/2}$  curve goes through a maximum. This occurs at

$$d_c = (4k_{MA})^2 \tag{45}$$

For values of  $d < d_c$ , it is assumed that the flow stress reaches a plateau and that grain-boundary effects dominate plastic flow. The Meyers–Ashworth model predicts a reduction in the H–P slope as the grain size is decreased in accordance with experimental results. Since no grain-boundary sliding is incorporated, no negative H–P slope is predicted. Fu et al. [103] extended the Meyers–Ashworth equation to the nanocrystalline regime. This is discussed further in Section 9.1. The application of the M–A equation to iron and copper, as well as the Hall–Petch slopes and experimental points, are marked in Fig. 46. The decrease in H–P slope as the grain size is reduced is well represented by the M–A treatment.

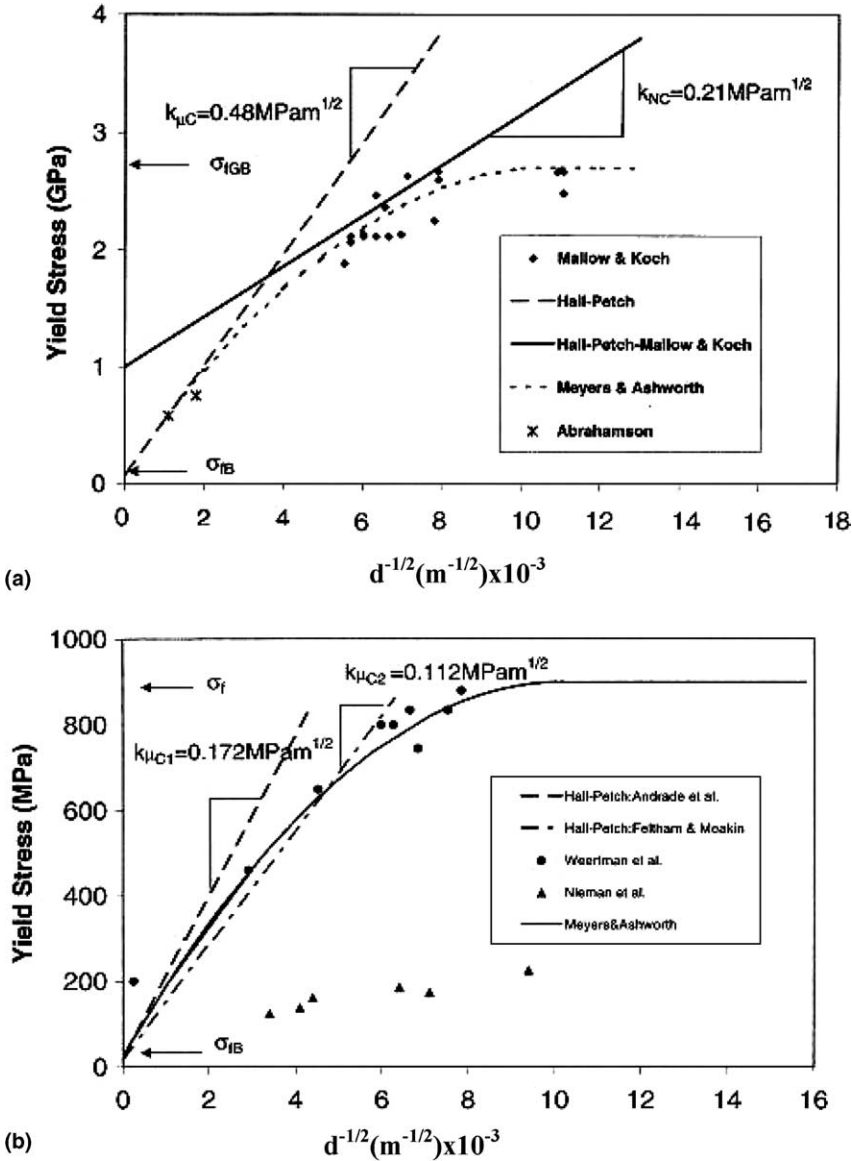


Fig. 46.  $\sigma_y$  versus  $D^{-1/2}$  relationship for (a) iron and (b) copper [265].

Kim et al. [273] used a phase mixture model analogous to Meyers–Ashworth [266] and developed an analytical model including the work hardened mantle regions and grain-boundary sliding. Fig. 43(b) shows the model that they have used, in which the grains are cubic. Kim et al. [251] considered a phase mixture model (discussed in Section 7.2) in which a polycrystalline material is regarded as a mixture of crystalline phase and a grain-boundary phase to describe the plastic deformation behavior of fine-grained materials. The mechanical properties of the crystallite phase was modeled as being viscoplastic, which involves dislocation activity and diffusion creep. Fig. 47(a) shows the calculated stress–strain curves for Cu of various grain sizes and at different strain rates. The flow

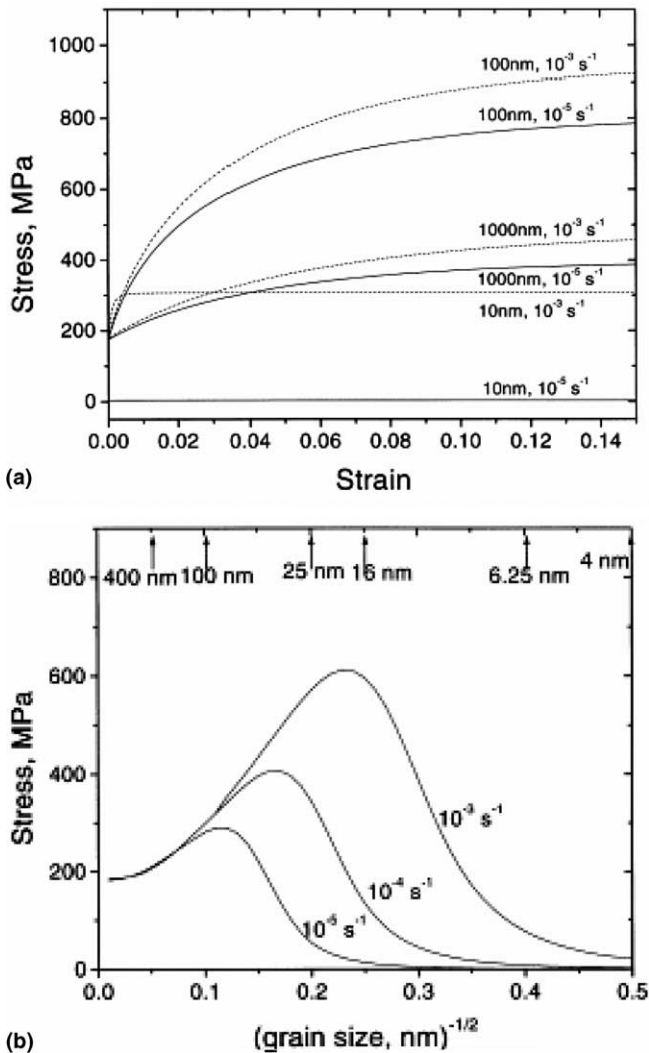


Fig. 47. (a) Stress–strain curve for the crystalline phase of Cu for different crystallite sizes and strain rates. Solid and dashed curves are for the strain rates of  $10^{-3} \text{ s}^{-1}$  and  $10^{-5} \text{ s}^{-1}$ , respectively; (b) Grain size dependence of the 0.2% offset stresses for a Cu crystallite (Hall–Petch curves) for the strain rates of  $10^{-3}$ ,  $10^{-4}$ , and  $10^{-5} \text{ s}^{-1}$  [251].

stress increases with decreasing grain size. Fig. 47(b) illustrates the effect of  $d$  on the strength of the crystallite phase. For all strain rates, the stress first increased and then decreased as the grain size is reduced. The total strain rate of the crystallite was calculated by considering contributions from the dislocation, the boundary diffusion and the lattice diffusion mechanisms. The dominant deformation mechanisms for the crystallite phase as a function of grain size are depicted in Fig. 48(a).

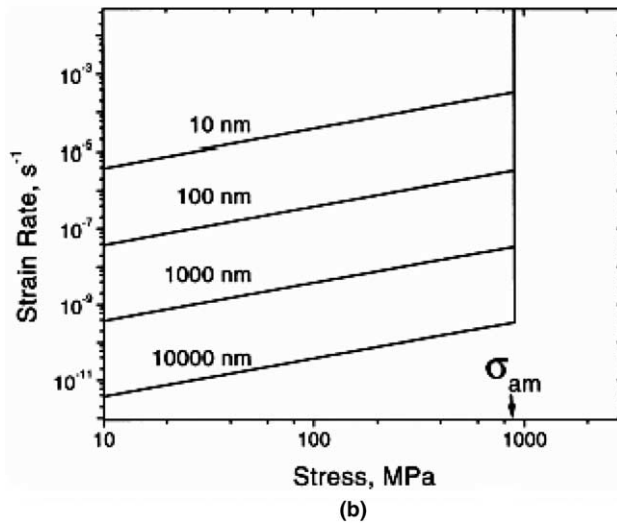
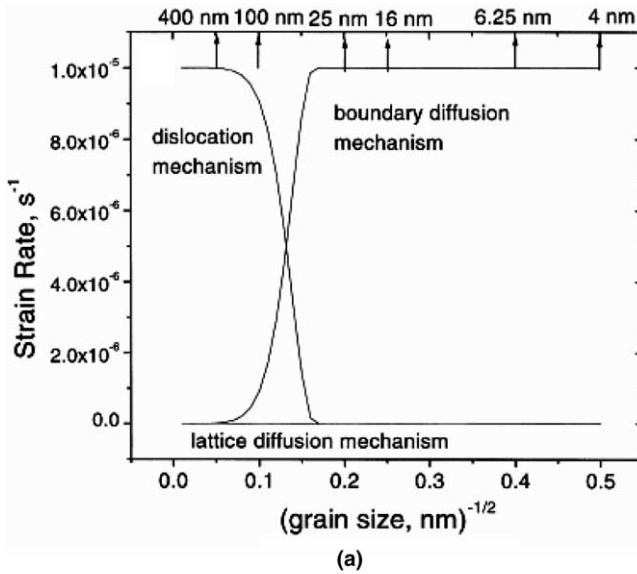


Fig. 48. (a) Grain size dependence of all three contributions to the total imposed strain (dislocation mechanism, grain-boundary diffusion and lattice diffusion mechanism) in Cu for the total imposed strain rates of  $10^{-3} \text{ s}^{-1}$ . (b) Effect of grain size on the stress dependence of the creep rate for the grain-boundary phase of Cu ( $\sigma_{\text{am}}$  denotes the strength of amorphous Cu) [251].

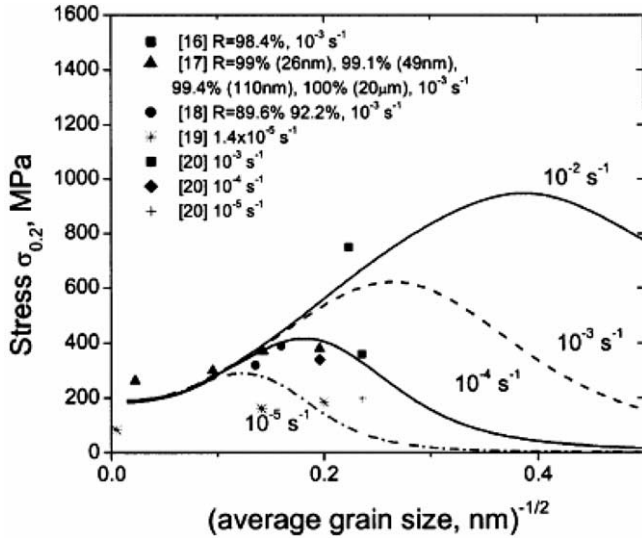


Fig. 49. Average grain size dependence of  $\sigma_{0.2}$  for fine grained Cu at strain rates of  $10^{-2}$ ,  $10^{-3}$ ,  $10^{-4}$ , and  $10^{-5} \text{ s}^{-1}$  calculated using a log-normal distribution of the grain volume [251].

The deformation mechanism of the grain-boundary phase was modeled as a diffusional flow of matter through the grain boundary. A plot of the strain rate of the grain-boundary phase versus the applied stress is presented in Fig. 48(b). The strain rate increases with the stress until the stress reaches the strength of amorphous material,  $\sigma_{\text{am}}$ . The slope is independent of grain size. The predicted results are shown in Fig. 49 and have both positive and negative Hall–Petch regions in comparison with experimental results from the literature. The strain rate has a significant effect on the positive/negative HP transition: the transition, which is in the nanometer size, is shifted to lower strain rates for larger grain sizes. These results are similar to the ones by Fu et al. [104] (Fig. 40).

#### 7.4. Grain-boundary rotation/grain coalescence

Recent observations by Ma and coworkers [107–109,276] point out the interesting possibility, that nanosized grains rotate during plastic deformation and can coalesce along directions of shear, creating larger paths for dislocation movement. Fig. 50 shows this in schematic fashion. The orientations of the slip systems with highest Schmid factors are represented by a short line in each grain (Fig. 50(a)). As plastic deformation takes place, two neighboring grains might rotate in a fashion that brings their orientation closer together (Fig. 50(b)). This leads to the elimination of the barrier presented by the boundary between them, providing a path for more extended dislocation motion (Fig. 50(c)). This mechanism can actually lead to softening and localization, and is consistent with the limited ductility often exhibited by nanocrystalline metals.

One way by which grains can rotate is by disclination motion. Murayama et al. [274] first observed disclinations in a mechanically milled Fe sample and suggested that the generation of partial disclination defects provides an alternative mechanism to grain-boundary sliding, which possibly allows rotation of nanosized crystals during mechanical milling.

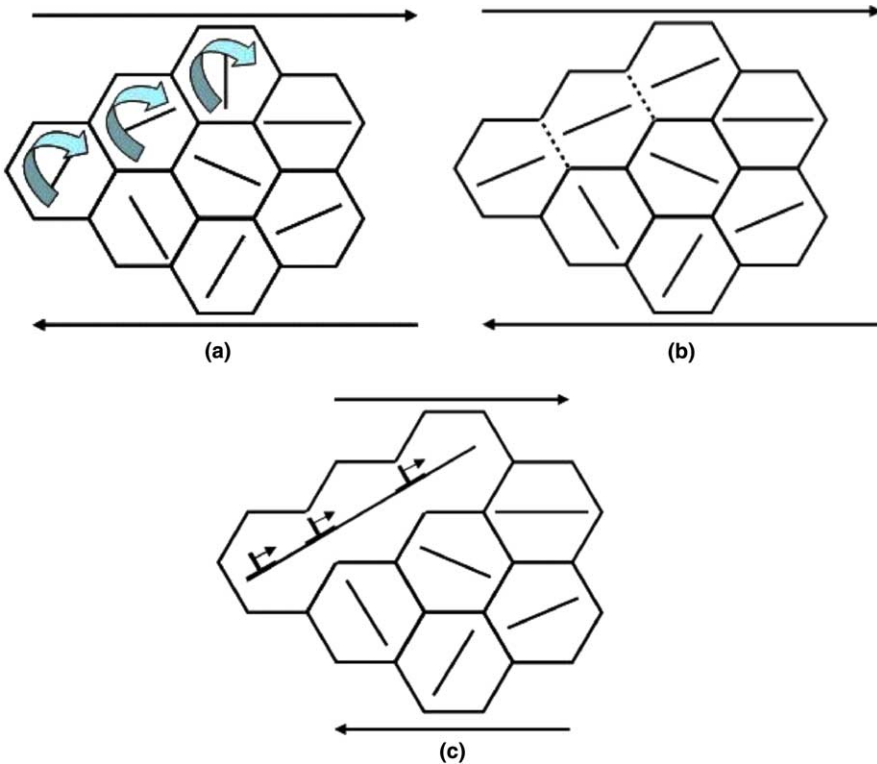


Fig. 50. Rotation of neighboring nanograins during plastic deformation and creation of elongated grains by annihilation of grain boundary.

A disclination is a line defect characterized by a rotation of the crystalline lattice around its line [275]. Motion of a disclination dipole, which is a combination of two disclinations, causes plastic flow accompanied by crystal lattice rotation behind the disclinations. Fig. 51 shows the rotation of a grain when a nanocrystalline metal is subjected to tension. This is accomplished by disclinations as postulated by Ovid'ko [275]. Two opposite arrows

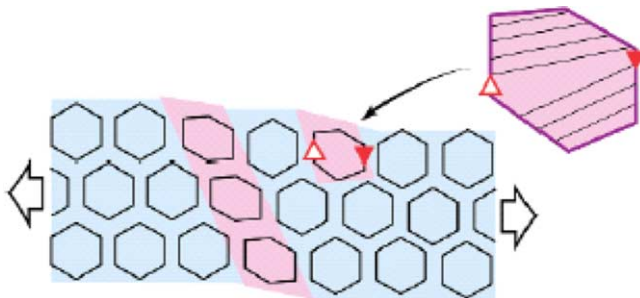


Fig. 51. Rotation deformation of nanocrystalline material under loading; grain undergoing rotation is shown with two opposite arrows and is represented in magnified fashion in upper right corner [275].



indicate the clockwise direction of rotation of a grain. The insert in Fig. 51 shows a magnified view of a grain with non-parallel lines representing disclinations.

HRTEM observation by Murayama et al. [274] of milled Fe sample showed two wedge-shaped regions that together form a partial disclination dipole. The TEM image demonstrates that it is possible to directly observe the individual dislocations that constitute partial disclination dipoles in metals at the atomic level, even in mechanically milled powders that have undergone severe plastic deformation.

It was proposed that the set of terminating planes that constitute the individual partial disclinations, such as the one circled and labeled I in Fig. 52(c), can also be considered terminating tilt grain boundaries [267,276]. Terminating tilt grain boundaries contained

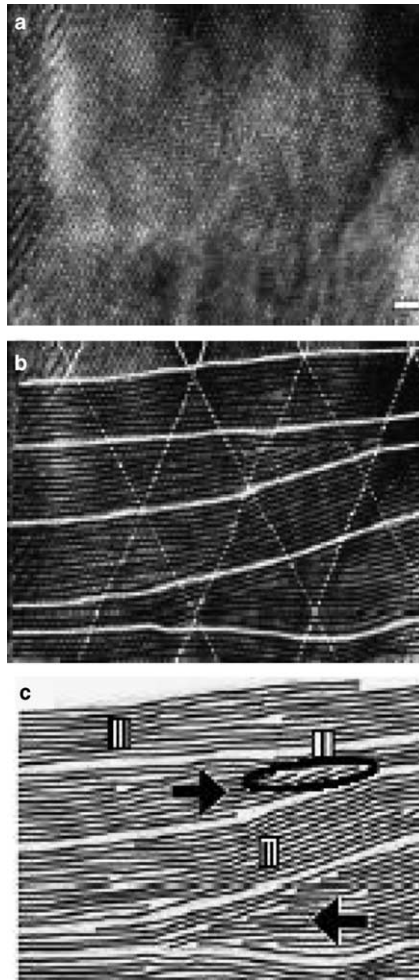


Fig. 52. (a) HRTEM image of mechanically milled, nanocrystalline Fe powder. (b) White lines shown superimposed periodically on the three sets of  $\{110\}$  planes in (a) highlight the distortion of the nearly horizontal set of  $\{110\}$  planes. (c) Nearly horizontal black and white lines in (b) magnified from the HRTEM image so that they are more clearly visible. Scale bar in (a), 1.0 nm [274].

missing dislocations, and these were replaced by rotational elastic deformation in the crystal [277]. It was further suggested that such a configuration can be interpreted as a wedge of material added to or removed from an ideal crystal, as illustrated in Fig. 53. This is evident from the wedge shape of the bent white lines in Fig. 52(b) and (c). The crystal rotation produced by the partial disclinations in Fig. 52 is also evident. For example, the  $\{110\}$  planes located between the two partial disclinations (labeled II in Fig. 52 (c)) are rotated  $\sim 9^\circ$  relative to the  $\{110\}$  planes located outside the dipole. This observation was claimed

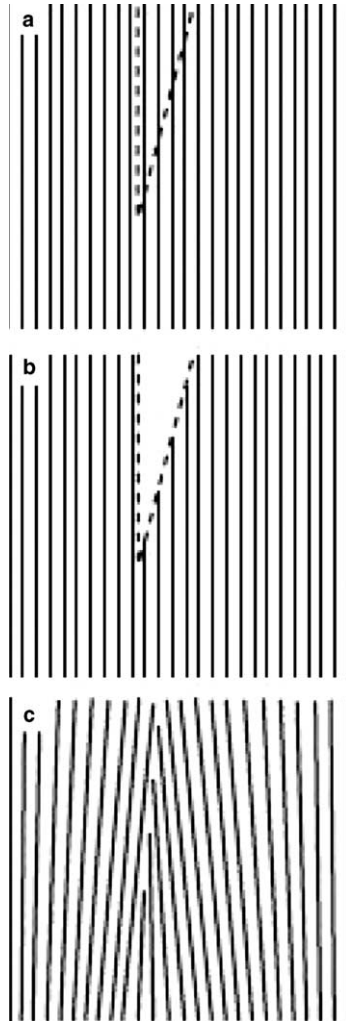


Fig. 53. Illustration of the elastic distortion associated with a partial wedge disclination (or terminating tilt grain boundary). (a) A set of planes in a perfect crystal, such as the perfect  $\{110\}$  planes seen in Fig. 52. A wedge-shaped piece of material is removed from the crystal in (b), and the new surfaces are allowed to close in (c) to fill the wedge. The resulting crystal in (c) contains a terminating tilt grain boundary, i.e., a terminating array of edge dislocations, and considerable elastic distortion, which increases the elastic strain energy of the remaining solid [274].

to provide direct confirmation that crystals can rotate during severe plastic deformation by the action of partial disclinations.

Murayama et al. [274] claimed that the large stress field associated with partial wedge disclinations makes it difficult for other deformation defects to move through the metal, thus imparting it higher strength. It was further argued that the reorientation associated with the generation and interaction of partial wedge disclinations assist in the grain break-down mechanism. Thus, disclinations contribute both to deformation and strengthening. It was suggested as an alternative deformation mechanism to grain-boundary sliding.

### 7.5. Shear-band formation

The deformation mode of nanocrystalline materials is known to change as the grain size decreases into the ultrafine regime. For all smaller grain sizes ( $d < 300$  nm) shear band development is often observed to occur immediately after the onset of plastic deformation. This has been correlated to changes in strain hardening behavior at those grain sizes (discussed in Section 5.4), since the ability to work harden by the increase in dislocation density is lost. Shear bands have been observed by Wei et al. [371] in both low and high strain-rate tests. It was observed that under dynamic loading, conventional polycrystalline iron did not exhibit localized deformation. Fig. 54 compares the low-rate compressive deformation response of iron with two different grain sizes in the ultrafine grain size regime. The deformation characteristics in 54(b) ( $d = 268$  nm) are significantly non-uniform unlike 54(a) ( $d = 980$  nm) where deformation was found to be uniform. Shear band populations similar to Fig. 54(b) were observed in all specimens with grain sizes  $d < 300$  nm. For 268 nm-Fe, the response under high-rate loading leading to a similar strain was found to be similar as under low-rate loading (Fig. 54(c)).

The development of shear bands in quasistatic deformation was studied by Wei et al. [110] in quasistatic deformation (Fig. 55(a) and (b)); on increasing the strain from 3.7% to 7.8% in a nanocrystalline Fe sample, the number of shear bands increases from

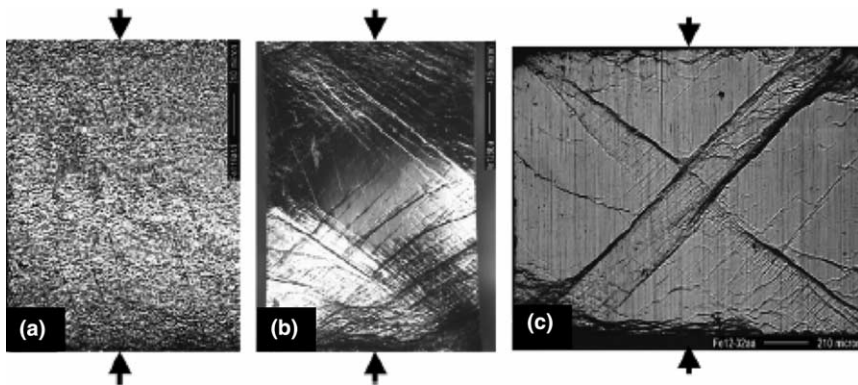


Fig. 54. Change in deformation mode of ultrafine grained consolidated iron with grain size for uniaxial compression: (a) uniform low-rate deformation with  $d = 980$  nm,  $\epsilon = 13.7\%$ ; (b) non-uniform low-rate deformation with  $d = 268$  nm and (c) non-uniform high-rate deformation with  $d = 268$  nm; Loading axis is vertical [371].

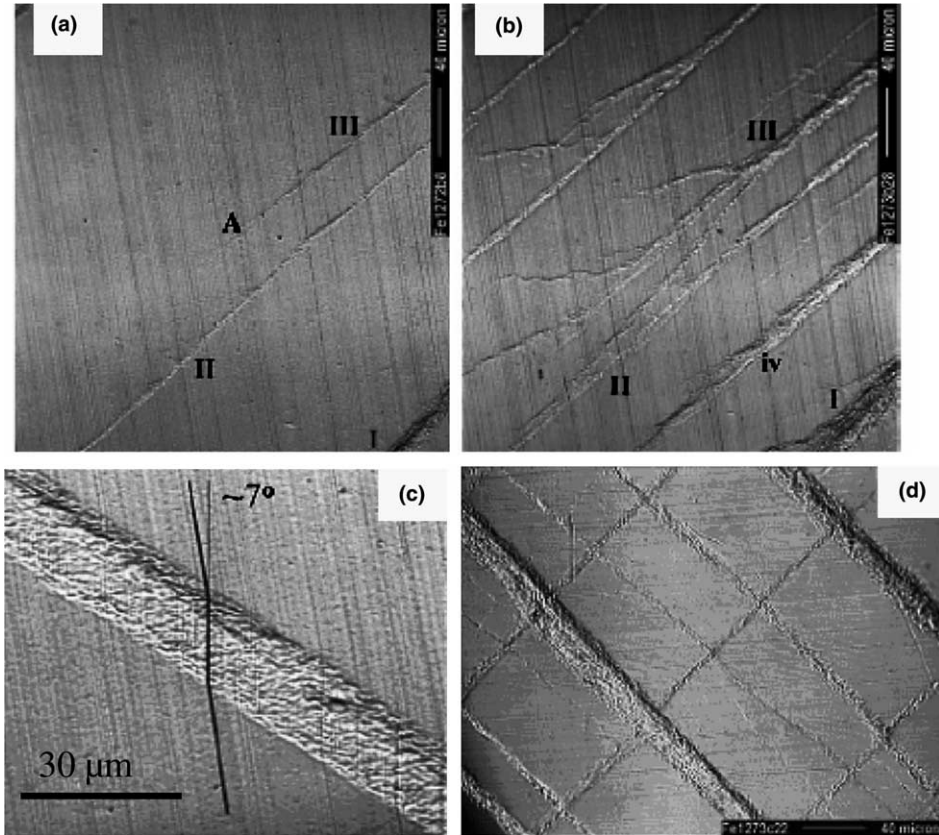


Fig. 55. Evolution and development of shear bands in 268 nm-Fe: (a,b) observation of shear bands at the same location at different nominal strain levels: (a) 3.7%; (b) 7.8%. (c) Shear strain developed in shear band immediately after onset of plastic deformation (0.3% plastic strain). (d) Shear band network formed at strain of 7.8% [371].

3 to 8. The shear bands (Fig. 55(a) and (b)) were marked I, II, and III to compare the growth process of each individual band as the strain increased. Label A denotes a shear band tip. Fig. 55(c) shows a high-magnification view of a single shear band [121]. Fig. 55(d) shows an organized network of shear bands. It can be concluded that they play an important role in plastic deformation of ultrafine grained Fe. It was observed by Jia et al. [121] in ball milled fine-grained Fe samples that the basic mechanism of shear banding does not appear to change between the low-rate and high-rate loading and the failure mechanism is governed by grain size rather than strain rate.

TEM observations of the shear bands from outside and within the shear bands in 110 nm-Fe deformed in compression at low rates are shown in Fig. 56. A typical picture obtained from within the shear band showed elongated grains containing high dislocation densities. Fig. 56(b) obtained from a region outside the shear band, showed equiaxed grains. The distortion angle is approximately  $7^\circ$ , corresponding to a shear strain of 0.12.

These observations correspond to the mechanism of grain-boundary rotation envisaged in Fig. 50. The equiaxed grain structure is replaced by elongated grains through plastic

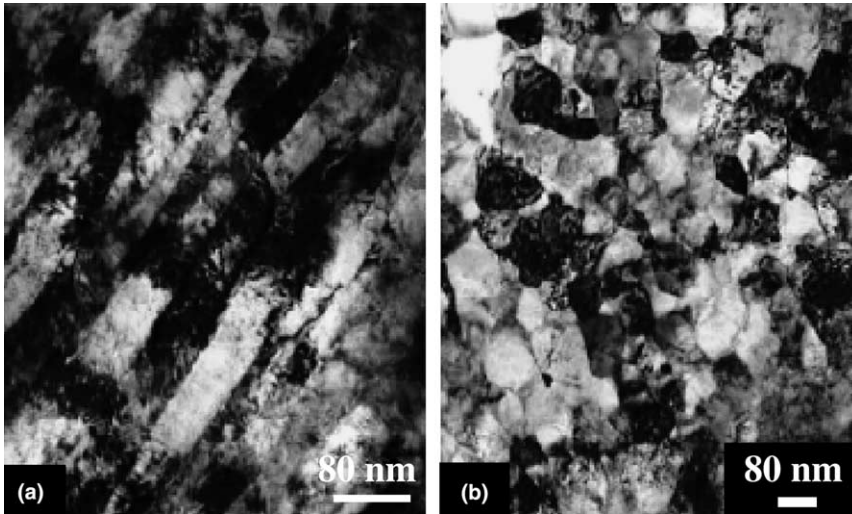


Fig. 56. TEM micrograph taken within (a) and outside (b) a shear band in 138 nm-Fe [121].

deformation inside the shear band. It is interesting to mention at this point that nanosized grains were also observed by Meyers et al. [279] in adiabatic bands. Fig. 57 shows shear bands in AISI 304L SS where the original grain size of the as received material was  $\sim 30 \mu\text{m}$ . The grains within the band were equiaxed and smaller by two orders of magnitude (100–200 nm) than the grains outside the band (original microstructure). Similar ultrafine grained structures were observed in Ti [280,281], Cu [282,286], Al–Li [283,284], and brass [285].

Shear bands formed by the deformation of hat-shaped samples and the thick walled cylinder technique [287,288] exhibiting equiaxed grains with diameters of 0.05–0.2  $\mu\text{m}$  with relatively low dislocation density, led Meyers and Pak [289] to suggest that the structure was due to dynamic recrystallization. Dynamic recrystallization in shock-conditioned copper was first observed by Andrade et al. [282]; in tantalum it was first observed by Meyers et al. [290] and Nesterenko et al. [291] and confirmed by Nemat-Nasser et al. [292]. In Al–Li alloys, Chen and Vecchio [293] and Xu et al. [294] observed dynamic recrystallization. The microstructure of these different crystal structures (HCP, FCC, BCC) was remarkably similar.

Meyers et al. [278,280,283] suggested a rotational recrystallization mechanism in titanium, and this was supported by Meyers et al. [295], Andrade et al. [282] for copper, and Nesterenko et al. [291] for tantalum. Rotational recrystallization occurs as a series of steps in which the homogeneous distribution of dislocations rearranges itself into elongated dislocation cells, then as deformation progresses, these cells become elongated sub-grains and finally these break up into approximately equiaxed micrograins. It is proposed that the relaxation of the broken-down elongated sub-grains into an equiaxed microcrystalline structure can occur by minor rotations of the grain boundaries lying along the original elongated boundaries. The mechanism by which the ultrafine grained size is produced within an adiabatic shear band is thought to be similar to the one in UFD processes such as ECAP.

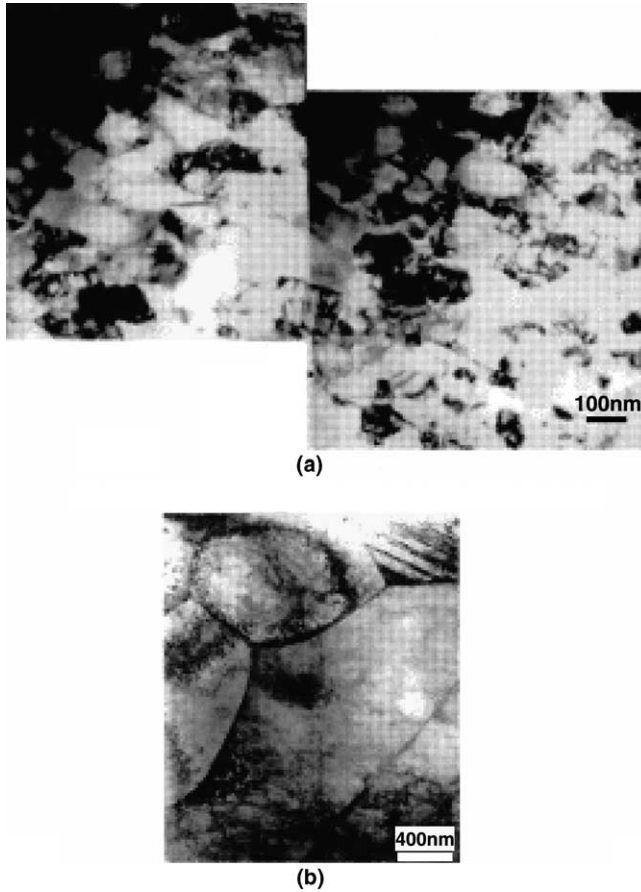


Fig. 57. (a) Ultrafine grain structure ( $d \sim 100\text{--}200\text{ nm}$ ) inside adiabatic (high strain rate:  $\sim 10^4\text{ s}^{-1}$ ) shear band in AISI 304L SS and (b) large grains ( $30\text{ }\mu\text{m}$ ) comprising initial microstructure outside bands [279].

### 7.6. Gradient models

In conventional constitutive models, the stress is considered to be a function of strain, strain rate, and temperature. In gradient models, the stress is also assumed to be a function of the gradient of a variable. This gradient has taken several forms, depending on the researcher. In any case, the gradient introduces a spatial scale into the constitutive description. This length scale has been successfully used to describe the effect of grain size, all the way from the nanocrystalline to the monocrystalline domains, into the calculation of the strength.

An attractive approach to the analytical prediction of the grain-size dependence is through strain-gradient plasticity. Strain-gradient plasticity is a recent development that incorporates a length scale in the analytical treatment of plasticity problems. It enables the prediction of the effect of indentation size on the hardness of metals and ceramics, the effect of hard particles in the work hardening of metals, grain size, and other effects. Originally proposed by Aifantis [296] in the context of shear localization, it has been

extended to a variety of problems by Fleck et al. [297,298] and Gao et al. [302,303]. From the dislocation perspective, the evolution of statistically stored and geometrically necessary dislocations, first proposed by Ashby [8], provides the underlying physics. The physical processes envisaged for the grain-size dependence of yield and flow stresses involve a length scale. Fleck et al. [297,298] apply the geometrically necessary ( $\rho_g$ ) and statistically stored ( $\rho_s$ ) dislocation densities to determine the athermal component of the flow stress, through the conventional Taylor expression:

$$\tau_\mu = \alpha Gb(\rho_g + \rho_s)^{1/2} \quad (46)$$

where  $\alpha$  is a geometrical factor,  $G$  is the shear modulus and  $b$  the Burgers vector. The evolution of  $\rho_s$  and  $\rho_g$  is affected  $\gamma$  by  $d\gamma/dl$  ( $\gamma$  is the shear strain and  $l$  is a length scale), which determine the mean free path,  $\lambda$ . Thus, they arrive at (the thermal component of  $\tau$ ,  $\tau^*$ , is assumed to be independent of grain/obstacle size):

$$\tau = \tau^* + \tau_G = \tau^* + \alpha Gb \left( \frac{\chi_e}{b} + \frac{\varepsilon_e^2}{\lambda_{II} b} \right)^{1/2} \quad (47a)$$

where  $\chi_e$  is a scalar measure of curvature and  $\varepsilon_e$  is the effective plastic strain;  $\lambda_{II}$  is the work hardening rate in Stage II (linear hardening).  $\chi_e$  is directly related to the strain gradient,  $d\gamma/dl$ . The length scale,  $l$ , can be taken as the grain size,  $d$ , or a fraction thereof. By making  $l = d$ , one arrives at:

$$\tau = \tau^* + \tau_G = \tau^* + \alpha Gb^{1/2} \left( \frac{\Delta\gamma}{d} + \frac{\varepsilon_e^2}{\lambda_{II}} \right)^{1/2} \quad (47b)$$

This theoretical framework does not incorporate the formation of a grain boundary work-hardened layer. Furthermore, it does not predict a grain-size dependence of yield stress, since both the curvature and plastic strain is zero prior to plastic deformation. As work hardening builds up, the effect manifests itself, resulting in an increased work hardening for decreasing grain size. It is the objective of this paper to provide some additional insights. The strain gradient theory does not take into consideration the difference in dislocation density observed between the grain interiors and the grain-boundary regions. A framework incorporating the strain gradient concepts and more attuned to the physics of the problem would be to track the dislocation densities in both grain interior and boundary. This has been done by Fu et al. [103], who introduced the gradient of the angle of maximum shear stress with respect to the external traction direction. This is described in Section 9.1.

## 7.7. Twinning

Two types of twins are considered here: mechanical and growth (or recrystallization, or annealing) twins. Although they are crystallographically related, the phenomenology is completely different. Both play a role in nanocrystalline materials.

### 7.7.1. Mechanical twins

Mechanical twinning and slip can be considered as competing processes. Indeed, Meyers et al. [348] developed a constitutive treatment for twinning based on this. In FCC metals and alloys, the twinning stress is directly related to the stacking fault energy.

As early as 1960, Venables [299] expressed the twinning shear stress,  $\tau_T$  as a function of source size,  $l$ , and stacking-fault energy,  $\gamma$ :

$$\frac{\tau_T}{G} = \frac{\gamma}{Gb} + \frac{\alpha b}{l} \quad (48)$$

Venables' [34] equation predicts an increase in twinning stress with increasing stacking-fault energy and decreasing source size. Narita and Takamura [300] also found a similar relationship after analyzing several FCC metals and alloys:

$$\frac{\tau_T}{G} = \frac{\gamma}{2b_p G} \quad (49)$$

where  $b_p$  is the Burgers vector of the partial dislocation.

Fig. 58 shows the relationship between a normalized twinning stress and a normalized stacking-fault energy. This fit was obtained by Voehringer [301]; the line was extended and the presumed twinning stresses for Ni and Al added. It is seen that the twinning stress for Al is quite high. The decrease in grain size is expected to render deformation twinning more difficult. At least, this is what conventional materials science predicts in the micrometer regime. This has been analytically expressed by Meyers et al. [306] in terms of two H–P relationships, one for twinning and one for slip:

$$\sigma_T = \sigma_{0T} + k_T d^{-1/2} \quad (50a)$$

$$\sigma_S = \sigma_{0S} + k_S d^{-1/2} \quad (50b)$$

where the first equation refers to twinning and the second to slip. There is considerable evidence in the literature that  $k_T \geq k_S$ . Fig. 59 shows the slip and twinning domains in a temperature versus strain rate plot for iron. It is clear that, as the grain size is decreased, the twinning domain shrinks. Eventually, it completely disappears.

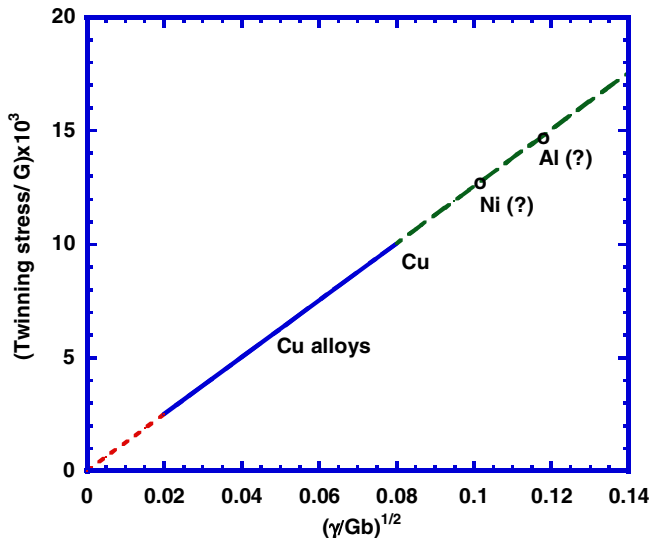


Fig. 58. Effect of stacking fault energy on twinning stress.



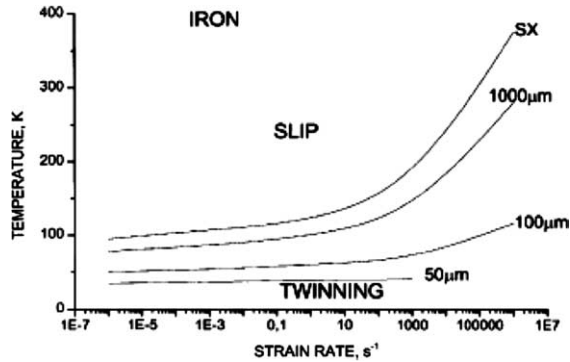


Fig. 59. Calculated effect of grain size on the twinning domain in pure iron [306].

This trend is confirmed by, e.g., El-Danaf et al. [307] who showed that, in a Co–Ni–Cr–Mo alloy, mechanical twinning could not be induced for grain sizes of 7 and 1  $\mu\text{m}$ , while larger grain sizes twinned. In FCC metals, extreme deformation regimes (either low temperatures or high strain rates) have to be applied to produce twinning. Andrade et al. [282] showed that for small grain sizes even high shock pressures could not generate twinning. Aluminum, which has a stacking-fault energy higher than Cu, could not twin either at high shock pressures or by deformation close to 0 K.

It is therefore surprising that molecular dynamics simulations by Yamakov et al. [308] predicted mechanical twinning in the deformation of a nanocrystalline aluminum-like metal. Fig. 60 shows a snapshot at a plastic strain of 0.12 for aluminum with a grain size of 45 nm. The grey lines indicate regions where the stacking sequence has been altered. Several processes of plastic deformation involving grain boundaries are seen:

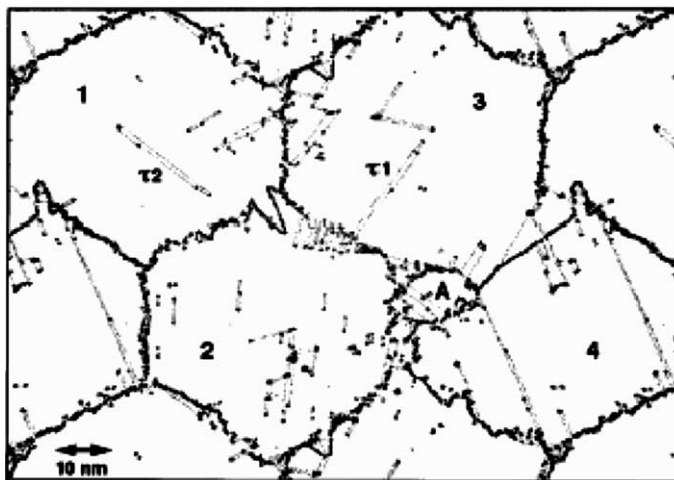


Fig. 60. MD simulation of nanocrystalline aluminum-like solid ( $d = 45 \text{ nm}$ ) having been subjected to plastic strain of 0.12; grey lines enclose regions with altered stacking sequence [308].

1. Heterogeneous nucleation of twin lamellae from the grain boundaries (e.g.,  $\tau_1$  in Grain 3).
2. Homogeneous nucleation of twin lamellae from the grain interior (e.g.,  $\tau_2$  in Grain 1).
3. Growth of twin lamellae to form a new grain (Grain A).

These twins and twin faults reacted with dislocations and formed complex twin networks, including coherent twin boundaries.

These MD simulations by Yamakov et al. [308,309] were followed, in 2003, with the first observations of twins in aluminum by Chen et al. [310]. Fig. 61 shows TEM micrographs at increasing magnifications of aluminum that was subjected to plastic deformation. Fig. 61(a) shows planar defects within the nanograins. In Fig. 61(b) one can see that these defects are twins and stacking faults. The atomic resolution micrograph of Fig. 61(c), which comes from the boxed area in (b) is clear evidence of twinning. These twins in nanocrystalline aluminum were confirmed in TEM by Liao et al. [311], among others. This finding has triggered a considerable debate, since aluminum has among FCC metals, one of the highest SFE:  $\sim 160$  mJ/m<sup>2</sup>. Nanotwins are also being found in other nanostructured metals, such as stainless steels (Fig. 62) [312].

It is early to propose a mechanism for deformation twinning in nanocrystalline metals, but some preliminary comments are of order. Meyers et al. [306] calculated the critical nucleus size for twinning as a function of applied stress using the Eshelby strain ellipsoid formalism. This analysis predicts a critical nucleus radius,  $r_C$ , equal to

$$r_C = \frac{5\pi G\gamma_{TB}}{4\tau'_T} \quad (51)$$

where  $\gamma_{TB}$  is the twin-boundary energy (directly related to the stacking-fault energy) and  $\tau'_T$  is the local (and not global) twinning shear stress. The critical radius is plotted against the normalized shear stress in Fig. 63 for Cu, Al, Ni, and Ag. At a local stress level of 500 MPa, characteristic of nanocrystalline metals, the critical radius is on the order of 50 nm for Cu and Al; for Ni, it is even higher. What this indicates is that the critical nucleus approach becomes untenable at grain sizes below 100 nm. There are at least three possible reasons for this: (a) the conventional nucleation mechanism breaks down in the nanoscale; (b) there are local stress concentrations (triple points, etc.) that raise the stress significantly above the 500 MPa level, propitiating smaller critical radii; (c) the partial dislocation separation increases in the nanoscale domain, aiding twinning. The last possibility is discussed further in Section 7.8.

### 7.7.2. Growth twins

The effect of growth (or annealing, or recrystallization) twins has also been investigated, and results are encouraging. Effort into optimizing strength and ductility [278,304] has shown that annealing twins can play a significant role. Wang et al. [304] produced microstructures consisting of a combination of nanoscale/ultrafine grains (80–200 nm) along with about 25% volume fraction of coarser grains (1–3  $\mu$ m). They rolled the Cu to 93% at liquid nitrogen temperature and then annealed it at temperatures below 200 °C. The original heavily cold worked Cu had a high dislocation density along with some grains less than 200 nm. Annealing resulted in a mixture of coarse and fine grained microstructure. The authors suggest that the excellent combination of strength and ductility is the result of (1) multi-axial stress states in the confined grains, (2) growth twins in the larger grains,

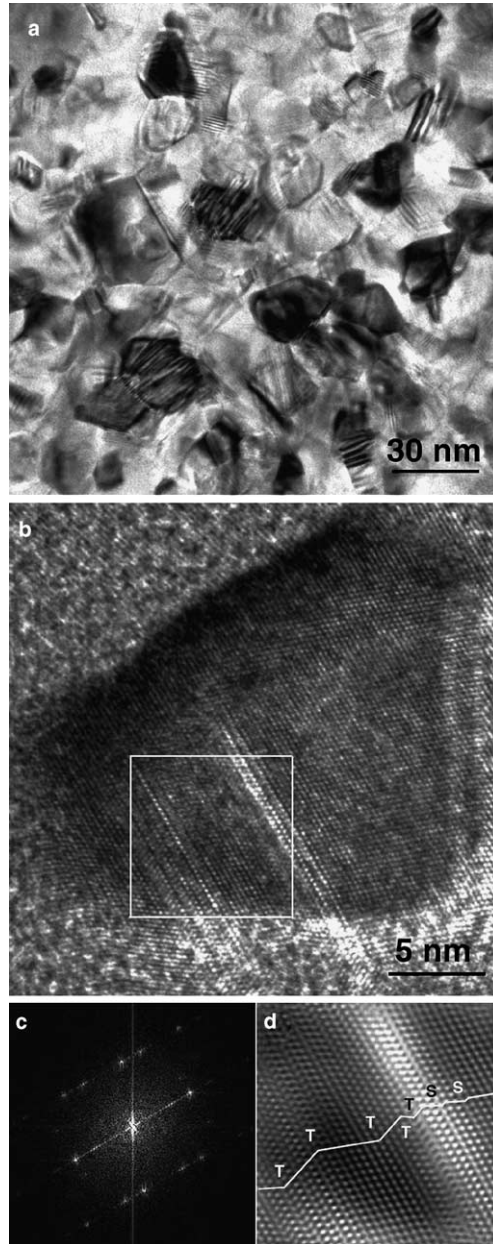


Fig. 61. TEM micrographs of nanocrystalline aluminum deformed by grinding: (a) overall view of nanograins with planar features within grains; (b) multiple deformation twins and stacking faults and (c) blowup of box in (b) showing atomic resolution and zig-zag due to twinning [92].

and (3) preferential accommodation of strain in the larger grains. The grain size distribution allows for significant strain hardening which prevents localized deformation and premature fracture.

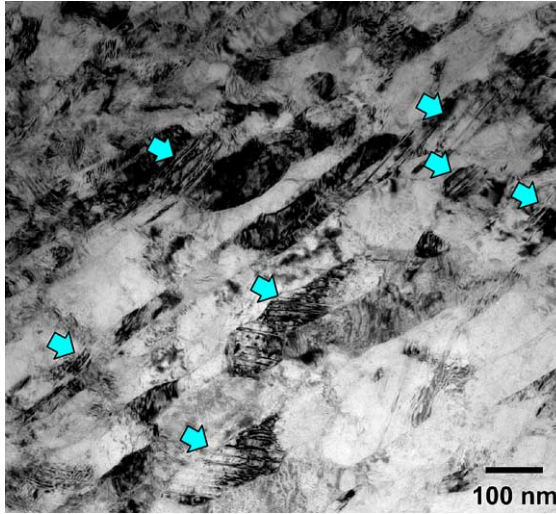


Fig. 62. Nanocrystalline AISI 305 SS produced within shear localization region in high-strain rate deformation [372].

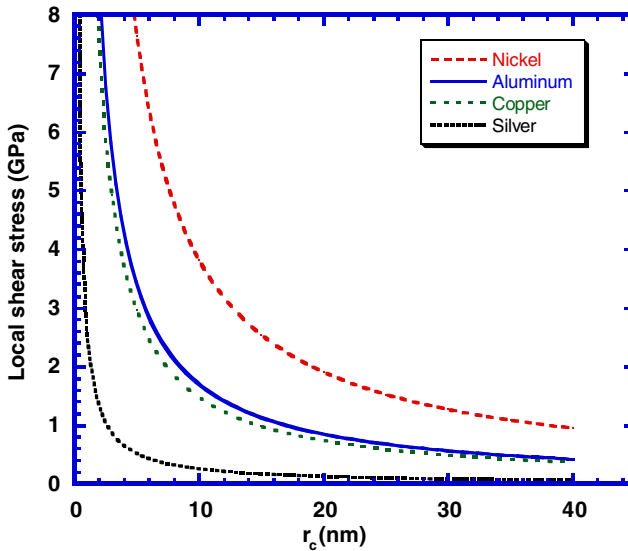


Fig. 63. Critical shear stress required for the activation of a twin nucleus as a function of size; notice that nucleus size is in the nanocrystalline domain for stresses on the order of the flow stress of nanocrystalline metals.

Lu et al. [305] showed that a good trade-off between mechanical strength and electrical conductivity in copper could be made by introducing a high density of nanoscale growth twins. They demonstrated a tensile strength about 10 times higher than that of conventional coarse-grained copper, while retaining an electrical conductivity comparable to that of pure copper. They argued that the increased strength comes from the effective blockage

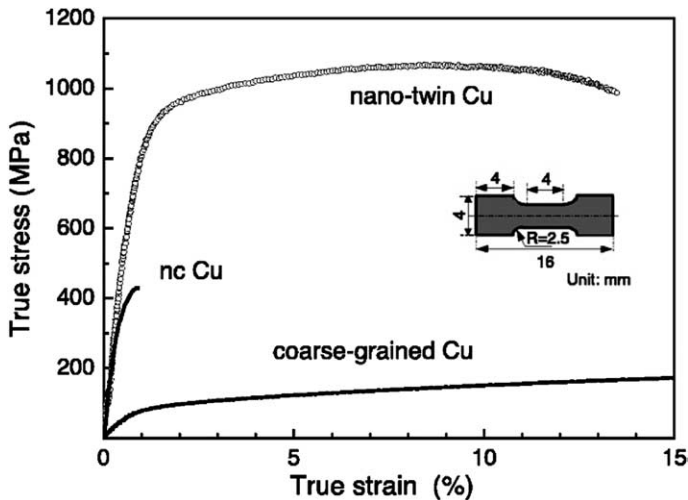


Fig. 64. Effect of nanotwin density on the mechanical response of copper [305].

of dislocation motion by numerous coherent twin boundaries that possess an extremely low electrical resistivity unlike other types of grain boundaries. Fig. 64 shows the plot of mechanical response of Cu sample with nanotwins in comparison with that for a coarse-grained and nanocrystalline sample. The uniform elongation increases from 1% to 10% with the introduction of nanotwins.

### 7.8. Grain-boundary dislocation creation and annihilation

Prompted by molecular dynamics simulations carried out primarily by Van Swygenhoven and coworkers [111,255,258,313–320] and by TEM observations showing a low dislocation density after appreciable plastic deformation, a combined grain-boundary source-sink model is evolving. When the grain size is reduced to the nanocrystalline regime, the mean free path of dislocations generated at grain-boundary sources is severely limited. Rather than cross slipping and generating work hardening, these dislocations can run freely until they meet the opposing grain boundary, which acts as a sink. Thus, the dislocation density remains low throughout the plastic deformation process, and work hardening is not significant. Fig. 65 shows this model in a schematic fashion. Dislocations, which were generated at one grain boundary, run unimpeded until they encounter the opposing grain boundary (on right-hand side). It was seen in Section 7.3 that grain-boundary ledges are responsible for generation of plastic flow in the conventional polycrystalline regime. However, as the grain size falls below 20 nm, the grain boundaries will become virtually free of ledges, and intrinsic and extrinsic grain-boundary dislocations have to be “pushed out” into the grains. Another significant difference is that the mean free path of dislocations is limited by the grain size, and therefore dislocation reactions, cross slip, and other mechanisms of dislocation multiplication are effectively prohibited.

Molecular dynamics simulations in the recent past have helped the materials community to gain a better understanding of the deformation mechanisms in nanocrystalline materials, especially relating the role of the grain boundary in deformation process

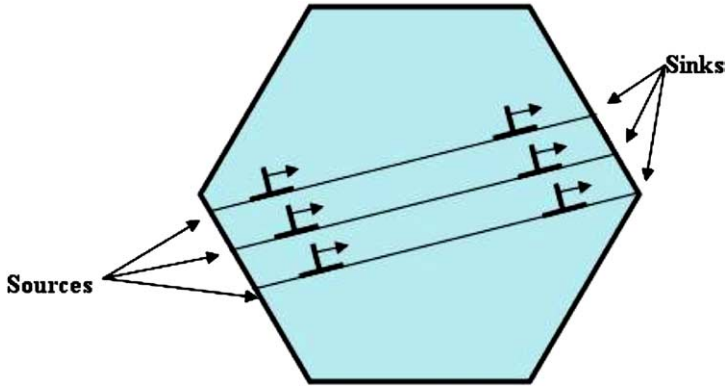


Fig. 65. Grain boundary source-sink model.

[256,313–320]. Recent simulations have also reported a transition with decreasing grain size from plasticity related to dislocation activity towards a plasticity that is primarily accommodated in the grain boundary. This is treated in Section 7.2.

Fig. 66 [319] shows the emission of dislocations from grain boundary in specimens subjected to indentation. Nanoindentation techniques coupled with atomic scale simulation have shown that dislocations can be emitted, absorbed, and even reflected from grain boundaries [319]. The sample used was constructed using Voronoi polyhedra, with 15 grains having a mean diameter of 12 nm. The samples were indented with an indenter that had a size smaller than the grain size. The load was increased to a critical value whereby a dislocation homogeneously nucleated with a corresponding reduction in the indenter load. As indentation progresses (Fig. 66), a dislocation is emitted from just beneath the indenter, and propagates to the nearest grain boundary. On further indentation, the leading partial of the dislocation is completely absorbed by the grain boundary. On continuing the indentation, the trailing partial is also absorbed. The process of dislocation absorption is accompanied by an increase of the number of grain-boundary dislocations, rearrangement of grain-boundary dislocations, and a change in the grain-boundary structure. As indentation is continued, a large number of the dislocations that are emitted under the indenter start interact with the surrounding grain boundaries, some of them are absorbed, and some of them are reflected back to the plastic zone. Moreover, grain boundaries also act as sources of dislocations that are emitted into the plastic zone. This suggests that both the local stress and the coherency of a grain boundary play a combined role in the interaction between the grain boundary and the incoming dislocation.

The processes identified through MD simulations have been studied analytically, and can indeed be predicted by using basic concepts from dislocation theory. It is instructive to calculate the stresses required for emission of dislocations from grain boundaries in the absence of ledges. Fig. 67 shows a dislocation being emitted from a grain boundary. To a first approximation, this dislocation is assumed to form, at the moment of release from grain boundary, a semicircle with radius  $r = d/2$ . The shear stress required to accomplish this is

$$\tau = \frac{\alpha Gb}{r} = \frac{2\alpha Gb}{d} \quad (52)$$

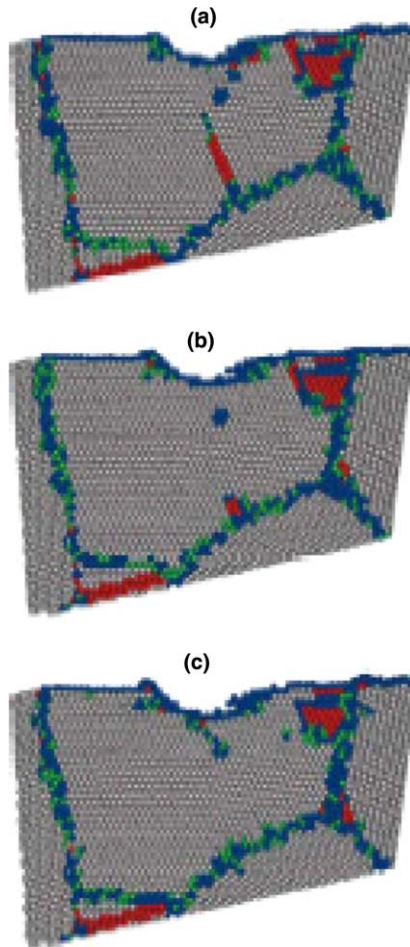


Fig. 66. A series of snapshots, showing the atomic structure of a sample involving a dislocation as a function of indenter depth [319].

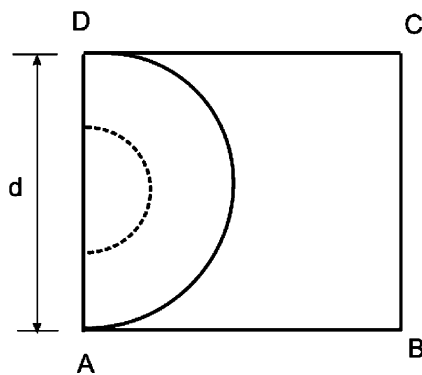


Fig. 67. Perfect dislocation emitted from grain boundary as a loop.

where  $0.5 \leq \alpha \leq 1$ . The stress predicted from Eq. (52) is quite high. For instance, for copper with a grain size of 50 nm, and assuming  $\alpha = 0.5$ ,  $b = 0.25$  nm, one obtains  $\tau = 242$  MPa. For  $d = 20$  nm,  $\tau = 603$  MPa. These values are somewhat higher than nanocrystalline strengths, but on the same order of magnitude.

Another, more realistic scenario is one in which a dislocation is emitted at a grain boundary and travels to the opposite grain boundary, leaving behind two sides, as shown in Fig. 68. Calculations were proposed by Liao et al. [325] and Asaro et al. [326]. We will present here a modified version of their analysis. Fig. 68 shows a dislocation emitted from the grain boundary AD. We assume a cubic grain, shown in Fig. 68(a). This dislocation, which we assume to be of edge character, leaves behind two trailing screw dislocations AB and DC. Fig. 68(b) shows the tridimensional picture. An array of such dislocations was emitted from the left-hand boundary and traveled an average distance  $x$  into the grain. The left-hand side of the grain is deformed by a shear strain  $\gamma$ . We will equate the work

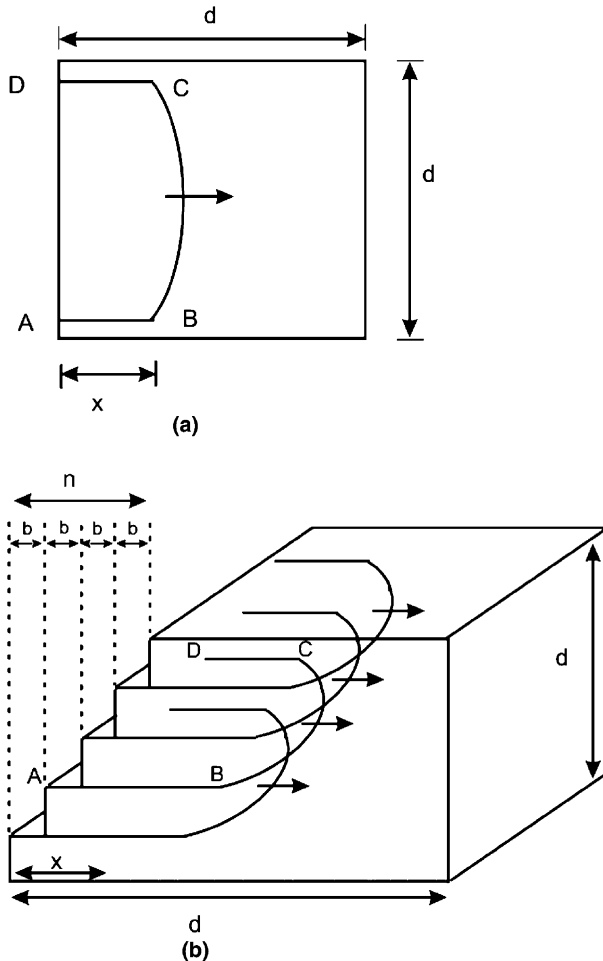


Fig. 68. (a) Dislocation traveling through nanograin and leaving behind two segments AB and CD; (b) dislocations traveling through nanograin in parallel planes and creating a shear strain  $\gamma$ .



of deformation,  $dW$ , to the increase in energy due to the formation of the segments AB and CD on all loops,  $dE$ . This requires neglecting the frictional stresses as well as the energy required to emit the dislocations from boundary.

$$dW = \tau\gamma V \quad (53)$$

$V$  is the deformed volume:

$$V = xd^2 \quad (54)$$

The shear strain  $\gamma$  is equal:

$$\gamma = nb/d \quad (55)$$

where  $n$  is the number of dislocations emitted from the boundary. Thus:

$$dW = nbx\tau d \quad (56)$$

The energy of the dislocations is equal to the product of their length (counting only the screw segments) by the term  $\alpha Gb^2$ , the energy per unit length:

$$dE = 2nx\alpha Gb^2 \quad (57)$$

Equating Eqs. (56) and (57), we get:

$$\tau = \frac{2\alpha Gb}{d} \quad (58)$$

Eq. (58) is identical to Eq. (52). If one considers the emission of partials instead of perfect dislocations, one makes the substitution

$$b_p = \frac{b}{\sqrt{3}} \quad (59)$$

Thus:

$$\tau = \frac{2\alpha Gb}{\sqrt{3}d} \quad (60)$$

The actual global stresses at which dislocations are emitted from grain boundaries can actually be considerably lower because of the stress concentration effect from adjacent boundaries. Triple points are stress concentrators, as shown by Gharemani and Hutchinson [327].

The stacking-fault energy determines the separation of partials through an equation of the form (e.g., [321]):

$$s = \frac{Gb_1b_2}{2\pi\gamma} \left( \cos\theta_1 \cos\theta_2 + \frac{\sin\theta_1 \sin\theta_2}{1-\nu} \right) \quad (61)$$

where the two partials are 1 and 2 and their Burgers vectors make angles of  $\theta_1$  and  $\theta_2$  with the dislocation line. Taking  $\theta_1 = \theta_2 = 30^\circ$ ,  $b_1 = b_2 = b_p$ , and  $\nu = 0.3$  one obtains:

$$s = \frac{Gb_p^2}{2.2\pi\gamma} \quad (62)$$

For aluminum, a metal with high stacking-fault energy ( $\gamma = 166 \text{ mJ/m}^2$ ),  $s \sim 1 \text{ nm}$ . For copper,  $s$  increases to  $\sim 3.2 \text{ nm}$ . It is therefore surprising that twins and stacking faults have been observed in these metals, when the grain size is decreased to the nanocrystalline

regime. Asaro et al. [326] and Asaro and Suresh [328] arrived at the following expression for the stress required, based on similar energetic arguments:

$$\tau = \frac{Gb}{3d} + \frac{d-s}{d} \frac{\gamma}{b} \quad (63)$$

The equilibrium (zero stress) separation of partials being considerably smaller than  $d$ , the term  $(d-s)/d$  can be taken as one. Thus, Eqs. (52), (60) and (63) have predictions that are on the same order. The grain boundaries in nanocrystalline metals are often non-equilibrium boundaries that possess a dislocation density higher than equilibrium boundaries. Fig. 69(a) shows a TEM micrograph of non-equilibrium boundaries in aluminum [322]. The dislocations at the boundary are marked. Fig. 69(b) shows a sketch with the atomic positions and dislocation configurations in an equilibrium boundary. By comparing a non-equilibrium boundary (TEM in Fig. 69(a)) with the equilibrium boundary, it can be seen that the former has an excess of dislocations. These “non-equilibrium” dislocations are ready candidates for emission into the grain interiors. Thus, we accept that the grain boundaries can be effective sources of dislocations. Sutton and Balluffi [323] and Murr [324] discuss these grain-boundary dislocations in much detail. The emission of a partial dislocation from a grain boundary in a nanocrystalline metal is shown schematically in Fig. 70. The leading partial forms the loop ABCD, while the trailing partial forms the loop AB’C’D. The stacking-fault ribbon is marked by hashed lines. The separation  $s$  is shown in the figure. Asaro et al. [326], Liao et al. [325] and Zhu et al. [312] used an energetic analysis to show that the equilibrium separation of partials is larger in the nanocrystalline domain than in a monocrystal. The argument is simple. As the trailing partial is moved

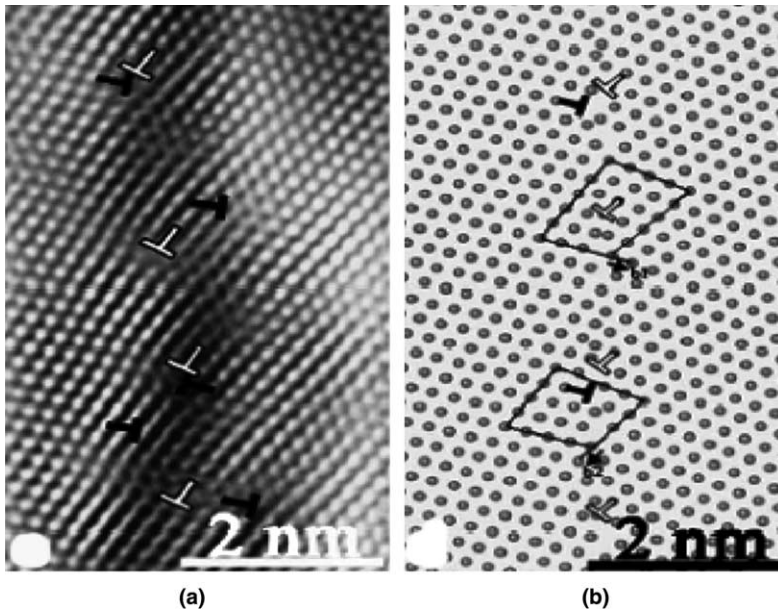


Fig. 69. Atomic positions and dislocation configurations in (a) non-equilibrium and (b) equilibrium grain boundary in Al [322].

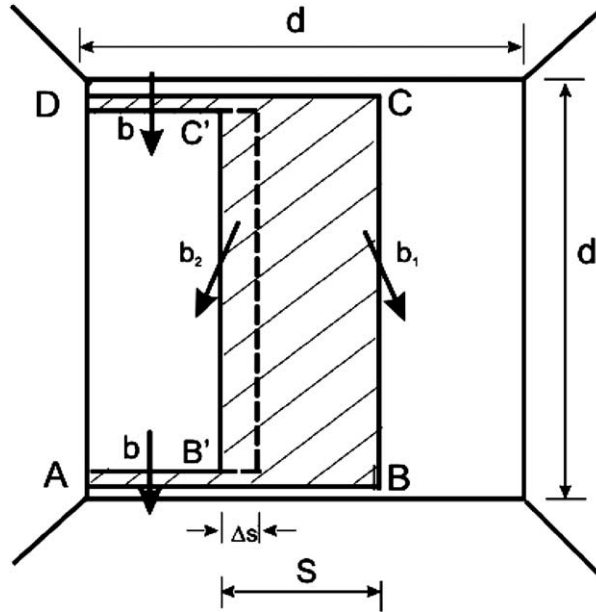


Fig. 70. Stacking-fault ribbon generated by successive nucleation of partial dislocations in grain boundary and motion into grain interior; grey area represents stacking fault.

by  $\Delta s$ , to the right, the side partials comprising the  $AB'$  and  $DC'$  portions of the loop are lengthened. This term has to be incorporated into the energetic balance. This leads to a new equilibrium separation,  $s_n$ . Liao et al. [325] showed that the ratio  $s_n/s$  is equal to

$$\frac{s_n}{s} = \frac{\gamma}{\gamma - \frac{Gb^2(8+\nu)}{24\pi(1-\nu)d} \ln \frac{d}{b}} \tag{64}$$

where  $b$  is the Burgers vector of the perfect dislocation. When an external stress  $\tau$  is applied, the separation is further increased to

$$\frac{s_n}{s} = \frac{\gamma}{\gamma - \frac{Gb^2(8+\nu)}{24\pi(1-\nu)d} \ln \frac{d}{b} - \tau b_1} \tag{65}$$

Fig. 71 shows the effect of grain size on the ratio  $s_n/s$  for different values of the applied stress. It is clear that for large values of  $d$ , the ratio approaches 1. As the applied stress is increased the ratio rises more rapidly. It can be concluded that partial separation is much more pronounced in the nanocrystalline domain and that this effect can have a profound effect on the mechanical response, favoring twinning and stacking fault formation.

The expression arrived at by Zhu et al. [312] and Liao et al. [325] for the flow stress based on partial emission is

$$\tau_P = \frac{1}{\sin \alpha} \left( \frac{Gb_P}{2\pi d} \ln \frac{d}{b_P \sqrt{3}} + \frac{\gamma}{b_P} \right) \tag{66}$$

where  $\alpha$  is the angle between partials. In comparison with Eqs. (52), (56) and (63), a more accurate expression for the dislocation energy was used; it has an upper cutoff radius of  $d$ .

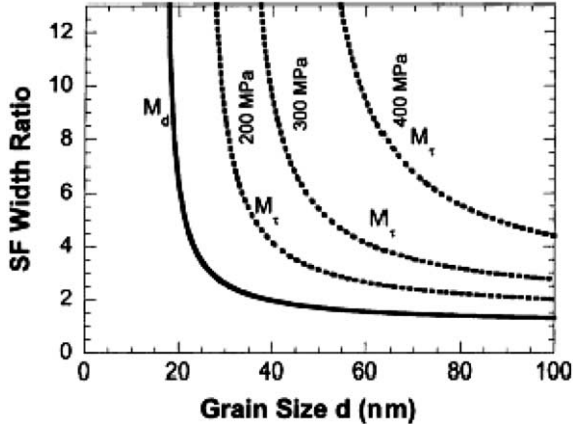


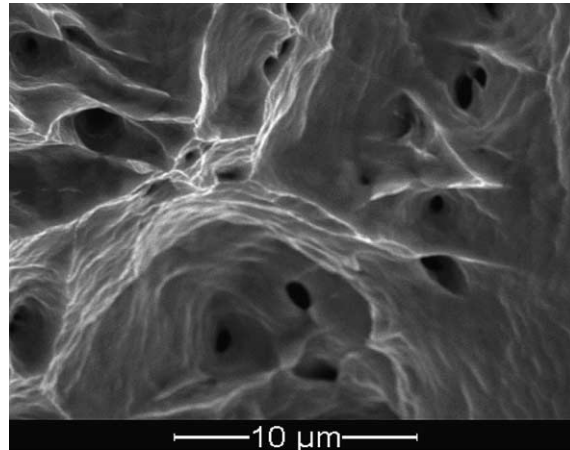
Fig. 71. Normalized stacking-fault width as a function of grain size for various levels of applied stress level [325].

This is the reason for the logarithmic term. The emission of perfect and partial dislocations are therefore competing mechanisms and the one requiring the least stress will be generated.

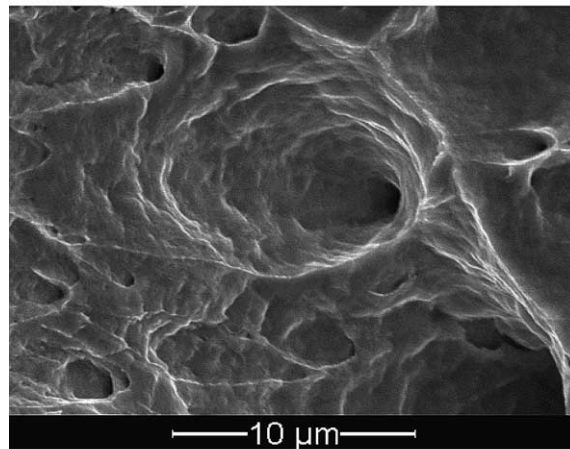
## 8. Fracture

Fracture is a complex phenomenon of initiation, propagation, and coalescence of micro(nano)voids or micro(nano)cracks leading to the separation of a body into two or more parts. In ultrafine grained copper produced by ECAP, the fracture morphology was found to be similar to the one in conventional polycrystalline copper. This is shown in Fig. 72. The SEM micrographs show, at the bottom of the dimples, holes which are the initiation sites for fracture. The interpretation for the similarity in the fracture morphology is that the initiation sites (in this case, most probably inclusions) have the same distribution for the two conditions, since the material composition is the same. Therefore, since the fracture morphology is dictated by the inclusions, it is reasonable to assume that the dimple size will be the same.

For nanocrystalline metals, the situation is more complex. In the absence of heterogeneous nucleation sites such as those in Fig. 72, the scale of the fracture surfaces is, by virtue of the reduced grain size, reduced. In nickel (FCC), the room-temperature fracture surface consists of dimples. Xiao et al. [329] and Mirshams et al. [330] show fractographs that are classified as transgranular ductile. The spacing/size of dimples, however, is considerably larger than the grain size in their specimens: 19 nm. Fig. 73(a) shows the fracture surface. The dimples are on the order of  $1\ \mu\text{m}$ . Annealing at  $200\ ^\circ\text{C}$  retains the dimpled structure if no dopants are present. Since nanocrystalline metals are thermally unstable, grain growth is known to occur in an irregular fashion. This is exemplified in Fig. 74. Nanocrystalline Ni annealed to  $500\ ^\circ\text{C}$  for 1 h shows an extraordinary fracture surface, consisting of runaway growth of some grains, shown in Fig. 74(a) and (b). These grains have a cubic shape. The fracture in the regions with smaller grains has a morphology that changed from dimpled transgranular to intergranular. This is due to the impurity atoms that concentrate on the grain boundaries and weaken them. It can be seen that the grain size is considerably larger than the original grain size, in spite of the relatively low anneal-



(a)



(b)

Fig. 72. SEM micrographs of (a) annealed polycrystalline and (b) ultrafine grained copper: 8 ECAP passes leading to a total shear strain of 8.

ing temperature, which would not produce significant grain growth in Ni with conventional grain size.

The results by Kumar et al. [331] are in full agreement with Fig. 73. The stereopair shown in Fig. 75 shows the same dimples in electrodeposited Ni. The size of the dimples is also considerably larger than the grain size. The interpretation given by them is shown in Fig. 76. The mechanisms responsible for void initiation are:

1. Existing voids at grain boundaries and triple points.
2. Voids created by dislocation emission from grain boundaries.
3. Voids created by grain-boundary sliding which leaves wedges at triple junction.
4. Cavities created by the action of grain-boundary sliding on the ledges.

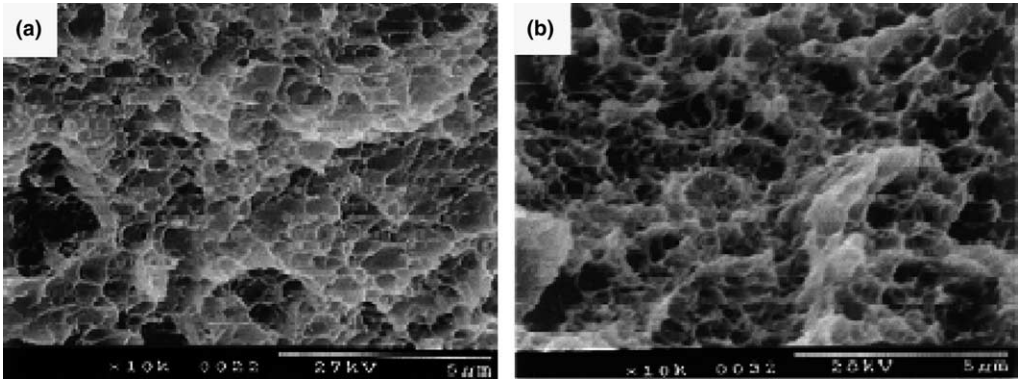


Fig. 73. SEM fractographs of Ni: (a) as-received nanocrystalline Ni and (b) after annealing at 200 °C (from Xiao et al. [329]).

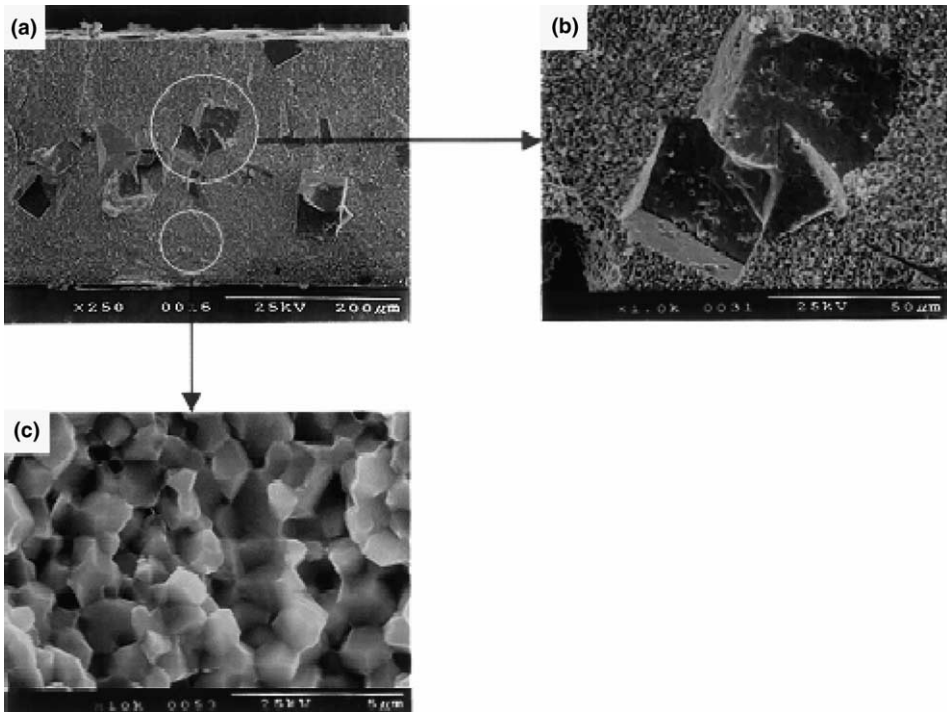


Fig. 74. SEM fractographs of Ni annealed at 500 °C. (a) A cross-section overview of fracture surface and (b) a high magnification view of some large grains in (a) and (c) a high magnification view of some small grain area in (a) (from Xiao et al. [329]).

These three initiation mechanisms are shown in Fig. 76. The spacing of these initiation sites, which is larger than the grain size, determines the dimple size. The hypothetical dimple size is shown in Fig. 76(d).

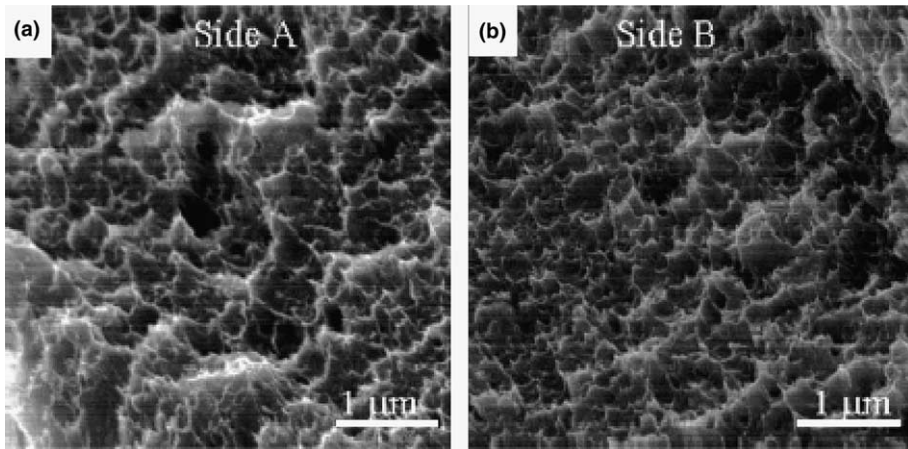


Fig. 75. Dimpled structure observed in stereopair (a,b) in fracture surface of nanocrystalline nickel (electrodeposited); notice size of dimples that is considerably larger than grain size [331].

Recent observations by the authors reveal that the fracture surface of nanocrystalline metals might be more complex than envisaged before. Fig. 77 shows low and high magnifications of a fracture surface created by tensile rupture of a nanocrystalline foil (300  $\mu\text{m}$  thickness). The macroscopic view of the fracture shows features similar to the conchoidal fracture of glass, which is shown as a comparison in Fig. 77(b). The presumed direction of propagation of the crack is shown in figure. This “quasibrittle” mode is consistent with the high stress level as well as limited ductility of the nanocrystalline nickel. However, closer inspection of the fracture surface (Fig. 77(c)) reveals dimples similar to the ones shown in Figs. 73 and 75.

The fracture surface generated by breaking the foil in bending had a different appearance. It was characterized by river markings that correspond to steps separating regions of ductile fracture (Fig. 78(a) and (b)). The presumed direction of fracture is also shown in figure. Upon closer examination, the flat surfaces consist of dimples (Fig. 78(c)), while the steps are regions of intense shear where all details are smeared out (Fig. 78(d)). This shows that localization between regions of ductile tearing is an inherent characteristic of fracture of nanocrystalline metals. This dual ductile/shear response is the result.

## 9. Numerical modeling

Closed form solutions for polycrystalline plastic flow on any size scale are beyond classical analytical solution methods, making numerical methods a must. Finite element methods and molecular dynamics are the two numerical methods used to model nanocrystalline materials. Before reviewing the modeling efforts, a discussion of the strengths and weaknesses of the two methods is worthwhile.

The finite element method is a continuum modeling method, and therefore has no intrinsic length scale. Length scale effects must be introduced through the material models

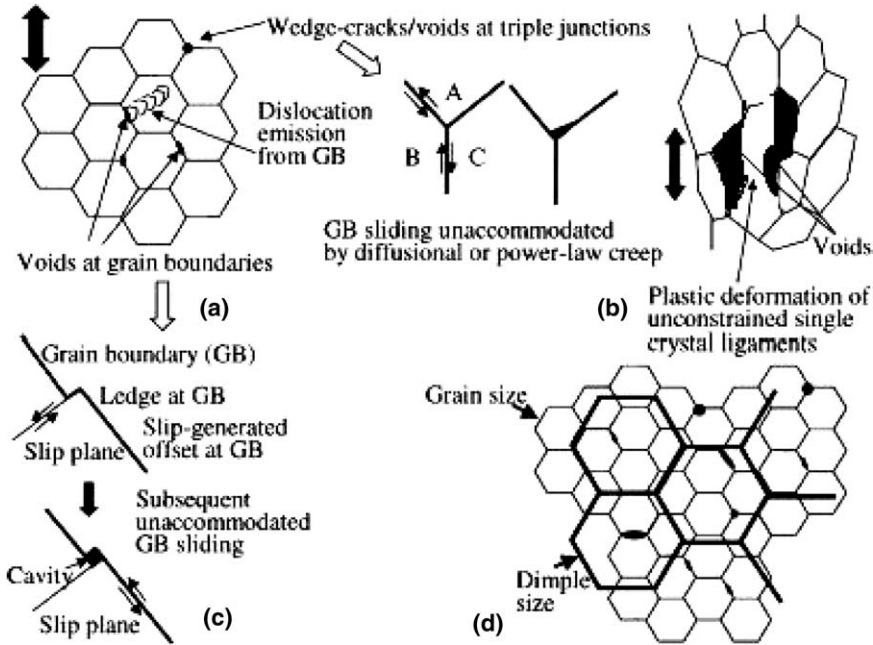


Fig. 76. Schematic illustration showing how deformation evolves in the nanocrystalline nickel and leads to (a) dislocation emission from grain boundaries, void formation/growth at grain boundaries and triple junctions, grain-boundary sliding; (b) the formation of partially unconstrained ligaments that deform plastically; (c) generation of cavities at grain-boundary ledges and (d) the interaction of these various features to produce final dimple size [331].

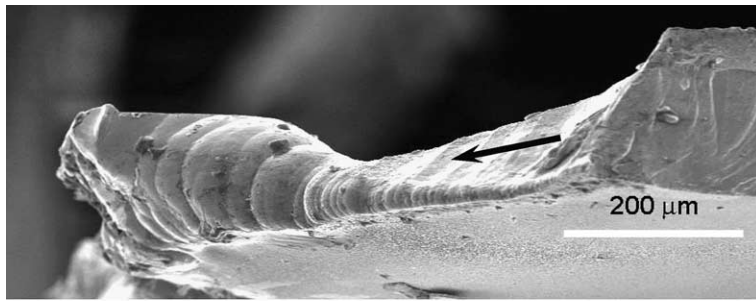
in the finite element calculation. The absence of an intrinsic length scale in the finite element method is valuable computationally since it allows the simulations of crystalline systems having dimensions several orders of magnitude apart [104] with approximately the same amount of computational work.

At the nanocrystalline level, the primary issue is whether a continuum model is valid. Crystal plasticity, for example, is based on dislocation motion, however the dimensions of the individual grains in a nanocrystalline material may be small enough that traditional dislocation structures do not exist or do not behave in the classical manner.

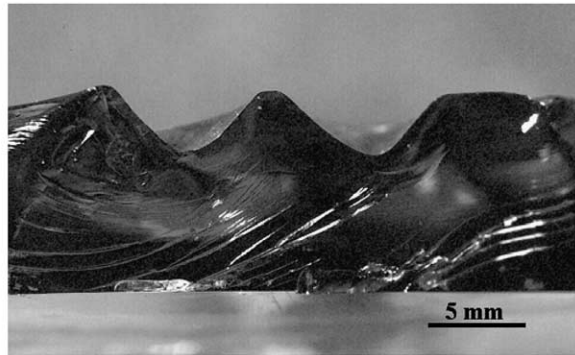
Issues that are handled naturally by molecular dynamics, such as grain-boundary slip, require the development of separate, specialized models to include their phenomenology in finite element models. For phenomena that exist only at the length scales being investigated, obtaining the material constants and verifying the accuracy of the model independently from the systems being investigated is a major challenge.

In contrast, molecular dynamics directly models the atoms and therefore directly incorporates the atomic length scales of the crystal directly into the computation. Individual atoms interact through forces defined by potential functions. These potential functions are phenomenological approximations, derived from insights obtained from quantum mechanical simulations of small systems. Creating the potential functions is a research area in its own right, and will not be discussed further.

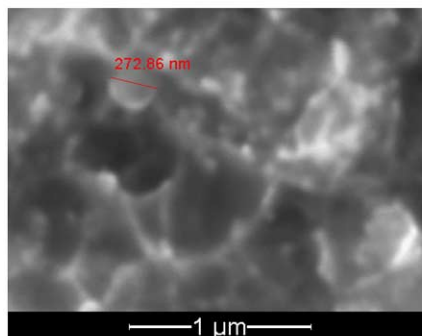




(a)



(b)



(c)

Fig. 77. Fracture of pulse electrodeposited nanocrystalline nickel: (a) overall view of surface of 300 μm thick foil; (b) fracture of glass showing conchoidal features and (c) high magnification image showing dimples (sample courtesy E. Bringa, LLNL).

While molecular dynamics is very attractive, it is not without its own limitations. The first limitation is associated with time scales. The solution in a molecular dynamics simulation is advanced in time using an explicit time integration method that imposes a stability limit on the time step size. In practice, the time step size is a few percent of the period of atomic vibration. All current molecular dynamics calculations therefore occur at extremely high strain rates that are generally inaccessible experimentally.

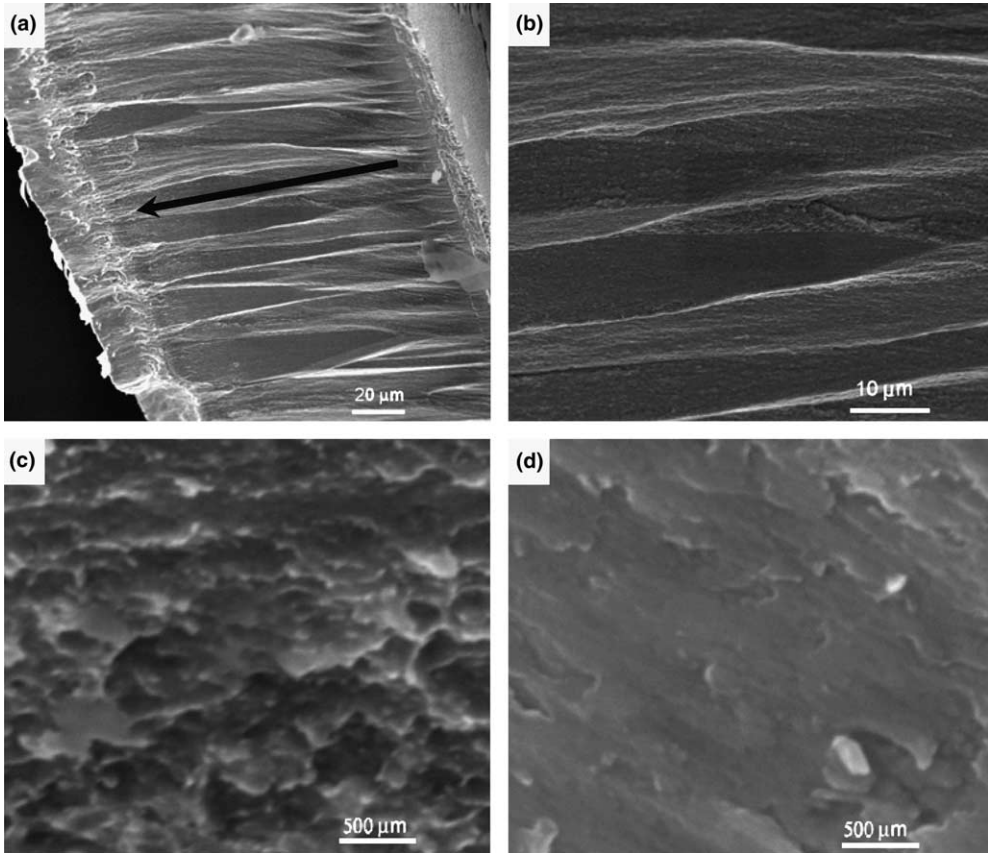


Fig. 78. Stepped fracture surface containing smooth steps produced by bending nanocrystalline Ni foil until fracture: (a) river pattern with plateaus and steps; (b) closer view of (a); (c) dimpled fracture in plateaus and (d) shear surface in steps.

A second limitation with molecular dynamics is also one of its strengths, the intrinsic length scale. Even with the largest computers available today, the largest sample that may be simulated is nanocrystalline, which makes direct comparisons to macroscopic experiments impossible.

Third, the initial configuration of a molecular dynamics simulation is only in equilibrium if the system contains no imperfections. Introducing defects into a perfect crystal, whether they are stacking faults or a grain boundary, introduces perturbations into the structure for which the equilibrium configuration is unknown. Relaxation methods are used to approach equilibrium, but the time period required for stress equilibration generally exceeds the duration of the simulation, making true equilibrium prohibitively costly.

Independent of the method used for the solution, the spatial domain is filled with grains generated by Voronoi tessellation. The domain is “seeded” with randomly distributed points, each of which will be the center of a grain. Most researchers seed the domain so that the resulting grains are of nearly uniform size and equiaxed. The grain interior consists of all points that are closer to its seed point than any other seed. The boundary

between two grains therefore consists of the points that are equidistant from their two seeds, which are calculated efficiently by specialized numerical methods. A characteristic of the Voronoi tessellation is all the grains are convex, i.e., there are no reentrant corners.

The computational methods available for simulating nanocrystalline materials are clearly imperfect, however they are still capable of providing important insights into the behavior of nanoscale materials. Since finite element methods and molecular dynamics are areas with a large number of active researchers, and nanomaterials have been identified as important area for research by both government agencies and industry, there will probably be considerable progress in the development of both methods in the near future. The work reviewed below should therefore be regarded as pioneering work in the area of nanocrystalline materials, and not as definitive treatises.

### 9.1. Finite element simulations

A length scale is introduced into a finite element model of a polycrystal material by

1. Using a material model having a length scale.
2. Modifying the behavior of the grain boundary, thereby introducing a length scale as the ratio of the grain-boundary volume to its surface area.
3. Modeling the grain boundary with a finite thickness, which directly imposes a length scale.

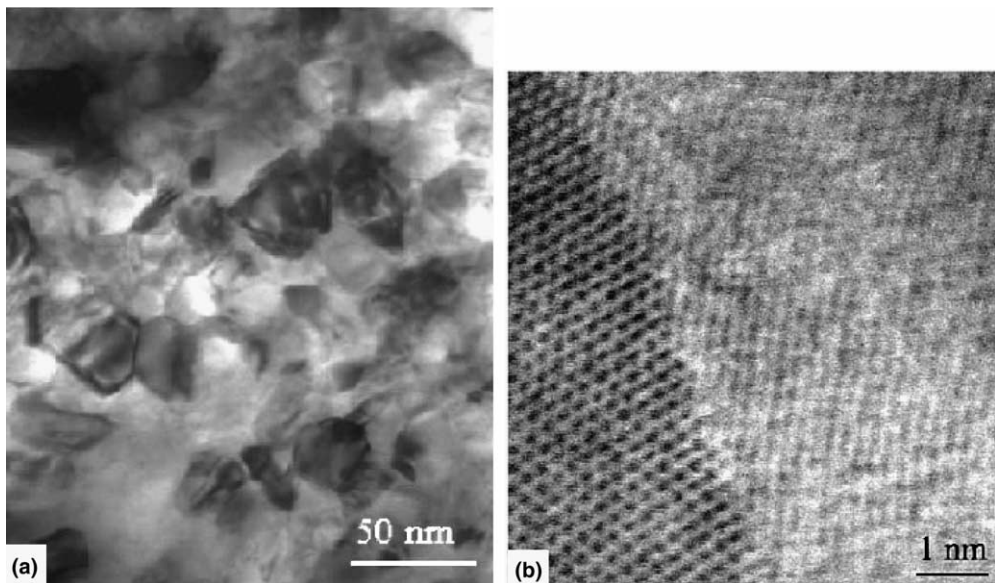


Fig. 79. As-received electrodeposited nc-Ni: (a) bright-field TEM image showing nanocrystalline grain structure and (b) image showing a clean atomically faceted grain boundary [332].

Kim et al. [251] modeled the plastic deformation of nanocrystalline materials with a constitutive equation based on the evolution of the dislocation density, and included a contribution from diffusion controlled plastic flow. Estrin [137] proposed a crystal plasticity model that includes gradient terms for double-slip geometry, and second derivatives, having a diffusion-like character, were incorporated for cross-slip.

Anand et al. [332] introduced cohesive elements along the grain boundaries to model grain-boundary slip. These cohesive elements have evolution equations for both the normal and tangential tractions based on the amount of slip and separation between adjacent grains, including both reversible elastic and inelastic components. The interior of the grains was modeled with single crystal plasticity. They applied their model to the study of nanocrystalline nickel (Fig. 79) and compared the results to experiments. It was observed that dislocation density in Ni grains after plastic deformation decreased, as shown in Fig. 80, suggesting that dislocation annihilation might be taking place at the grain boundaries or oppositely signed dislocations.

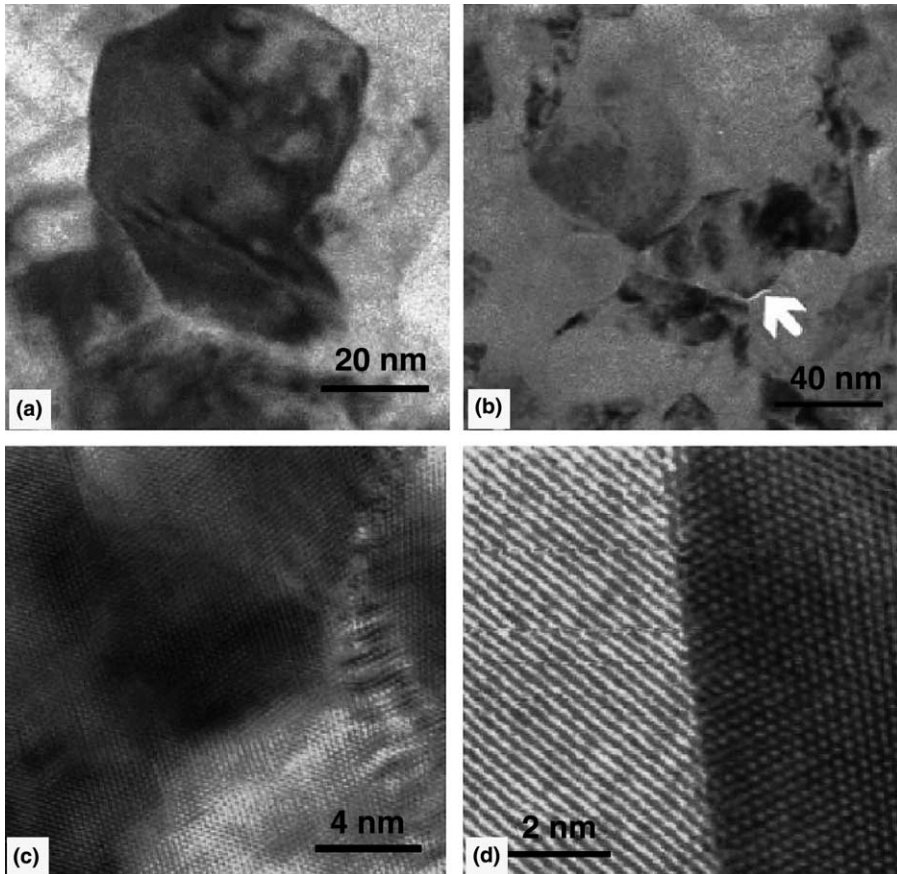


Fig. 80. Microstructure of nc-Ni after 4% plastic strain in compression: (a) bright-field TEM image showing a few dislocations within a grain; (b) a possible crack at a grain-boundary triple junction; (c) substantially dislocation-free grains and possibly a low-angle grain boundary and (d) clean grain boundaries with no evidence of residual dislocation debris left after the deformation [332].

Fig. 81 shows contours of a measure of an equivalent plastic strain in the grains corresponding to four different points, labeled a through d, on the stress–strain response, Fig. 81(a). Fig. 81(b) shows no plastic strain in the grain interiors.

The macroscopic stress–strain curves for meshes with different grain sizes are shown in Fig. 82. They observed that the non-linearity of the stress–strain response is primarily due to the inelastic response of the grain boundaries. Plastic deformation of the interior of the grains was rarely observed prior to grain-boundary cracking.

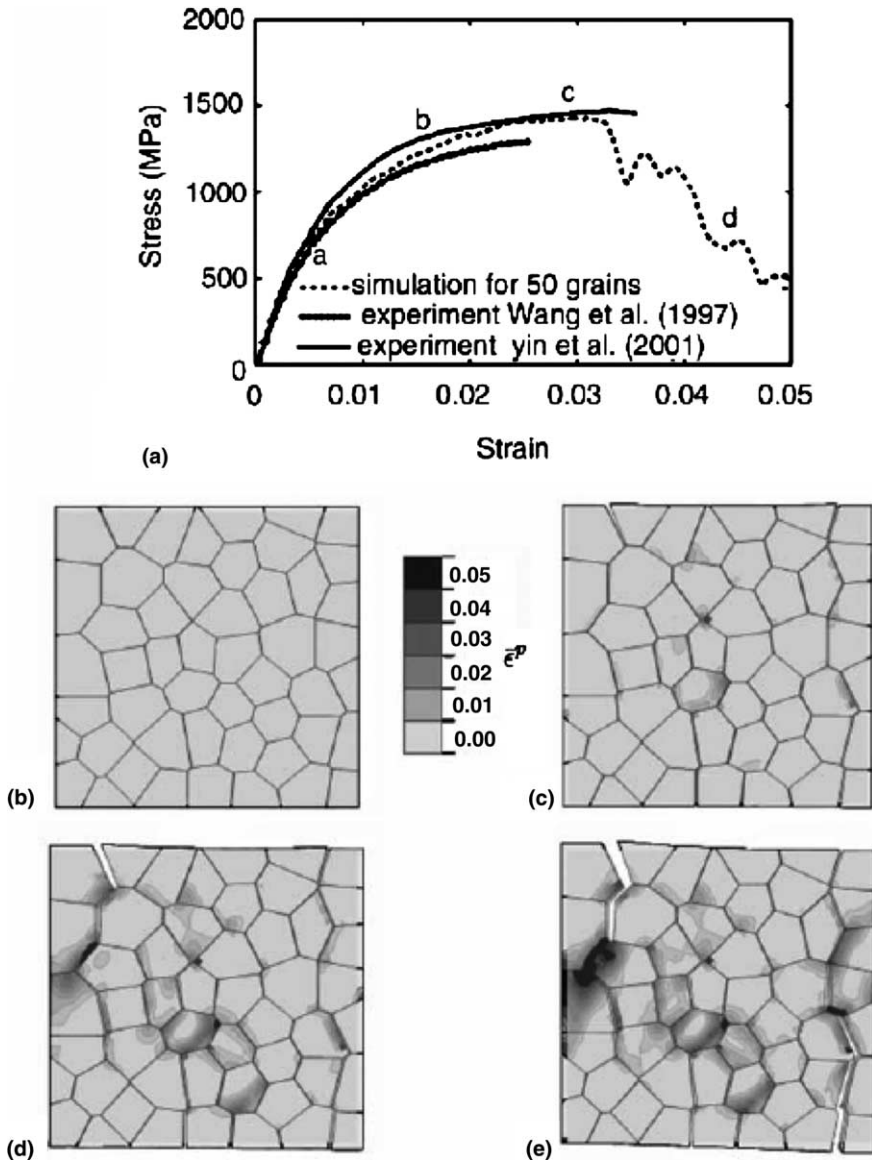


Fig. 81. (a) Stress–strain curve from the simulation. (b) Contour plots (b)–(e) of the equivalent plastic strain in the grain interiors corresponding to different macroscopic strain level [332].

Fu et al. [87] in their investigations modeled each copper grain as consisting of two parts: a grain boundary of finite thickness and the grain interior. The thickness of the grain boundary is a non-linear function of the grain diameter. A series of two-dimensional

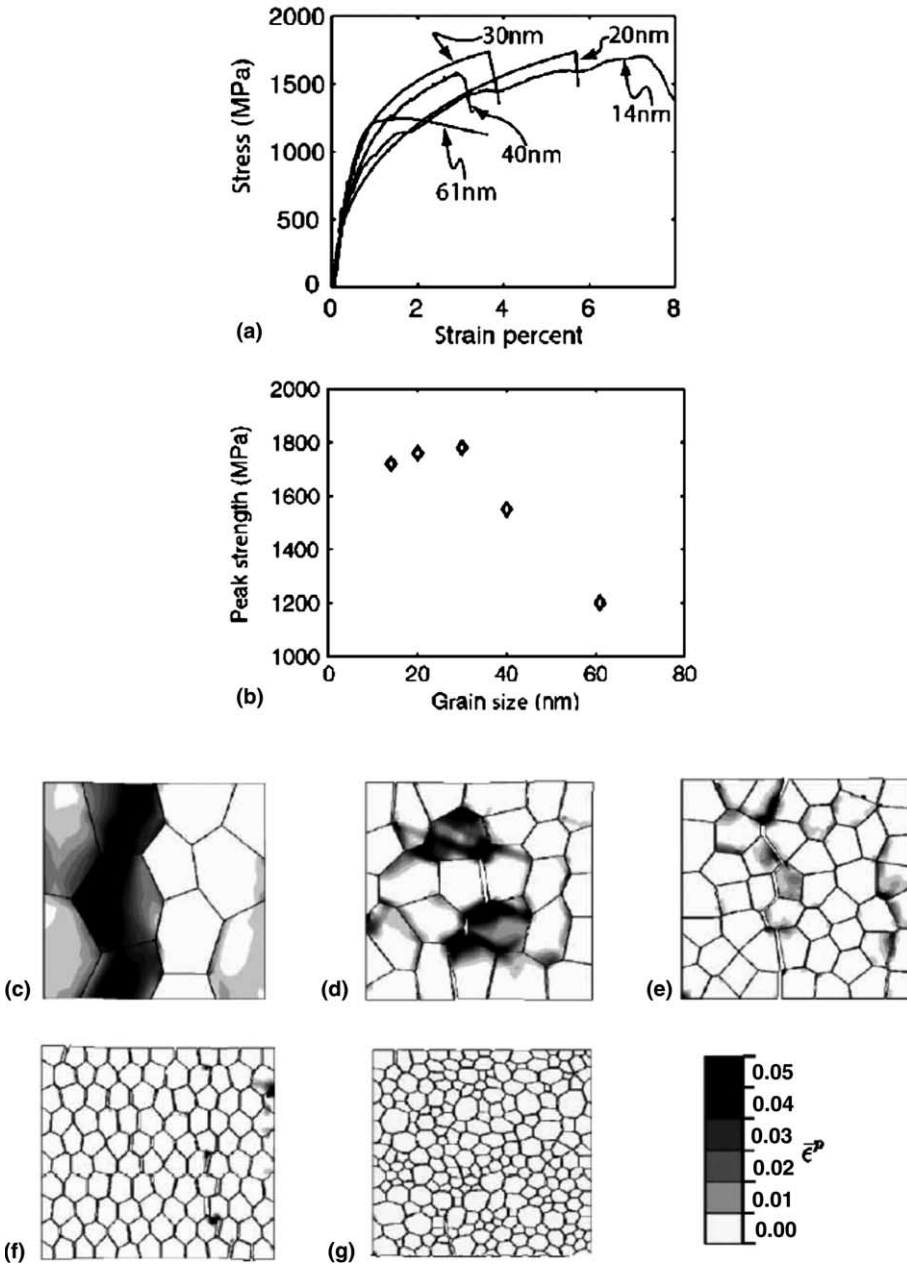


Fig. 82. (a) Stress–strain curves for different grains sizes. (b) Peak strength versus grain sizes. Plots (c) through (g) show contours of the equivalent plastic in the grain interiors corresponding to the strain levels right after peak stress for the 61, 40, 30, 20 and 14 nm average grain-sized microstructures [332].

representative volume elements having roughly 100 grains and grain sizes ranging from 26 nm to 100  $\mu\text{m}$  were subjected to compression. The grain geometry remained constant so that only ratio of the grain-boundary thickness to the grain diameter was responsible for the changes in the patterns of deformation. Fig. 83 shows different grain sizes, distinguished by different ratios between grain-boundary and bulk dimensions.

Four different models, varying by the material models used for the grain boundaries and interiors, were investigated:

In the first investigations [104], the grains correspond to one of three crystallographic orientations (marked by double circles in Fig. 84(a)) corresponding to soft, medium,

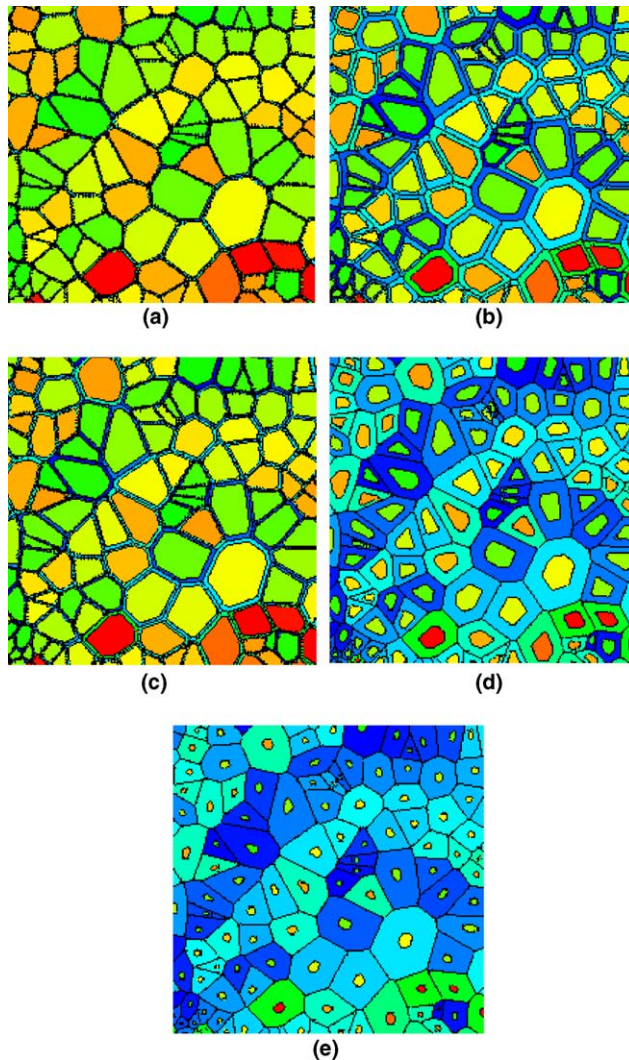


Fig. 83. Simulated polycrystalline aggregate used in computations: (a)  $D = 100 \mu\text{m}$ ,  $t = 3.33 \mu\text{m}$ ; (b)  $D = 10 \mu\text{m}$ ,  $t = 0.665 \mu\text{m}$ ; (c)  $D = 1 \mu\text{m}$ ,  $t = 0.133 \mu\text{m}$ ; (d)  $D = 0.1 \mu\text{m}$ ,  $t = 0.0265 \mu\text{m}$  and (e)  $D = 0.026 \mu\text{m}$ ,  $t = 0.0103 \mu\text{m}$  [265].

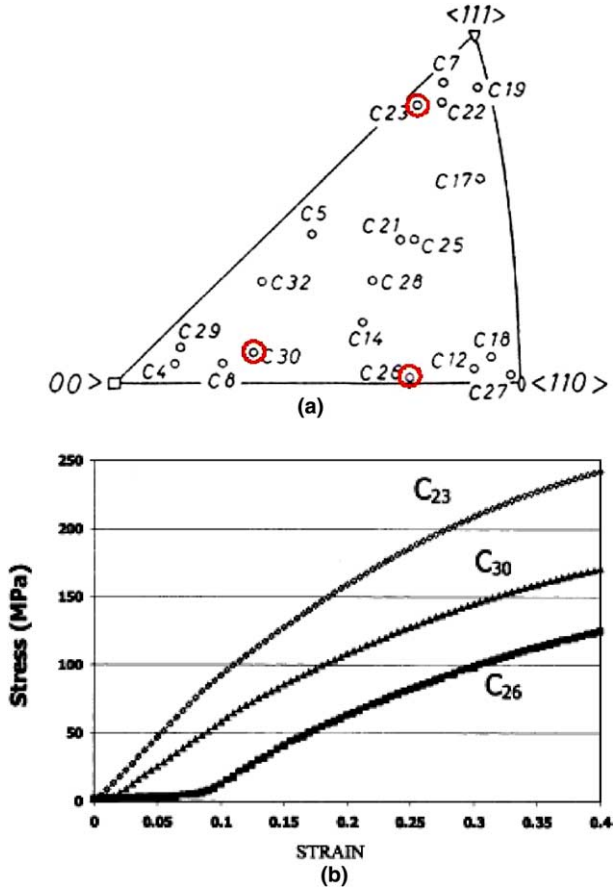


Fig. 84. (a) Three crystallographic orientations (marked by double circles) considered in computations (experimental results from Diehl); notice the equivalent isotropic elastic moduli marked for each orientation. The denominations C23, C26, and C30 are from Diehl. (b) Mechanical response of the grain in the three crystallographic directions [103].

and hard orientations. The mechanical response of grain interior in these directions is shown in Fig. 84(b). The grains are isotropic, with the elastic modulus and plastic hardening curve depending on the orientation, with the data taken from Diehl [333] and Suzuki et al. [334]. The grain boundaries were modeled with perfect plasticity.

Later work, [335] introduced single crystal plasticity for the grain interior and the Voce equation to model the hardening of the grain boundaries. Fig. 85 shows the stresses and strains observed within the polycrystalline aggregate for a grain size of 20 nm.

The next model, [335] used single crystal plasticity for both the grain interior and boundary, with the interior and boundary having a common orientation but different hardening properties. Up to fifty different random orientations were used. This model reveals the evolution of localization which occurs during work hardening. Fig. 86 shows such an area.

The final model, [335] replaces the separate grain interior and boundary model with a hardening model that is related to the dislocation density evolution. The evolution is



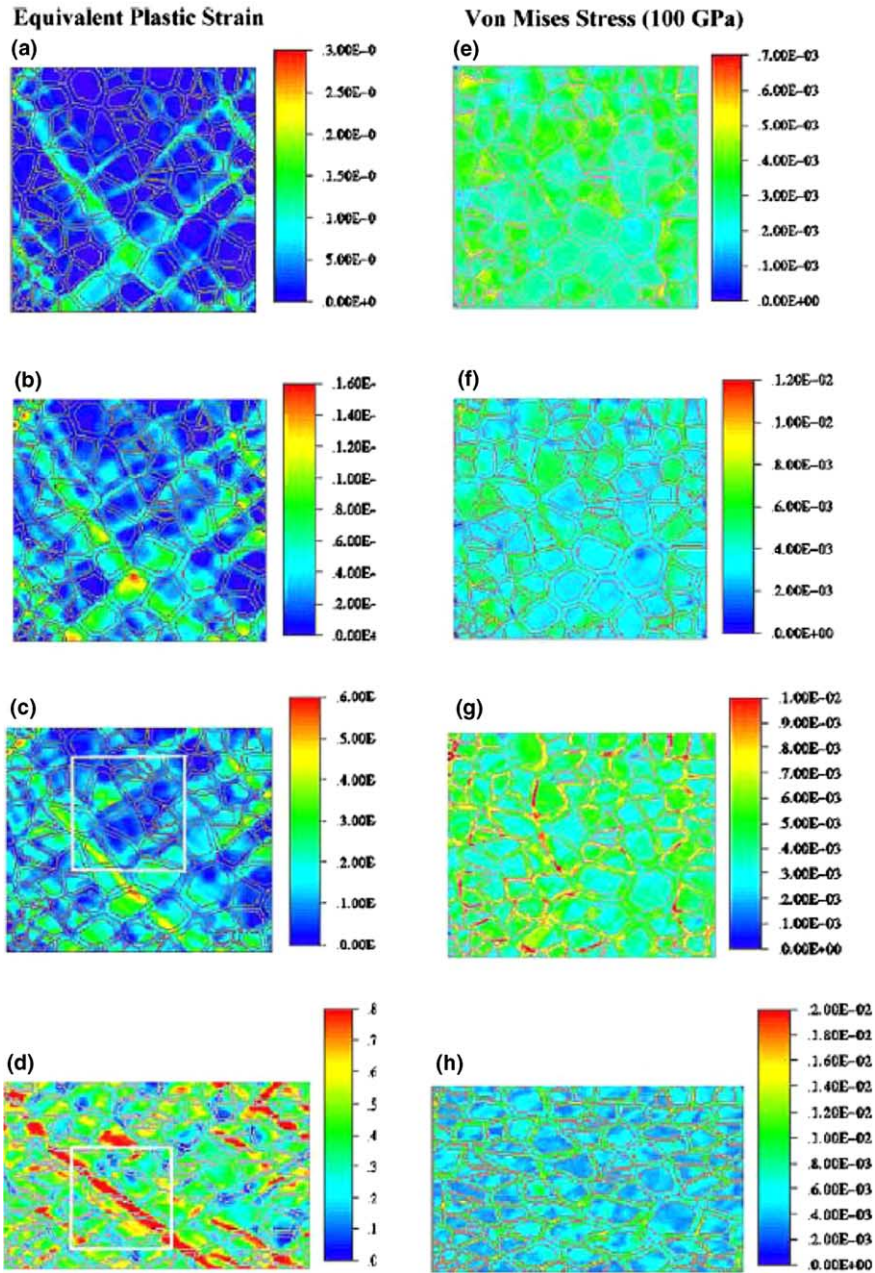


Fig. 85. Compression of polycrystalline copper ( $D = 26$  nm), left column shows equivalent strains: (a) 0.0033; (b) 0.035; (c) 0.1432; (d) 0.4141; right column (e)–(h) shows the corresponding von Mises stresses, colors describe stress and strain levels [335].

governed by the change in the orientation of the plane of maximum shear stress, with is measured by the gradient of the maximum shear stress angle. Fig. 87 shows the

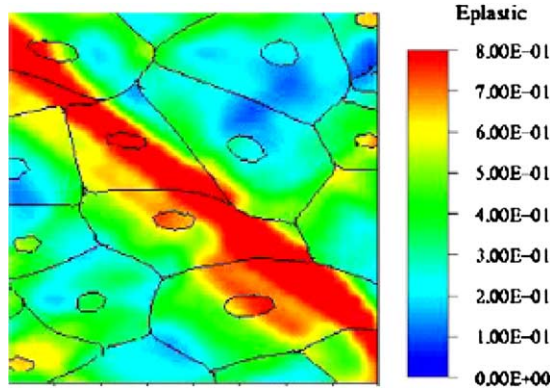


Fig. 86. Close-up showing details of plastic deformation with shear localization [335].

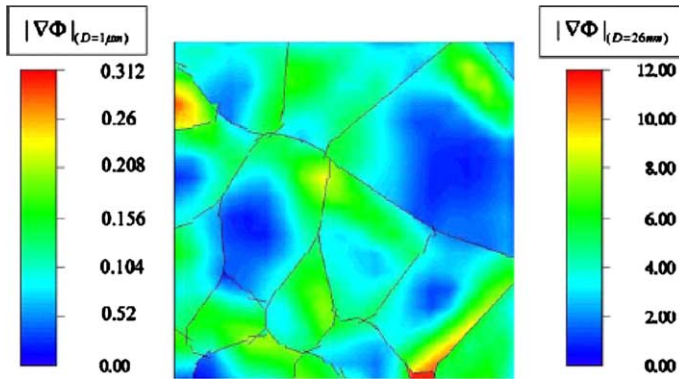


Fig. 87. Distribution of magnitude of gradient of angle of maximum shear stress throughout polycrystalline aggregate. Left hand scale:  $d = 1 \mu\text{m}$ ; right-hand scale:  $d = 26 \text{ nm}$  [335].

distribution of magnitude of gradient of angle of maximum shear stress throughout polycrystalline aggregate.

The calculations were carried out with a multi-material Eulerian finite element formulation [336]. Except at the largest strains, which were considerably larger than required to compare to experimental data, the deformations were small enough that the calculations could have been performed with a Lagrangian formulation. The computational models successfully predicted the grain size effects, but the variation in the experimental data is considerable, making it impossible to fine-tune the models. Fig. 88 shows the computed results compared to experiments for grain sizes in nanocrystal range; the experimental results fall in a wide range.

Grain boundary slip was investigated by considering the limiting cases of perfect bonding and perfect frictionless grain-boundary slip [104]. The constraint of perfect grain-boundary bonding increased the flow stress in comparison to perfect slip by approximately 200 MPa at an equivalent plastic strain 0.2, at which point both models began to behave in a nearly perfect-plastic manner.

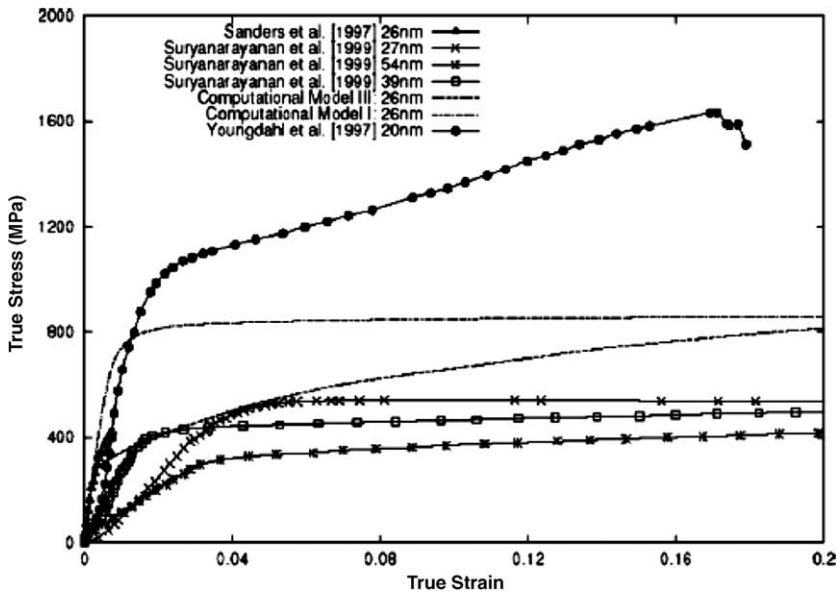


Fig. 88. Computed results compared to experiments for grain sizes in nanocrystal range [335].

## 9.2. Molecular dynamics simulations

Van Swygenhoven and her colleagues have dominated the simulation of nanocrystalline metals. One of their earliest studies [256,314,315,318,319] and Yamakov and coworkers [308,309,354,360] focused on nickel, with a mean grain size ranging from 3.4 to 12 nm with high angle grain boundaries. The orientations of the crystals were random, and the interiors of the grains were free from initial defects. Two additional realizations with a mean grain diameter of 5.2 nm and low angle grain boundaries were also simulated. Numerical relaxation was used to reduce the stresses at the grain boundaries. The samples were loaded under uniaxial tension with a stress of 1.5 GPa. The deformation mechanisms were studied by visual inspection of slices through the grains, and stress–strain curves were calculated during the simulations.

The strain rates induced by the stress were found to be proportional to  $1/d$  for grains less than 10 nm in diameter, while the strain rate in the larger grains was independent of their size. For the grains  $<10$  nm, grain-boundary slip was the dominant deformation mechanism. For the samples with low angle grain boundaries, there was intra grain slip from partial dislocations.

In an investigation of the role of the grain-boundary structure [256,314], simulations of nickel and copper with mean grain sizes ranging from 5 to 12 nm and high angle grain boundaries were performed. The models had between 100,000 and 1,200,000 atoms and used periodic boundary conditions. They differ only in their size, having the same grain shapes and initial lattice orientations. Fig. 89 shows the strain rate versus the inverse of the grain size for the Ni and Cu samples. Below grain sizes of 8 nm, they observed a negative Hall–Petch slope. Based on their calculations at these small grain sizes, they surmise that there is no damage accumulation during deformation, similar to superplasticity.

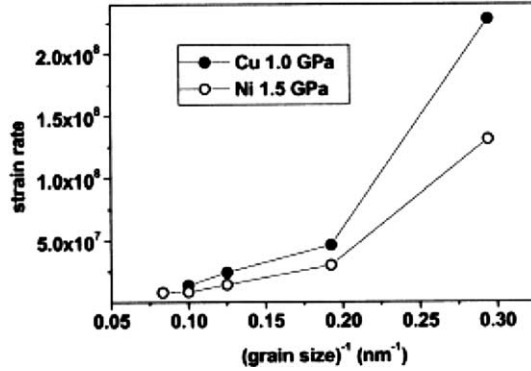


Fig. 89. Strain rate as a function of mean grain size for Cu and Ni [256].

They also concluded that the grain boundary in nanocrystalline FCC metals has similar short range structure of grain boundaries found in conventional polycrystalline materials.

Analytical modeling was combined with molecular dynamics studies of columnar structures [315] to explain why columnar structures show a  $1/d$  Hall–Petch slope. They argued that on average, a dislocation will traverse the slip plane across the entire grain, thereby defining a length scale on the order of the grain size. Fig. 90 displays the atomic configuration

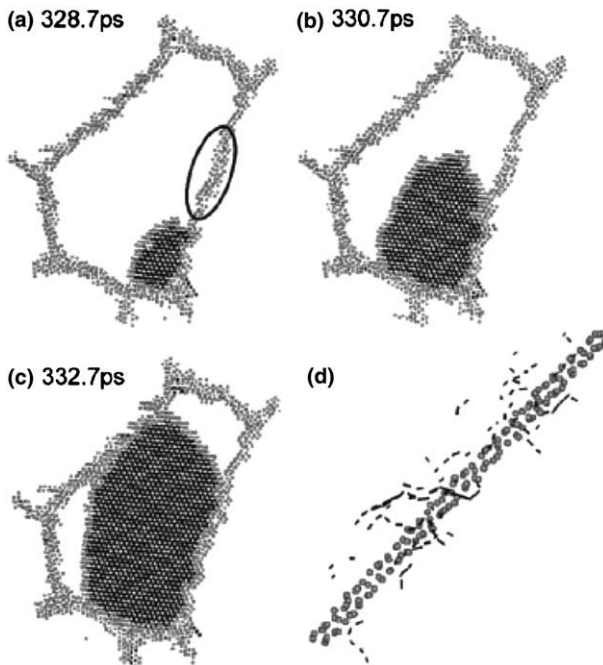


Fig. 90. Atomic configuration at different deformation times, of non-fcc atoms in a  $\{111\}$  plane of the central grain, detailing the nucleation and propagation of a partial dislocation [315].

ration at different times of deformation, of the non-fcc atoms in the  $\{111\}$  plane of the partial dislocation. In addition, they explained that the difference in the level of dislocation activity between the two-dimensional columnar grains and the three-dimensional grains is due to geometrical restrictions on the available slip systems. Fig. 91 demonstrates that with increased partial dislocation activity and thus an increased stacking fault density, dislocation locks (arrow B) become more likely. This might affect the characteristic area a dislocation sweeps in its slip plane, and thus limit the inverse  $d$  dependence on the strain rate.

An excellent summary of the limitations and general results of molecular dynamics studies is presented in Derlet et al. [318]. They comment that in their own work, they use a minimum of 15 grains, and increase the number to 125 in order to see the collective effects of grain interactions. They also remark that the grain boundaries are generally not equilibrium grain boundaries and are sensitive to how the grains are numerically synthesized. In their Voronoi-generated models, the grains are usually in compression and the grain boundaries in tension. However, there are regions of compression and tension in the grain boundaries depending on the misfit areas.

Their summary [318] of the mechanical behavior of molecular dynamics simulations indicates that the plasticity is dominated by intergrain deformation mechanisms below  $\sim 10$  nm. Only partial dislocations are observed below 30 nm. They conclude that the only meaningful information that can be extracted from MD simulations is the classification of the atomic processes occurring during the deformation.

While most of the simulations of nanocrystalline materials involve uniaxial deformations, other dynamic phenomena have been studied. For example, Samaras et al. [317] explored the formation of stacking fault tetrahedra due to irradiation. A single atom (the primary knock-on atom) is given a kinetic energy of 5–30 keV, which induces a molten region surrounding it. Heat is removed by velocity scaling. Their results, which agree

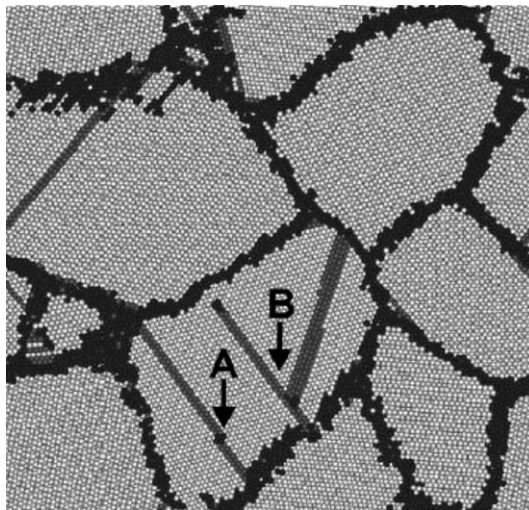


Fig. 91. A cross-section of a deformed 12 nm grain size Ni sample containing 15 grains. Light grey atoms indicate the grains, black the GB regions, and dark grey the hexagonal close-packed atoms [315].

with experiments, show that an initial kinetic energy of at least 10 keV is required for the formation of stacking fault tetrahedra in nanocrystalline nickel.

Nanoindentation is modeled by defining a moving repulsive potential [319]. The simulation contained 15 grains of gold with a mean diameter of 12 nm and the indenter had a radius of 40 Å. The indentation remained elastic to a depth of 5.4 Å, and the simulation was continued to a depth of slightly more than 25 Å. During the indentation, dislocations were nucleated and the evolution of the dislocation network was tracked. Figs. 92 and 93 provides a series of snapshots, showing the atomic structure and the stress distribution, of a section of a sample involving two different dislocations.

Imperfect polycrystalline structures have been recently studied [320]. Nanocrystalline aluminum with a mean grain diameter of 12 nm was modeled with and without grown-in twin boundaries (Fig. 94) and it was found that the rate of plastic deformation was higher for a given applied stress level for the grains with the grown-in twin boundaries due to twin migration. Fig. 95 displays the deformation curves for different Al samples at an applied uniaxial tensile stress of 1.2 GPa. The strain–time curves indicate that the presence of pre-twins in the nano sized grains facilitate plastic deformation. The orientation of twins also plays a role. They demonstrated that twinning cannot be the dominant mechanism in defect-free systems, but that in the presence of pre-twins, twin boundary migration is the dominant mechanism.

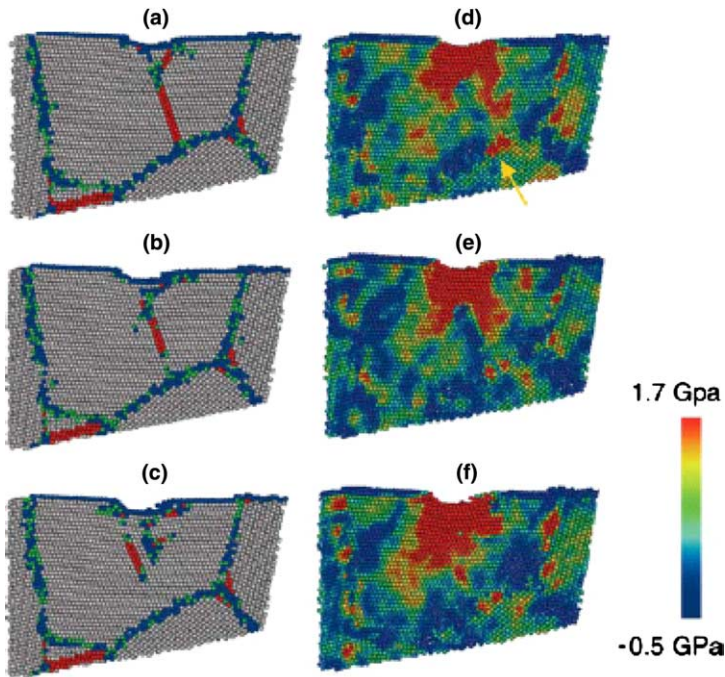


Fig. 92. A series of snapshots, showing the atomic structure and the stress distribution, of a section of the sample involving a dislocation. Figures (a)–(c) show the atomic structure of this section at indentation depths of 7.9, 8.6 and 9.6 Å [319].

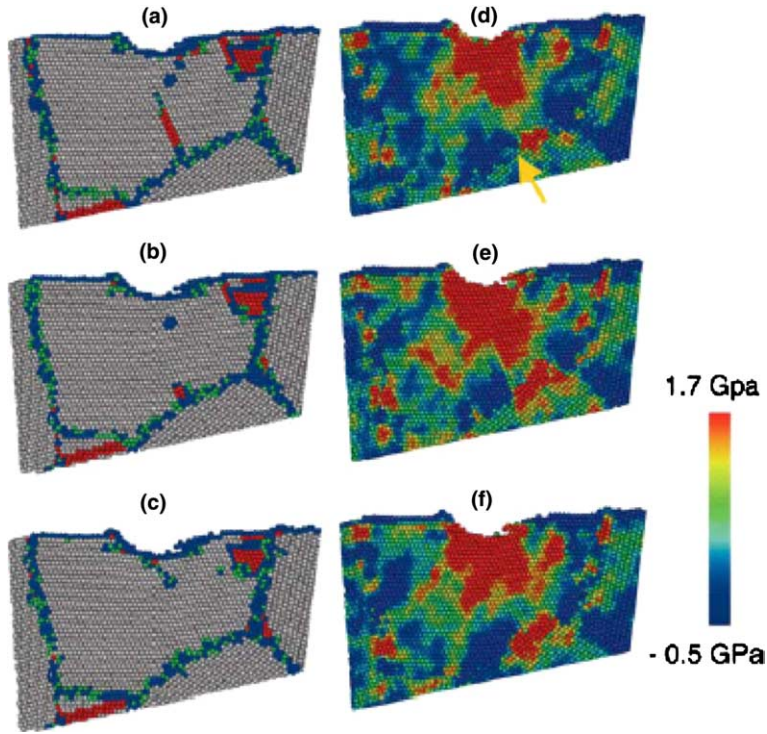


Fig. 93. A series of snapshots, showing the atomic structure and the stress distribution, of a section of the sample involving a dislocation. Figures (a)–(c) shows the atomic structure of this section at indentation depth of 11.9, 12.9 and 13.9 Å. Figures (d)–(f) show the atomic stress distribution of this section at the same indentation depths [373].

Kadau et al. [337] performed a molecular dynamics study of nanocrystalline Al undergoing tensile loading. Two different strategies were used to generate the initial microstructure. In the first, a Voronoi construction was used, giving an initial density that approached the theoretical ideal (>97%) and a grain-boundary thickness that was independent of grain size. The second method compacted individual grains under high pressure, sintered them at 600 K, released the pressure and reduced the temperature to ambient conditions, and then allowed the microstructure to relax for 45 ps. The densities using the sintering process ranged from 83% to 97% of the theoretical density.

An inverse Hall–Petch effect was found, with a linear relationship between the flow stress and the inverse of the density, leading the researchers to conclude that the deformation mechanism for small grains is related to the surface-to-volume ratio. They also report that their data scales well with  $d^{-1/2}$ , the scaling expected with the Hall–Petch effect. The difficulty in discriminating the proper exponent may be related to the relatively narrow range of grain sizes (3.15–9.46 nm). Fig. 96 shows their predicted strengths as a function of grain size.

In looking at their results for the sintered samples, they observed that the samples sintered at the higher pressures had the higher flow stresses. They also observed that the high pressure sintered sample had a higher flow stress than the equivalent Voronoi

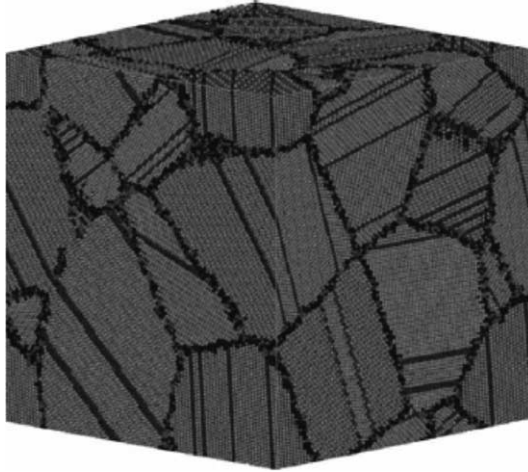


Fig. 94. The twinned nc-Al sample with an average grain diameter of 12 nm [320].

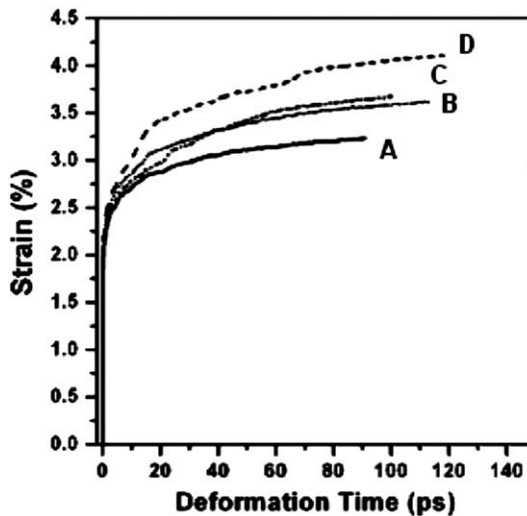


Fig. 95. Deformation curves for the 12-nm grain size nc samples, (A) Al with defect-free grains; (B) Al samples with pre-twin boundaries are rotated into another  $\{111\}$  family of planes; (C) Al sample with twins/grain reduced to two and (D) Al sample with twin boundaries, at an applied uniaxial tensile stress of 1.2 GPa [320].

microstructure, leading them to speculate that the sintering process produced more mechanically stable grain boundaries than the Voronoi construction. The sintered samples with the highest porosity exhibited more pronounced void growth and less grain-boundary sliding than the higher density samples. Fracture in the low density samples initiated at the voids and then propagated along the grain boundaries.

The more recent MD computations by Froseth et al. [338] depict the emission of individual partial dislocations from the grain boundary. The enhanced partial separation is



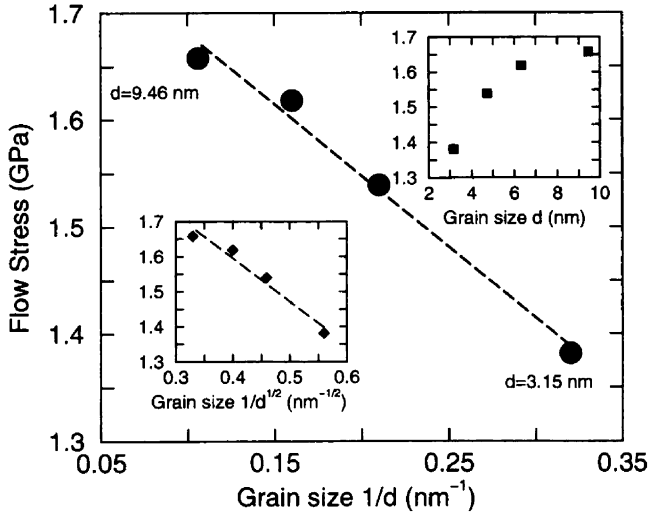


Fig. 96. Negative Hall–Petch slope computed by Kadau et al. using molecular dynamics for aluminum [337].

discussed in Section 7.8. Using the equations from Hirth and Lothe [347], they describe the partial dislocation separation for a screw dislocation aligned with [110] as:

$$s = \frac{(2 - 3\nu)Gb_1^2}{8\pi(1 - \nu)(\gamma - \frac{\nu b}{2})} \tag{67}$$

$b_1$  is the Burgers vector of the partial dislocation. The symbols are the same ones defined in Section 7.8. It can be seen that the separation,  $s$ , is dependent on the applied stress. For an edge dislocation, the separation is independent on the stress:

$$s = \frac{(2 + \nu)Gb_1^2}{8\pi(1 - \nu)\gamma} \tag{68}$$

For a screw dislocation, the partial spacing tends to infinity when:

$$\tau = \frac{2\gamma}{b_1} \tag{69}$$

The stacking fault energy for aluminum being approximately 150 mJ/m<sup>2</sup>, the stress corresponding to this critical event is approximately 1.7 GPa.

A depiction of the MD simulations by Froseth et al. [338] is shown in Fig. 97. The applied stress is 1.6 GPa and the aluminum grain size is a 12 nm. In (a) a partial dislocation has been emitted from the lower left hand corner of the grain. A second partial is emitted in (b) and the dark atoms represent the faulted region. The partials move through the grain (Fig. 97(c)) and eventually are absorbed into the upper boundary. Froseth et al. [338] discuss the spacing of partials and comment on the fact that is not uniform along the dislocation line.

### 9.3. The quasicontinuum method

This method, developed by Tadmor et al. [339,340], consists of having a central core, where the critical phenomena occur, in which MD is implemented. This central core is

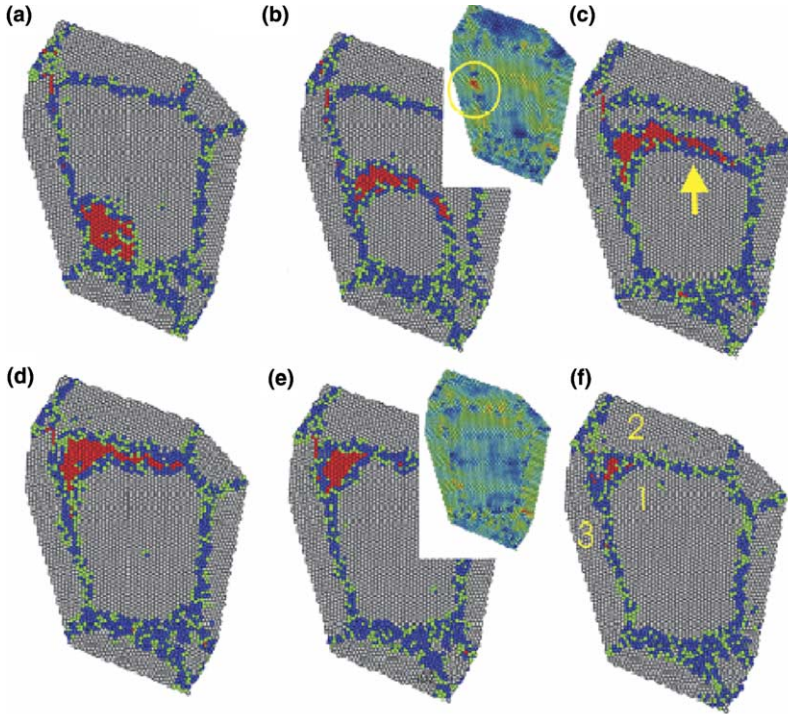


Fig. 97. MD sequence showing the formation of partial dislocation and its expansion throughout grain; notice trailing partial that recomposes perfect lattice (b,c). Red atoms are between partials (Frøseth AG, Derlet PM, Van Swygenhoven H. *Acta Mater* 2004;52:5870).

surrounded by the material modeled by FEM. In essence, it is a hybrid between MD and FEM. An example of how the QC method can be used to reveal details of dislocation generation at grain boundaries is shown in Fig. 98(a). A  $\Sigma 9$  coincidence lattice (CSL) boundary subjected to shear is modeled by Sansoz and Molinari [341]. By allowing atom shuffling the shear stress at which plastic deformation occurs along the grain boundary is decreased from 5.5 GPa to 1.5 GPa. Fig. 98(b) shows the corresponding atomic position for the atoms in the three regimes I, II, and III. The  $\Sigma 9$  boundary is horizontal and runs through the middle of the simulations. Atoms with perfect FCC lattice positions are dark, while GB atoms, atoms in stacking faults are light. In Regime I, nothing happens, since the stress is below the 5.5 GPa level. In Regime II, activity of atoms indicating shuffling is seen at the grain boundary, through the increased number of light atoms. The emission of stacking faults from boundaries is shown in Regime III.

#### 9.4. Shock wave propagation in nanocrystalline metals

Atomistic simulations of shock wave propagation in nanocrystals were carried out by Bringa et al. [342]. The calculations demonstrate that the width of the wave is a function of grain size, pressure, and time. It is interesting that Meyers [343] and Meyers and Carvalho [344] had calculated analytically the width of the shock front for polycrystalline

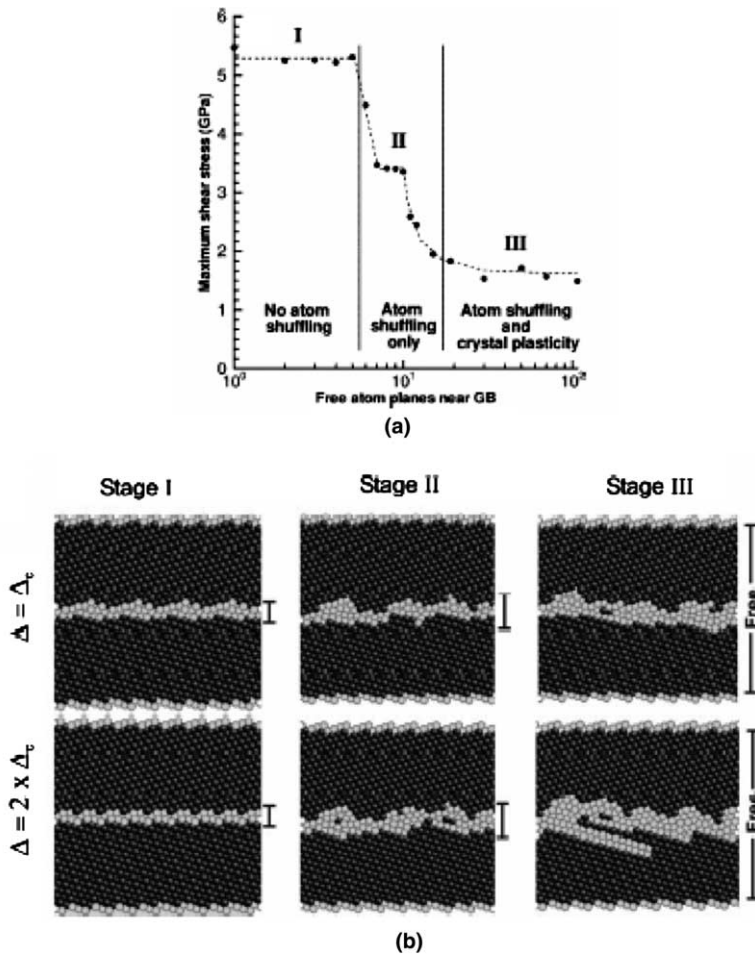


Fig. 98. Quasicontinuum modeling of shear along  $\Sigma 9$  CSL grain boundary in copper: (a) different regimes, assuming increasing (from I to III) number of atomic layers free to move and (b) grain-boundary activity (indicated by light atoms) for the three regimes, at two levels of displacement:  $\Delta_c$  and  $2\Delta_c$  [341].

copper and compared their results with measurements by Jones and Holland [364]. The atomistic calculations match the analytical calculations of Meyers [343] and Meyers and Carvalho [344], which, in turn, agreed with measurements of Jones and Holland [364] in the microcrystalline regime, as shown in Fig. 99.

The MD simulations reveal the details of the propagation of a shock wave through the nanocrystalline metal. Fig. 100 shows snapshots at two different times. The simulations suggest that the effect of grain boundary in the width of the wave front is small compared to the effect of anisotropy from crystal to crystal. This is the reason why the continuum model by Meyers [343] was able to predict the front dispersion due to polycrystallinity. The dispersion of the wave calculated by MD, represented by the shock front width  $\Delta Z$ , normalized to the grain size, versus grain size, at three pressure levels: 22, 34, and 47 GPa is shown in Fig. 101. It shows that the shock front thickness decreases with

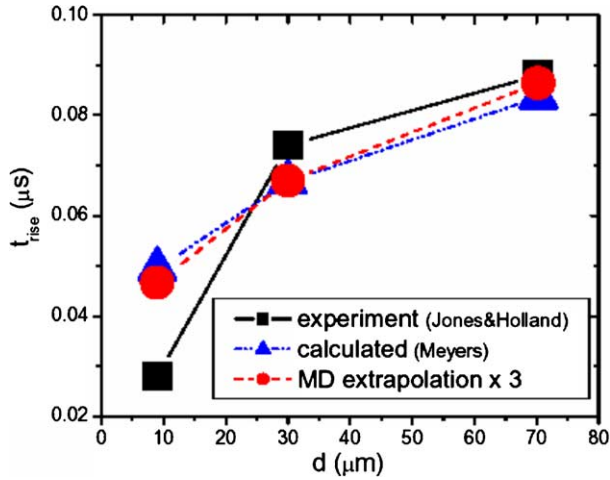


Fig. 99. Experimentally measured (Jones and Holland), analytically calculated (Meyers) and MD prediction of rise time of shock wave in copper in conventional grain size domain [342].

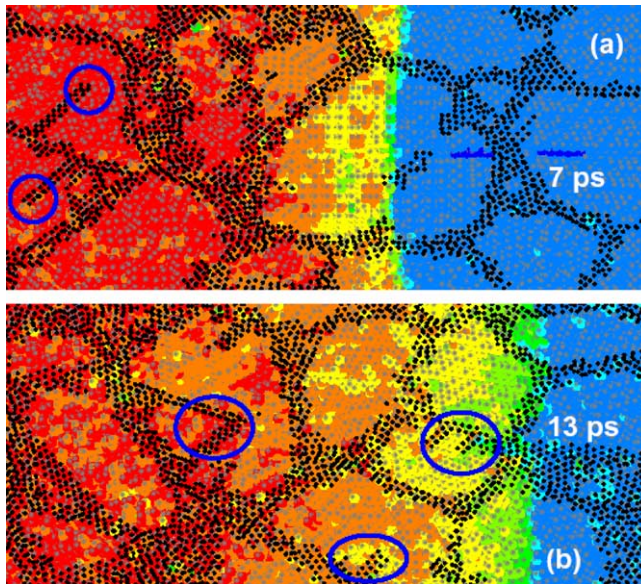


Fig. 100. MD simulation showing wave front at two different times. Grain boundary atoms are shown as small black dots.  $d=5$  nm,  $P = 22$  GPa,  $U_p = 0.5$  km/s and strain = 10%. Atoms are colored according to their kinetic energy (red, high-moving at  $U_p$ ; blue, low-unshocked). The upper frame shows a sharp front inside the grains, with some refraction due to orientation. Note that the energy levels track the GB, and that in frame (b) the front itself tracks the shape of one of the grains. Some of the stacking faults generated by the wave (emitted from grain boundaries) are marked with blue circles [342].

decreasing grain size (although the ratio increases) and with increasing pressure. These simulations lead to a better understanding of the physics governing shock width. One

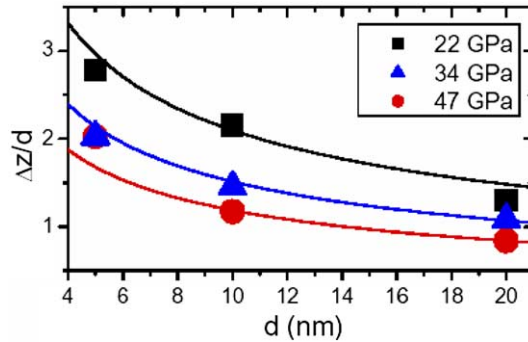


Fig. 101. Shock front width  $\Delta Z$  calculated by MD, normalized to the grain size, versus grain size, at three pressure levels: 22, 34, and 47 GPa and pressure (from [342]).

of the possible applications of nanocrystalline metals, due to the greater sharpness of the shock front propitiated by the small grain size is as targets in the National Ignition Facility (NIF) at Lawrence Livermore National Laboratory. The nanocrystalline grain size would ensure that the fluctuations in the shock front remain small, decreasing the probability for unwelcome instabilities.

## 10. Summary and conclusions

This article reviews the mechanical properties of nanocrystalline materials, with emphasis on the fundamental physical mechanisms responsible for the specific behaviors. It is now well established that nanocrystalline materials exhibit a high strength, albeit not as high as the extrapolated Hall–Petch prediction from the conventional regime of grain sizes (10–300  $\mu\text{m}$ ). Concomitantly, they tend to exhibit much reduced ductility, due in part to a low work hardening rate leading to early strain localization and failure. However, there are situations where the ductility is surprisingly high and efforts at engineering the nanostructure are under way. Given below is a summary of the main conclusions at which one can arrive by reviewing the extensive literature that continues to be published.

- (a) *Synthesis/processing*: The synthesis method has a deep effect on the mechanical properties of nanocrystalline and ultrafine grained materials. The synthesis methods based on powder densification tend to yield voids and imperfectly bonded boundaries. This, in turn, has a profound effect on mechanical properties, decreasing the elastic constants, strength, and ductility. New techniques that are evolving and present a bright potential include pulse powder deposition and severe plastic deformation. The pulsed electrodeposition method can produce a high density of growth twins which have been found responsible for a significant enhancement of ductility. Other synthesis methods, such as severe plastic deformation, lead to an ultrafine grain size and, in extreme cases, to nanocrystalline grain size without internal voids. Equal Channel Angular Pressing (ECAP) is the most often used of these techniques. However, it can only most often produce ultrafine grains, on the order of 100 nm or higher.

- (b) *Grain-boundary structure*: There is no evidence that the grain boundaries in nanostructured materials are significantly different from the ones in conventional polycrystals. Early reports of an “amorphous” layer of considerable thickness have not been confirmed and could be due to incomplete densification. So, one can assume safely a boundary a few atomic distances thick. However, it is safe to assume that the number of grain-boundary ledges is reduced because of the size. The reorientation/rotation of the nanosized boundaries is also significantly enhanced in comparison with conventional boundaries.
- (c) *Yield stress*: The yield strength of nanocrystalline materials has been measured and there is a consensus that the H–P relationship breaks down with a decrease in slope in the 1  $\mu\text{m}$ –100 nm range. There are scattered reports of a plateau or a negative slope in the H–P relationship for grains <20 nm.
- (d) *Ductility*: Nanocrystalline metals are characterized by a low work-hardening rate, which is a direct consequence of the low density of dislocations encountered after plastic deformation. This low work hardening rate leads to tensile instability and a low tensile ductility. There are reports of increased ductility in nanocrystalline metals, induced by the presence of a large density of growth twins in the structure.
- (e) *Strain rate sensitivity*: There are conflicting results in the literature. Whereas some experiments (up to  $\dot{\epsilon} \sim 10^4 \text{ s}^{-1}$ ) report normal strain rate sensitivity, others report an enhanced value. This enhanced strain rate sensitivity in FCC metals for grain sizes <100 nm is indicative of a change in deformation mechanism. Indeed, the strain rate sensitivity,  $m$ , is related to the activation volume,  $V$ , through (e.g., [345,346])

$$V = bA = BkT \left( \frac{\partial \ln \dot{\gamma} / \dot{\gamma}_0}{\partial \tau} \right)_T = \frac{BkT}{m\tau_0} \quad (70)$$

where  $A$  is the activation area,  $\dot{\gamma} / \dot{\gamma}_0$  is a normalized shear strain rate, and  $B$  is a parameter has been variously quoted as equal to 1 (e.g., [345]) or 3/2 [85]. An increase in  $m$ , results in a decrease in  $V$ . Fig. 102 shows a plot of  $V$  as a function of grain size for copper and nickel [328]. It is clear that there is a significant decrease

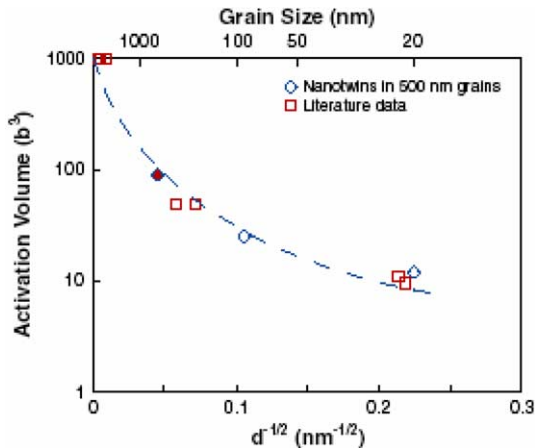


Fig. 102. Plot of the effect of grain size on the activation volume, measured in units of  $b^3$  for pure Cu and Ni from literature [328].

in  $V$  in the nanocrystalline domain. Indeed, Conrad quotes the following experimental value for  $V$  for copper with grain size in the 10 nm range:

$$V = 1.2b^3$$

The prediction from Fig. 102 is around  $10b^3$ . The decreased activation area (or volume) is a direct consequence of the reduced dislocation interaction (for FCC metals) when the principal rate controlling mechanism in plastic deformation changes from work hardening through dislocation forest intersection for conventional polycrystals (with characteristic activation volumes off  $10^3b^3$ ), to other mechanisms with a much reduced  $V$ . The most probable are:

- Kink pair movement
- Peierls–Nabarro barriers
- Dislocation-boundary interactions
- Grain-boundary shear (this is the mechanism chosen by Conrad [85]).

For the BCC structure this change in strain-rate sensitivity is not observed in the nanocrystalline regime. For instance, for iron with  $d = 20 \mu\text{m}$ ,  $m = 0.08$ ; when  $d$  is reduced to 80 nm,  $m = 0.09$  [121]. Thus, the same rate controlling mechanism is thought to operate at the two grain sizes.

- (f) *Creep*: There are several studies in the literature, reporting a decrease in creep resistance by virtue of Coble creep in which the creep rate is proportional to  $d^{-3}$ . Nevertheless, conflicting results report a creep resistance much higher than the Coble prediction. This could be due to the contamination of the grain boundaries with impurities, which act as “brakes” to grain-boundary sliding.
- (g) *Fatigue*: The  $S$ – $N$  (Wöhler) response of nanocrystalline metals to cyclic loading is superior to that of their conventional grain-sized counterparts, principally by virtue of the increased yield stress. In contrast to results of the cyclic behavior of uncracked specimens through  $S$ – $N$  response, the fracture mechanics studies report a faster  $da/dN$  crack growth velocities in cyclic loading for nanocrystalline metals. This has been attributed to the finer fracture scale, which propitiates a smoother path for crack propagation.
- (h) *Mechanisms of plastic deformation*: A number of mechanisms have been proposed:
- Pile-up breakdown
  - Grain-boundary sliding
  - Core and mantle model
  - Grain boundary dislocation creation and annihilation
  - Grain-boundary rotation
  - Shear band formation
  - Gradient model
  - Mechanical twinning

Although all these mechanisms may play a role under specific internal (grain size, composition, etc.) or external (temperature, strain rate, stress state), a few seem dominant in the nanocrystalline regime. These major mechanisms are discussed below. We divide the grain sizes into three domains:

$1 \mu\text{m} > d > 100 \text{ nm}$ : This grain size is being commonly referred as ‘ultrafine grain size.’ A core-and-mantle model seems to describe the response well. The models

are based on dislocation generation at or adjacent to grain boundaries and on the formation of work-hardened grain boundary layers. As Li [259] proposed in 1963, the existence of grain-boundary ledges with spacing of 10–100 nm provides an ample supply of “starter” dislocations that, upon emission into the grains, cross-slip and multiply, creating a work hardened layer close to the grain boundaries. As the grain size is reduced, the ratio between volume fractions of the “mantle” and “core” increases, providing an increase in yield stress that can be expressed as a power equation  $d^{-n}$ , where  $n$  usually takes a value around at 1/2 for grain sizes  $>1 \mu\text{m}$  and  $n \leq 1/2$  in the region  $1 \mu\text{m} > d > 100 \text{ nm}$ .

$100 \text{ nm} > d > 20 \text{ nm}$ : In this region, the H–P slope gradually decreases with decreasing  $d$ . The grain-boundary ledges can no longer supply dislocations in this regime because their spacing ( $l < 30b$ ) becomes large with respect to the grain size. The dislocations emitted from grain boundaries encounter less and less chances of cross-slipping and multiplying in grains. Dislocations generated at grain boundaries can, in the lower limit of this size range, travel through the grains relatively unimpeded and annihilate in the opposing boundary. This can be carried out without significant work hardening, since the density remains constant. This leads to shear localization.

$20 \text{ nm} > d > 1 \text{ nm}$ : In this regime, the grain-boundary effects dominate the deformation process. The separation between partial dislocations in FCC metals increases, as will be explained below. There is, in connection with the increased tendency for partial dislocation emission from grain boundaries, a greater ease for mechanical twinning. Grain-boundary sliding becomes important in this regime and has been identified by Conrad [85] and other researchers as the principal mechanism. The controversial negative Hall–Petch slope has been attributed to the dominance of

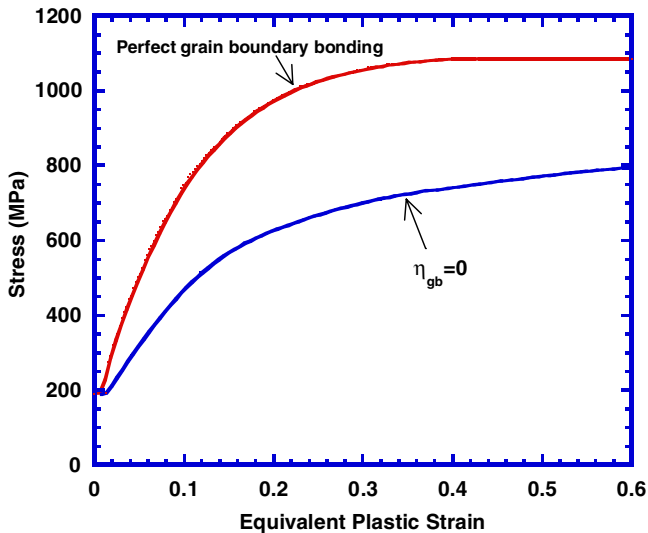


Fig. 103. Computed mechanical response of nanocrystalline copper ( $d = 20 \text{ nm}$ ) assuming that grain boundaries have zero viscosity; the strength is still 2/3 of that of the equivalent material with perfect grain boundaries, proving that grain-boundary sliding can only be responsible for a fraction of plastic strain and that plastic deformation *within* grains has to be the dominant mechanism [103].



grain-boundary sliding. However, grain-boundary sliding cannot occur by itself and needs associated plastic deformation. This is eloquently demonstrated by the computer calculations of Fu et al. [335] and shown in Fig. 103. The grain-boundary shear strength was completely eliminated for one of the simulations, effectively creating a grain-boundary layer with zero viscosity. One would expect, at first, that the materials strength (in this case copper with a grain size of 20 nm) would drop to zero. This is not the case and the nanocrystalline copper retains approximately 2/3 of its original mechanical response. This is also discussed in Section 7.2, where a coupled plastic deformation process is calculated. Hence, one concludes that grain-boundary sliding can contribute, at most, one-third of the plastic strain, under the most favorable conditions.

$1 \text{ nm} > d > 0 \text{ nm}$ : Effectively, we move gradually from a nanocrystalline to an amorphous state, whose deformation is dominated by regions of intense shear.

- (i) *The role of stacking faults and twinning*: The surprising discovery of deformation twins in nanocrystalline aluminum by Ma et al. [310] has initiated a new cycle of study within this domain. Aluminum is a high stacking fault metal ( $\gamma = 166 \text{ mJ/m}^2$ ) and previous attempts (low temperature deformation, shock compression) had failed to yield mechanical twinning. Indeed, the current knowledge of mechanical twinning (e.g., [348]) predicts exactly the opposite; reduction of grain size makes twinning more difficult. This discovery, coupled with MD simulations showing profuse partial dislocation emission from grain boundaries, led to analyses [325,326] that predict an increased separation of partials at the high stress levels at which nanocrystalline FCC metals flow plastically. There seems to be clear indications that there is a threshold grain size at which perfect dislocations decompose into partials. Fig. 104 shows the calculations by Zhu et al. [312] for aluminum. Three stresses are

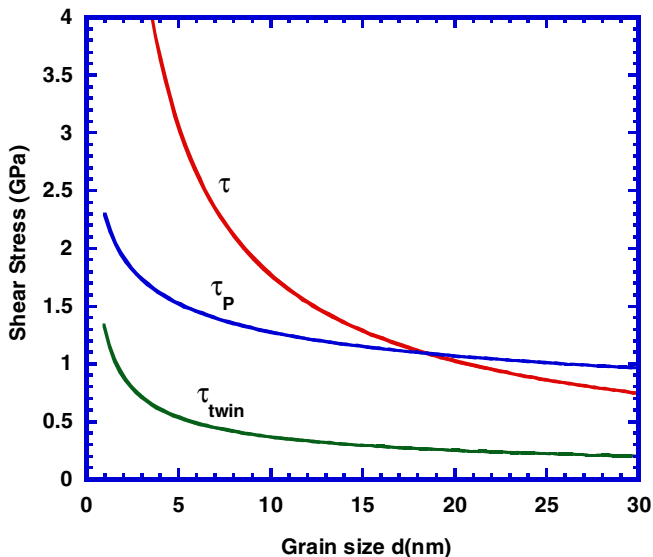


Fig. 104. Stresses required for emission of perfect dislocation ( $\tau$ ), partial dislocation ( $\tau_p$ ), and twinning ( $\tau_{\text{twin}}$ ) as a function of grain size in the nanocrystalline regime for aluminum, assuming a value of  $\alpha = 135^\circ$  [312].

plotted against  $d$ :  $\tau$ , the stress required to move a perfect dislocation;  $\tau_p$ , the stress required to move partials; and  $\tau_{\text{twin}}$ , the stress required to emit a twin from boundary. For the specific angle between the shear stress and dislocation line ( $=135^\circ$ ), the stress for partials becomes smaller than the stress for perfect dislocations for  $d \leq 17$  nm. This analysis is based on the equations presented in Section 7.8. The twinning stress  $\tau_{\text{twin}}$  is lower than both  $\tau$  and  $\tau_p$ . This is because it is easier to emit a second partial dislocation from a boundary adjacent and at a twin separation from the first partial. Thus, once a partial is emitted, conditions become ripe for twinning. The mechanical twins observed and modeled (by MD) in nanocrystalline metals are only a few atomic layers thick and therefore only require a few partial dislocations gliding on parallel planes. Thus, the critical event for deformation twinning is the separation between partials.

- (j) *Fracture*: It is generally assumed that the ductile fracture of nanocrystalline FCC metals reveals a predominance of dimples with a scale that is severely reduced in comparison with conventional polycrystals. Nevertheless, the dimple size is several times the grain size indicating initiation at discrete sites that are, most often, triple junctions and grain boundaries [331]. Recent observations also reveal regions of dimples intercalated with shear steps in nanocrystalline Ni. Shear localization is a significant failure mechanism.
- (k) *Ceramics*: A large number of nanocrystalline ceramics have been synthesized. One limitation in ceramics is the difficulty in densification. Large pressures and high temperatures are required and this can lead to grain growth. Nevertheless, ceramic nanocomposites have been successfully densified. One of the principal advantages of nanocrystalline ceramics over their conventional counterparts is the possibility of superplasticity at much higher strain rates, rendering the process of superplasticity more realistic.
- (l) *Computer simulations*: Essentially two approaches have been implemented. Continuum modeling (FEM) and molecular dynamics (MD). A third level of modeling, intermediate between these two, is dislocation dynamics (DD). There is also a hybrid between MD and FEM, called the quasicontinuum method. The most important and significant results have been obtained by MD and are, indeed, leading our knowledge. The prediction of increased partial dislocation spacing, of dislocation generation and annihilation at grain boundaries are of special significance. A limitation of this technique is that the deformation times ( $\sim 10^{-9}$  s) are lower by many magnitudes than actual times at conventional strain rates (a few seconds to a few minutes). Nevertheless, the predictions from MD are leading our understanding of nanocrystalline materials. Indeed, this technique is ideally suited for the study of nanocrystalline metals because volumes as large as  $1 \mu\text{m}^3$  can be ‘tested.’ For conventional polycrystals, such a volume would not be representative of the material but for a nanocrystalline metal with a grain size of 50 nm, the simulation incorporates  $10^4$  grains.

## Acknowledgements

Support by the National Science Foundation under the Grants DMI-9612017 and CMS-0210173 (NIRT) is acknowledged. Discussions and collaborations with R.J. Asaro, B.K. Kad, M.E. Kassner, and G. Thomas are gratefully appreciated. Graduate students

Florence Tu, Hussam Jarmakani, and Buyang Cao provided valuable help in manuscript preparation. Prof. R.W. Armstrong reviewed the early manuscript and provided valuable criticism. We also present our sincere gratitude to Professor T.B. Massalski and the anonymous referees who guided us patiently through several versions of this manuscript and contributed to its clarity and comprehensiveness. Dr. E. Bringa kindly shared with us the results of his MD simulations on shock-front thickness before they were published and we used some of their results; he also provided us with a nanocrystalline Ni specimen that was used in the fractographic analysis.

## References

- [1] Gleiter H. Nanocrystalline materials. *Prog Mater Sci* 1989;33:223–315.
- [2] Gleiter H. In: Proceedings of the 9th IVC-V, Madrid, Spain; 1983. p. 397.
- [3] Suryanarayana C. Nanocrystalline materials. *Intl Mat R* 1995;40:41–64.
- [4] Cohen JB. *Metall Trans A—Phys Metall Mater Sci* 1992;23:2685–97.
- [5] Artz E. *Acta Mater* 1998;46:5611.
- [6] Birringer R. *Mater Sci Eng A* 1989;117:33.
- [7] Hall EO. *Proc Phys Soc B* 1951;64:747.
- [8] Petch NJ. *J Iron Steel Inst* 1953;174:25.
- [9] Ashby MF. *Philos Mag A* 1982;46:737.
- [10] Wurschum R, Herth S, Brossmann U. *Adv Eng Mater* 2003;5:365–72.
- [11] Andres RP, Averbach RS, Brown WL, Brus LE, Goddard III WA, Kaldor SG, et al. *Mater Res* 1989; 4: 704.
- [12] Mehl RF, Cahn RW. Historical development. Physical metallurgy. North Holland; 1983.
- [13] Koch C. Bulk behavior of nanostructured materials. In: Siegel RW, Hu E, Roco MC, editors. Nanostructure science and technology, a worldwide study. Final Report by WTEC Panel 1999; p. 93.
- [14] Embury JD, Fisher RM. *Acta Metall* 1966;14:147.
- [15] Armstrong RW, Chou YT, Fisher RM, Louat N. *Philos Mag* 1966;14:943.
- [16] Langford G, Cohen M. *Trans ASM* 1969;62:623.
- [17] Rack HJ, Cohen M. Influence of recovery on the tensile behavior of highly-strained iron alloys. In: Murr LE, Stein C, editors. *Fron Mat Sci* 1976:365.
- [18] Schladitz HJ. *Z Metallkd* 1968;59:18.
- [19] Lashmore DS, Jesser WA, Schladitz DM, Schladitz HJ, Wilsdorf HGF. *J Appl Phys* 1977;48:478.
- [20] Gleiter H. Materials with ultrafine grain size. In: Hansen N, editor. Deformation of polycrystals: mechanisms and microstructures. Roskilde: Risø National Laboratory 1981; p. 15.
- [21] Siegel RW. Mechanical properties and deformation behavior of materials having ultrafine microstructures. In: Nastasi M, Parkin DM, Gleiter H, editors; 1993. p. 509.
- [22] Gleiter H. *Acta Mater* 2000;48:1–29.
- [23] Niemann GW, Weertman JR, Siegel RW. *Scripta Metall Mater* 1990;24:145.
- [24] Niemann GW, Weertman JW, Siegel RD. *Mater Res Soc Symp Proc* 1991;206:493.
- [25] Niemann GW, Weertman JR, Siegel RW. *Nanostruct Mater* 1992;1:185.
- [26] Sanders PG, Weertman JR, Barker JG. *J Mater Res* 1996;11:3110.
- [27] Youngdahl J, Sanders PG, Eastman JA, Weertman JR. *Scripta Mat* 1997;37:809.
- [28] Suryanarayana C. *Prog Mater Sci* 2001;46:1–184.
- [29] Fecht HJ, Hellstern E, Fu Z, Johnson WL. *Metall Trans A* 1990;21:2333.
- [30] Eckert J, Holzer JC, Krill III CE, Johnson WL. *J Mater Res* 1992;7:1751.
- [31] Fecht HJ. Nanophase materials. In: Hadjipanayis GC, Siegel RW, editors. vol. 260; 1994. p. 125.
- [32] Perez RJ, Hunag B, Lavernia EJ. *Nanostruct Mater* 1996;7:565.
- [33] Lau ML, Jiang HG, Perez RJ, Juarez-Islas J, Lavernia EJ. *Nanostruct Mater* 1996;7:847.
- [34] Huang B, Perez RJ, Lavernia EJ. *Mater Sci Eng A* 1998;255:124.
- [35] Park YS, Chung KH, Kim NJ, Lavernia EJ. *Mater Sci Eng A* 2004;374:211.
- [36] Erb U. *Nanostruct Mater* 1995;6:533–8.
- [37] Shen YF, Lu L, Lu QH, Jin ZH, Lu K. *Scripta Mater* 2005;52:989.
- [38] Lu L, Shwaiger R, Shan ZW, Dao M, Lu K, Suresh S. *Acta Mater* 2005;53:2169.

- [39] Lu K. *Mater Sci Eng* 1996;R16:161–221.
- [40] Liebermann HH. Amorphous metallic alloys. In: Luborsky, FE, editor; 1988. p. 26.
- [41] Lu K, Wang JT, Wei WD. *J Appl Phys* 1991;69:522.
- [42] Tong HY, Wang JT, Ding BZ, Jiang HG, Lu KJ. *Non-Cryst Sol* 1992;150:444.
- [43] Liu XD, Wang JT, Ding BZ. *Scripta Metall Mater* 1993;28:59.
- [44] Nicolaus MM, Sinning HR, Haessner F. *Mater Sci Eng A* 1992;150:101.
- [45] Scott MG. Amorphous metallic alloys. In: Luborsky FE; 1988. p. 144.
- [46] Azam N, Lenaour L, Rivera S, Grosjean P, Sacovy P, Delaplace J. *J Nucl Mater* 1979;83:298.
- [47] Iwahashi Y, Wang JT, Horita Z, Nemoto M, Langdon TG. *Scripta Mater* 1996;35:143–6.
- [48] Furukawa M, Berbon PB, Horita Z, Nemoto M, Tsenev NK, Valiev RZ, et al. Production of ultrafine-grained metallic materials using an intense plastic straining technique. *Towards Innovat Superplast I* 1997; 233:177–84.
- [49] Berbon PB, Tsenev NK, Valiev RZ, Furukawa M, Horita Z, Nemoto M, et al. *Metall Mater Trans—Phys Metall Mater Sci A* 1998;29:2237–43.
- [50] Furukawa M, Horita Z, Langdon TG. *Adv Eng Mater* 2001;3:121–5.
- [51] Alexandrov IV, Zhu YT, Lowe TC, Valiev RZ. *Powder Metall* 1998;41:11–3.
- [52] Alexandrov IV, Valiev RZ. *Scripta Mater* 2001;44:1605–8.
- [53] Lowe TC, Valiev RZ. *J Mineral Met Mater Soc* 2000;52:27–8.
- [54] Valiev RZ. *Ann Chim—Sci Mater* 1996;21:369–78.
- [55] Valiev RZ, Alexandrov IV. *Nanostruct Mater* 1999;12:35–40.
- [56] Valiev RZ, Islamgaliev RK, Alexandrov IV. *Prog Mater Sci* 2000;45:103–89.
- [57] Valiev RZ, Aleksandrov IV. *Phys Met Metall* 2002;94:S4–S10.
- [58] Valiev RZ, Korznikov AV, Alexandrov IV. *Ann Chim—Sci Mater* 2002;27:1–2.
- [59] Valiev RZ, Alexandrov IV. *Ann Chim—Sci Mater* 2002;27:3–14.
- [60] Valiev RZ. *Thermec* 2003;426(4):237–44.
- [61] Agnew SR, Elliott BR, Youngdahl CJ, Hemkar KJ, Weertman JR. *Mater Sci Eng A—Struct Mater Properties Microstruct Process* 2000;285:391–6.
- [62] Sanders PG, Youngdahl CJ, Weertman JR. *Mater Sci Eng A—Struct Mater Properties Microstruct Process* 1997;234:77–82.
- [63] Iwahashi Y, Horita Z, Nemoto M, Langdon TG. *Acta Mater* 1998;46:3317–31.
- [64] Nemoto M, Horita Z, Furukawa M, Langdon TG. *Met Mater Intl* 1998;4:1181–90.
- [65] Langdon TG, Furukawa M, Nemoto M, Horita Z. *J Miner Metals Mater Soc* 2000;52:30–3.
- [66] Furukawa M, Horita Z, Nemoto M, Langdon TG. *J Mater Sci* 2001;36:2835–43.
- [67] Horita Z, Fujinami T, Langdon TG. *Mater Sci Eng A—Struct Mater Properties Microstruct Process* 2001;318:34–41.
- [68] Horita Z, Lee S, Ota S, Neishi K, Langdon TG. *Superplast Adv Mater, Icsam-2000* 2001;357:471–6.
- [69] Furukawa M, Horita Z, Nemoto M, Valiev RZ, Langdon TG. *Mater Characteriz* 1996;37:277–83.
- [70] Zhilyaev AP, Nurislamova GV, Kim BK, Baro MD, Szpunar JA, Langdon TG. *Acta Mater* 2003;51: 753–65.
- [71] Zhilyaev AP, Lee S, Nurislamova GV, Valiev RZ, Langdon TG. *Scripta Mater* 2001;44:2753–8.
- [72] Sanders PG, Eastman JA, Weertman JR. *Acta Mater* 1997;45:4019.
- [73] Wachtman JB. In: Wachtman JB, editor. *Mechanical and thermal properties of ceramics*. NBS Washington: NBS Special Publication; 1963. p. 139.
- [74] MacKenzie JK. *Proc Phys Soc B* 1950;63:2.
- [75] Suryanarayana R, Frey CA, Sastry SML, Waller BE, Buhro WE. Processing and properties of nanocrystalline materials. In: Suryanarayana C, Singh J, Froes FH. Warrendale: TMS; 1996.
- [76] Nieman GW, Weertman JR, Siegel RW. *J Mater Res* 1991;6:1012–27.
- [77] Koch CC, Morris DG, Lu K, Inoue A. *MRS Bull* 1999;24:54.
- [78] Koch CC. *Nanocryst Mater* 2003;18:9.
- [79] Swygenhoven HV, Caro A. *Nanostruct Mater* 1997;9:669–72.
- [80] Schiotz J, DiTolla FD, Jacobsen KW. *Nature* 1998;391:561.
- [81] Yip S. *Nature* 1998;391:669.
- [82] Swygenhoven HV, Caro A, Spaczer M. *Acta Mater* 1999;47:3117–26.
- [83] Yamakov V, Wolf D, Salazar M, Phillpot SR, Gleiter H. *Acta Mater* 2001;49:2713–22.
- [84] Yamakov V, Wolf D, Phillpot SR, Mukherjee AK. *Nature* 2002;1:45.
- [85] Conrad H. *Met Mater Trans* 2004;35A:2541.

- [86] Conrad H, Narayan J. *Acta Mater* 2002;50:5067.
- [87] Zhang X, Wang H, Scattergood RO, Narayan J, Koch CC. *Acta Mater* 2002;50:3995.
- [88] Zhang X, Wang H, Scattergood RO, Narayan J, Koch CC. *Acta Mater* 2002;50:3527.
- [89] Zhang X, Wang H, Scattergood RO, Narayan J, Koch CC. *Acta Mater* 2002;50:4823.
- [90] Valiev RZ, Alexandrov IV, Zhu YT, Lowe TC. *J Mater Res* 2002;17:5–8.
- [91] Hanaoui A, Van Swygenhoven H, Derlet PM. *Acta Mater* 2002;50:3927.
- [92] Chen MW, Ma E, Hemkar KJ, Sheng HW, Wang YM. *Science* 2003;300:1275.
- [93] Zhu YT, Liao X. *Nature Mater* 2004;4:351.
- [94] Lu L, Schwaiger R, Shan ZW, Dao M, Lu K, Suresh S. *Acta Mater* 2005;53:2169.
- [95] Schuh CA, Nieh TG, Iwasaki H. *Acta Mater* 2003;51:431–43.
- [96] Koch CC. *Scripta Mater* 2003;49:657–62.
- [97] Chokshi AH, Rosen A, Karch J, Gleiter H. *Scripta Mater* 1989;23:1679–84.
- [98] Hoffer HJ, Averbach RS. *Scripta Metall Mater* 1990;24:2401–6.
- [99] Lu K, Wei WD, Wang JT. *Scripta Metall Mater* 1990;24:2319–23.
- [100] Hughes GD, Smith SD, Pande CS, Johnson HR, Armstrong RW. *Scripta Metall* 1986;20:93–7.
- [101] Nieman GW, Weertman JR, Siegel RW. *Scripta Metall* 1989;23:2013–8.
- [102] Weertman JR. *Mater Sci Eng A* 1993;166:161–7.
- [103] Fu HH, Benson DJ, Meyers MA. *Acta Mater* 2001;49:2567–82.
- [104] Volpp T, Göring E, Kuschke WM, Artz E. *Nanostruct Mater* 1997;8:855.
- [105] Iyer RS, Frey CA, Sastry SML, Waller BE, Buhro WE. *Mater Sci Eng A—Struct Mater Properties Microstruct Process* 1999;264:210–4.
- [106] Carsley JE, Fisher A, Milligan WW, Aifantis EC. *Metall Mater Trans A—Phys Metall Mater Sci* 1998;29:2261–71.
- [107] Jia D, Wang YM, Ramesh KT, Ma E, Zhu YT, Valiev RZ. *Appl Phys Lett* 2001;79:611–3.
- [108] Wang YM, Ma E, Chen MW. *Appl Phys Lett* 2002;80:2395–7.
- [109] Jia D, Ramesh KT, Ma E. *Scripta Mater* 2000;42:73.
- [110] Wei Q, Jia D, Ramesh KT, Ma E. *Appl Phys Lett* 2002;81:1240–2.
- [111] Van Swygenhoven H, Caro A. *Appl Phys Lett* 1997;71:1652–4.
- [112] Malow TR, Koch CC, Miraglia PQ, Murty KL. *Mater Sci Eng A* 1998;252:36.
- [113] Gray GT, Lowe TC, Cady CM, Valiev RZ, Aleksandrov IV. *Nanostruct Mater* 1997;9:477–80.
- [114] Wang N, Wang ZR, Aust KT, Erb U. *Mater Sci Eng A—Struct Mater Properties Microstruct Process* 1997;237:150–8.
- [115] Tanimoto H, Sakai S, Mizubayashi H. *Nanostruct Mater* 1999;12:751–6.
- [116] Kong QP, Cai B, Lu L, Lu K. *Def Diff Met* 2001;188:45–58.
- [117] May J, Höppel HW, Göken M. *Scripta Mater*, in press.
- [118] May J, Höppel HW, Göken M. In: Horita Z, Langdon TG, editors. *Proceedings of the 3rd international conference on nanomaterials by severe plastic deformation, Nanospd 3, Fukuoka, Japan, 2005*.
- [119] Höppel HW, May J, Göken M. *Adv Eng Mat* 2004;6:781.
- [120] Zhang X, Wang H, Scattergood RO, Narayan J, Koch CC, Sergueeva AV, et al. *Acta Mater* 2002;50:4823–30.
- [121] Jia D, Ramesh KT, Ma E. *Acta Mater* 2003;51:3495–509.
- [122] Kocks UF, Argon AS, Ashby MF. *Prog Mater Sci* 1975;19:1.
- [123] Zerilli F, Armstrong RW. *J Appl Phys* 1990;68:1580.
- [124] Palumbo G, Thorpe SJ, Aust KT. *Scripta Metall Mater* 1990;24:1347–50.
- [125] Wang N, Wang Z, Aust KT, Erb U. *Acta Mater* 1995;43:1905–10.
- [126] Chokshi AH. *Scripta Mater* 1996;34:1905–10.
- [127] Wang DL, Kong QP, Shui JP. *Scripta Metall Mater* 1994;31:47–51.
- [128] Deng J, Wang DL, Kong QP, Shui JP. *Scripta Metall Mater* 1995;32:349–52.
- [129] Nieman GW, Weertman JR, Siegel RW. *Scripta Metall Mater* 1990;24:145–50.
- [130] Hahn H, Averbach RS. *J Am Ceram Soc* 1991;74:2918.
- [131] Sanders PG, Rittner M, Kiedaisch E, Weertman JR, Kung H, Lu YC. *Nanostruct Mater* 1997;9:433–40.
- [132] Ogino Y. *Scripta Mater* 2000;43:149–53.
- [133] Wang N, Wang Z, Aust KT, Erb U. *Mater Sci Eng A* 1997;237:150–8.
- [134] Cai B, Kong QP, Lu L, Lu K. *Mater Sci Eng A* 2000;286:188–92.
- [135] Li YJ, Blum W, Breutinger F. *Mater Sci Eng A* 2004;387–389:585–9.
- [136] Grabovetskaya GP, Ivanov KV, Kolobov YR. *Ann Chim Sci Mater* 2002;27:89–98.

- [137] Estrin Y, Gottstein G, Shvindlerman LS. *Scripta Mater* 2004;50:993–7.
- [138] Yamakov V, Wolf D, Phillipot SR, Gleiter H. *Acta Mater* 2002;50:61–73.
- [139] Haslam AJ, Yamakov V, Moldovan D, Wolf D, Phillipot SR, Gleiter H. *Acta Mater* 2004;52:1971–87.
- [140] Chokshi AH. *Scripta Mater* 2003;48:791–6.
- [141] Yin WM, Whang SH, Mirshams RA. *Acta Mater* 2005;53:383–92.
- [142] Whitney AB, Sanders PG, Weertman JR. *Scripta Metall Mater* 1995;33:2025–30.
- [143] Yan DS, Qiu HB, Zheng YS, Gao L. *Nanostruct Mater* 1997;9:441–50.
- [144] Vinogradov AY, Stolyarov VV, Hashimoto S, Valiev RZ. *Mater Sci Eng A* 2001;318:163–73.
- [145] Pelloux RM. In: Burke JJ, Weiss V, editors. *Ultrafine-grain metals*. Syracuse University Press; 1970. p. 231.
- [146] Patlan V, Higashi K, Kitagawa K, Vinogradov A, Kawazoe M. *Mater Sci Eng A* 2001;319–321: 587–91.
- [147] Patlan V, Vinogradov A, Higashi K, Kitagawa K. *Mater Sci Eng A* 2001;300:171–82.
- [148] Vinogradov A, Patlan V, Kitagawa K, Kawazoe M. *Nanostruct Mater* 1999;11:925.
- [149] Chung CS, Kim JK, Kim HK, Kim WJ. *Mater Sci Eng A* 2002;337:39–44.
- [150] Kim HK, Choi ML, Chung CS, Shin DH. *Mater Sci Eng A* 2003;340:243–50.
- [151] Schino AD, Kenny JM. *Mater Lett* 2003;57:3182–5.
- [152] Hanlon T, Kwon Y-N, Suresh S. *Scripta Mater* 2003;49:675–80.
- [153] Chapetti MD, Miyata H, Tagawa T, Miyata T, Fujioka M. *Mater Sci Eng A* 2004;381:331–6.
- [154] Mughrabi H, Hoppel HW, Kautz M. *Scripta Mater* 2004;51:807–12.
- [155] Ding HZ, Mughrabi H, Hoppel HW. *Fatigue Fract Eng Mater Struct* 2002;25:975.
- [156] Kim HK, Lee YI, Chung CS. *Scripta Mater* 2005;52:473–7.
- [157] Chapetti MD, Miyata H, Tagawa T, Miyata T, Fujioka M. *Int J Fatigue* 2005;27:235–43.
- [158] Lukas P, Kunz L, Svoboda M. *Mater Sci Eng* 2005;A391:337–41.
- [159] Duan RG, Zhan GD, Kuntz JD, Kear BH, Mukherjee AK. *Scripta Mater* 2004;51:1135–9.
- [160] Kear BH, Colaizzi J, Mayo WE, Liao SC. *Scripta Mater* 2001;44:2065–8.
- [161] Li J, Ye Y, Shen L, Chen J, Zhou H. *Mater Sci Eng A* 2005;390:265–70.
- [162] Buscaglia V, Viviani M, Buscaglia MT, Nanni P, Mitoseriu L, Testino A, et al. *Powder Technol* 2004;148: 24–7.
- [163] Lu W, Schmidt H. *J Eur Ceram Soc* 2005;25:919–25.
- [164] Anilkumar M, Ravi V. *Mater Res Bull*, in press.
- [165] Chang YQ, Xu XY, Luo XH, Chen Cp, Yu DP. *J Cryst Growth* 2004;264:232.
- [166] Zhang YC, Qiao T, Hu XY. *J Solid State Chem* 2004;177:4093.
- [167] Finocchio E, Busca G. *Catal Today* 2001;70:213.
- [168] Ehre D, Gutmanas EY, Chaim R. *J Eur Ceram Soc*, in press.
- [169] Thangadurai P, Sabarinathan V, Bose AC, Ramasamy S. *J Phys Chem Solids* 2004;65:1905–12.
- [170] Gaikwad SP, Dhesphande SB, Kholam YB, Samule V, Ravi V. *Mater Lett* 2004;58:3474–6.
- [171] Zhang F, Yang SP, Wang WM, Chen HM, Wang ZH, Yu XB. *Mater Lett* 2004;58:3285–9.
- [172] Forrester JS, Zobec JS, Phelan D, Kisi EH. *J Sol State Chem* 2004;177:3553–9.
- [173] Silva JB, Brito W, Mohallem NDS. *Mater Sci Eng B* 2004;112:182–7.
- [174] Bhagwat M, Ramaswamy V. *Mater Res Bull* 2004;39:1627–40.
- [175] Dhage SR, Choube VD, Samule V, Ravi V. *Mater Lett* 2004;58:2310–3.
- [176] Chen L, Gu Y, Qian Y, Shi L, Yang Z, Ma J. *Mater Res Bull* 2004;39:609–13.
- [177] Lemos FCD, Longo E, Leite ER, Melo DMA, Silva AO. *J Solid State Chem* 2004;177:1542–8.
- [178] Rajesh K, Sivakumar B, Pillai PK, Mukundan P, Warriar KKG, Nair VR. *Mater Lett* 2004;58:1687–91.
- [179] Li Y, Zhao J, Wang B. *Mater Res Bull* 2004;39:365–74.
- [180] Feng X, Bai YJ, Lu B, Zhao YR, Yang J, Chi JR. *J Cryst Growth* 2004;262:420.
- [181] Zhang TS, Ma J, Kong LB, Hing P, Kilner JA. *Solid State Ionics* 2004;167:191–6.
- [182] Han Y, Li S, Wang X, Chen X. *Mater Res Bull* 2004;39:25–32.
- [183] Luan W, Gao L, Kawaoka H, Sekino T, Niihara K. *Ceram Int* 2004;30:405–10.
- [184] Piticescu RM, Moisin AM, Taloi D, Badilita V, Soare I. *J Eur Ceram Soc* 2004;24:931–5.
- [185] Pradhan AK, Zhang K, Loutts GB. *Mater Res Bull* 2004;39:1291–8.
- [186] Kim HT, Han YH. *Ceram Int* 2004;30:1719–23.
- [187] Lascalea GE, Lamas DG, Perez L, Cabanillas ED, de Reca NEW. *Mater Lett* 2004;58:2456–60.
- [188] Frolova EV. *Mater Sci Eng C* 2003;23:1093–7.
- [189] Dhage SR, Kholam YB, Deshpande SB, Ravi V. *Mater Res Bull* 2003;38:1601–5.
- [190] Lichtenberger O, Pippel E, Woltersdorf J, Riedel R. *Mater Chem Phys* 2003;81:195–201.

- [191] Nersisyan HH, Lee JH, Won CW. *Mater Res Bull* 2003;38:1135–46.
- [192] Lee YI, Lee JH, Hong SH, Kim DY. *Mater Res Bull* 2003;38:925–30.
- [193] Cheng QM, Interrante LV, Lienhard M, Shen Q, Wu Z. *J Eur Ceram Soc* 2005;25:233–41.
- [194] Panda AB, Pathak A, Nandagoswami M, Pramanik P. *Mater Sci Eng B* 2003;97:275–82.
- [195] Xue JM, Wan DM, Wang J. *Solid State Ionics* 2002;151:403–12.
- [196] Gu Y, Qian Y, Chen L, Zhou F. *J Alloys Compd* 2003;352:325–7.
- [197] Nordahl CS, Messing GL. *J Eur Ceram Soc* 2002;22:415–22.
- [198] Markmann J, Tschöpe A, Birringer R. *Acta Mater* 2002;50:1433–40.
- [199] Kim BC, Lee JH, Kim JJ, Ikegami T. *Mater Lett* 2002;52:114–9.
- [200] Bab MA, Zelis-Mendoza L, Damonte LC. *Acta Mater* 2001;49:4205–13.
- [201] Zhu X, Kunyu Z, Baochang C, Qiushi L, Xiuqin Z, Tieli C, et al. *Mater Sci Eng C* 2001;16:103–5.
- [202] Lu J, Ueda K, Yagi H, Yanagitani T, Akiyama Y, Kaminskii AA. *J Alloys Compd* 2002;341:220–5.
- [203] Laberty-R C, Ansart F, Deloget C, Gaudon M, Rousset A. *Mater Res Bull* 2001;36:2083–101.
- [204] Li JG, Ikegami T, Lee JH, Mori T. *Acta Mater* 2001;49:419–26.
- [205] Choy KL. *Mater Sci Eng C* 2001;16:139–45.
- [206] Zawadzki M, Wrzyszczyk J, Strek W, Hreniak D. *J Alloys Compd* 2001;323–324:279–82.
- [207] Jose R, James J, John AM, Sundararaman D, Divakar R, Koshy J. *Nanostruct Mater* 1999;11:623–9.
- [208] Das RN. *Mater Lett* 2001;47:344–50.
- [209] Lu CH, Saha SK. *Mater Res Bull* 2000;35:2135–43.
- [210] Li JG, Sun X. *Acta Mater* 2000;48:3103–12.
- [211] Juarez RE, Lamas DG, Lascalea GE, Walsöe de Reca NE. *J Eur Ceram Soc* 2000;20:133–8.
- [212] Yue Z, Zhou J, Li L, Zhang H, Gui Z. *J Magn Magn Mater* 2000;208:55–60.
- [213] Das RN, Pramanik P. *Mater Lett* 1999;40:251–4.
- [214] Liao SC, Chen YJ, Mayo WE, Kear BH. *Nanostruct Mater* 1999;11:553–7.
- [215] Shantha K, Varma KBR. *Mater Sci Eng B* 1999;56:66–75.
- [216] Jiang JS, Yang XL, Gao L, Guo JK, Jiang JZ. *Nanostruct Mater* 1999;12:143–6.
- [217] Haber JA, Gunda NV, Buhro WE. *J Aerosol Sci* 1998;29:637–45.
- [218] Ragulya AV. *Nanostruct Mater* 1998;10:349–55.
- [219] Popp U, Herbig R, Michel G, Müller E, Oestreich C. *J Eur Ceram Soc* 1998;18:1153–60.
- [220] Lamas DG, Juárez RE, Caneiro A, Walsöe de Reca NE. *Nanostruct Mater* 1998;10:1199–207.
- [221] Lamas DG, Lascalea GE, Reca NEW. *J Eur Ceram Soc* 1998;18:1217–21.
- [222] Pinckney LR, Beall GH. *J Non-Cryst Solids* 1997;219:219–27.
- [223] Pal M, Brahma P, Chakravorty D, Bhattacharyya D, Maiti HS. *Nanostruct Mater* 1997;8:731–8.
- [224] Zhang Z, Zhu Y, Hu L. *Nanostruct Mater* 1996;7:453–9.
- [225] Durán P, Villegas M, Capel F, Recio P, Moure C. *J Eur Ceram Soc* 1996;16:945–52.
- [226] Qui HB, Gao L, Qiao HC, Guo JK, Yan DS. *Nanostruct Mater* 1995;6:373–6.
- [227] Kats-Demyanets A, Chaim R. *Nanostruct Mater* 1995;6:851–4.
- [228] Bykov Y, Gusev S, Eremeev A, Holoptsev V, Malygin N, Pivarunas S, et al. *Nanostruct Mater* 1995;6:855–8.
- [229] Bravo-Leon A, Morikawa Y, Kawahara M, Mayo MJ. *Acta Mater* 2002;50:4555–62.
- [230] Wakai F, Kondo N, Ogawa H, Nagano T, Tsurekawa S. *Mater Charac* 1996;37:331.
- [231] Jimenez-Melendo M, Rodriguez-Dominguez A, Bravo-Leon A. *J Am Ceram Soc* 1998;81:2761.
- [232] Mayo MJ, Seidensticker JR, Hague DC, Carim AH. *Nanostruct Mater* 1999;11:271–82.
- [233] Mondal P, Klein A, Jaegermann W, Hahn H. *Solid State Ionics* 1999;118:331–9.
- [234] Betz U, Hahn H. *Nanostruct Mater* 1999;12:911–4.
- [235] Betz U, Scipione G, Bonetti E, Hahn H. *Nanostruct Mater* 1997;8:845–53.
- [236] Winnubst AJA, Boutz MMR, He YJ, Burggraaf AJ, Verweij H. *Ceram Int* 1997;23:215–21.
- [237] He YJ, Winnubst AJA, Sagel-Ransijn CD, Burggraaf AJ, Verweij H. *J Eur Ceram Soc* 1996;16:601–12.
- [238] Sánchez-Bajo F, Cumbre FL, Guiberteau F, Domínguez-Rodríguez A, Tsodikov MV. *Mater Lett* 1998;33:283–9.
- [239] Gutiérrez-Mora F, Domínguez-Rodríguez A, Jiménez-Melendo M. *Nanostruct Mater* 1999;11:531–7.
- [240] Mayo MJ. *Nanostruct Mater* 1997;9:717–26.
- [241] Mayo MJ. *Mater Des* 1993;14:323.
- [242] Pande CS, Masumura RA, Armstrong RW. *Nanostruct Mater* 1993;2:323–31.
- [243] Hughes GD, Smith SD, Pande CS, Johnson HR, Armstrong RW. *Scripta Mater* 1986;20:93–7.

- [244] Armstrong RW, Hughes GD. The limiting strength properties of nanocrystalline materials. In: Chubng YW, editor. *Advanced materials for the twenty-first century: The Julia Weertman symposium*. TMS; 1999. p. 409–20.
- [245] Smith TR, Armstrong RW, Hazzledine PM, Masamura RA, Pande CS. *Mater Res Soc Proc* 1995;362:31–7.
- [246] Koch CC. *J Non-Cryst Solids* 1990;117:670–8.
- [247] Nieh TG, Wadsworth J. *Scripta Metall Mater* 1991;25:955–8.
- [248] Ball A, Hutchinson MM. *J Mater Sci* 1969;3:1.
- [249] Hahn H, Mondal P, Padmanabhan KA. *Nanostruct Mater* 1997;9:603.
- [250] Conrad H, Narayan J. *Scripta Mater* 2000;42:1025.
- [251] Kim HS, Estrin Y, Bush MB. *Acta Mater* 2000;48:493–504.
- [252] Konstantinidis DA, Aifantis EC. *Nanostruct Mater* 1998;10:1111.
- [253] Kim HS, Bush MB, Estrin Y. *Mater Sci Eng A* 1999;276:180.
- [254] Kim HS, Hong SI. *Acta Mater* 1999;47:2059.
- [255] Van Swygenhoven H, Derlet PM. *Phys Rev B* 2001;64.
- [256] Van Swygenhoven H, Caro A, Farkas D. *Scripta Mater* 2001;44:1513–6.
- [257] Meyers M, Benson D, Fu HH. *Advanced materials for the 21st century*. In: Chung YW, Dunard D, Liaw P, Olson G, editors; 1999.
- [258] Van Swygenhoven H, Spaczer M, Caro A. *Acta Mater* 1999;47:561.
- [259] Li JCM. *Trans Met Soc* 1963;227:239.
- [260] Li JCM. *JAP* 1961;32:525.
- [261] Raj R, Ashby M. *J Met Trans* 1971;2A:1113.
- [262] Li JCM, Chou YT. *Met Trans* 1970;1:1145.
- [263] Ashby MF, Verall RA. *Acta Mater* 1973;21:149.
- [264] Ashby MF. *Philos Mag* 1970;21:399.
- [265] Benson DJ, Fu HH, Meyers MA. *Mater Sci Eng A* 2001;319–321:854–61.
- [266] Meyers M, Ashworth E. *Philos Mag A* 1982;46:737.
- [267] Hirth JP, Lothe J. *Theory of dislocations*. New York: McGraw-Hill; 1982.
- [268] Thompson AW. *Work hardening in tension and fatigue*. In: Thompson AW, editor; 1977.
- [269] Margolin H. *Acta Mater* 1998;46:6305.
- [270] Gray GT. *Nanostruct Mater* 1997;9:477.
- [271] Murr LE, Hecker SS. *Scripta Mater* 1979;13:167.
- [272] Sun S, Adams BL, Shet C, Saigal S, King W. *Scripta Mater* 1998;39:501.
- [273] Kim HS, Estrin Y, Bush MB. *Mater Sci Eng A* 2001;316:195.
- [274] Murayama M, Howe JM, Hidaka H, Takaki S. *Science* 2002;295:2433–5.
- [275] Ovid'ko IA. *Science* 2002;295:2386.
- [276] Jiang X, Jia CL. *Appl Phys Lett* 1996;69:3902–4.
- [277] Michler J, von Kaenel Y, Stiegler J, Blank E. *J Appl Phys* 1998;83:187–97.
- [278] Ma E. *Scripta Mater* 2003;49:663–8.
- [279] Meyers MA, Xu YB, Xue Q, Perez-Prado MT, McNelly TR. *Acta Mater* 2003;51:1307–25.
- [280] Meyers M, Pak HR. *Acta Mater* 1986;34:2493.
- [281] Meyers MA, Subhash G, Kad BK, Prasad L. *Mech Mater* 1994;17:175.
- [282] Andrade UR, Meyers MA, Vecchio KS, Chokshi AH. *Acta Metall Mater* 1994;42:3183.
- [283] Chen RW, Vecchio KS. *J Phys IV* 1994;4:C8-4591.
- [284] Xu YB, Zhong WL, Chen YJ, Shen LT, Liu Q, Bai YL, et al. *Mater Sci Eng A* 2001;299:287.
- [285] Li Q, Xu YB, Lai ZH, Shen LT, Bai YL. *Mater Sci Eng A* 2000;276:127.
- [286] Meyers MA, Andrade U, Chokshi AH. *Metall Mater Trans A* 1995;26:2881.
- [287] Nesterenko VF, Lazaridi AN, Pershin SA. *Fizika Goreniya Vzyva* 1989;25:154.
- [288] Nesterenko VF, Bondar MP, Ershov IV. *High pressure science and technology*. In: Schidt SC, Shanner JW, Samara GA, Ross M, editors. *High pressure science and technology*. New York: AIP Press; 1994.
- [289] Grebe HA, Pak HR, Meyers MA. *Met Trans* 1985;16A:711.
- [290] Meyers M, Chen YJ, Marquis FDS, Kim DS. *Metall Mater Trans A* 1995;26:2493.
- [291] Nesterenko VF, Meyers MA, LaSalvia JC, Bondar MP, Chen YJ, Lukyanov YL. *Mater Sci Eng A* 1997;229:23.
- [292] Nemat-Nasser S, Issacs JB, Liu M. *Acta Mater* 1998;46:1307.
- [293] Chen RW, Vecchio KS. *J Phys IV* 1994;4:C8-459.
- [294] Xu YB, Zhong LB, Chen YJ, Shen LT, Liu Q, Bai YL, et al. *Mater Sci Eng A* 2001;299:287.



- [295] Meyers MA, Andrade UR, Chokshi AH. *Metall Mater Trans A* 1995;26:2881.
- [296] Aifantis EC. *Int J Plast* 1987;3:211.
- [297] Fleck NA, Hutchinson JW. *J Mech Phys Sol* 1993;41:1825.
- [298] Fleck NA, Muller GM, Ashby MF, Hutchinson JW. *Acta Metall Mater* 1994;42:475.
- [299] Venables JA. *Philos Mag* 1961;6:379.
- [300] Narita N, Takamura J-I. In: Nabarro FRN, editor. *Dislocations in solids*. Amsterdam: Elsevier; 1992. p. 135.
- [301] Vöhringer O. *Sonderdruck Aus Heft* 1972;11:1119.
- [302] Gao H, Huang JY, Nix WD, Hutchinson JW. *J Mech Phys Sol* 1999;47:1239.
- [303] Gao H, Huang JY, Nix WD, Hutchinson JW. *Mech Phys Sol* 2000;48:99.
- [304] Wang Y, Chen M, Zhou F, Ma E. *Nature* 2002;419:912–5.
- [305] Lu L, Shen Y, Chen X, Qian L, Lu K. *Science* 2004;304:422.
- [306] Meyers MA, Voehringer O, Lubarda V. *Acta Mater* 2001;49:4025.
- [307] El-Danaf E, Kalidindi SR, Doherty RD. *Metall Mater Trans* 1999;30A:1223.
- [308] Yamakov V, Wolf D, Phillpot SR, Gleiter H. *Acta Mater* 2002;50:5005.
- [309] Yamakov V, Wolf D, Phillpot SR, Gleiter H. *Acta Mater* 2003;51:4135.
- [310] Chen M, Ma E, Hemker KJ, Sheng H, Wang Y, Cheng X. *Science* 2003;300:1275.
- [311] Liao XZ, Zhou F, Lavernia EJ, He DW, Zhu YT. *Appl Phys Lett* 2003;83:5062.
- [312] Zhu YT, Liao SG, Srinivasan SG, Zhao YH, Baskes MI, Zhou F, et al. *Appl Phys Lett* 2004;85:5049.
- [313] Van Swygenhoven H, Spaczer M, Farkas D, Caro A. *Nanostruct Mater* 1999;12:323.
- [314] Van Swygenhoven H, Caro A, Farkas D. *Mater Sci Eng A* 2001;309–310:440.
- [315] Van Swygenhoven H, Derlet PM. *Scripta Mater* 2002;47:719–24.
- [316] Van Swygenhoven H, Dalla Torre F, Victoria M. *Acta Mater* 2002;50:2957–3950.
- [317] Van Swygenhoven H, Derlet PM, Victoria M, Samaras M. *Nucl Inst Meth Phys Res B* 2003;202:51–5.
- [318] Van Swygenhoven H, Derlet PM, Hasnaoui A. *Scripta Mater* 2003;49:629–35.
- [319] Van Swygenhoven H, Derlet PM, Hasnaoui A. *Acta Mater* 2004;52:2251–8.
- [320] Van Swygenhoven H, Derlet PM, Froseth A. *Acta Mater* 2004;52:2259–68.
- [321] Kelly A, Groves GW. *Crystallography and crystal defects*. Addison-Wesley; 1970. p. 235.
- [322] Huang JY, Zhu YT, Jiang H, Lowe TC. *Acta Mater* 2001;49:1497.
- [323] Sutton AP, Balluffi RW. *Interfaces in crystalline materials*. Oxford; 1995.
- [324] Murr LE. *Interfacial phenomena in metals and alloys*. Reading, MA: Addison-Wesley; 1975.
- [325] Liao XZ, Srinivasan SG, Zhao YH, Baskes MI, Zhu YT, Zhou F, et al. *Appl Phys Lett* 2004;84:3564.
- [326] Asaro RJ, Krysl P, Kad B. *Philos Mag* 2003;83:733.
- [327] Gharemani F, Hutchinson JW. *J Am Ceram Soc* 1990;73:1548.
- [328] Asaro RJ, Suresh S. *Acta Mater* 2005;53:3369.
- [329] Xiao C, Mirshams RA, Whang SH, Yin WM. *Mater Sci Eng A* 2001;301:35.
- [330] Mirshams RA, Xiaoh CH, Whang SH, Yin WM. *Mater Sci Eng A* 2001;315:21.
- [331] Kumar KS, Suresh S, Chrsholm MF, Horton JA, Wang P. *Acta Mater* 2003;51:387.
- [332] Wei YJ, Anand L. *J Mech Phys Sol* 2004;52:2587–616.
- [333] Diehl J. *Z Metall* 1956:331.
- [334] Suzuki H, Ikeda T. *J Phys Soc* 1956;1:382.
- [335] Fu HH, Benson DJ, Meyers MA. *Acta Mater* 2004;52:4413–25.
- [336] Benson DJ. *Comput Meth Appl Mech Eng* 1992;99:235.
- [337] Kadau K, Germann TC, Lomdahl PS, Holian BL, Kadau D, Entel P, et al. *Metall Mater Trans* 2004;35A:2719.
- [338] Froseth AG, Derlet H, Van Swygenhoven H. *Acta Mater* 2004;52:5863.
- [339] Tadmor EB, Ortiz M, Phillips R. *Philos Mag A* 1996;73:1529.
- [340] Shenoy VB, Miller R, Tadmor EB, Rodney D, Phillips R, Ortiz M. *J Mech Phys Solids* 1999;47:611.
- [341] Sansoz F, Molinari JF. *Scripta Mater* 2004;50:1283.
- [342] Bringa EM, Caro A, Victoria M, Park N. *JOM* 2005;57:67.
- [343] Meyers MA. *Mater Sci Eng* 1977;30:99.
- [344] Meyers MA, Carvalho MS. *Mater Sci Eng* 1976;24:131.
- [345] Okazaki K, Conrad H. *Trans JIM* 1972;13:205.
- [346] Schoeck G, Wielke B. *Scripta Metall* 1976;10:771.
- [347] Hirth JP, Lothe J. *Theory of dislocations*. Wiley; 1982.
- [348] Meyers MA, Vöhringer O, Lubarda VA. *Acta Mater* 2001;49:4025.

- [349] Gleiter H. *Nanostruct Mater* 1992;1:1.
- [350] Suryanarayana C, Koch CC. *Hyperfine Interact* 2000;130:5–44.
- [351] Mohamed FA, Li Y. *Mater Sci Eng A* 298:1–15.
- [352] Kumar KS, Van Swygenhoven H, Suresh S. *Acta Mater* 2003;51:5743–74.
- [353] Veprek S, Veprek-Heijman MGJ, Karvankova P, Prochazka J. *Thin Solid Films* 2005;476:1–29.
- [354] Wolf D, Yamakov V, Phillipot SR, Mukherjee A, Gleiter H. *Acta Mater* 2005;53:1.
- [355] Fougere GE, Weertman JR, Siegel RW, Kim S. *Scripta Metall Mater* 1992;26:1879–83.
- [356] Lu K, Sui ML. *Scripta Mater* 1993;28:1465.
- [357] Song HW, Guo SR, Hu ZQ. *Nanostruct Mater* 1999;11:203.
- [358] Chattopadhyay PP, Pabi SK, Manna I. *Z Metall* 2000;91:1049–51.
- [359] Takeuchi S. *Scripta Mater* 2001;44:1483.
- [360] Yamakov V, Wolf D, Phillipot SR, Mukherjee AK, Gleiter H. *Philos Mag Lett* 2003;83:385–93.
- [361] Weertman JR, Farkas D, Hemker K, Kung H, Mayo M, Mitra R, et al. *MRS Bull* 1999;24:44.
- [362] Hsu MS, Meyers MA, Berkowitz A. *Scripta Metall Mater* 1995;32:805.
- [363] Weertman JR, Farkas D, Kung H, Mayo M, Mitra R, Swygenhoven H. *MRS Bull* 1999;24:44.
- [364] Jones OE, Holland JR. *Acta Metall* 1968;16:1037.
- [365] Morris DG. *Mechanical behavior of nanostructured materials*. Trans Tech Publication Ltd; 1998.
- [366] Lee KM, Lee DJ, Ahn H. *Mater Lett* 2004;58:3122.
- [367] Zhou F, Liao XZ, Zhu YT, Dallek S, Lavernia EJ. *Acta Mater* 2003;51:2777–91.
- [368] Aihara T, Akiyana E, Aoki K, El-Eskandarany M, Habazaki H, Hashimoto K, et al. In: Inoue A, Hashimoto K, editors. *Amorphous and nanocrystalline materials*; 2000. p. 103.
- [369] Wei Q, Cheng S, Ramesh KT, Ma E. *Mater Sci Eng A* 2004;381:71.
- [370] Conrad H. *Met Mater Trans* 2004;35A:2681.
- [371] Wei Q, Kecskes L, Jiao T, Hartwig KT, Ramesh KT, Ma E. *Acta Mater* 2004;52:1859–69.
- [372] Xue Q, Liao XZ, Zhu YT, Gray GT. *Mater Sci Eng*, in press.
- [373] Swygenhoven HV, Derlet, PM, Hasnaoui A. *Interaction between dislocations and grain boundaries under an indenter—a molecular dynamics simulation*.
- [374] Weertman J. In: Koch C, editor. *Nanostructured materials*. Norwich, NY: Noyes Publications; 2002. p. 393–417.